

**ON ELASTIC-PLASTIC CRACKS
BETWEEN DISSIMILAR MEDIA**

by

EDWARD ZYWICZ

B.S.E.M., UNIVERSITY OF ILLINOIS, 1983

S.M.M.E., MASSACHUSETTS INSTITUTE OF TECHNOLOGY, 1986

SUBMITTED IN PARTIAL FULFILLMENT
OF THE REQUIREMENTS FOR THE
DEGREE OF
DOCTOR OF PHILOSOPHY
IN MECHANICAL ENGINEERING

at the

MASSACHUSETTS INSTITUTE OF TECHNOLOGY
May 1988

©Massachusetts Institute of Technology, 1988

Signature of Author _____
Department of Mechanical Engineering
May 31, 1988

Certified by _____
Professor David M. Parks
Thesis Supervisor

Accepted by _____
Professor Ain Ants Sonin, Chairman
Departmental Committee on Graduate Studies

Archives
MASSACHUSETTS INSTITUTE
OF TECHNOLOGY

SEP 06 1988

On Elastic-Plastic Cracks Between Dissimilar Media

by

Edward Zywickz

Submitted to the Department of Mechanical Engineering
on May 31, 1988 in partial fulfillment of the
requirements for the Degree of Doctorate of Philosophy in
Mechanical Engineering

Abstract

The asymptotic elastic behavior of interfacial cracks occurring between two dissimilar isotropic media is reviewed. Distinct solutions, based on differing assumptions regarding crack-tip boundary conditions, can be generated. The assumption of traction-free crack-tip faces generally leads to oscillatory singular asymptotic fields which mathematically cause crack-face interpenetration, an inconsistency which can be alleviated by alternatively assuming asymptotic (frictionless) contact. Both cases produce singular crack-tip stresses which cannot be sustained in materials capable of limited plastic flow, and small scale yielding (SSY) should be considered.

Conditions for SSY within surrounding dominant elastic regions of both traction-free and frictionless contact are considered, and the subset of admissible loads producing physically realistic conditions are identified for each crack-tip idealization. Approximate closed form expressions for the plastic zone size and shape are obtained as the locus of points where the elastically-calculated Mises stress equals the tensile yield strength, σ_{ys} . In defining elastic and plastic traction-free crack-tip fields, both a magnitude and phase angle are required. The SSY interfacial load phase angle (ILPA), defined as $\zeta_0 = \angle \mathbf{K} + \epsilon \ln \left(\mathbf{K} \bar{\mathbf{K}} / \sigma_{ys}^2 \pi \cosh^2(\pi \epsilon) \right)$ where $\angle \mathbf{K}$ is the phase angle of the complex traction-free stress intensity factor \mathbf{K} and ϵ is the bi-material constant, naturally arises when calculating the approximated plastic zone and conveniently defines the phase angle of the inelastic traction-free fields. The traction-free crack-tip plastic zone size and shape as well as ζ_0 periodically evolve as $|\mathbf{K}|$ increases, while the closed crack-tip plastic zone shape differs little from the homogeneous mode II shape and only depends functionally on the closed bi-material stress intensity factor \mathbf{K}_{II}^c and weakly on the bi-material constant.

Precise SSY numerical calculations for an elastic/perfectly-plastic material atop a rigid or elastic substrate indicate that the plane-strain asymptotic traction-free crack-tip stress fields in the plastically-deforming material are composed of various elastic and plastic sectors. Deep within the plastic zone, no oscillatory stress variations occur, however, a cusp in the slip-line field couples portions of the stress state to the radial distance for certain loads. Generally the maximum interfacial tractions occur for negative ζ_0 when inelastic sectors completely surround the crack-tip. For positive ζ_0 an elastic crack-face sector grows as the ζ_0 increases, and the interfacial shear strains in the plastically deforming medium are small, independent of the actual interfacial sector type. Crack-face contact within the plastic zone may occur at values of ζ_0 when elastic contact outside the plastic zone does not occur. The closed bi-material crack-tip asymptotic stress fields in plane-strain for an elastic/perfectly-plastic material bonded

to a rigid substrate are composed of two fan and two constant state sectors in the deforming region. Compressive crack-face tractions persist even when contained inelastic deformation is included.

Asymptotic interfacial and crack-face tractions appear constant in the crack tip region, but both normal and shear tractions jump at the crack-tip. The asymptotic elastic potential for the lower-elastic stress state is logarithmically singular for non-zero asymptotic interfacial shear tractions, thus inelastic crack-tip deformation in the “elastic” region is anticipated for deformable media. Validity conditions regarding use of an elastic lower half-space and linearized kinematics and the formation of a blunted crack-tip are presented.

Thesis Supervisor: Dr. David M. Parks

Title: Associate Professor of Mechanical Engineering

Acknowledgement

I would like to thank Prof. Abeyaratne, Prof. Argon, and Prof. Rice for being on my thesis committee and for their help in addressing the problem undertaken herein.

I want to extend my thanks to my friends, fellow grad-students, and co-workers for many helpful discussions, some related to and others unrelated to engineering, and for making the environment pleasant and quite bearable during my stay at MIT. I also appreciate all the help Richard Stringfellow gave in helping me revise this thesis.

I wish to acknowledge the generous donations of the Data General Corporation, and the academic license provided from Hibbit, Karlsson, and Sorsensen, Incorporated.

And lastly, I must address the issue of my advisor, Prof. D. M. Parks. In my years working for him, he has let me bounce and spin much as a pinball does in a pinball machine. Sometimes it felt as though I was rebounding aimlessly among the bumpers. But, in times of trouble he always redirected my course with just enough care and (usually) persistence to aim me toward the right pins. And on several occasions when I appeared to be stalling out, it was not below him to cheat and *tilt* a little. For all that I have learned from him and for his guidance, I would just like to let him know that I truly appreciate it.

The work described herein was supported in part by the Office of Naval Research under grant No. N00014-84-K0495, 'Interfaces in Metal Matrix Composites,' and in part by NSF under contract DMR 84-18718.

Table of Context

Abstract	2
Acknowledgement	4
Table of Context	5
Chapter 1 : Introduction and Statement of Problem	10
1.1 Introduction	10
1.1.1 Interfacial Fracture Mechanics Length Scales	11
1.1.2 Considerations of Interface and Crack-Tip Idealizations	13
1.1.3 Homogeneous Fracture Mechanics	15
1.2 Statement of Purpose	17
1.2.1 Statement of Boundary Problem	18
Chapter 2 : Elastic Interfacial Cracks	21
2.1 History and Solution Discussion	21
2.1.1 Traction-Free Crack Faces	21
2.1.1 Closed Crack-Tip Faces	28
2.2 Inferred Plastic Behavior	34
2.2.1 Traction-Free Crack Faces	36
P2 Abstract	37
P2.1 Introduction	38
P2.2 SSY Plastic Zone Approximation	39
P2.3 Discussion	41

P2.3.1 Mathematical Considerations	41
P2.3.2 Zone Growth Considerations	45
P2.3.3 Comparisons	45
P2.3.4 Valid Solution Domain	47
P2.4 Conclusion	57
P2 References	60
P2.A Appendix A : Mises Equivalent Stress Derivation	61
P2.B Appendix B : Interfacial Crack Example	64
2.2.1.1 Additional Discussion	66
2.2.2 Closed Frictionless Crack-Tip Fields	67
2.2.2.1 Plastic Zone Approximation	67
2.2.2.2 Mathematical Features	69
2.2.2.3 Valid Solution Domain	69
2.2.2.4 Comparisons	72
2.2.2.5 Contact Length Approximation	74
2.2.2.6 Conclusion	74
2.3 Small Scale Contact	75
2.3.1 Loading Restrictions for SSC	76
2.3.2 Correspondence of K_{II}^c to \mathbf{K}	77
2.3.3 Accuracy of Contact Length Estimation	79
2.3.4 SSC Summary	81
2.4 Overview	82
2.4.1 Load Map	82
2.4.2 Conclusion	85
Chapter 3 : Description of Solution Technique	87
3.1 Crack-Tip Model Formulation	87

3.1.1 Traction-Free Crack-Tip Faces: Boundary Layer Approach	89
3.1.1.1 Theoretical Considerations	90
3.1.1.2 Boundary Layer Verification	93
3.1.2 Closed Crack-Tip Faces	100
3.2 Elastic/Perfectly-Plastic Constitutive Relationship	100
3.2.1 Kinematics	101
3.2.2 Notation	101
3.2.3 Constitutive Relationship	102
3.2.4 Constitutive Integration Operator	102
3.3 FE Model Considerations	106
3.3.1 Traction-Free Crack-Tip Face Model	107
3.3.1.1 Boundary Layer Implementation	107
3.3.1.2 FE Mesh	108
3.3.1.3 Procedures	111
3.3.2 Traction-Free Crack-Tips: Existence of Stress Oscillations Within the Plastic Zone	112
3.3.3 Closed Crack-Tip Faces	113
 Chapter 4 : Elastic-Plastic Interfacial Crack-Tip Fields	 114
4.1 Asymptotic Crack-Tip Forms	114
4.1.1 Summary of Slip-Line Theory	115
4.1.2 Stationary and Quasi-Static Crack-Tip Forms	116
4.2 Traction-Free Crack-Tip Model	123
4.2.1 Deformable Upper Half-Plane	124
4.2.1.1 Asymptotic Crack-Tip Behavior	124
4.2.1.2 Assemblage of Crack-Tip Fields	136
4.2.1.3 Interfacial Traction and Crack-Tip Fields	137
4.2.1.4 Comparison	138

4.2.1.5 Asymptotic Strain Distribution and CTOD	139
4.2.1.6 Path Dependence of J -Integral	145
4.2.2 Solution in the Lower Elastic Half-Plane	146
4.2.2.1 Formulation of an Elasticity Potential	148
4.2.2.2 Asymptotic Characteristics	155
4.2.2.3 Comparison	157
4.2.3 Parametric Study	157
4.2.3.1 Plastic Crack-Tip Fields and Interfacial Traction	161
4.2.3.2 Strain Distribution and CTOD	167
4.2.3.3 Path Dependence of J -Integral	170
4.2.3.4 Conclusion	171
4.3 Closed Crack-Tip Model	173
4.3.1 Plastic Field	173
4.3.2 Elastic Field	178
4.3.3 Conclusion	182
4.4 Limitations	182
4.4.1 Physical Attributes	184
4.4.2 Evolutionary Limitations	185
Chapter 5 : Summary and Discussion	190
5.1 Summary	190
5.2 Discussion	196
5.2.1 Crack-Face Contact	196
5.2.2 Unifying ILPA	197
5.2.3 Anticipated Experimental Observations	198
5.2.4 Influence of Material Properties on Separation	201
5.2.5 Suggested Additional Work	203

References	205
Appendix A : Boundary Layer Formulation	210
A.1 Energy Considerations	211
A.1.1 Formulation of Equivalent Stiffness Matrix	211
A.1.2 Evaluation of Spring Constants	216
A.2 Boundary Considerations	217
Appendix B : Elastic Wedge Stress Potential	220
Appendix C : User-Written Software	223
C.1 Elastic/Perfectly-Plastic UMAT	223
C.2 Traction-Free Crack-Tip Model	232
C.2.1 Spring Coefficients	232
C.2.2 MPC Subroutine	238
C.3 Closed Crack-Tip : MPC Subroutine	244

Chapter 1

Introduction and Statement of Problem

1.1 Introduction

Efforts in the creation, design, and manufacturing of advanced materials, such as metal matrix composites (MMC), laminated composites, ceramics, and metallic polycrystallines, which may or may not contain second phase particles, have been hampered, from the viewpoint of mechanical performance, due to a lack of knowledge about the processes occurring along the interfaces separating the individual constituents or microstructural boundaries. It is widely recognized that laminated materials can have unique failure modes attributable solely to their layered structure. For example, multi-layered electronic boards are known to fail from thermal cycling along their lamination joints. In MMC, the fiber-matrix interface is the controlling factor in overall composite strength and toughness (Cooper and Kelly, 1969; Ochiai and Murakami, 1981). The approaches used to assess the interfacial stresses have been either: to assume a perfect mathematical interface, which allows the evaluation of the necessary interfacial tractions to preserve overall integrity of the interface; or to postulate the existence of a crack-like defect and analyze it using conventional linear elastic fracture mechanics (LEFM) approaches (*e.g.*, in MMC see Buchholz and Herrman, 1983; Ioakimidis and Theocaris, 1979). No extreme analytical problems are typically encountered in investigating ideal interfaces, but that approach sheds little light on the actual chain of events

in the failure process. On the other hand, LEFM does describe the strength of the singularity, but it also predicts infinite interfacial stresses upon extrapolation to the crack tip. Additionally, the linear material behavior and infinitesimal strain assumptions may be violated near the crack tip. From the mechanical property design viewpoint (*e.g.*, types and thicknesses of fiber coatings in MMC, desirable second phase particles in metallic alloys, binder properties for ceramics), knowledge of the actual interfacial stresses are important, especially in front of a crack, in order to prevent catastrophic material failure or to control the failure mode.

Since the exact failure sequence of bonded dissimilar media remains as yet not fully understood, two major issues pertaining to interfacial separation remain. Of course the primary question is: “what are the interfacial bi-material crack-tip tractions leading to separation?” Because crack deflection is also a possibility, identifying the local crack-tip stress and strain fields are important, especially when non-linear material constitutive relations are used.

1.1.1 Interfacial Fracture Mechanics Length Scales

The size scales associated with problems in which some form of interfacial separation is experienced span a very large range. The geophysical size scale in plate tectonics represents a reasonable upper bound. Here the crust of the earth, which is made up of plate-like structures floating atop a viscous jelly-like mantle, continuously moves, causing massive quantities of potential energy to be stored up as elastic strain energy and released at local premordial fracture or fault sites (Hobbs, Means, and Williams, 1976). In these circumstances the transition or interfacial zone between the two plates may be many meters wide and consist of a variety of different geomorphic media. At more common engineering size scales are the fracture phenomena associated with welding metal structures together. In the welding process two separate pieces are joined together by fusing their common boundary, possibly introducing a filler agent. Due to the melting and solidification process during fusing, the material properties of

the weld usually differ substantially from that of the surrounding bulk material, and flaws may be introduced and embedded into the weld. (Attention is specifically focused upon those flaws which are in or adjoint to and lay parallel to the weld.) The size of the interfacial zone is the weld thickness, which may or may not be small compared to the surrounding structure or flaw. For many diffusion type interfaces, such as seen in Gr/Al MMC, where reactive fiber or coating material is consumed by the matrix, the fracture path is thought to follow the weakest portion of the deteriorated interface. In these cases the interfacial size is governed by the diffusion and product reaction kinetics of the coating and matrix species, and the interface size may be relatively small. For example, Everett *et al.* (1986) determined that a thin aluminum coating, applied by physical vapor deposition to a polycrystalline pyrolytic graphite sample, creates an "intermixing zone" approximately 70 to 80 nm thick. A slightly smaller interfacial zone length is obtained for brittle intergranular fracture, as often occurs in polycrystalline metals and ceramics. In metallic polycrystallines there often exist grain boundary defects, such as decoherent boundaries, carbides or sulfides, which weaken the boundary. In ceramics, the consolidation process never yields perfectly dense ceramics, thus many voids exist along the grain boundaries which act as nucleation sites. The size of the interfacial zone in intergranular fracture is approximately the size of the grain boundary, and for metallic polycrystallines the grain boundary is typically on the order of ten Burger's vectors (approximately 2.5 nm). At about the same size scale are the initial phenomena associated with certain types of ductile fracture in metals. Here a second phase particle, such as a carbide or oxide, embedded in the matrix acts as a nucleation site for void formation. When sufficient tractions exist along the particle surface or the necessary deformation accumulates in the matrix, the boundary between the particle and the matrix separates, and after sufficient additional loading, gives way to a completely separated particle and a micro void. Again, the interfacial zone thickness may be on the order of several Burger's vectors.

The ability to resolve the fracture phenomena is limited to the minimum size scale

chosen to describe the individual constituents. In continuum mechanics, a representative volume is chosen whose macro-response sums up all the individual micro features within it (Fung, 1977). For inelastic deformation in metals, the nature of discrete slip events requires a representative volume which has a characteristic dimension of several hundred to several thousand Burger's vectors. (For metals, an average Burger's vector is approximately 2.5×10^{-10} m.) This means that deformable metallic or intermetallic based interfacial zones which are only several Burger's vectors thick cannot be accurately represented by the usual continuum models and require additional considerations to be properly modeled. For thicker interfaces, such as in the Gr/Al system discussed earlier, an average material response may be obtainable and used to define a "thin", but finite, transitional layer between the constituents. However, defining the material constitutive behavior across this diffusion zone must be accomplished by use of a discrete "averaged" layer, rather than by a continuous boundary layer. As the thickness of the interfacial zone increases, the use of continuous "continuum interfaces" becomes justifiable.

1.1.2 Considerations of Interface and Crack-Tip Idealizations

For many physical situations, several continuum modeling simplifications can be made. If the interfacial constitutive behavior is not substantially different from that of either one of the adjoint media, it can be approximated by using the properties of that adjoint medium and by merely extending that material's domain. The interface can be idealized as a perfect zero-thickness mathematical interface which is required to carry the interfacial tractions and maintain the local strain compatibility requirements. For weaker interfaces, interfacial sliding or opening may be allowed after sufficient traction or strain levels are achieved. An alternative approach to interfaces is to prescribe a traction-displacement relationship along the interface, which allows for different shear and normal traction-displacement behavior and allows the interface to separate (Nutt and Needleman, 1987). Use of these continuum models requires that the flaw mod-

eled and the limit of stress and strain resolution be very large compared to the actual interfacial thickness and the appropriate continuum length scale.

For relatively “thin” and “strong” interfaces, a perfect zero-thickness mathematical interface can be used to obtain “upper” limits to the stress and deformation in the crack-tip vicinity. An upper limit is produced in the sense that in order for the interface and surrounding regions to maintain their integrity, they must be capable of withstanding these stresses and deformations. Although such interface models are not capable of accurately describing the entire crack-tip deformation process, they do provide some insight into the conditions just prior to crack growth.

In the study of homogeneous fracture mechanics, attention is typically focused upon the asymptotic behavior of the fields as the crack tip is approached. Under certain conditions the crack-tip fields are described for a wide range of loadings, materials, and geometries by a single set of field equations whose magnitudes are scaled by the material properties and a stress intensity factor. Small scale yielding (SSY) is the most commonly referred class of crack-tip loading conditions for materials capable of inelastic deformation. In SSY use of asymptotic solutions is acceptable as long as the extent of non-linear deformation is contained within a region which is “small” compared to the next characteristic geometrical dimension in the problem. Crack and ligament length, specimen thickness or width, and distance to the point of load application are just a few examples of characteristic geometrical dimensions in a problem. In SSY the fields far away from the inelastic crack-tip deformation, but at distance small compared to the geometrical dimension, are well reproduced by the elastic asymptotic solutions (Rice, 1974). Within the SSY crack-tip idealization, a variety of work describing the fields within the inelastic zone has been performed.

In continuum fracture mechanics, the crack tip is commonly modeled as mathematically sharp. In actuality, crack-tip opening and blunting occurs in many microscopically ductile materials (*e.g.*, cast iron, aluminum, and copper), resulting from continuous deformation or discrete slip steps. For strain hardening materials in SSY, McMeeking

(1977) showed that the crack-tip opening displacement (CTOD) is linearly dependent upon the strength of the surrounding singularity, as measured by the J -Integral (Rice, 1968a). McMeeking also showed that by normalizing the radial distance from the crack-tip by the CTOD, the steady state values of the normalized stress and strain distributions are independent of J . In general, at radial distances large compared to the blunted CTOD, the crack-tip stress and strain behavior appears as if the crack tip is mathematically sharp, even though local crack-tip blunting may be occurring.

1.1.3 Homogeneous Fracture Mechanics

In conventional homogeneous fracture mechanics, the next step after LEFM in determining continuum crack-tip stresses has been to account for contained material non-linearity effects. For the homogeneous mode III case, Hult and McClintock (1956) solved exactly the small scale yielding continuum crack-tip stress field for an elastic/perfectly-plastic material idealization. They analytically calculated the actual size and location of the plastic zone along with the stress and strain distribution in the crack-tip plastic zone and in the surrounding elastic region. Recognizing that similar behavior should occur in the planar modes I and II, various approximate methods were developed in an attempt to account for crack-tip plasticity. In order to correct the plane-stress mode I stress intensity factor for local crack-tip inelastic deformation, which mathematically lengthens the apparent crack size, Dugdale (1960) postulated that the crack-tip yielded region could be idealized as a concentrated zero-thickness yield strip extending from the crack tip. He postulated that the only non-zero stress component was the stress normal to the crack face and that its value was equal to the tensile flow strength of the material. To determine the actual crack-tip stress intensity factor K_I , Dugdale first calculated the size of the yield strip, c , and defined an effective crack length, l_e , to be equal to the original crack length, l , plus the length of the yield strip(s); *i.e.*, $[l_e = l + c]$. To model the yield strip, he imposed the appropriate closing tractions on the effective crack tip(s) over a distance which corresponded to the yield

strip length (c). By superimposing the actual far-field loads, he was then able to determine the elastic stress intensity factor for his crack model. Using different crack-tip plasticity idealizations, others [Barenblatt (1962); Bilby, Cottrell, and Swinden (1963)] have used similar “matched asymptotic boundary layer” approaches to alter the effective crack to achieve better elasticity solutions. For an in-depth explanation and historical review of crack-tip “strip” models for contained inelastic deformation and their physical interpretation, the reader is referred to Kanninen and Popelar (1985).

To describe the continuum crack-tip fields deep within the actual crack-tip plastic zones, other methods were utilized. Based upon various assumptions, Rice (1968b) postulated that the Prandtl (slip-line) distribution represented the stress state at a plane-strain mode I crack tip, and numerical calculations performed by Rice and Tracey (1973) showed that the crack-tip stress distribution for an elastic/perfectly-plastic mode I crack was indeed well characterized by the Prandtl distribution. The Prandtl slip-line model assumes the material is perfectly plastic and that a stress potential can be constructed which satisfies the necessary boundary conditions (traction-free crack tips) and equilibrium requirements. Although this model allowed for determination of the finite stress field, the strain field is undefined. However, in certain regions of the stress field, a portion of the strain field behavior could be inferred. For example, in a fan region the behavior of the $\gamma_{r\theta}$ strain component is found to be singular ($\gamma_{r\theta} \propto 1/r$, where r is the radial distance from the crack tip). Thus, the inclusion of material non-linearities was not sufficient to remove all crack-tip stress and strain singularities.

Hutchinson (1968) and Rice and Rosengren (1968) considered the continuum structure of the planar crack-tip fields for power-law strain-hardening materials using deformation theory [strain \propto (stress) ^{n}]. (These fields shall henceforth be referred to as HRR fields.) From the compatibility, constitutive, and equilibrium relationships, the necessary requirements for the existence of a strain potential and a stress potential were established. By using the boundary conditions and assuming a separable form, an eigenvalue problem emerged whose solution determined the radial dependences of the

stress, displacement, and strain fields. Using the characteristic root, a fourth order differential equation was numerically solved to determine the actual angular dependences of these fields. The overall magnitude of the stress and strain fields were determined by their radial and angular dependences and scaled by the strength of the crack-tip singularity, as measured by the path independent J -Integral (Rice, 1968a). For finite values of the strain-hardening exponent, both the stress and strain fields were found to be singular as the crack tip was approached, and as observed previously, the inclusion of non-linear material constitutive behavior does not remove all singularities at the mathematically sharp crack tip. Although perfect plasticity can be considered by taking the limit as $n \rightarrow \infty$, no unique strain field was identifiable.

Development of HRR type singularity fields involves several key assumptions. A total deformation theory of plasticity is used along with linear kinematics (small strain theory) and a monotonically increasing stress-strain relationship. For deformation theory to accurately describe the constitutive behavior, no local stress unloading is admissible and the loading at all material points must be nearly radial. Thus the application of deformation theory is generally restricted to proportional loading. Since small strain theory is used, these solutions do not incorporate any field characteristics which are attributable to crack-tip blunting, and they are only applicable at limited, finite distances from the crack tip. Also, it should be noted that the HRR fields are obtained by retaining only the dominant term in the stress and strain potentials.

1.2 Statement of Purpose

The basic interfacial SSY crack tip characteristics for a specific set of loading and geometric conditions and material idealizations will be provided. The stationary crack-tip fields for specific material idealizations will be represented via closed form expressions, based upon natural dimensional and dimensionless variable groupings. First, a general non-linear idealized bi-material boundary value (BV) problem will be identified, including specific constitutive relationships. Known solutions to the linear elastic BV problem

will be reviewed and implications concerning the non-linear BV problem behavior and associated natural groupings will be extracted from the asymptotic elasticity solutions. From this assembled parametric framework, far-field loadings which produce the geometrical idealizations considered in the BV problem (traction-free crack-tip faces or closed crack-tip faces) will be stated. Next, a discussion of the solution technique for solving the non-linear problem will be presented. Representative forms for the general crack-tip fields will be presented and assembled to construct the complete crack-tip fields for various material choices. Inferred trends of the constructed fields, as functions of material variables, will be identified. Limitations regarding the applicability of these results, will be expressed in terms of the mathematical assumptions made in solving the BV problem and in terms of physical material characteristic associated with interfacial crack problems. Finally, speculative implications, relevant to all interfacial fracture mechanics problems, concerning separation mechanisms will be made.

1.2.1 Statement of Boundary Value Problem

The mechanics problem considered herein is a plane-strain interfacial crack between two isotropic solids, as depicted in *Figure 1.1*. The interface or diffusion boundary layer between the two solids is idealized as having zero thickness. The constitutive response for the material in the upper half (Region 1) is idealized as being elastic/perfectly-plastic, and the material in the lower half is considered to have a linear elastic constitutive relationship. Far-field applied loads are restricted to SSY and to those which result in either traction-free crack faces or crack faces which have (frictionless) contact over a large region, compared to their plastic zone size. (This restriction is enforced only from the edge of the plastic zone outwards away from the crack tip.) The far field loads are assumed to produce a set of displacements near the crack tip which can be represented by a continuous family of self-similar modes whose magnitudes are scaled by the crack-tip singularity. Hence, the family of boundary condition modes which are considered are limited to those which satisfy the general isotropic bi-material crack

problem with either traction-free crack faces or closed crack-tip faces.

The objectives of analyzing these BV problems are: (a) to determine the size, shape, and growth characteristics of the plastic zone in Region 1; (b) to identify the SSY asymptotic elastic and plastic fields deep within the plastic zone; (c) to identify the evolution of strains near the interface as well as the evolution of interfacial tractions with applied load.

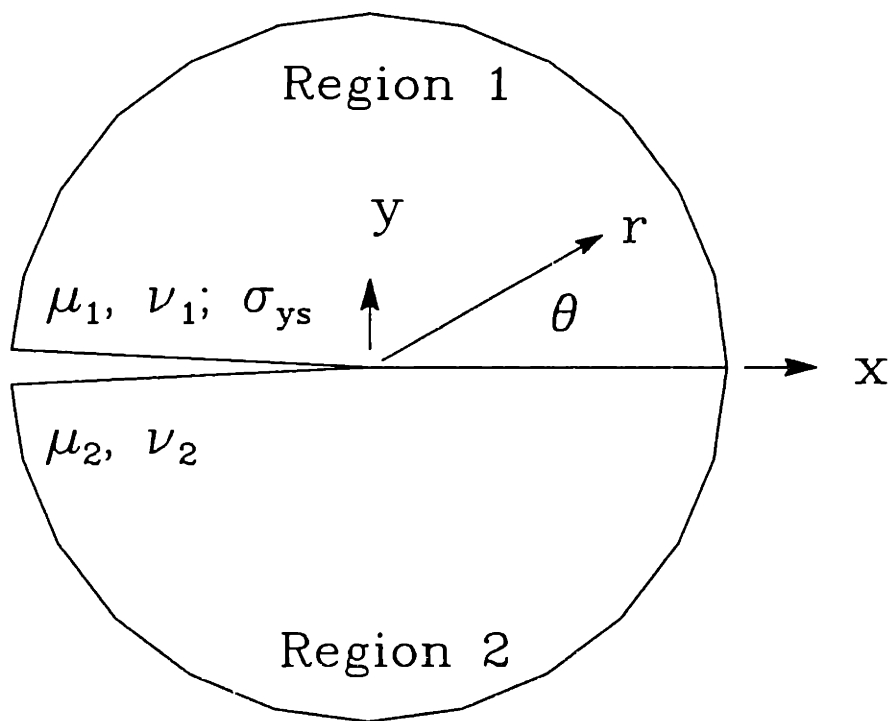


Figure 1.1 Schematic traction-free bi-material interfacial crack-tip region, including polar (r, θ) and Cartesian (x, y) coordinates and domain numbering convention.

Chapter 2

Elastic Interfacial Cracks

2.1 History and Solution Discussion

Applied mechanics can provide a framework for modeling interfacial cracks. Within this framework, there currently exist two specific geometric idealizations which are used to investigate the local interfacial crack-tip fields around a mathematically perfect zero-thickness interface. Both idealizations require continuity of interfacial tractions and displacements, with the basic difference between the two being the physical interpretation given to the near-tip crack faces. The first model assumes that the crack faces are “traction-free” while the other assumes that the crack faces are in “contact,” but free to slide relative to one another (frictionless). The following sections review the important aspects of each crack-tip model.

2.1.1 Traction-Free Crack Faces

The asymptotic solution for a traction-free crack tip located between two elastically dissimilar isotropic media was first addressed and partially solved by Williams (1959). He used for the Airy stress function a general power series expansion about the crack tip of the form

$$\phi = r^2 \sum_j A_j r^{\lambda_j} F_j(\theta, \lambda_j), \quad (2.1)$$

where r is the radial distance from the crack tip, θ is the angle measured from the interface, A_j and λ_j are admissible constants, and $F_j(\theta, \lambda_j)$ is an admissible function.

Enforcing displacement and traction continuity across the interface and traction-free crack-tip faces lead to an eigenvalue problem composed of eight simultaneous equations from which λ_j and acceptable forms of $F_j(\theta, \lambda_j)$ were determined. Williams first assumed that λ_j was a real number and was unable to obtain a solution to the characteristic equation. He concluded that λ_j must be a complex number and found that two possible series solutions exist:

$$\lambda_j = \begin{cases} j \pm i \frac{1}{\pi} \coth^{-1}(\mathcal{D}) \\ (j + \frac{1}{2}) \pm i \frac{1}{\pi} \tanh^{-1}(\mathcal{D}) \end{cases} \quad j = 0, \pm 1, \pm 2, \pm 3, \dots, \quad (2.2)$$

where for plane strain

$$\mathcal{D} = \frac{2\mu_1 \left(1 - \frac{\nu_2}{1-\nu_2}\right) - 2\mu_2 \left(1 - \frac{\nu_1}{1-\nu_1}\right) - (\mu_1 - \mu_2)}{2\mu_1 \left(1 - \frac{\nu_2}{1-\nu_2}\right) + 2\mu_2 \left(1 - \frac{\nu_1}{1-\nu_1}\right)}. \quad (2.3)$$

Here μ_k is the shear modulus, ν_k is Poisson's ratio, and the subscript k is 1 in the upper domain and 2 in the lower domain. In Eq.(2.2), both sets of roots exist only when $\mathcal{D} = 1$, and both have infinite imaginary components ($\coth^{-1}(\pm 1) = \tanh^{-1}(\pm 1) = \pm \infty$). For commonly used engineering materials (*i.e.*, those with positive Poisson's ratio less than 1/2), $|\mathcal{D}| < 1/2$; thus, only the series associated with $\tanh^{-1}(\mathcal{D})$ is defined. Since \coth^{-1} is not defined for arguments with a magnitude less than unity, the set of roots with integer real portions ($\Re(\lambda_j) = j$) must be excluded from the total solution.

In deriving the characteristic equation for the case of purely real roots, it is speculated that at some point Williams incorrectly divided through by $\sin(\pi\lambda_j)$. This led him to conclude erroneously that no purely real roots [$\Re(\lambda_j) = \lambda_j$] exist, when, quite to the contrary, the solution to $\sin(\pi\lambda_j) = 0$ actually produces an acceptable set of whole integer roots. (Note, division by $\sin(\pi\lambda_j)$ is only valid if $\sin(\pi\lambda_j) \neq 0$!) Thus, the complete solution to the bi-material interfacial crack problem with traction-free crack tips consists of half-integer complex powers of r , termed "Williams type," and real whole integer powers of r . For cracks with $\mathcal{D} = 0$, the complete set of roots for the homogeneous crack problem is recovered.

Rice (1988) has subsequently assembled the asymptotic expansion of a complete interfacial crack solution consisting of the Williams series [with eigenvalues $\lambda_j = (j +$

$1/2) + i(1/\pi) \tanh^{-1}(\mathcal{D})]$ and a material dependent constant multiplying the real whole-integer power series ($\lambda_j = j$). In terms of standard Muskhelishvili (Muskhelishvili, 1953) functions the general solution is given by

$$\phi'_1(z) = e^{-\pi\epsilon} z^{-\frac{1}{2}-i\epsilon} \sum_N a_N z^N + \frac{2C_2}{C_1 + C_2} \sum_M b_M z^M, \quad (2.4)$$

$$\Omega'_1(z) = e^{\pi\epsilon} z^{-\frac{1}{2}+i\epsilon} \sum_N \bar{a}_N \bar{z}^N - \frac{2C_2}{C_1 + C_2} \sum_M \bar{b}_M \bar{z}^M, \quad (2.5)$$

$$\phi'_2(z) = e^{\pi\epsilon} z^{-\frac{1}{2}-i\epsilon} \sum_N a_N z^N + \frac{2C_1}{C_1 + C_2} \sum_M b_M z^M, \quad (2.6)$$

and

$$\Omega'_2(z) = e^{-\pi\epsilon} z^{-\frac{1}{2}+i\epsilon} \sum_N \bar{a}_N \bar{z}^N - \frac{2C_1}{C_1 + C_2} \sum_M \bar{b}_M \bar{z}^M. \quad (2.7)$$

In these expressions, the bi-material constant, ϵ (imaginary part of the complex root λ_j), is defined as

$$\epsilon = \frac{1}{2\pi} \ln \left[\frac{\frac{\eta_1}{\mu_1} + \frac{1}{\mu_2}}{\frac{\eta_2}{\mu_2} + \frac{1}{\mu_1}} \right] \quad (2.8)$$

and

$$C_k = \frac{\eta_k + 1}{\mu_k}, \quad (k = 1, 2). \quad (2.9)$$

Here $z = x + iy = re^{i\theta}$ is the location measured from the crack tip, $\eta_k = 3 - 4\nu_k$ for plane strain and $\eta_k = (3 - \nu_k)/(1 + \nu_k)$ for plane stress, and the subscript k is used again to refer to the material in the upper half when equal to 1 and to the material in the lower half when equal to 2. The individual stress components are related to the Muskhelishvili stress potentials by the following relationships:

$$\sigma_{zz} + \sigma_{yy} = 2[\phi' + \bar{\phi}'] \quad (2.10)$$

and

$$\sigma_{yy} - \sigma_{zz} + i2\sigma_{zy} = 2[(\bar{z} - z)\phi'' - \phi' + \Omega']. \quad (2.11)$$

Discarding infinite energy terms and retaining only the most dominant term as $r \rightarrow 0$, the local crack-tip stresses behave as follows:

$$\sigma(r, \theta) \sim \frac{1}{\sqrt{r/2a}} \left\{ A(\theta) \cos[B(\theta) + \epsilon \ln \frac{r}{2a}] + C(\theta) \sin[D(\theta) + \epsilon \ln \frac{r}{2a}] \right\}, \quad (2.12)$$

where $r/2a$ is the radial distance from the crack tip normalized with respect to crack length, θ is the angle measured from the interface, and $A(\theta)$, $B(\theta)$, $C(\theta)$, and $D(\theta)$ are functions dependent upon loading, material constants, and angle θ .

Complete solutions to various problems concerning cracks between dissimilar media were obtained by England (1965), Erdogan (1965), and Rice and Sih (1965) using Kolosov-Muskhelishvili and other transformations to express the stress potentials. Additionally, Rice and Sih calculated stress intensity factors for a semi-infinite crack with point loads and for a finite crack between two semi-infinite media loaded by wedge forces or remote far-field loads.

The in-plane two-dimensional bi-material stress intensity factor, \mathbf{K} , as defined by Hutchinson, Mear, and Rice (1987), is given by

$$\mathbf{K} = \lim_{r \rightarrow 0} \sqrt{2\pi r} \frac{[\sigma_{yy}(r, \theta = 0) + i\sigma_{zy}(r, \theta = 0)]}{r^{i\epsilon}}, \quad (2.13)$$

where $\sigma_{yy}(r, \theta = 0)$ and $\sigma_{zy}(r, \theta = 0)$ are the interfacial normal and shear stresses, respectively. Note, the elastic material properties enter into the stress intensity factor via the bi-material constant, unlike the homogeneous case. Since \mathbf{K} is a complex number, it can be written as

$$\mathbf{K} = K_I + iK_{II}, \quad (2.14)$$

where K_I and K_{II} are the real and imaginary components of the stress intensity factor, respectively. Using the definition

$$\mathbf{K} = (k_I + ik_{II})\sqrt{\pi} \cosh(\pi\epsilon), \quad (2.15)$$

Rice and Sih's (1965) original stress intensity factors, k_I and k_{II} are interpreted in a consistent manner. *Table 2.1* contains the stress intensity factors for several geometries (Shih and Asaro, 1987).

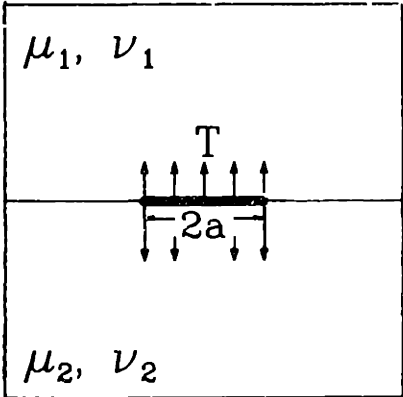
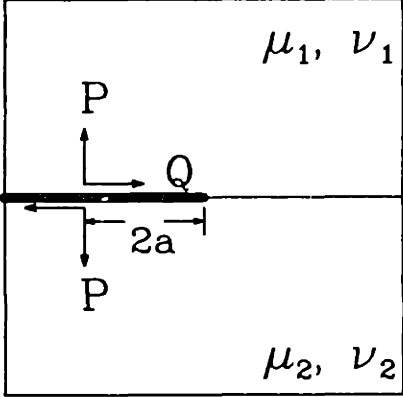
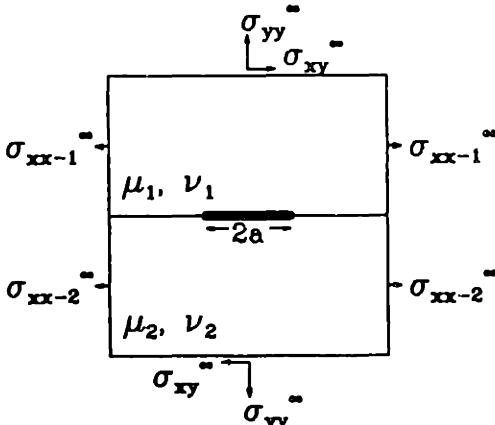
Crack Geometry	Stress Intensity Factor	Reference
<p>Infinite Plate</p> 	$K = T (1 + i2\epsilon) \times \sqrt{\pi a} (2a)^{-i\epsilon}$	<p>England, 1965</p>
<p>Semi-Infinite Plate</p> 	$K = (P + iQ) \cosh(\pi\epsilon) \times (2a)^{-i\epsilon} / \sqrt{\pi a}$	<p>Rice and Sih, 1965</p>
<p>Infinite Plate</p> 	<p>For crack tip at $x = a$,</p> $K = (1 + i2\epsilon) (\sigma_{yy}^{\infty} + i\sigma_{xy}^{\infty}) \times \sqrt{\pi a} (2a)^{-i\epsilon}$	<p>Rice and Sih, 1965</p>

Table 2.1 Bi-material stress intensity factor for various interfacial crack geometries.

Using Griffith's virtual work argument, Willis (1971) formally calculated the increment of elastic energy dissipation associated with an increment of crack-face advancement for the general anisotropic crack. (He evaluated the elastic energy release rate.) Willis did this by formulating a "stress concentration vector," whose components are K_I , K_{II} , and K_{III} , and equated it with the the specific surface energy to establish a "stability relationship." For the planar isotropic case, Rice (1988) gave the energy release rate in terms of the complex stress intensity factor as

$$\mathcal{G} = \frac{C_1 + C_2}{16 \cosh^2(\pi \epsilon)} \mathbf{K} \bar{\mathbf{K}}, \quad (2.16)$$

where \mathcal{G} is the energy release rate per unit thickness.

Although the asymptotic stress fields and stress intensity factors are easily calculated, their interpretation is not straightforward as in the homogeneous case. For example, the elasticity solution for the bi-material traction-free crack-tip problem possesses some unusual characteristics. Asymptotically, the stress, strain, and displacement fields oscillate with radial distance, and this oscillation in the displacement field causes the crack faces to contact and mathematically interpenetrate. England (1965), using the asymptotic solution for an internally pressurized Griffith crack with length $2a$, calculated the crack-face contact length, δ , by determining the distance from the crack tip to where crack-face interpenetration would occur. For this geometry he found that

$$\frac{\delta}{2a} = 1.26 \times 10^{-4}. \quad (2.17)$$

Since England's calculation was evaluated for $\epsilon = 0.1748$, the maximum value of the bi-material constant in plane strain for materials with positive Poisson's ratio, he concluded that for more realistic property choices the contact distance would be even smaller. For the same Griffith crack geometry but loaded by remote tensile and shear tractions, Rice (1988) calculated values of $\delta/2a$ which were appreciably larger than Eq.(2.17) for certain loading conditions.

Additional complications exist in the definition of the stress intensity factor \mathbf{K} . Rice (1988) pointed out that the interpretation of K_I and K_{II} is ambiguous since K_I and K_{II}

individually do not correspond physically to a pure opening mode or a pure shear mode. Furthermore, the choice of physical units used in determining the numerical value of the stress intensity factor affects the ratio of K_I and K_{II} for any given boundary value problem. Using the definition of \mathbf{K} given by Hutchinson, Mear, and Rice (1987) in Eq.(2.13) results in the following generic stress intensity factor:

$$\mathbf{K} = \underline{\sigma}^\infty C e^{-i\epsilon \ln l} \sqrt{\pi l}, \quad (2.18)$$

where $\underline{\sigma}^\infty$ is a resultant traction expressed as a complex number with the dimensions of stress, C is a non-dimensional complex geometric constant, and l is the characteristic geometric length of the problem, such as crack or ligament length, distance from the crack tip to point of load application, *etc.* Examining Eq.(2.18) reveals that when different length units (*e.g.*, m, inches, cm) are assigned to l , $\angle \mathbf{K}$ changes. [Here $\angle(\)$ refers to the phase angle of the complex argument (), and the $\angle \mathbf{K}$ is chosen such that $-\pi < \angle \mathbf{K} < \pi$.] Thus, an infinite number of stress intensity factors, all with different ratios of K_I to K_{II} (and different units), could exist which all yield identical stress states. *This implies that the decomposition of \mathbf{K} is meaningless since only in the degenerate case, when $\epsilon = 0$, does modal decomposition of K_I and K_{II} take on any unique or significant meaning.*

The units associated with the bi-material stress intensity factor are unique in that they differ from the homogeneous stress intensity factor by $l^{-i\epsilon}$. For example, typical units of \mathbf{K} may be $\text{MPa}(\text{m})^{0.5-0.0332i}$. To remove this uncommon dimension, $(\text{m})^{-0.0332i}$, Shih and Asaro (1987) defined a stress intensity vector \mathbf{Q} such that, as $r \rightarrow 0$ on $\theta = 0$, $\sigma_{yy} + i\sigma_{zy} \rightarrow \mathbf{Q}(r/l)^{i\epsilon}/\sqrt{2\pi r}$. This expression differs from Eq.(2.13) by the factor $l^{-i\epsilon}$. This approach uniquely identifies $\angle \mathbf{K}$, and when used in Shih and Asaro's elasticity expressions produces, at a fixed point, the identical stress state as compared with the previous definition. However, several problems arise in using Shih and Asaro's stress intensity vector \mathbf{Q} . The choice of l becomes ambiguous when several geometric lengths exist. For example, in a compact tension specimen (CTS), at least three lengths exist which could be used, namely the thickness, the width, and the crack or ligament length,

and uncertainties clearly exist regarding the appropriate choice of the normalizing length dimension. Second, Shih and Asaro's definition may yield confusion because two different loadings which produce identical stress intensity vectors only produce identical crack-tip stress fields when ϵ is the same for both cases. Although the definition of Hutchinson *et al.* requires additional unusual dimensions to be carried along; the possible non-uniqueness problem is totally circumvented. Therefore, for convention, the definition given by Hutchinson *et al.*, Eq.(2.13), is used in the remainder of this study.

2.1.2 Closed Crack-Tip Faces

In an attempt to eliminate the unsatisfactory aspects of the oscillatory singularity in the traction-free crack-tip model, various other crack-tip models have been proposed. Comninou (1977a) included a frictionless contact zone at the crack tip of a Griffith crack which transmitted only compressive normal tractions and required both traction and displacements to be continuous over the intact interface. Comninou then formulated a singular integral equation to describe the dislocation density which was necessary to produce closed crack tips. She also used the Williams technique of expressing a general power series Airy stress function, Eq.(2.1), about a closed crack tip with crack-face friction (Comninou, 1977b) and without crack-face friction (Comninou, 1977a). By enforcing continuity of tractions and displacements across the interface and by requiring continuous (compressive) normal tractions and normal displacements on the closed crack face, an eigenvalue problem of eight simultaneous equations arose from which acceptable values of λ_j and forms of $F_j(\theta, \lambda_j)$ were determined.

The results of her numerical solution of the singular integral equation and her frictionless crack-tip expansion agreed, demonstrating that as $r \rightarrow 0$, the dominant stress field around the closed crack tip is given by

$$\sigma_{rr} = \frac{-K_{II}^c}{4\sqrt{2r}} \left\{ 5(1 \mp \beta) \sin \frac{\theta}{2} - (3 \pm \beta) \sin \frac{3\theta}{2} \right\}, \quad (2.19)$$

$$\sigma_{\theta\theta} = \frac{-K_{II}^c}{4\sqrt{2r}} \left\{ 3(1 \mp \beta) \sin \frac{\theta}{2} + (3 \pm \beta) \sin \frac{3\theta}{2} \right\}, \quad (2.20)$$

and

$$\sigma_{r\theta} = \frac{K_{II}^c}{4\sqrt{2r}} \left\{ (1 \mp \beta) \cos \frac{\theta}{2} + (3 \pm \beta) \cos \frac{3\theta}{2} \right\}, \quad (2.21)$$

where, using Comninou's convention for numbering material domains,

$$\beta = \frac{\mu_2(\eta_1 - 1) - \mu_1(\eta_2 - 1)}{\mu_2(\eta_1 + 1) + \mu_1(\eta_2 + 1)}. \quad (2.22)$$

Here K_{II}^c is the strength of the singularity, and the *upper* and *lower* signs are used in the lower and upper material domains, respectively. To ensure compressive tractions in the contact zone, loadings are restricted such that $K_{II}^c > 0$ for $\beta > 0$ and $K_{II}^c < 0$ for $\beta < 0$.

A note of caution: Comninou reversed the ordering of the material domains as compared to the convention used by Williams (1957), and others. *Figure 2.1* shows the crack-tip geometry Comninou assumed. *In her work the material in the upper domain is referred to by the subscript 2, and the material in the lower domain is referred to by the subscript 1.* Switching the ordering of the material domains changes the sign of the bi-material constants β and ϵ . For convention, in the present work β will be defined with the subscript 1 in the *lower* domain, and ϵ will be defined with the subscript 1 in the *upper* domain. Using this convention, β is related to ϵ via

$$\epsilon = \frac{1}{2\pi} \ln \left[\frac{1 - \beta}{1 + \beta} \right]. \quad (2.23)$$

Along the interface, the shear component is the only dominant asymptotic stress term that is non-zero, and it behaves as $\sigma_{r\theta}(r, \theta = 0) = K_{II}^c/\sqrt{2r}$. This implies that the additional load carried by the interface, which results from the presence of the crack, is asymptotically only supported by interfacial shear tractions. Note that the interface still supports normal tractions which arise from the far-field loading and from the complete local solution, even in the crack-tip vicinity, and these normal tractions may be on the order of 25 times the tensile far-field opening traction (Comninou, 1977a). The

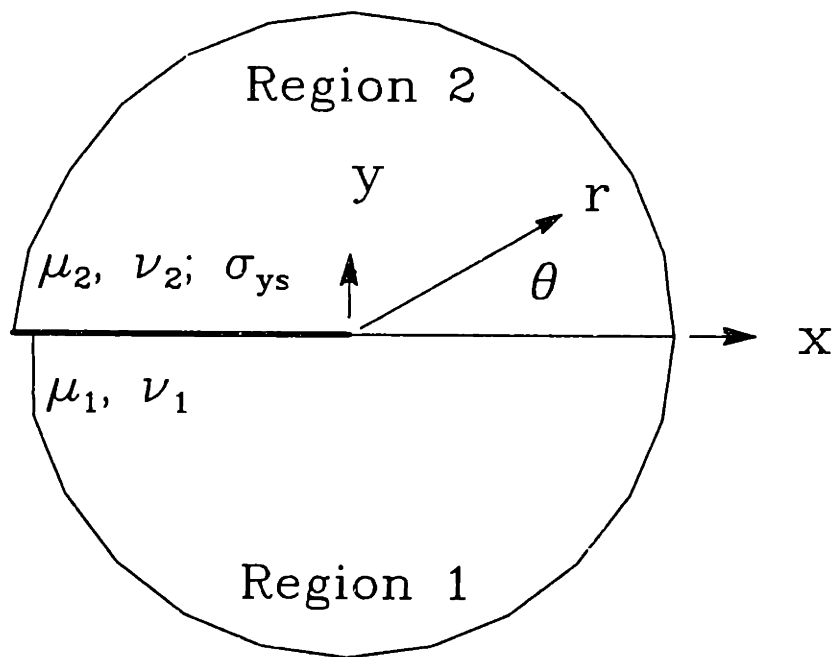


Figure 2.1 Schematic closed bi-material interfacial crack-tip region, including polar (r, θ) and Cartesian (x, y) coordinates and domain numbering convention.

(compressive) normal traction in the contact zone is singular — $\sigma_{yy} = -K_{II}^c \beta / \sqrt{2r}$ as the crack tip is approached — and is bounded as the crack opening (gap) is approached. To be precise, Comninou mathematically requires the normal traction to be equal to zero in the contact zone at the point where crack opening initiates. [A standard moving Hertzian contact boundary condition (Johnson, 1985).]

The complete set of admissible roots for Comninou's Williams type crack-tip expansion contains two series with *real* values. The two admissible series of roots which produce finite crack-tip strain energy and no concentrated crack-tip forces are

$$\lambda_j = \begin{cases} j \\ j + \frac{1}{2}, \end{cases} \quad (2.24)$$

where j is a non-negative integer. (Note, this spectrum of admissible roots is the same as that found for the homogeneous crack problem.) The other roots of interest are $\lambda = 0$, which corresponds to a uniform (domain wise constant) stress field, and $\lambda = 1/2$, which represents a positive square-root stress field ($\sigma \propto \sqrt{r}$). The constraints on the uniform stress field are that σ_{yy} , σ_{xy} , and ϵ_{zz} are continuous along the interface. To satisfy these conditions a “stress jump across (the) interface” (Rice and Sih, 1965) is generally required, and because the crack faces are free of shear traction, $\sigma_{xy} = 0$. It is interesting to note that all half-integer roots ($\lambda = j + 1/2$) in the closed crack-tip expansion, produce no normal interfacial tractions [$\sigma_{rr}(r, \theta = 0) = \sigma_{\theta\theta}(r, \theta = 0) = 0$].

Comninou calculated a stress intensity factor, K_{II}^c , for her model. It is obtained by taking the limit as $r \rightarrow 0$ in the crack-tip region, and is given as

$$K_{II}^c \equiv \lim_{r \rightarrow 0} \left\{ \sqrt{2r} \sigma_{xy}(r, \theta = 0) \right\}. \quad (2.25)$$

Note, Eq.(2.25) produces stress intensity factors having the same dimensions as in the homogeneous case, but differs from the usual homogeneous stress intensity factor definitions by a factor of $\sqrt{\pi}$. (Comninou (1977a) actually calculates two stress intensity factors for her model, however the stress intensity factors are always proportional to each other for $\beta \neq 0$ and are used nearly interchangeably to scale a single set of crack-tip field equations.) Excluding the compressive contact tractions, the crack-tip

fields can be regarded as being quasi-homogeneous “mode II.” In other words, for the homogeneous case, $\beta = 0$, the stress state expressed in Eqs.(2.19) to (2.21) reduces to that found for homogeneous mode II loading (Comninou, 1977a).

Gautesen and Dundurs (1987) were able to solve exactly an additional integral in Comninou’s formulation for the case of remote tensile loading of a Griffith crack geometry. By writing equivalent series expansions and using some appropriate small argument approximations, they found that, for $\beta > 0$ ($\epsilon < 0$), the total normal stress directly ahead of the closed crack tip is equal to

$$\sigma_{yy}(r = 0^+, \theta = 0) = \frac{\sigma_{yy}^\infty \beta_0}{\pi k_g} \sqrt{1 + \frac{\beta_0^2}{\pi^2}} \left[1 + \mathcal{O}(k_g^2) \right], \quad (2.26)$$

where

$$\beta_0 = \ln \left[\frac{1 + \beta}{1 - \beta} \right] = -2\pi\epsilon \quad (2.27)$$

and

$$k_g^2 = 16 \exp \left\{ -\frac{\pi^2}{\beta_0} \left[\frac{2}{\pi} \tan^{-1} \left(\frac{\beta_0}{\pi} \right) + 1 \right] \right\}. \quad (2.28)$$

Here σ_{yy}^∞ is the far-field opening stress. They show that for opening loads, as $\beta \rightarrow 0$ (or alternatively as $\epsilon \rightarrow 0$), the extent of the crack-tip contact vanishes. Additionally, the stress intensity factor K_{II}^c for $\beta > 0$ ($\epsilon < 0$) of such a Griffith crack loaded by the far-field stress σ_{yy}^∞ is given by

$$K_{II}^c = \sigma_{yy}^\infty \sqrt{a} \left\{ \sqrt{1 + \frac{\beta_0^2}{\pi^2}} + \mathcal{O}(k_g^2) \right\}, \quad (2.29)$$

where $2a$ is the crack length. For the range $0 < \beta \leq 0.5$ ($0 > \epsilon \geq -0.175$), $K_{II}^c / (\sigma_{yy}^\infty \sqrt{a})$ varies by less than 6%.

When the contact zone is small compared to crack length, results from Comninou’s model are consistent with those found by others. For remote tensile loading, she determined that the contact zone is smaller than the maximum first contact calculated by England. She further found that the global stress field away from the immediate

crack-tip region still contains the oscillatory singularity and is not significantly different from the stress field previously obtained. Also, the inclusion of contact zones in Comninou's model eliminates the oscillatory nature of the singularity in the very near crack-tip field.

For arbitrary far-field shear, σ_{xy}^∞ , and normal, σ_{yy}^∞ , loading of a Griffith crack geometry, the crack-face contact length is not always small compared to crack length and the oscillatory stress field may never be recovered, even at relatively large distances from the crack-tip. Comninou and Schmueser (1979) found that for a Griffith crack geometry with $\beta > 0$, at fixed values of σ_{yy}^∞ , the contact length at the right hand crack tip increases when positive remote shear is applied, and for fixed values of σ_{xy}^∞ , increases as the level of remote normal stress decreases to compressive levels. Simultaneously, as the contact length at the right hand crack tip increases, the contact length at the left hand crack tip decreases. *Table 2.2* lists the right hand contact length δ for various combinations of far-field loads applied to a Griffith crack geometry. (The notation used is the same as that used previously to define \mathbf{K} for the infinite plate in *Table 2.1*.) For a pure far-field shear load ($\sigma_{yy}^\infty = 0$) and for a compressive normal load, substantial contact lengths exist. Any predictions based upon a "traction-free crack-tip" model for the right hand crack tip under positive shear, with even modest levels of applied normal stress (say for $\beta = 0.5$, $\sigma_{yy}^\infty \leq 3\sigma_{xy}^\infty$), are ill-founded and clearly unjustifiable, since the contact length is so large (e.g., for $\beta = 0.5$, $\delta/2a > 0.1$).

$\sigma_{yy}^\infty/\sigma_{xy}^\infty$	$\delta/2a$
0.50	0.068
0.25	0.23
0	0.33
-0.25	0.60
-0.50	0.78
-0.75	0.88
-1.00	0.92

Table 2.2 Contact lengths at the right hand crack tip of a Griffith crack geometry loaded by far-field stress; $\beta = 0.5$ and $\sigma_{xy}^\infty > 0$ (Comninou and Schmueser, 1979).

In addition to Comninou, others have included various crack-tip models in an attempt to remove the oscillatory singularity and accurately account for contact. For certain geometries and loadings, Atkinson (1982) showed, by several examples, that the elastic energy release rate is virtually unaffected by the precise details of the very near crack-tip model used. In general, such crack-tip modeling may remove the oscillatory behavior locally, but does not remove all the singularities at the crack tip. As with all infinitesimal elasticity solutions, they are only valid in the region where the assumptions of linear material response as well as small strains and rotations, are not violated.

2.2 Inferred Plastic Behavior

From the expressions for the local elastic asymptotic crack-tip stresses, it is clear that unbounded stresses arise as the crack tip is approached. The applicability of linear elastic models must therefore be examined in terms of the mathematical assumptions and the material idealizations used in deriving them. Based upon the tensile behavior of most polycrystalline metals, it is clear that linear elasticity is not an appropriate idealization very near the crack tip, where unbounded stresses are predicted, because nonlinear deformation is anticipated. The inclusion of continuum non-linear material behavior, such as power law strain-hardening or elastic/perfectly-plastic, allows for better representation of the actual material response for many materials and situations. When continuum length assumptions apply, local crack-tip plasticity is typically found embedded within the singular elasticity fields and separated by a transitional “boundary layer.” The parametric framework which describes the non-linear to linear material transition should be obtainable by considering the elastic field along the transition boundary. The aim of this section is to describe the boundary characteristics of the continuum non-linear zone in terms of far-field loads and material properties by assuming that the non-linear zone boundary can be approximated by the loci of points whose elastically-calculated Mises equivalent stress, $\bar{\sigma}$, is equal to the tensile

yield strength of the material, σ_{y_0} . Using this assumption and the two asymptotic elasticity solutions, Eqs.(2.4) to (2.7) and Eqs.(2.19) to (2.21), a consistent parametric framework for describing the plastic-zone characteristics is assembled.

Several quantities are needed in this framework. First, a representative plastic zone characteristic dimension r_p , given in terms of the far-field applied load and material properties, is required in order to determine if SSY conditions are satisfied. It will be shown that a natural choice for the characteristic dimension is $r_p = \mathbf{K}\bar{\mathbf{K}}/\sigma_{y_0}^2 \pi \cosh^2(\pi\epsilon)$ for the traction-free crack-tip model and $r_p^c = 3K_{II}^c/2\sigma_{y_0}^2$ for the closed crack-tip face model. In general, σ_{y_0} is the tensile yield strength of the material in either domain, but henceforth shall refer to the tensile yield strength of the plastically deformable material in the upper domain of *Figures 1.1* and *2.1*. Next, it is necessary to determine the size and shape of the plastic zone, in terms of the applied load. It will be shown that traction-free crack-tip plastic zone growth occurs in a periodic manner with respect to increasing stress intensity factor \mathbf{K} , and the tractions along the plastic zone boundary also change in a periodic manner, because the tractions simultaneously evolve with the plastic zone. In the closed crack-tip model, it will be shown that the plastic zone growth is self-similar, and that the size of the plastic zone can be scaled by the closed crack-tip characteristic plastic zone dimension r_p^c . Because a single unique plastic zone shape does not exist during loading for the traction-free model, as it does for the closed crack-tip model, an additional quantity describing the phase of the plastic zone will be introduced. The interfacial load phase angle (ILPA), ζ_0 , defined as

$$\zeta_0 = \angle\mathbf{K} + \epsilon \ln \left[\frac{\mathbf{K}\bar{\mathbf{K}}}{\sigma_{y_0}^2 \pi \cosh^2(\pi\epsilon)} \right], \quad (2.30)$$

accounts for all possible loading combinations while it compensates for plastic zone growth within the oscillatory field. It uniquely characterizes the plastic zone shape, plastic zone tractions, and determines whether crack-face contact is occurring at the plastic zone edge.

Finally, and most importantly, conditions defining the applicability of each model as well as any possible combination of models, will be identified. It will be assumed that

the traction-free crack-tip model is the governing model, in regards to identifying when each model is appropriate. It is chosen because it analytically exists in closed form and all necessary quantities used in the closed crack-tip face model can be approximated from it when the contact length is small compared to crack length. For certain loading conditions, it will be shown that the closed crack-tip face model is applicable because significant crack-face contact exists. Based upon the value of the ILPA, explicit domains for which the characteristic plastic zone dimension in each model is acceptable, as compared to the length of the crack-face opening or closure, will be identified.

It will be shown that these two continuum interfacial crack-tip models will describe most, but not all, possible crack loadings. For certain circumstances, even when the size of the plastic zone is small compared to crack length, neither of these interfacial crack-tip models will appropriately describe the actual crack-tip behavior. Justification for use of this framework will be made by comparing its elastically based predictions against various precise solutions for actual strain hardening materials. This agreement will warrant the use of this framework for all monotonically increasing strain hardening constitutive relationships [strain \propto (stress)ⁿ] which include an initial linearly elastic ($n = 1$) range.

2.2.1 Traction-Free Crack Faces

The following section is a paper submitted to the Journal of Applied Mechanics by the author and Prof. D. M. Parks which derives an approximate expression for the plastic zone from the asymptotic Williams type oscillatory elasticity solution. It discusses predicted plastic zone size, shape, and growth characteristics, introduces various key bi-material interfacial variables, and gives formal validity conditions, in terms of K , material properties, geometry, and bi-material interfacial variables, for the applicability of the traction-free crack tip BV problem outlined in Chapter 1.

For consistency, all equations, figures, and sections referenced from this paper will be identified using the prefix (P2.).

ELASTIC YIELD ZONE AROUND AN INTERFACIAL CRACK TIP

by

Edward Zywickz

and

David M. Parks

Department of Mechanical Engineering
Massachusetts Institute of Technology
Cambridge, Massachusetts 02139 USA

Abstract

A closed form approximate solution for a small scale yielding (SSY) plastic zone around a planar interfacial crack-tip, occurring between two dissimilar ideally-bonded elastic half-spaces, is obtained by equating the elastically-calculated Mises equivalent stress with the material yield strength, σ_{ys} . The dimensionless parameter $\zeta(\theta)$, which is defined as $\zeta(\theta) = \angle\mathbf{K} + \epsilon \ln r_p(\theta)$, where $\angle\mathbf{K}$ is the phase angle of the complex stress intensity factor \mathbf{K} , ϵ is the bimaterial constant, and $r_p(\theta)$ is the polar representation of the plastic zone radius, naturally arises. The SSY interfacial load phase angle (ILPA), defined as $\zeta_0 = \angle\mathbf{K} + \epsilon \ln \left(\mathbf{K}\bar{\mathbf{K}} / \sigma_{ys}^2 \pi \cosh^2(\pi\epsilon) \right)$, leads to periodic zone growth. The ILPA characterizes the overall applied load phase by combining the oscillatory radial phase shift, attributable to the increase in zone size due to increased loading, with $\angle\mathbf{K}$. At a particular angle θ_0 from the uncracked interface, the plastic zone radius thus calculated is independent of $\angle\mathbf{K}$, proportional to $\mathbf{K}\bar{\mathbf{K}}$, and has no oscillatory radial phase dependence. The derived plastic zone expression reproduces the shape characteristics, and it modestly reproduces the zone size when compared with solutions for an elastic/perfectly-plastic solid adjoint to an elastic solid. As the strain hardening exponent in the plastically deforming medium decreases, agreement between the approximation and various accurate numerical solutions improves. In the limiting case when $\epsilon = 0$, the well-known homogeneous elastic solutions for pure mode I and mode II are recovered, as well as all possible mixed mode combinations. Approximate validity conditions for the existence of Williams type asymptotic fields (traction-free crack faces) are presented.

1 Introduction

Much effort has recently been focused on interfaces which exist between dissimilar media, with specific attention being directed toward media separation or fracture events. Publications on the subject, such as Shih and Asaro (1987), Hutchinson *et al.* (1987), and Rice (1988) clarify several aspects of the original oscillatory stress solution obtained by Williams (1959) for an interfacial crack and attempt to apply or further extend traditional (homogeneous) fracture mechanics approaches to interface cracking phenomena. Elastic interfacial crack-tip fields between isotropic media are well characterized, although only a limited number of geometries have had their stress fields and stress intensity factors solved exactly. Ting (1986) has presented a rigorous framework for determining the degree of singularity and the asymptotic characteristics for the general interfacial crack between two elastic anisotropic materials. When non-linear material responses are included, no explicit unifying characterization presently exists to unite the various fracture parameters. However, dimensional analysis by Rice (1988) and by Shih and Asaro (1987) lead to symbolic functional relationships consistent with the present results.

Insight concerning contained crack-tip inelastic deformation zones (in the small scale yielding, SSY, sense) can be obtained by considering the characteristics contained within the elasticity solution. One approximate method which has been used to determine the plastic zone shape and size around a crack tip in a homogeneous medium is equating the elastically-calculated Mises or Tresca equivalent stress with the yield stress of the material (McClintock and Irwin, 1965; Rooke, 1963). The locus of all points satisfying this condition is considered to be the plastic zone boundary which separates the exterior elastic region from the interior plastically yielding region. The changes in plastic zone size and shape with respect to the applied load or stress intensity factor(s) can then be estimated from this expression.

The goal of this work is to present a closed form approximate plastic-zone solution for an interfacial crack between isotropic linear elastic media, and propose various dimensional and dimensionless quantities, which naturally arise in the derivation, as interfacial fracture parameters that uniquely characterize the interface crack-tip region. Comparisons will be made between the approximate solution and various precise numerical solutions to demonstrate its accuracy. Conditions which determine the validity of this expression will be stated.

2 SSY Plastic Zone Approximation

The problem considered is a planar interfacial crack, as shown in *Figure 1*, whose constituents have shear moduli μ_j ($j = 1, 2$) and Poisson's ratios ν_j . (Subscripts 1 and 2 refer to the upper and lower domains, respectively.) Far field loads produce a local elastic stress field which is well characterized by the complex stress intensity factor \mathbf{K} and asymptotic interfacial crack-tip stress fields. Following Hutchinson *et al.* (1987), the stress intensity factor is defined such that as, as $r \rightarrow 0$ on $\theta = 0$, $\sigma_{yy} + i\sigma_{xy} \rightarrow \mathbf{K}r^{i\epsilon}/\sqrt{2\pi r}$. For the interfacial "Griffith" crack configuration, this definition for \mathbf{K} differs from that given by Shih and Asaro (1987) by the complex term $e^{-i\epsilon \ln 2a}$. (See Rice (1988) for calculated examples of \mathbf{K} for various geometries and for the interfacial stress fields.) The bimaterial constant, ϵ , which modulates the stress and displacement oscillation period, is defined as

$$\epsilon = \frac{1}{2\pi} \ln \left[\frac{\left(\frac{\kappa_1 + \frac{1}{\mu_2}}{\mu_1} \right)}{\left(\frac{\kappa_2 + \frac{1}{\mu_1}}{\mu_2} \right)} \right], \quad (1)$$

where $\kappa_j = 3 - 4\nu_j$ for plane strain and $\kappa_j = (3 - \nu_j)/(1 + \nu_j)$ for plane stress.

The general stress field for an isotropic elastic solid can be represented by the Muskhelishvili potential representation (Rice, 1988),

$$\sigma_{xx} + \sigma_{yy} = 2 \left[\phi' + \bar{\phi}' \right] \quad (2)$$

and

$$\sigma_{yy} - \sigma_{xx} + i2\sigma_{xy} = 2 \left[(\bar{z} - z)\phi'' - \phi' + \Omega' \right]. \quad (3)$$

Retaining only the dominant asymptotic term as $r \rightarrow 0$, the plane strain elastic potentials in the upper domain are

$$\phi'_1 = a_0 e^{-\pi\epsilon} z^{-\frac{1}{2}-i\epsilon}, \quad (4)$$

and

$$\Omega'_1 = \bar{a}_0 e^{\pi\epsilon} z^{-\frac{1}{2}+i\epsilon}. \quad (5)$$

Using Eqs.(2) to (5), an expression for the Mises equivalent stress in region 1 can be obtained. (Appendix A contains the complete general series potential functions and

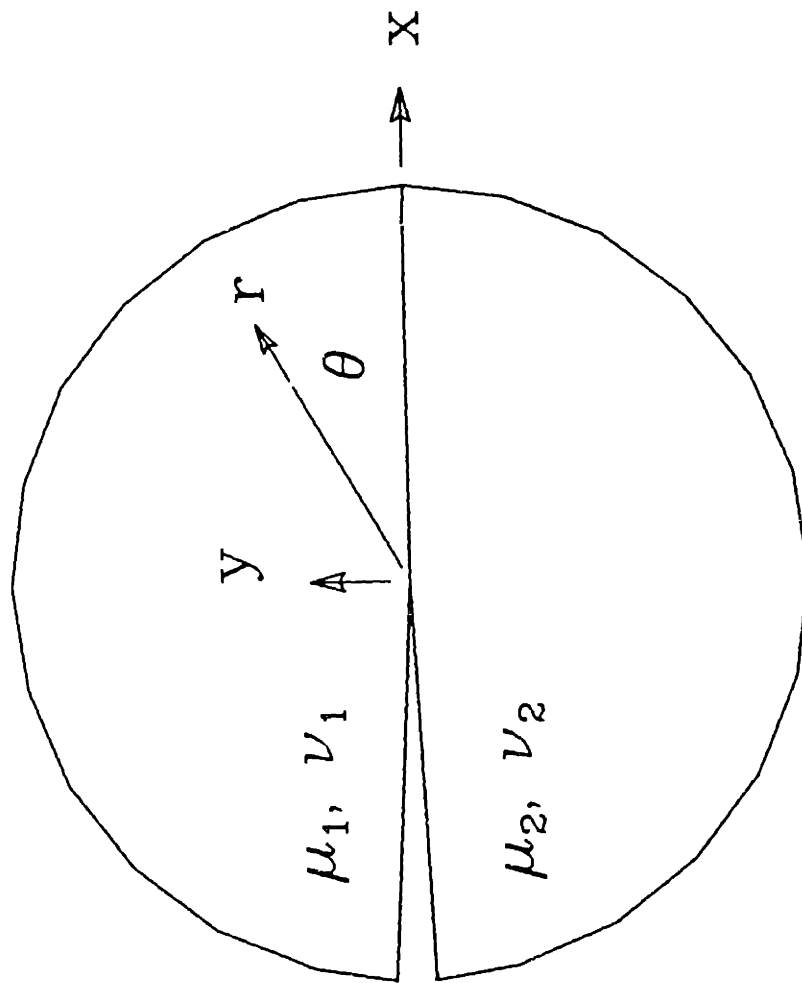


Figure 1 Schematic interfacial crack tip.

formally calculates the Mises equivalent stress.) Equating the Mises equivalent stress, $\bar{\sigma}$, Eq.(A.27) with the material yield strength, σ_{y0} , and solving for the radius yields

$$r_p(\theta) = \frac{\mathbf{K}\bar{\mathbf{K}}}{\sigma_{y0}^2 \pi \cosh^2(\pi\epsilon)} \frac{1}{8} \times \left\{ \begin{aligned} &\cos 2\zeta(\theta) \left[-3(1 + \cos 2\theta) - 6\epsilon \sin 2\theta + (8D - 6)e^{2\epsilon(\theta-\pi)} \cos \theta \right] \\ &+ \sin 2\zeta(\theta) \left[3 \sin 2\theta - 6\epsilon(\cos 2\theta - 1) - (8D - 6)e^{2\epsilon(\theta-\pi)} \sin \theta \right] \\ &+ e^{2\epsilon(\theta-\pi)} \left[\left(\frac{3}{2} - 6\epsilon^2 \right) (\cos 2\theta - 1) + 6\epsilon \sin 2\theta + (8D - 3) \right] + 3e^{2\epsilon(\pi-\theta)} \end{aligned} \right\}, (6)$$

where

$$D = \nu_1^2 - \nu_1 + 1 \quad (7)$$

and

$$\zeta(\theta) = \angle \mathbf{K} + \epsilon \ln r_p(\theta). \quad (8)$$

Here θ is the angle measured from the interface, $r_p(\theta)$ is the plastic zone radius from the crack tip, and $\angle \mathbf{K}$ is the phase angle of the (complex) stress intensity factor defined with a branch cut at $\theta = \pi$ such that $\pi > \angle \mathbf{K} > -\pi$. ($\angle \mathbf{K} = \arctan(\Im \mathbf{K} / \Re \mathbf{K})$, which in the homogeneous case, $\epsilon = 0$, reduces to $\angle \mathbf{K} = \arctan(K_{II}/K_I)$). For plane stress conditions, Eqs.(6) and (8) are still valid; however, Eq.(7) is redefined as $D = 1$ and the plane stress value for ϵ must be used.

This approximation is valid only when a dominant elastic crack field exists and the maximum extent of the plastic zone is small compared to crack length (l) or other characteristic dimensions (maximum $r_p \ll l$). Further clarification will be stipulated in section 3.4.

3 Discussion

3.1 Mathematical Considerations

Several interesting mathematical features arise from Eq.(6). Foremost, the dimensionless $\zeta(\theta)$ is naturally obtained in the derivation. It removes the dimensional problems associated with assigning length units in \mathbf{K} definitions (Rice, 1988) since $\zeta(\theta)$ is invariant as long as $r_p(\theta)$ and \mathbf{K} are expressed with the same length units. Recall the generic \mathbf{K} ,

$$\mathbf{K} = \underline{\sigma}^\infty C e^{-i\epsilon \ln l} \sqrt{\pi l}, \quad (9)$$

where $\underline{\sigma}^\infty$ is the far field load expressed as a complex number, C is a dimensionless complex geometric constant, and l is the characteristic dimension. Examination of Eq.(9) reveals that when different length units are used to express l , the $\angle \mathbf{K}$ changes. Eq.(9) can be rewritten as

$$\mathbf{K} = \|\underline{\sigma}^\infty\| \times \|C\| e^{i(\phi - \epsilon \ln l)} \sqrt{\pi l}, \quad (10)$$

where $\| \quad \|$ denotes the magnitude of a complex expression,

$$\phi = \angle \underline{\sigma}^\infty + \angle C, \quad (11)$$

and

$$\angle \mathbf{K} = \phi - \epsilon \ln l. \quad (12)$$

Substituting Eqs.(6), (11), and (12) into Eq.(8) yields

$$\zeta(\theta) = \phi - \epsilon \ln l + \epsilon \ln \left\{ \frac{\mathbf{K}\bar{\mathbf{K}}}{\sigma_{ys}^2 \pi \cosh^2(\pi \epsilon)} g(\theta, \epsilon, D, \zeta(\theta)) \right\}, \quad (13)$$

where $g(\theta, \epsilon, D, \zeta(\theta))$ is a non-dimensional function. Using Eq.(10), $\mathbf{K}\bar{\mathbf{K}}$ can be expressed as

$$\mathbf{K}\bar{\mathbf{K}} = \|\underline{\sigma}^\infty\|^2 \times \|C\|^2 \pi l. \quad (14)$$

Furthermore, Eq.(13) can be rearranged and simplified by using Eq.(14), and it reduces to

$$\zeta(\theta) = \phi + 2\epsilon \ln \left\{ \frac{\|\underline{\sigma}^\infty\| \times \|C\|}{\sigma_{ys} \cosh(\pi \epsilon)} \sqrt{g(\theta, \epsilon, D, \zeta(\theta))} \right\}. \quad (15)$$

From Eq.(15) it is clear that $\zeta(\theta)$ is dimensionless and independent of length units used to express \mathbf{K} . This is true as long as a single length measure is assigned to all l used when evaluating \mathbf{K} in, *e.g.*, Eq.(10).

For a wide range of engineering interface material properties, an angle θ_0 exists for which the coefficients

$$P_1 = -3(1 + \cos 2\theta) - 6\epsilon \sin 2\theta + (8D - 6)e^{2\epsilon(\theta - \pi)} \cos \theta \quad (16)$$

and

$$P_2 = 3 \sin 2\theta - 6\epsilon(\cos 2\theta - 1) - (8D - 6)e^{2\epsilon(\theta-\pi)} \sin \theta, \quad (17)$$

which multiply the trigonometric functions of $2\zeta(\theta)$ in Eq.(6), are both zero. Alternatively, a single expression for determining θ_0 is obtained by requiring the magnitude of the coefficient multiplying the term JJ in Eq.(A.22) to be zero. Thus, when $\theta = \theta_0$,

$$4(8D - 6)e^{2\epsilon(\theta_0-\pi)}(-3 \cos \theta_0 - 6\epsilon \sin \theta_0) + (18 - 72\epsilon) \cos \theta_0 + 72\epsilon^2 \sin 2\theta_0 + (8D - 6)^2 e^{4\epsilon(\theta_0-\pi)} + 72\epsilon^2 + 18 = 0. \quad (18)$$

Figure 2 shows the plane strain θ_0 , numerically obtained from Eq.(18), for various ν from 0 to 0.5 for the complete range of ϵ , assuming non-negative ν in each material. Note that, θ_0 is generally not the same under plane strain conditions as it is under plane stress conditions since, under each condition ϵ and D have different definitions. The existence of θ_0 indicates that radially, at angle θ_0 :

- (a) Plastic zone growth is independent of the applied loading phase, $\angle \mathbf{K}$.
- (b) The elastically-calculated Mises equivalent stress does not oscillate.
- (c) The plastic zone radius is proportional to $\mathbf{K}\bar{\mathbf{K}}$.

Substituting Eq.(6) into Eq.(8), and defining the SSY interfacial load-phase angle (ILPA), ζ_0 , as

$$\zeta_0 = \angle \mathbf{K} + \epsilon \ln \frac{\mathbf{K}\bar{\mathbf{K}}}{\sigma_{ys}^2 \pi \cosh^2(\pi \epsilon)}, \quad (19)$$

yields

$$\begin{aligned} \zeta(\theta) = \zeta_0 + \epsilon \ln \left\{ \cos 2\zeta(\theta) \left[-3(1 + \cos 2\theta) - 6\epsilon \sin 2\theta + (8D - 6)e^{2\epsilon(\theta-\pi)} \cos \theta \right] \right. \\ \left. + \sin 2\zeta(\theta) \left[3 \sin 2\theta - 6\epsilon(\cos 2\theta - 1) - (8D - 6)e^{2\epsilon(\theta-\pi)} \sin \theta \right] \right. \\ \left. + e^{2\epsilon(\theta-\pi)} \left[\left(\frac{3}{2} - 6\epsilon^2 \right) (\cos 2\theta - 1) + 6\epsilon \sin 2\theta + (8D - 3) \right] \right. \\ \left. + 3e^{2\epsilon(\pi-\theta)} \right\} - \epsilon \ln(8). \end{aligned} \quad (20)$$

Eq.(20) reveals that $\zeta(\theta)$ can be additively decoupled into a load-phase dependent quantity, ζ_0 , and a transcendental angular dependent function. Alternative definitions of ζ_0 , differing trivially by a pure constant, are possible. Such a constant could be chosen, *e.g.*, to approximately normalize the angular function to unity. Eq.(19) is a convenient expression for the SSY ILPA since it is an explicit single term representing

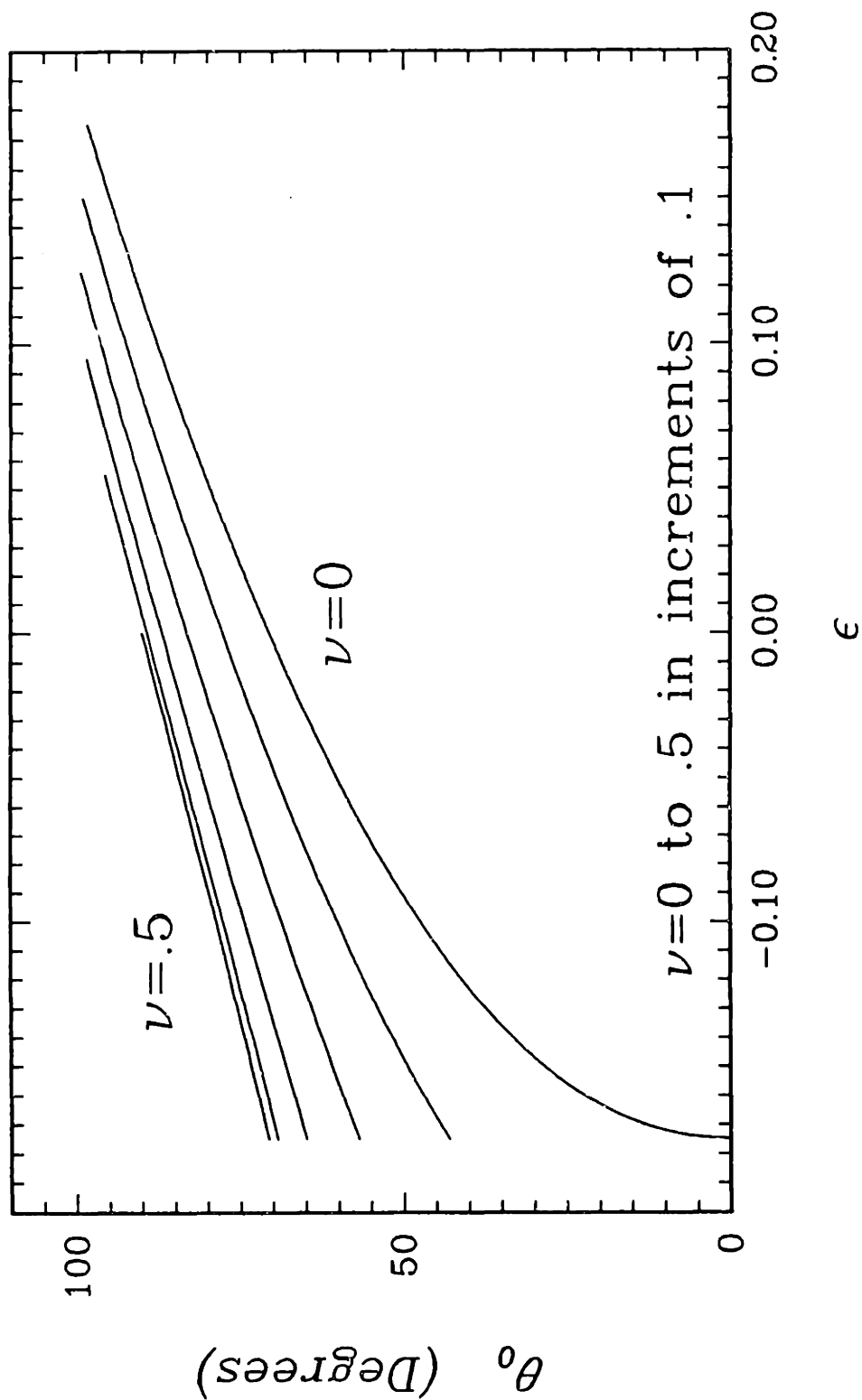


Figure 2 The angle θ_0 is shown for plane strain conditions over the complete range of ϵ for various values of ν from 0 to 0.5 in increments of 0.1.

the total load-phase angle and is common in all $\zeta(\theta)$. The ILPA totally describes the phase angle of the load by summing the loading phase shift, which is attributable to the change in zone size due to increases in loading, and the load-phase angle ($\angle\mathbf{K}$).

Another useful expression is obtained by evaluating Eq.(20) at $\theta = \theta_0$, in which case

$$\zeta(\theta_0) = \zeta_0 + \epsilon \ln \left\{ \frac{1}{8} \left(3e^{2\epsilon(\pi-\theta_0)} + e^{2\epsilon(\theta_0-\pi)} \left[\left(\frac{3}{2} - 6\epsilon^2 \right) (\cos 2\theta_0 - 1) + 6\epsilon \sin 2\theta_0 + (8D - 3) \right] \right) \right\}. \quad (21)$$

This expression may prove to be beneficial in investigating the effects of various material dependent parameters, since it does not contain any radially oscillatory terms, and it represents a real value of $\zeta(\theta)$.

3.2 Zone Growth Considerations

From the above expressions, the overall plastic zone growth characteristics with respect to increasing applied load (\mathbf{K}) during SSY, can be outlined. After sufficient initial loading has been applied to produce a continuum size plastic zone, the expressions for r_p become valid and applicable. Examination of Eqs.(6) and (20) shows that zone growth is quasi-proportional to $(\mathbf{K}\bar{\mathbf{K}}/\sigma_{ys}^2)$, and that the zone shape periodically repeats itself with every π increase in ζ_0 . For (very) large cracks, it is possible that the plastic zone may repeat its shape during loading. For every discrete value of ζ_0 , a unique zone shape and a unique set of tractions along r_p exist. *Figure 9* shows the plastic zone at various values of ζ_0 for $\epsilon = .170$ and $\nu = .342$. This suggests that ζ_0 uniquely describes the very local crack-tip fields within the zone as long as all previous loading experiences affect the current plastic state in the same manner. For the loading case where several cycles of ζ_0 have occurred, this would appear to be true. Since two loadings with unequal tractions can produce identical plastic zones, (*e.g.* $\zeta_0 = 90^\circ$ and $\zeta_0 = -90^\circ$ produce tractions with opposite signs), a full 2π evaluation of ζ_0 is required to determine all the local fields.

3.3 Comparisons

In the limiting homogeneous elastic case ($\epsilon = 0$), comparison with numerical solutions (Shih, 1974) indicate that the plastic zone shape and size for pure mode I and mode II, as well as for various mixed modes, are recovered. Comparing the approximate homogeneous plastic zones with plastic zones numerically obtained for strain hardening

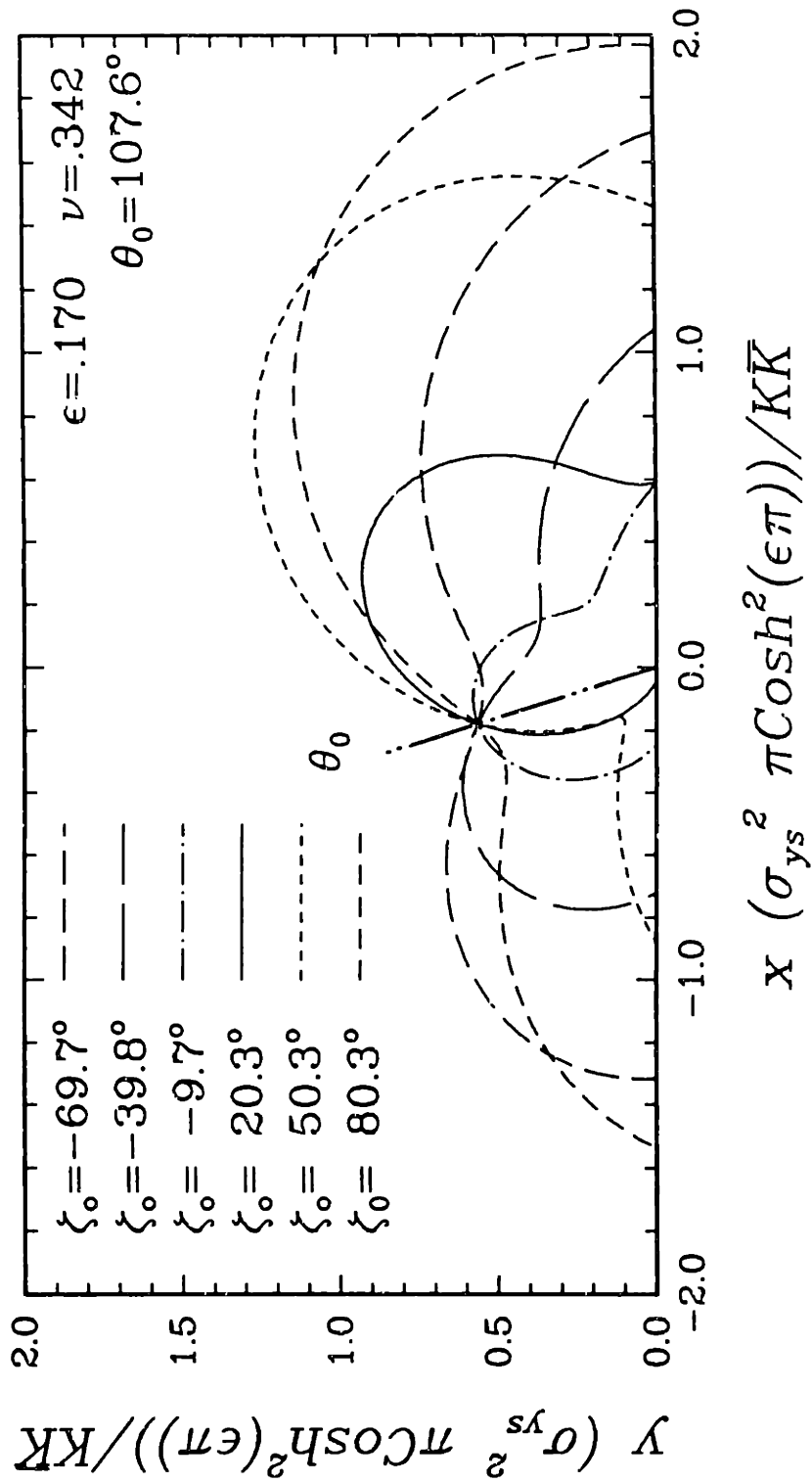


Figure 9 Approximate plastic zones for various ζ_0 values.

material shows that as the strain hardening exponent, n , increases (strain \propto (stress) ^{n}), the elastic approximation overestimates the plastic zone size behind the crack tip and underestimates it ahead of the crack tip. This is accompanied by slight distortional effects which tend to rotate the strain hardening plastic zone lobes toward the region in front of the crack as compared to the elastic approximation.

Figures 4 to 7 show finite element (FE) calculations of SSY plastic zones for an interfacial crack tip with an elastic/perfectly-plastic medium adjoint to an elastic medium (Zywicz, 1988), and the approximate plastic zones for several values of ϵ , ν_1 , μ_1 , and $\angle K$. Although the precise shape is not reproduced, the general size and distribution of the lobe(s) as well as their position(s) are well represented by the simple approximation. Examining *Figure 5* shows that the size scale is significantly different from that of the other figures, demonstrating the accuracy of the approximation in predicting overall size. *Figures 4 to 7* represent the worst case comparisons since perfect plasticity formally represents a strain hardening exponent of $n = \infty$. The jaggedness of the finite element calculated plastic zones is attributable to extrapolation/approximation errors and mesh discretization. Thus, the jaggedness should only be interpreted as an artifact of the discretization and plotting procedure. *Figures 8 and 9* show FE calculations of plastic zones for a Ramberg-Osgood strain hardening material, with strain hardening exponents $n = 3$ and $n = 10$, respectively, adjoint to a rigid material (Shih and Asaro, 1987), and the approximate plastic zones for several load levels. These FE calculations were performed for a Griffith type crack, similar to the one shown in *Figure 11*, with $\epsilon = .0935$, $2a = 2m$, and $\nu_1 = .3$, where the stress intensity factor for the geometry and loading is $K = 1.803\sigma^\infty e^{0.1201i}(m)^{\frac{1}{2}-0.0935i}$. Here σ^∞ represents the remote stress normal to the crack face (the σ_{yy} stress as shown in *Figure 11*), and σ_0 is the reference stress (or yield stress). The overall sizes and shapes are well characterized by the (asymptotic) approximation. As in the homogeneous case, when the strain hardening exponent is decreased, the elastic approximation becomes more precise. (Recall, the Ramberg-Osgood material idealization produces a linear elastic response for $n = 1$.) Although the plastic zone radii are not all identically the same at θ_0 , the extent of the plastic zone in the vicinity of θ_0 is indeed approximately the same for all loadings (ζ_0).

3.4 Valid Solution Domain

The plastic zone approximation is based upon the assumption that a dominant (Williams type) field exists, as defined in Eqs.(4) and (5), near the crack tip and transitionally

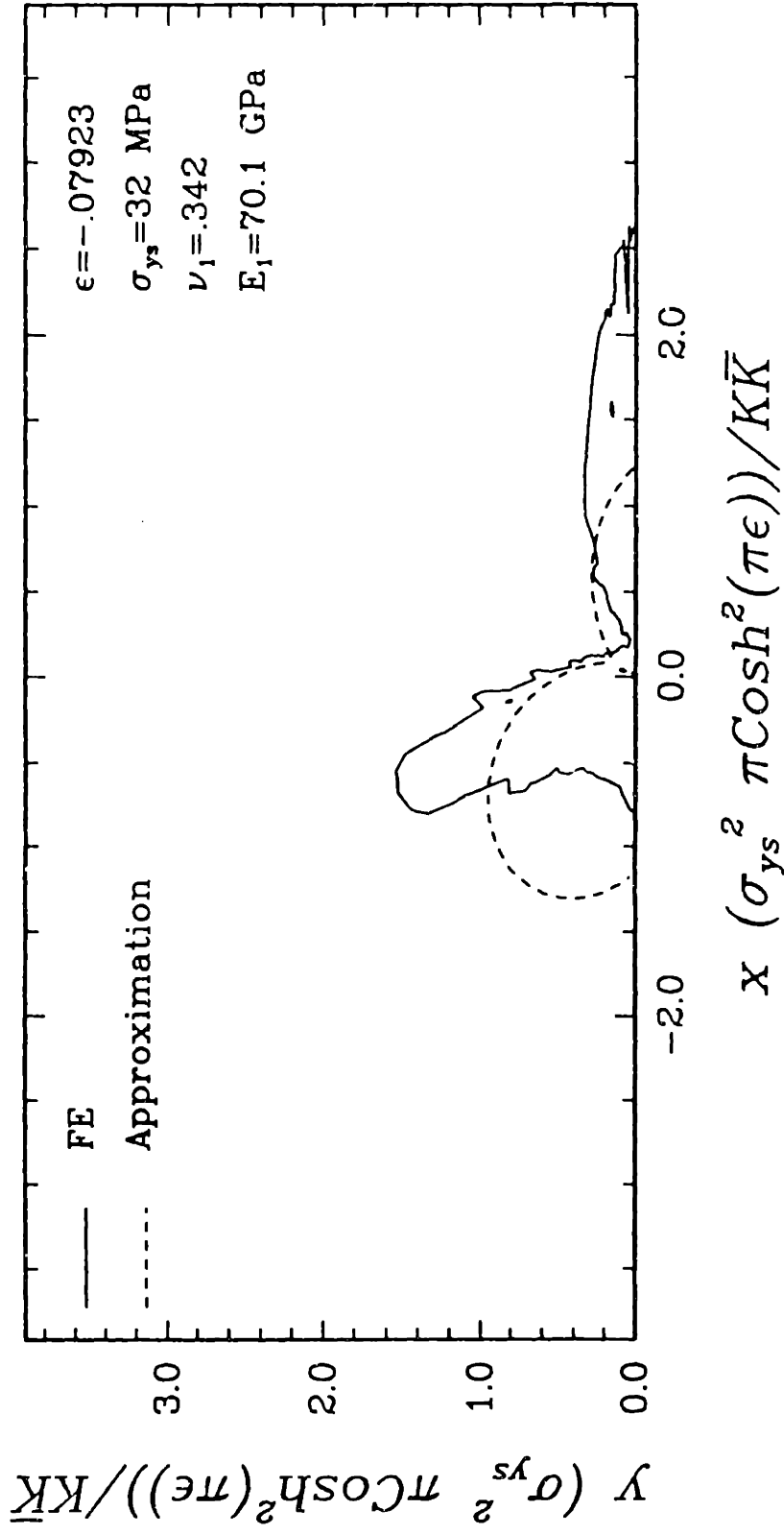


Figure 4 Plastic zone comparison between the elastic approximation and a finite element solution for an elastic/perfectly-plastic medium adjoint to an elastic medium; $\mathbf{K} = 50e^{-0.4636i} \text{MPa}(\text{m})^{\frac{1}{2} + 0.0793i}$; $\zeta_0 = -.432 (-24.7^\circ)$.

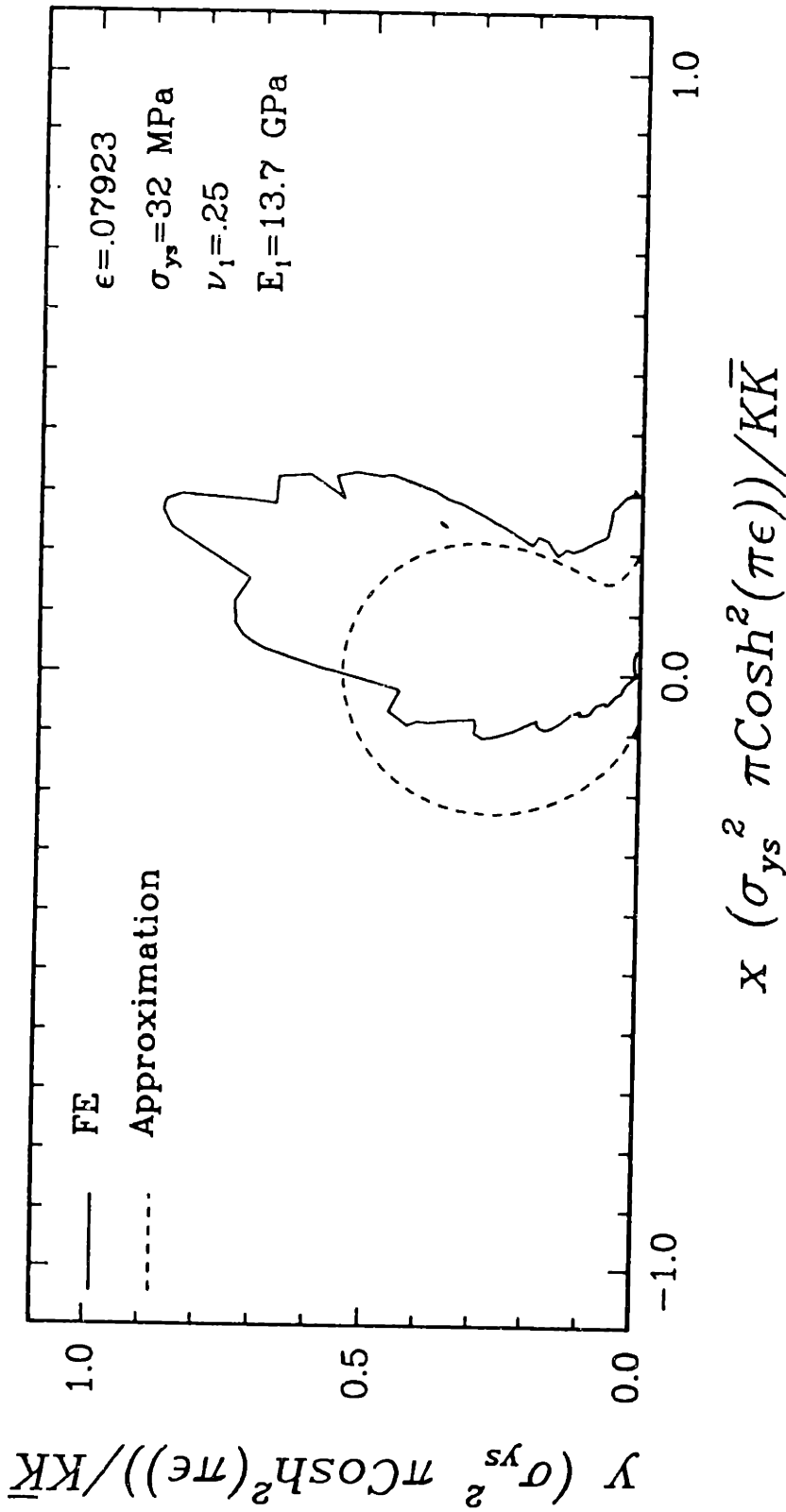


Figure 5 Plastic zone comparison between the elastic approximation and a finite element solution for an elastic/perfectly-plastic medium adjoint to an elastic medium; $\mathbf{K} = 30e^{-0.9272i} \text{MPa}(\text{m})^{\frac{1}{2} + 0.0793i}$, $\zeta_0 = -1.004 (-57.5^\circ)$.

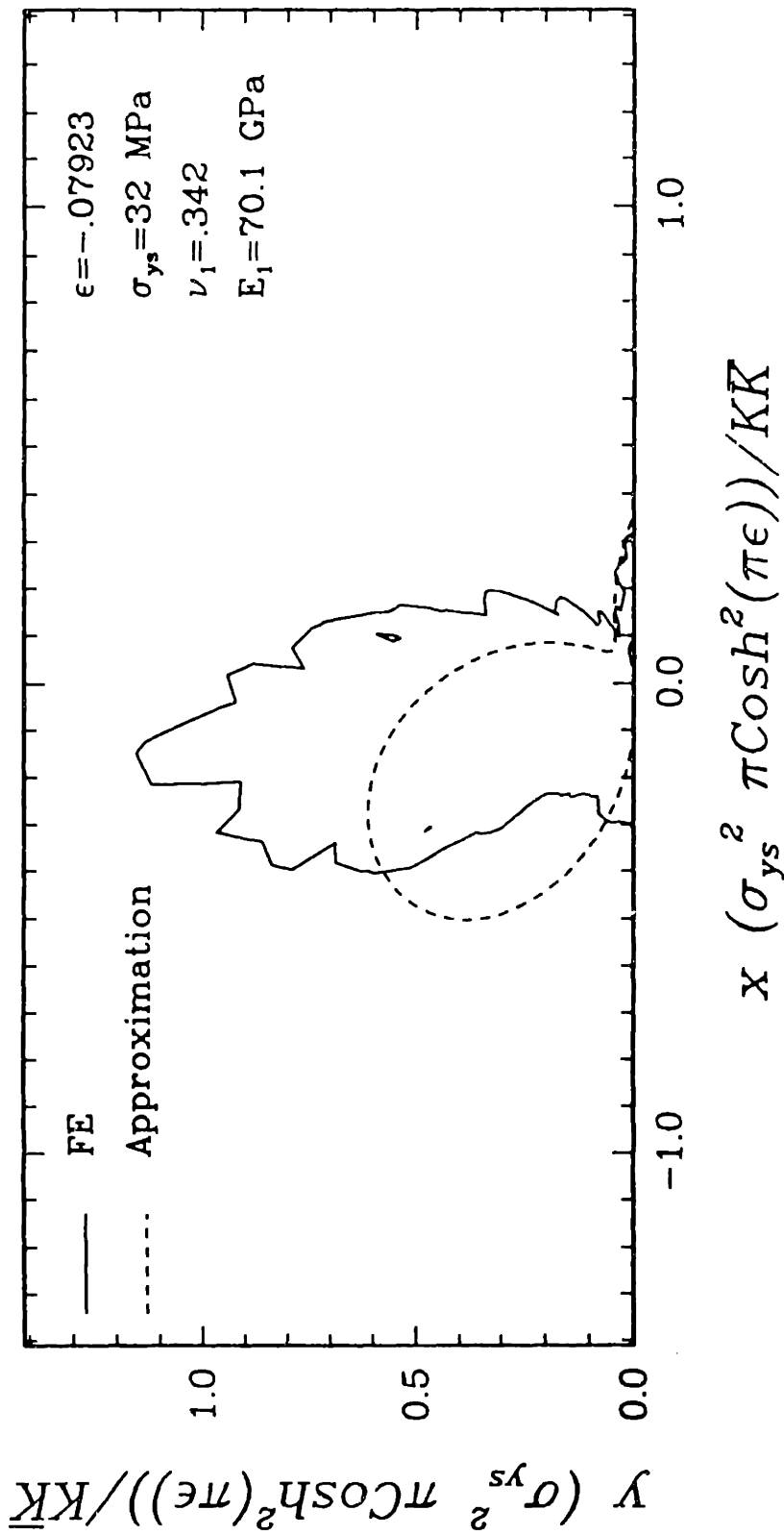


Figure 6 Plastic zone comparison between the elastic approximation and a finite element solution for an elastic/perfectly-plastic medium adjoint to an elastic medium; $\mathbf{K} = 56.7 e^{-0.07923i}$, $\zeta_0 = -.007 (-.42^\circ)$.

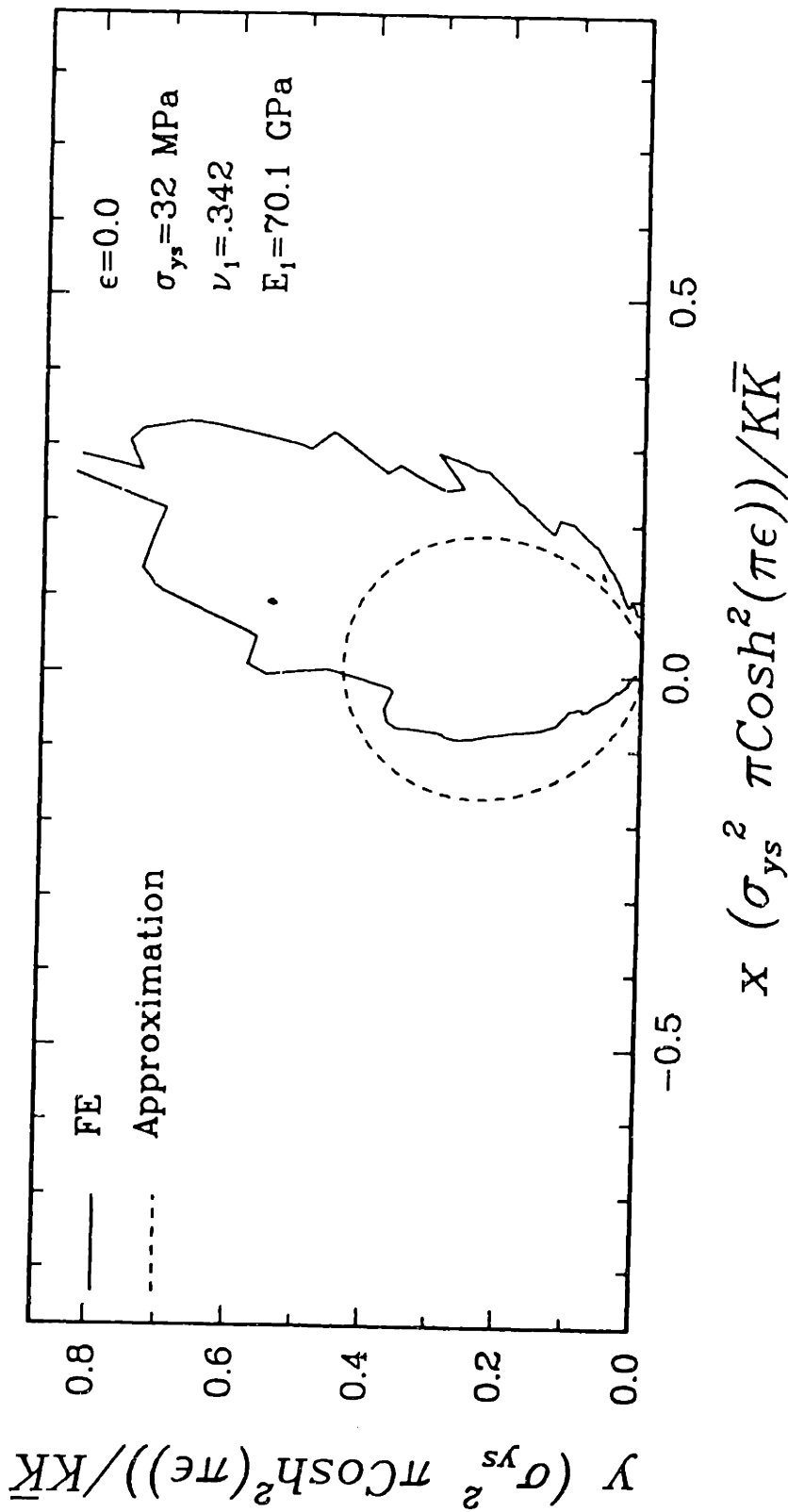


Figure 7 Plastic zone comparison between the elastic approximation and a finite element solution for an elastic/perfectly-plastic medium adjoint to an elastic medium; $K = 63.4e^{-0.0i} \text{MPa}(m)^{\frac{1}{2}+0.0i}$, $\zeta_0 = 0$.

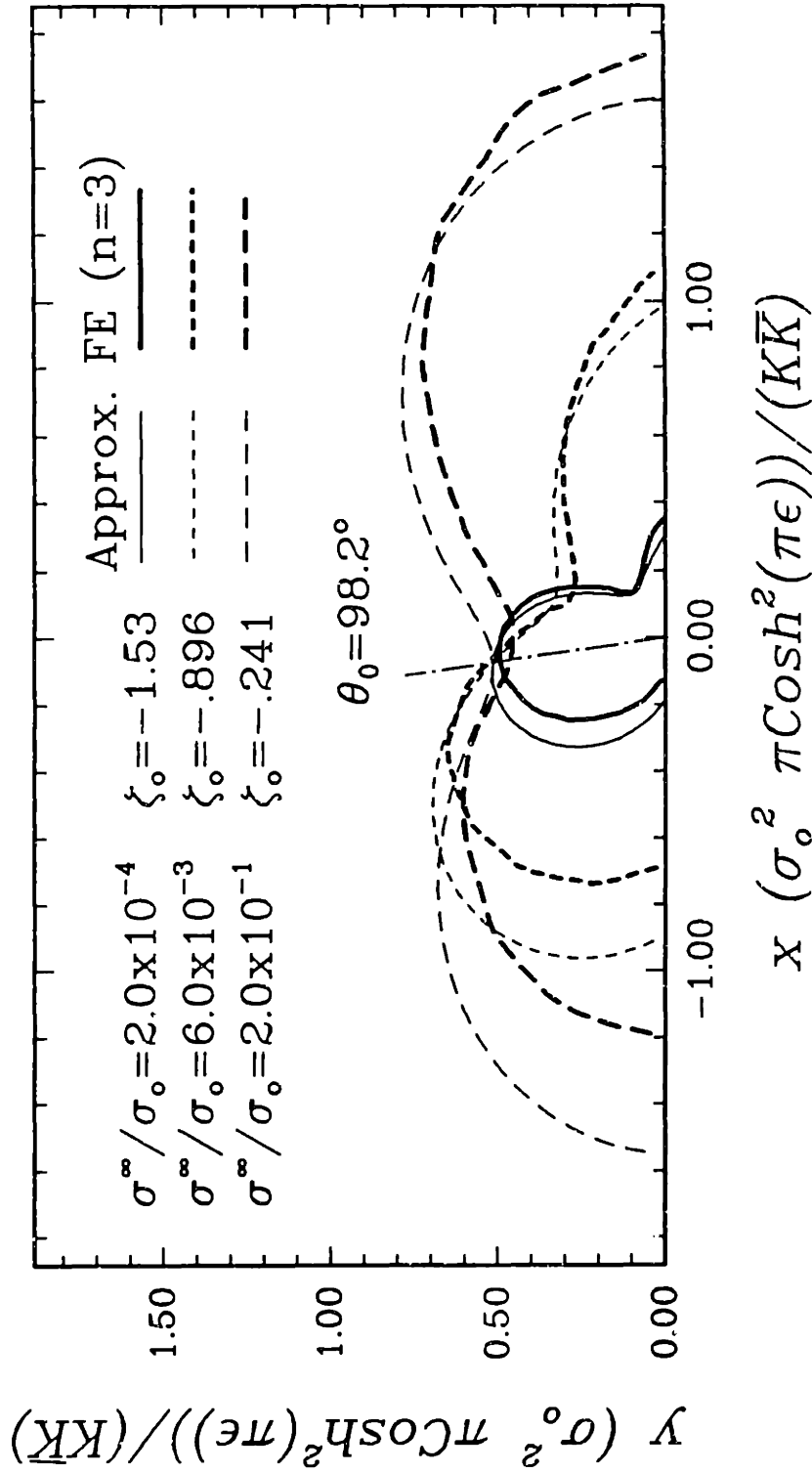


Figure 8 Plastic zone comparisons between the elastic approximation and a finite element solution for a strain hardening material, $n = 3$, (Shih and Asaro, 1987) for various ζ_0 ; $\mathbf{K} = \sigma^\infty 1.8025 e^{0.1201 \zeta_0} (\text{m})^{\frac{1}{2} - 0.0935 \zeta_0}$, $\epsilon = .0935$, $\nu = .3$.

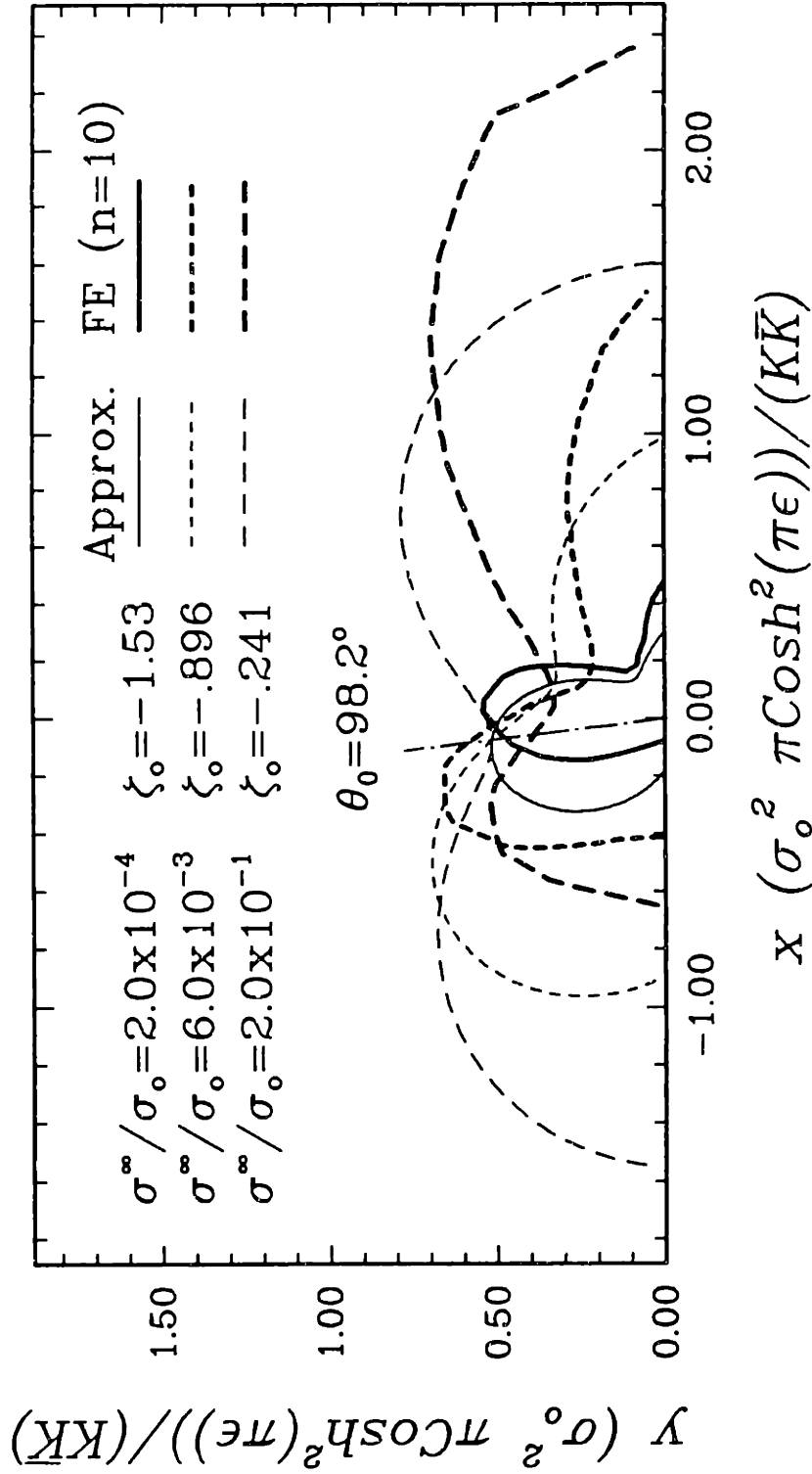


Figure 9 Plastic zone comparisons between the elastic approximation and a finite element solution for a strain hardening material, $n = 10$, (Shih and Asaro, 1987) for various ζ_0 ; $\mathbf{K} = \sigma^\infty 1.8025e^{0.1201i}(m)^{\frac{1}{2}-0.0935i}$, $\epsilon = .0935$, $\nu = .3$.

along the plastic zone boundary. This section develops a methodology, based upon exact elasticity solutions for a Griffith crack, for determining approximately when such a Williams type field exists, and thus defining the valid domain for the characterization of the plastic zone in terms of ζ_0 , \mathbf{K} , and material parameters.

In examining the exact elasticity solution for an interfacial crack between two semi-infinite media (Rice and Sih, 1965), the stress potentials can be additively decoupled into singular terms and homogeneous far field terms, and reduced to obtain the dominant asymptotic potentials. Consider Φ , the ϕ_1' stress potential for the Griffith crack, given by Rice and Sih (1965) which is,

$$\begin{aligned} \Phi = & \frac{(z - i2\epsilon a)}{\sqrt{z^2 - a^2}} \left(\frac{z + a}{z - a} \right)^{i\epsilon} \frac{\sigma_{yy}^\infty - i\sigma_{xy}^\infty}{1 + e^{2\pi\epsilon}} \\ & + \frac{\sigma_{zx_1}^\infty + \sigma_{yy}^\infty}{4} - \frac{\sigma_{yy}^\infty}{1 + e^{2\pi\epsilon}} + i \left(\frac{\sigma_{xy}^\infty}{1 + e^{2\pi\epsilon}} + \frac{2\mu_1\omega_1^\infty}{1 + \kappa_1} \right). \end{aligned} \quad (22)$$

Here the crack tips are located at $z = \pm a$, and ω_1^∞ is the far field rotation in Region 1. In the region near the crack tip, the stress potential can be represented by

$$\Phi \approx \Phi_{near} = P \left[\frac{(z - i2\epsilon a)}{\sqrt{z^2 - a^2}} \left(\frac{z + a}{z - a} \right)^{i\epsilon} \right], \quad (23)$$

where

$$P = \frac{\sigma_{yy}^\infty - i\sigma_{xy}^\infty}{1 + e^{2\pi\epsilon}}. \quad (24)$$

To obtain the asymptotic potential, substitute $z = a + x$ in to Eq.(23) and assume $\|x\| \ll a$ which yields

$$\Phi_{asympt.} = P \left[\frac{a(1 - i2\epsilon)}{\sqrt{2ax}} \left(\frac{2a}{x} \right)^{i\epsilon} \right] = \bar{\mathbf{K}} \frac{x^{-i\epsilon}}{\sqrt{2\pi x}} \frac{1}{1 + e^{2\pi\epsilon}}. \quad (25)$$

Using Eq.(A.23), Eq.(25) can be shown to be identical to Eq.(4).

By considering one potential of the exact elasticity solution for a Griffith type crack, Eq.(22), an error parameter can be constructed which represents the discrepancy between the exact solution and the (Williams type) dominant asymptotic solution, Eqs.(4) and (5). Normalizing Eq.(25) by the singular portion of Eq.(22), Eq.(23), yields

$$N = \frac{\Phi_{asympt.}}{\Phi_{near}} = \left(1 + \frac{\hat{x}}{.5 - i\epsilon} \right)^{-1} (1 + \hat{x})^{.5 - i\epsilon}. \quad (26)$$

Here $\hat{x} = x/2a$ is the normalized distance with respect to crack length, and N represents the portion of the singular potential term represented by the asymptotic potential, given by Eq.(25). Evaluating Eq.(26) along the interface at $\hat{x} = 0.1$ yields $N = 0.874$ for $\epsilon = 0$ while for the extreme values $\epsilon = \pm 0.1748$ (positive ν), $N = 0.889e^{\pm 0.0694i}$. For all ϵ , as $\hat{x} \rightarrow 0$, $N \rightarrow 1$. This, in conjunction with the previous observations, indicates that the asymptotic expression reproduces the singular term reasonably well over the entire domain where the singular potential term dominates. (From Eq.(22), it can be shown that at $\hat{x} \approx 0.13$, the singular term contributes to the total stress potential an amount, equal in magnitude, to that of the homogeneous term. For $|\hat{x}| < 0.13$, the singular portion dominates.)

Based upon the previous discussion, the asymptotic representation, Eqs.(4) and (5) or Eq.(25), is representative in the crack-tip region where

$$\frac{l}{10} \geq r \geq 0. \quad (27)$$

Here l is the characteristic dimension. (Note, a slight modification has been made for convenience, and that is to limit the domain to $l/10$ instead of $l/8$.) Such a conclusion is also typical of homogeneous crack solutions.

A second condition must also be satisfied if Eqs.(4) and (5) are to depict the actual dominant asymptotic behavior; namely, that any perturbations within the dominant asymptotic solution domain must be small compared to that domain and occur near the crack tip. Using a St. Venant's type argument, this can be expressed mathematically as

$$r_{\text{perturbation}_{\text{max}}} \leq \frac{3l}{100}. \quad (28)$$

Such perturbations could include plastic zones and crack-face contact and interpenetration, if present. (Note, Williams type fields, Eqs.(4) and (5), are based upon the condition that the crack faces are traction-free.) Eq.(28) represents a very conservative restriction and, depending upon the actual conditions, it may be appropriate to relax it somewhat.

The asymptotic crack-tip opening displacement (CTOD), Δu , as a function of r (Hutchinson *et al.*, 1987) is

$$\Delta u(r) = u(r, \theta = \pi) - u(r, \theta = -\pi) = \frac{(C_1 + C_2)K r^{i\epsilon} \sqrt{r}}{2\sqrt{2\pi}(1 + i2\epsilon) \cosh(\pi\epsilon)}, \quad (29)$$

where

$$\mathbf{u}(r) = u_y(r) + iu_x(r), \quad (30)$$

and C_j are defined according to Eq.(A.7). Following Eq.(A.24), ζ is introduced and is defined as

$$\zeta = \angle \mathbf{K} + \epsilon \ln r. \quad (31)$$

Substituting Eq.(31) into Eq.(29) yields

$$\Delta \mathbf{u}(r) = \frac{(C_1 + C_2) \|\mathbf{K}\| \sqrt{r} e^{i\zeta}}{2\sqrt{2\pi} \cosh(\pi\epsilon)(1 + i2\epsilon)}. \quad (32)$$

Crack face interpenetration occurs when, $\Delta u_y < 0 \Rightarrow \Re \Delta \mathbf{u} < 0$ or,

$$\cos \zeta + 2\epsilon \sin \zeta < 0. \quad (33)$$

The critical values ζ_l , the beginning and ending points of interpenetration, occur when

$$\cos \zeta_l + 2\epsilon \sin \zeta_l = 0 \quad (34)$$

or,

$$\tan \zeta_l = -\frac{1}{2\epsilon}. \quad (35)$$

Note that for the homogeneous case, the condition represented by Eq.(33) occurs any time a negative mode I loading is applied.

The previous condition on r , Eqs.(27) and (28), coupled with the oscillatory crack face behavior, can be restated as valid solution domain conditions in terms of ζ (via Eq.(31)), \mathbf{K} , and material parameters. Thus, Williams type fields, Eqs.(4) and (5), will exist transitionally along the plastic zone boundary if and only if

$$\cos \zeta + 2\epsilon \sin \zeta > 0 \quad \begin{cases} \epsilon > 0 & \zeta_0 \leq \zeta \leq \zeta_{max} \\ \epsilon < 0 & \zeta_{max} \leq \zeta \leq \zeta_0 \end{cases} \quad (36)$$

and

$$\frac{\mathbf{K}\bar{\mathbf{K}}}{\sigma_{ys}^2 \pi \cosh^2(\pi\epsilon)} \leq .03l, \quad (37)$$

where

$$\zeta_{max} = \angle \mathbf{K} + \epsilon \ln(.1l). \quad (38)$$

The condition depicted by Eq.(36) requires that no crack face contact or interpenetration occurs between the plastic zone boundary and the maximum valid extent of the dominant asymptotic domain. It also assumes that the size of the plastic zone along the crack face can be approximated by the characteristic length, $\mathbf{K}\bar{\mathbf{K}}/\sigma_{\nu}^2\pi\cosh^2(\pi\epsilon)$. *Figure 10* shows for plane strain the values of ζ , as a function of ϵ , which will not produce crack face interpenetration. For Eq.(36) to be true, both ζ_0 and ζ_{max} , as well as the entire path which connects them, must be in the unshaded region of *Figure 10*. Note that for $\epsilon = 0$ (homogeneous case) the admissible range is $|\zeta_0| < \pi/2$, corresponding to $K_I > 0$.

Conditions represented by Eqs.(36) to (38) are necessary, but not sufficient conditions for a Williams type field to exist. Crack closure beyond $l/10$ is possible and must be ruled by other considerations such as global geometrical and loading factors or by other solutions. However, for a (remotely loaded) Griffith crack, Comninou and Schmueser (1979) showed crack closure is continuous from the crack tip outwards; thus if closure exists beyond $l/10$, it will occur within $l/10$ (with respect to one crack tip). Henceforth, Eqs.(36) to (38) are also sufficient validity conditions for a Griffith type crack.

4 Conclusion

An approximate expression for the plastic zone around an interfacial crack-tip has been presented. It modestly reproduced the characteristic size and shape, as compared to various precise numerical solutions, with increasing accuracy as the strain hardening exponent approached unity. The overall crack-tip plastic zone size was found to be quasi-proportional to $(\mathbf{K}\bar{\mathbf{K}}/\sigma_{\nu}^2)$. Plastic zones were found to change shape with applied load in a periodic manner dependent upon interfacial load-phase angle (ILPA), ζ_0 . The ILPA was identified as a comprehensive single load-phase angle which determines the zone shape and tractions along the zone boundary, and may uniquely identify the behavior within the zone. Conditions for determining applicability of this expression were stated in terms of ζ_0 and ζ_{max} , where ζ_{max} is dependent upon the characteristic length in the problem.

From the previous derivations it appears that the ILPA (ζ_0), ϵ , (possibly ν), and the magnitude of \mathbf{K} (expressed as $\mathbf{K}\bar{\mathbf{K}}$ or J , where J is the J -Integral), are the local interfacial fracture mechanics variables needed to describe interfacial SSY behavior.

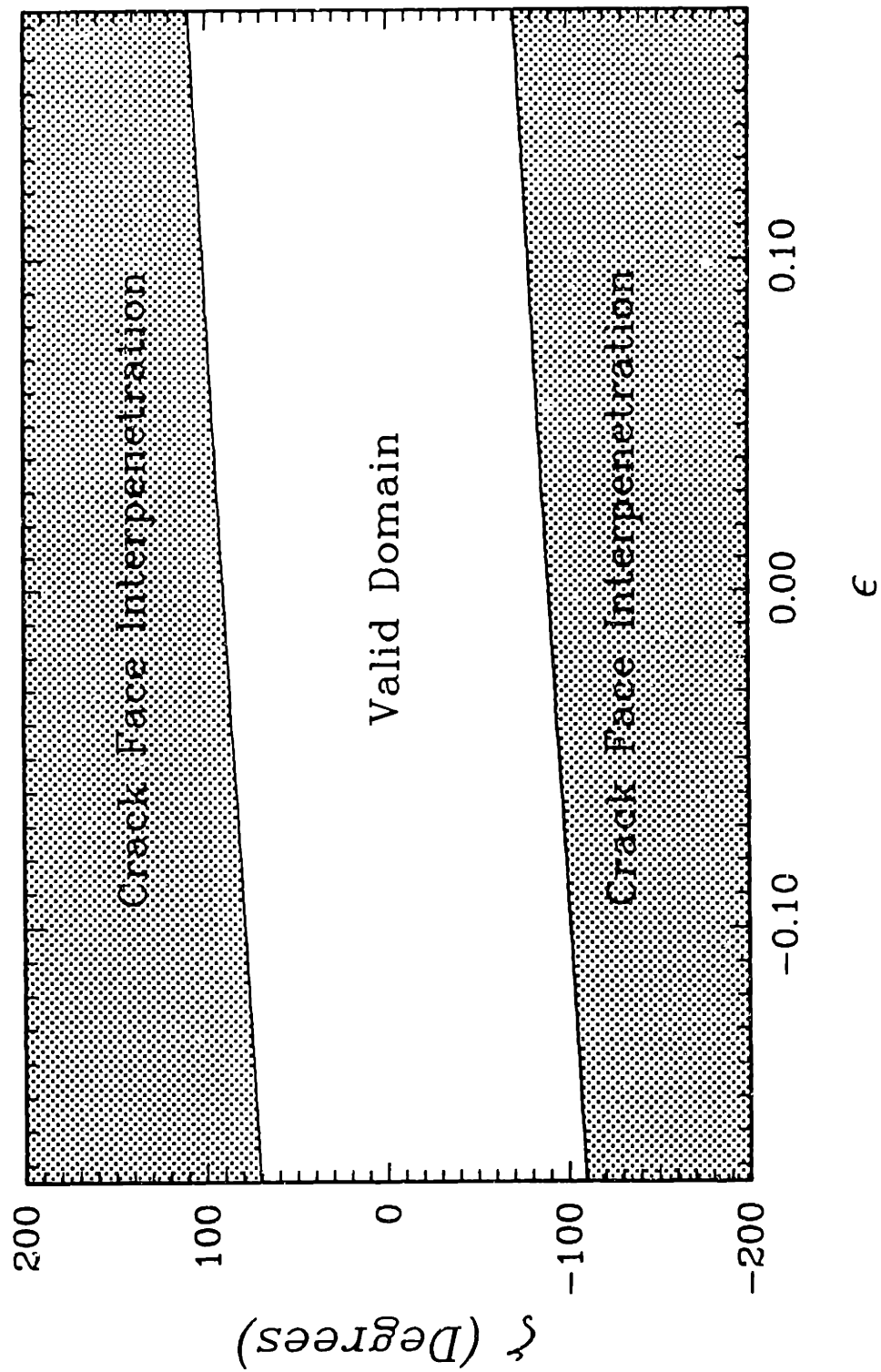


Figure 10 Crack-face interpenetration is shown as a function of ζ and ϵ , for plane strain conditions.

Following homogeneous fracture mechanics, it seems natural to construct interfacial fields analogous to HRR or slip-line fields, utilizing the same material idealizations and similar framework, but with the degree of local (plastic) mode mixity being now dependent upon ζ_0 . Using ζ_0 and the magnitude of the singularity as conditions describing the plastic zone boundary, the characteristics deep within the zone should be identifiable.

To familiarize the readers with the application of these concepts to interfacial fracture mechanics, a hypothetical example is included in Appendix B. It demonstrates how to determine various local crack-tip quantities.

Acknowledgments

Special gratitude is expressed to Prof. J. R. Rice for useful discussions. This work was supported by ONR under grant N00014-84-K-0495.

References

- Brown, S. B., Kim, H. K., and Anand, L., 1987, "An Internal Variable Constitutive Model for Hot Working Metals", Reports of Research in Mechanics of Materials, MIT, Cambridge; (submitted to International Journal of Plasticity).
- Comninou, M., and Schmueser, D., 1979, "The Interface Crack in a Combined Tension-Compression and Shear Field", ASME Journal of Applied Mechanics, Vol. 46, pp.345-348.
- Hertzberg, R. W., 1976, *Deformation and Fracture Mechanics of Engineering Materials*, J. Wiley, New York, pp.20.
- Hutchinson, J. W., Mear, M., and Rice, J. R., 1987, "Cracks Paralleling an Interface Between Dissimilar Media", Harvard University, Div. of Applied Science, Cambridge, (to appear in the ASME Journal of Applied Mechanics).
- McClintock, F. A., and Irwin, G. R., 1965, "Plasticity Aspects of Fracture Mechanics", *Fracture Toughness Testing and Its Applications*, ASTM STP 381, ASTM, Philadelphia, pp.84-114.
- Rooke, D. P., 1963, "Elastic Yield Zone Round a Crack Tip", Royal Aircraft Establishment, Farnborough, Tech. Note CPM 29.
- Rice, J. R., 1988, "Elastic Fracture Mechanics Concepts for Interfacial Cracks", ASME Journal of Applied Mechanics, Vol. 55, pp. 98-103.
- Rice, J. R., and Sih, G. C., 1965, "Plane Problems of Cracks in Dissimilar Media", ASME Journal of Applied Mechanics, Vol. 32, pp. 418-423.
- Shih, C. F., and Asaro, R., 1987, "Elastic-Plastic Analysis of Cracks on Bimaterial Interfaces; Part 1: Small Scale Yielding", Brown University, Providence, (to appear in the ASME Journal of Applied Mechanics).
- Shih, C. F., 1974, "Small-Scale Yielding Analysis of Mixed Mode Plane-Strain Crack Problems", *Fracture Analysis*, ASTM STP 560, ASTM, Philadelphia, pp.187-210.
- Ting, T. C., 1986, "Explicit Solution and Invariance of the Singularities at an Interface Crack in Anisotropic Composites," International Journal of Solids and Structures, Vol. 22, No. 9, pp.965-983.
- Williams, M. L., 1959, "The Stresses Around a Fault or Crack in Dissimilar Media", Bulletin of the Seismological Society of America, Vol. 49, pp.199-204.
- Zywicz, E., 1988, "On Elastic-Plastic Cracks Between Dissimilar Media", Ph. D. Thesis in progress, MIT, Mechanical Engineering, Cambridge.

Appendix A Mises Equivalent Stress Derivation

An asymptotic expression for the Mises equivalent stress around an interfacial plane strain crack tip, as a function of r and θ , is derived.

The general series potential functions for an interface crack, as expressed by Rice (1988), are

$$\phi'_1 = e^{-\pi\epsilon} z^{-\frac{1}{2}-i\epsilon} f(z) + 2C_2 g(z)/(C_1 + C_2), \quad (\text{A.1})$$

$$\phi'_2 = e^{\pi\epsilon} z^{-\frac{1}{2}-i\epsilon} f(z) + 2C_1 g(z)/(C_1 + C_2), \quad (\text{A.2})$$

$$\Omega'_1 = e^{\pi\epsilon} z^{-\frac{1}{2}+i\epsilon} \bar{f}(z) - 2C_2 \bar{g}(z)/(C_1 + C_2), \quad (\text{A.3})$$

and

$$\Omega'_2 = e^{-\pi\epsilon} z^{-\frac{1}{2}+i\epsilon} \bar{f}(z) - 2C_1 \bar{g}(z)/(C_1 + C_2), \quad (\text{A.4})$$

with

$$f(z) = \sum_{n=0}^{\infty} a_n z^n, \quad (\text{A.5})$$

$$g(z) = \sum_{n=0}^{\infty} b_n z^n \quad (\text{A.6})$$

and

$$C_j = (1 + \kappa_j)/\mu_j. \quad (\text{A.7})$$

Here μ_j are the shear moduli, $\kappa_j = 3 - 4\nu_j$ for plane strain and $\kappa_j = (3 - \nu_j)/(1 + \nu_j)$ for plane stress, ν_j are the Poisson's ratios, and the subscripts 1 and 2 refer to the domains above and below the interface, respectively.

From Eqs.(2) and (3) the individual stress components can be expressed as

$$\sigma_{zz} = \frac{1}{2} (B + \bar{B}), \quad (\text{A.8})$$

$$\sigma_{\nu\nu} = \frac{1}{2} (A + \bar{A}), \quad (\text{A.9})$$

and

$$\sigma_{xy} = \frac{-i}{2} (A - \bar{A}), \quad (\text{A.10})$$

where

$$A = (\bar{z} - z)\phi'' + \bar{\phi}' + \Omega', \quad (\text{A.11})$$

and

$$B = 2\phi' + \bar{\phi}' - \Omega' - (\bar{z} - z)\phi''. \quad (\text{A.12})$$

Here $i = \sqrt{-1}$ and a bar denotes the complex conjugate. For plane strain isotropic elastic solids, the Mises equivalent stress is

$$\bar{\sigma}^2 = (\sigma_{xx}^2 + \sigma_{yy}^2)D + (\sigma_{xx}\sigma_{yy})F + 3\sigma_{xy}^2, \quad (\text{A.13})$$

with

$$D = \nu^2 - \nu + 1 \quad (\text{A.14})$$

and

$$F = 2\nu^2 - 2\nu - 1, \quad (\text{A.15})$$

where ν is the Poisson's ratio of the solid. For plane stress isotropic elastic solids Eq.(A.13) is still valid, but Eqs.(A.14) and (A.15) are redefined as $D = 1$ and $F = -1$, respectively. After substituting Eqs.(A.8) to (A.10) into Eq.(A.13) and doing some *complex algebra*, Eq.(A.13) is written as

$$\bar{\sigma}^2 = \frac{1}{2} \Re \left\{ (D - 3)AA + (D + 3)A\bar{A} + DB\bar{B} + DBB + FAB + F\bar{A}\bar{B} \right\}. \quad (\text{A.16})$$

Further simplification is obtained by using Eqs.(A.11) and (A.12), so that Eq.(A.16) becomes

$$\begin{aligned} \bar{\sigma}^2 = & \Re \left\{ 3(\bar{z} - z)(z - \bar{z})\phi''\bar{\phi}'' - 6(\bar{z} - z)\phi''\bar{\phi}' + 6(\bar{z} - z)\phi''\bar{\Omega}' \right. \\ & \left. + (8D - 6)\phi'\phi' + (8D - 3)\phi'\bar{\phi}' + 3\Omega'\bar{\Omega}' - 6\Omega'\bar{\phi}' \right\}. \end{aligned} \quad (\text{A.17})$$

The asymptotic potential functions for the upper domain, Eqs.(4) and (5), are obtained by considering the dominant term in Eqs.(A.1) and (A.3) as $r \rightarrow 0$. At this point attention shall be focused upon the solution in the upper domain since the lower domain solution is obtainable by substituting $-\epsilon$ for ϵ . Differentiating Eq.(4), using $z = re^{i\theta}$, expanding out Eqs.(4) and (5), and defining

$$J = a_0 r^{-i\epsilon}, \quad (\text{A.18})$$

we obtain

$$\phi_1' = J e^{\epsilon(\theta-\pi)} e^{-i\frac{\theta}{2}} r^{-\frac{1}{2}}, \quad (\text{A.19})$$

$$\phi_1'' = J e^{\epsilon(\theta-\pi)} e^{-i\frac{3\theta}{2}} r^{-\frac{3}{2}} \left(-\frac{1}{2} - i\epsilon\right), \quad (\text{A.20})$$

and

$$\Omega_1' = \bar{J} e^{\epsilon(\pi-\theta)} e^{-i\frac{\theta}{2}} r^{-\frac{1}{2}}. \quad (\text{A.21})$$

Substituting Eqs.(A.19) to (A.21) into Eq.(A.17) yields

$$\begin{aligned} \bar{\sigma}^2 = \frac{1}{r} \Re \left\{ J J \left[(-3 - i6\epsilon)(e^{-i2\theta} - 1) - 6 + e^{2\epsilon(\theta-\pi)}(8D - 6)(\cos \theta - i \sin \theta) \right] \right. \\ \left. + J \bar{J} \left[e^{2\epsilon(\theta-\pi)}(1 - \cos 2\theta) \left(\frac{3}{2} + 6\epsilon^2 \right) - e^{2\epsilon(\theta-\pi)}(-3 - i6\epsilon)(e^{-i2\theta} - 1) \right. \right. \\ \left. \left. + e^{2\epsilon(\theta-\pi)}(8D - 3) + 3e^{2\epsilon(\pi-\theta)} \right] \right\}. \end{aligned} \quad (\text{A.22})$$

The constant a_0 is related to the complex stress intensity factor \mathbf{K} (Rice, 1988) via

$$a_0 = \frac{\bar{\mathbf{K}}}{2\sqrt{2\pi} \cosh(\pi\epsilon)}. \quad (\text{A.23})$$

Defining ζ as

$$\zeta = \angle \mathbf{K} + \epsilon \ln r, \quad (\text{A.24})$$

and using Eq.(A.18), we find

$$J J = \frac{\mathbf{K} \bar{\mathbf{K}}}{8\pi \cosh^2(\pi\epsilon)} (\cos 2\zeta - \sin 2\zeta), \quad (\text{A.25})$$

and

$$J \bar{J} = \frac{\mathbf{K} \bar{\mathbf{K}}}{8\pi \cosh^2(\pi\epsilon)}. \quad (\text{A.26})$$

The complete expression for the Mises equivalent stress is obtained by substituting Eqs.(A.25) and (A.26) into Eq.(A.22) and is

$$\begin{aligned} \bar{\sigma}^2 = \frac{\mathbf{K} \bar{\mathbf{K}}}{r 8\pi \cosh^2(\pi\epsilon)} \left\{ \cos 2\zeta \left[-3(1 + \cos 2\theta) - 6\epsilon \sin 2\theta + (8D - 6)e^{2\epsilon(\theta-\pi)} \cos \theta \right] \right. \\ \left. + \sin 2\zeta \left[3 \sin 2\theta - 6\epsilon(\cos 2\theta - 1) - (8D - 6)e^{2\epsilon(\theta-\pi)} \sin \theta \right] \right. \\ \left. + e^{2\epsilon(\theta-\pi)} \left[\left(\frac{3}{2} - 6\epsilon^2 \right) (\cos 2\theta - 1) + 6\epsilon \sin 2\theta + (8D - 3) \right] \right. \\ \left. + 3e^{2\epsilon(\pi-\theta)} \right\}. \end{aligned} \quad (\text{A.27})$$

Appendix B Interfacial Crack Example

A detailed hypothetical example demonstrating the procedures to characterize a plane strain interfacial Griffith-type crack between 1100-O Aluminum and 1080 Steel is presented. The geometry considered is shown in *Figure 11*, and the material properties are listed in *Table 1*. From Eq.(1), $\epsilon = .03373$. For this geometry, with the appropriate σ_{zz} , imposed such that the interface remains straight, the stress intensity factor for the right hand crack tip in terms of the far field stresses is (Rice, 1988)

$$\mathbf{K} = (\sigma_{yy} + i\sigma_{zy}) (1 + i2\epsilon) (2a)^{-i\epsilon} \sqrt{\pi a}.$$

The stress intensity factor for the left hand crack tip is the same as for the right hand crack tip because the applied load is symmetric. Substituting in for the numerical values $\sigma_{yy} = 1$ MPa, $\epsilon = 0.03373$, and $2a = 0.0508$ m yields,

$$\mathbf{K} = .2831e^{-0.03315i} \text{MPa(m)}^{\frac{1}{2}-0.03373i}.$$

Using Eq.(19), the ILPA is $\zeta_0 = -.33982$ radians (-19.47°). The characteristic plastic zone length $\mathbf{K}\bar{\mathbf{K}}/\sigma_{ys}^2 \pi \cosh^2(\pi\epsilon) = 1.577 \times 10^{-6}$ m. Evaluating Eq.(37) indicates that the characteristic plastic zone length is sufficiently small compared to crack length. (Alternatively, from Eqs.(6), (19), and (20) the maximum size of the plastic zone is 8.88×10^{-6} m and occurs at $\theta = 122^\circ$. Comparing r_p to the crack length gives, $r_p/2a = 1.748 \times 10^{-4}$.) From Eq.(38), $\zeta_{max} = -.2113$ radians (-12.11°). Checking Eq.(36) indicates that no crack face interpenetration is anticipated. Thus, at this loading all the SSY conditions and the assumption of no crack face interpenetration are satisfied.

Material	μ (GPa)	ν	σ_{ys} (MPa)
1100-O Al	26.1	.342	42.†
1080 Steel	80.7	.300	585.

Table 1 Material properties for 1100-O Aluminum and 1080 Steel (Hertzberg, 1976).
†Brown *et al.*, 1987.

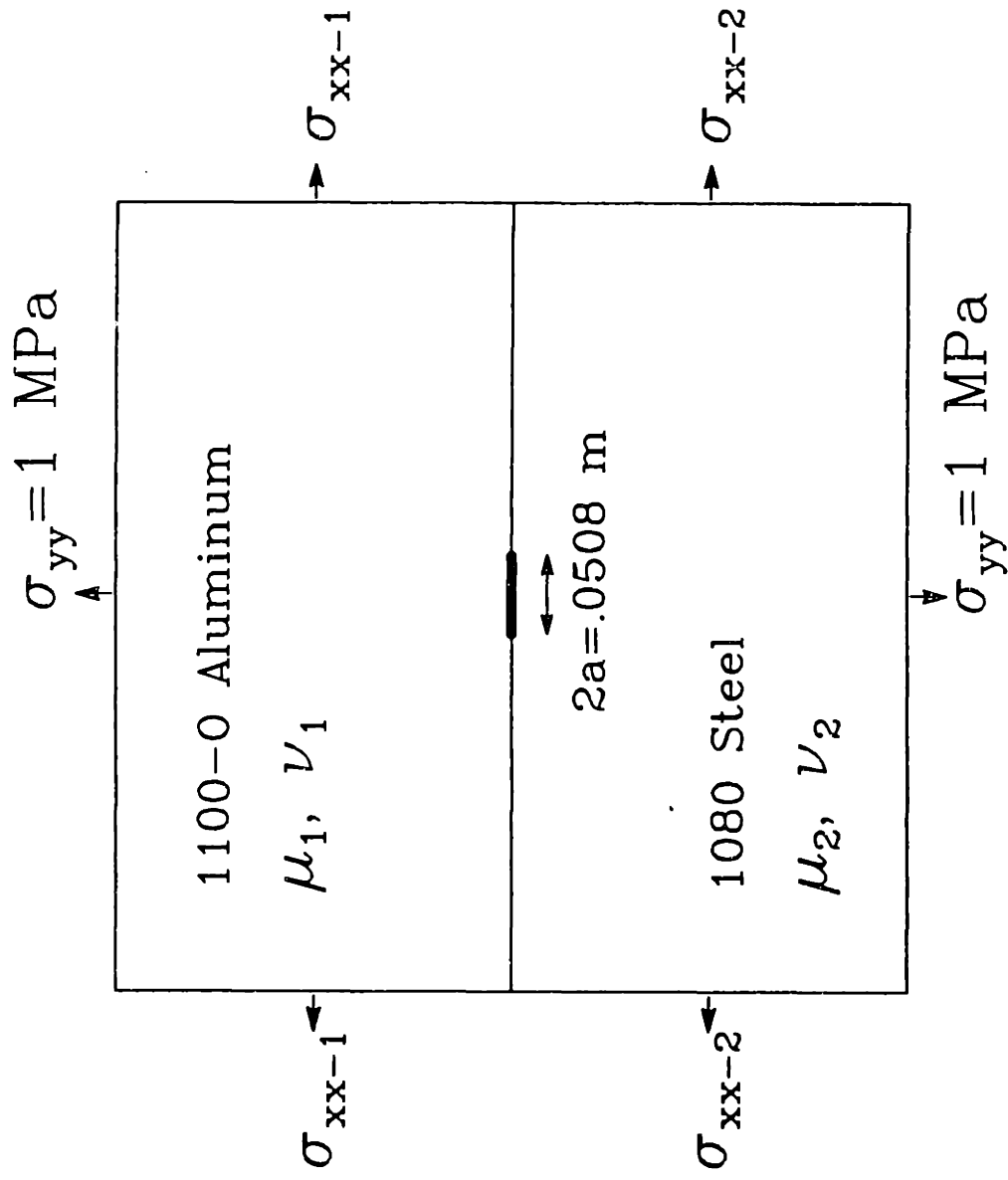


Figure 11 Geometry for a Griffith type interfacial crack.

Additional Discussion

Several additional comments can be made concerning the traction-free crack-tip plastic zone approximation. The oscillatory characteristic plastic zone dimension (r_p) is chosen to be equal to $\mathbf{K}\bar{\mathbf{K}}/\sigma_{vs}^2\pi\cosh^2(\pi\epsilon)$. This choice of r_p for the plastic zone size is a compromise because it roughly corresponds to twice the size of the smallest plastic zone (i.e., $\zeta_0 \approx 0^\circ$) and half the size of the largest plastic zone (i.e., $\zeta_0 \approx \pm 90^\circ$). This compromise in the choice of r_p affects the definition of ζ_0 , Eq.(P2.19), and the admissible loading conditions expressed in Eqs.(P2.36) and (P2.37). As pointed out earlier, the precise additive decomposition of ζ into ζ_0 and the transcendental angular function is arbitrary. Altering the chosen characteristic dimension r_p only adds a constant to ζ_0 for fixed values of ϵ . The actual choice of ζ_0 appears rather insignificant because changes in loading conditions (i.e., altering the ratio of far-field shear stress to normal stress) and zone growth show up as relative changes in ζ_0 .

Since ζ_0 is used in Eq.(P2.36) to define the extent of the plastic zone along the crack face, any overestimation of r_p may allow elastic contact to occur between the edge of the actual plastic zone and the radius identified by the (overestimated) nominal plastic zone. Based upon the elastic approximation for $\epsilon = 0.1748$, the maximum difference in ζ_0 between using the characteristic plastic zone dimension r_p and the maximum actual $r_p(\theta)$ from the elastic approximation is less than 7° . For smaller magnitudes of ϵ , the difference in ζ_0 is less. Additionally, the inclusion of a strain-hardening material idealization, $n > 1$, produces plastic zones which are greater than the elastic approximation. For example, when an elastic/perfectly-plastic constitutive idealization is used, the maximum "actual" plastic zone calculated is nearly equal to r_p for values of ζ_0 near 0° . (See *Figures P2.6* and *P2.7*.) Thus, overestimation of r_p may not pose a problem in all circumstances. Finally, when loading conditions produce an elastically predicted plastic zone size which marginally does or does not satisfy the non-contact crack-face conditions, Eq.(P2.36), a more accurate determination of plastic zone size and actual contact length is necessary.

In consideration of the actual plastic zone size predicted by the elastic approximation, the maximum plastic zone limitation expressed by Eq.(P2.37), is not as conservative as might first appear. The maximum size of the plastic zone for $\zeta_0 = 0^\circ$ and $\zeta_0 = 60^\circ$, from *Figure P2.9*, is approximately $0.5r_p$ and $2r_p$, respectively. Because little difference exists between the actual maximum plastic zone size and r_p , use of r_p is acceptable in the condition requiring the plastic zone size be small compared to the size of the zone where the asymptotic elastic field is valid, Eq.(P2.37).

2.2.2 Closed Frictionless Crack-Tip Fields

Following the derivation of the approximate plastic zone for the asymptotic traction-free crack-tip (Williams type) elastic field, an asymptotic elastic approximation for the plastic zone around a closed frictionless crack tip between two dissimilar isotropic elastic media will be derived. From it, growth characteristics and validity conditions will be obtained and expressed in terms of K_{II}^c , material properties, and geometry.

Plastic Zone Approximation

The problem considered here is a planar interfacial crack, as shown in *Figure 2.1*, whose constituents have shear moduli μ_j ($j = 1, 2$) and Poisson's ratio ν_j . Note that in the definition of β , the subscripts 1 and 2 now refer to the lower and upper material domains, respectively. Far-field loads produce a closed crack-tip region, and the closed crack-tip field is well characterized by the dominant asymptotic stress field given by Comninou (1977a), Eqs.(2.19) to (2.21).

For isotropic linear elastic plane-strain conditions, the second invariant of the stress tensor, the Mises equivalent tensile stress, $\bar{\sigma}$, is expressed as

$$\bar{\sigma}^2 = (\sigma_{rr}^2 + \sigma_{\theta\theta}^2)D + (\sigma_{rr}\sigma_{\theta\theta})F + 3\sigma_{r\theta}^2, \quad (2.31)$$

where, as before,

$$D = \nu^2 - \nu + 1 \quad (2.32)$$

and

$$F = 2\nu^2 - 2\nu - 1. \quad (2.33)$$

Since the stress field for the upper region is obtained by substituting “ $-\beta$ ” in place of “ β ” into the expressions for the lower region, attention is focused upon the lower region only. Substituting the dominant stress expressions, Eqs.(2.19) to (2.21), into Eq.(2.31) yields

$$\bar{\sigma}^2(r, \theta) = \left\{ \frac{K_{II}^c{}^2}{r} \frac{1}{32} \right\} \times \left\{ \begin{aligned} &(1 - \beta)^2 \left[3 + (64D - 48) \sin^2 \left(\frac{\theta}{2} \right) \right] + 3(3 + \beta)^2 \\ &+ 6(1 - \beta)(3 + \beta) \cos(2\theta) \end{aligned} \right\}, \quad (2.34)$$

where β , the Dundurs constant, is given by Eq.(2.22). The approximate plastic zone shape is taken to be the locus of points satisfying $\bar{\sigma} = \sigma_{ys}$, where σ_{ys} is the tensile yield strength of the material. The polar description of the plastic zone shape is given by

$$r_p(\theta) = \left\{ \frac{K_{II}^c{}^2}{\sigma_{ys}^2} \frac{1}{32} \right\} \times \left\{ \begin{aligned} &(1 - \beta)^2 \left[3 + (64D - 48) \sin^2 \left(\frac{\theta}{2} \right) \right] + 3(3 + \beta)^2 \\ &+ 6(1 - \beta)(3 + \beta) \cos(2\theta) \end{aligned} \right\}. \quad (2.35)$$

Here θ is the angle measured from the intact interface. For plane-stress conditions, Eq.(2.35) is still valid, but Eq.(2.32) is redefined as $D = 1$ and the plane-stress value for β must be used.

In deriving the plastic zone approximation, Eq.(2.35), it is assumed that the stress state along the plastic zone boundary is completely characterized by the dominant asymptotic stress field, given by Eqs.(2.19) to (2.21), and that all other stress contributions are negligible compared to the leading asymptotic term. At the tip of a Griffith crack loaded by remote tension, large normal interfacial tractions, as high as 25 times the remote far-field tensile stress, are obtained (Comninou, 1977a; Gautesen and Dundurs, 1987), and the presence of the normal interfacial traction is thought to be attributable to the admissible constant stress field ($\lambda = 0$). Evaluating the dominant asymptotic radial stress, Eq.(2.19), at $\theta = 90^\circ$, and using the value of K_{II}^c for a Griffith crack loaded in remote tension, Eq.(2.29), the dominant asymptotic stress component behaves as

$$\sigma_{rr}(r, \theta = 90^\circ) = -\sigma_{yy}^\infty \sqrt{\frac{a}{r}}, \quad (2.36)$$

where $2a$ is the crack length. Assuming that the observed normal interfacial tractions represent the magnitude of the $\sigma_{\nu\nu}$ stress component in the constant stress field, the constant stress field contribution to the overall stress field is small for radial distances $\sqrt{a/r} \gg P$, where P is the maximum normal interfacial traction normalized by $\sigma_{\nu\nu}^\infty$. In light of these possibly high normal interfacial tractions, the validity of Eq.(2.35) in SSY may be limited to loadings where $\sqrt{a/r_p(\theta)}_{\text{maximum}} \gg P$, for $\sigma_{\nu\nu} \neq 0$. Inclusion of the $\lambda = 0$ term in the description of the crack-tip fields, as described in the homogeneous case by Larsson and Carlsson (1973) and Rice (1974), could significantly enlarge the range of load amplitudes for which SSY analyses remain accurate.

Mathematical Features

The mathematical features describing the plastic zone are relatively simple and straightforward, as compared to those describing the oscillatory traction-free crack-tip plastic zone. Plastic zone growth is self-similar with similarity length scale $K_{II}^c / \sigma_{\nu\nu}^2$, and no oscillatory effects exist within the plastic zone region. The plastic zone shape and growth characteristics for the bi-material closed crack-tip solution are nearly identical to the well known homogeneous mode II solution, and in fact, in the degenerate case, $\beta = 0$, the asymptotic homogeneous mode II solution is completely recovered. *Figure 2.2(a)* shows the approximated plastic zone shapes for various values of β , with fixed Poisson's ratio, while *(b)* shows these shapes for several values of the Poisson's ratio, for $\beta = -0.20$. The approximated plastic zone shape differs little from that obtained in the homogeneous case, even for the extreme cases of $\beta = \pm 0.5$. From *Figure 2.2*, it appears that the plastic zone shape and growth characteristics are only weakly dependent upon β and ν .

Valid Solution Domain

The plastic zone approximation is based upon the assumption that a dominant field, as defined by the asymptotic expressions Eqs.(2.19) to (2.21), exists near the closed

Approximate Plastic Zone

Closed Crack-Tip Face

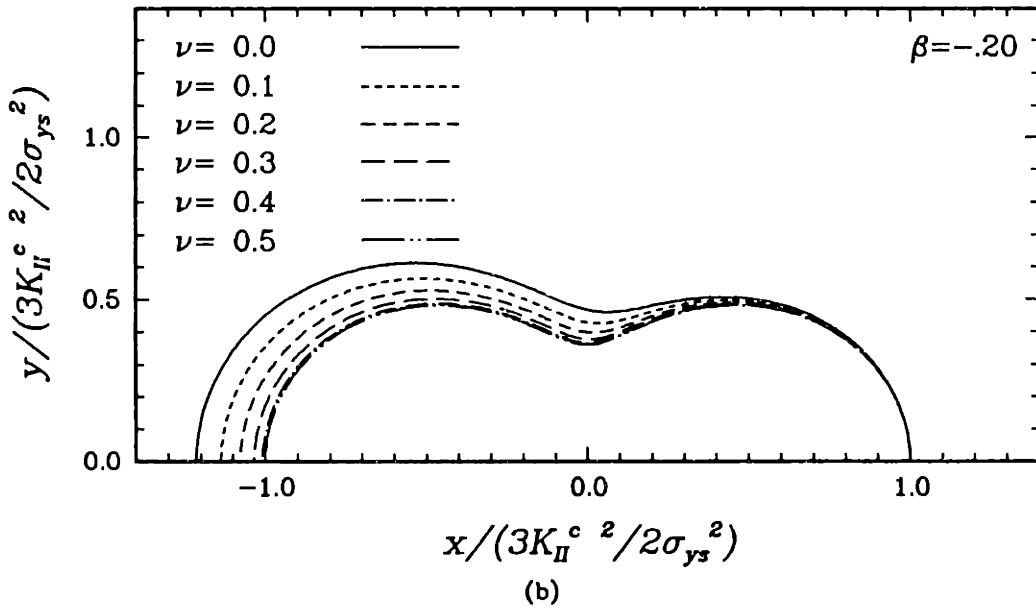
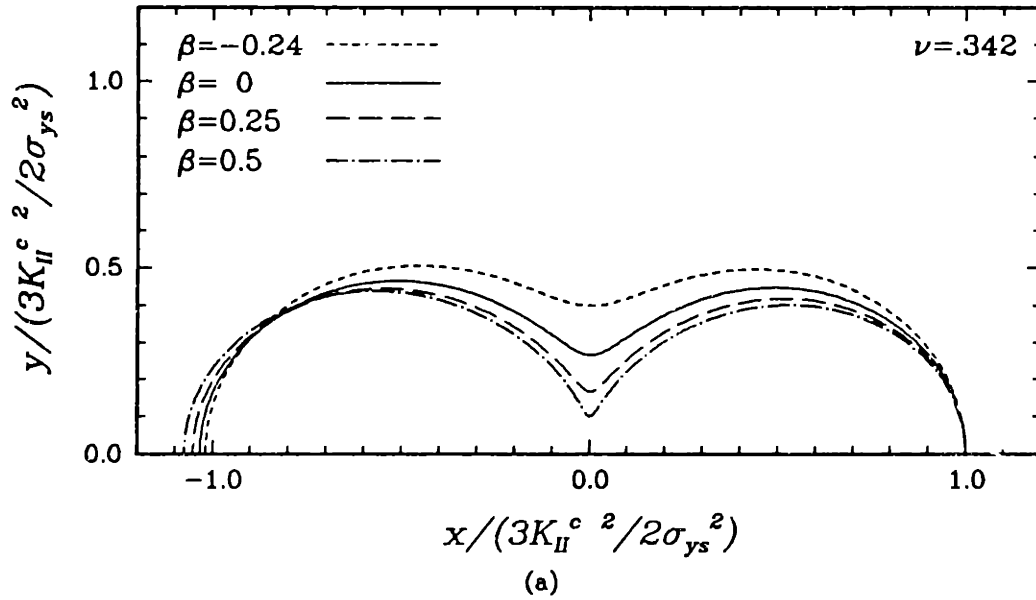


Figure 2.2 Approximate contact SSY plastic zones [Eq.(2.35)] (a) for various values of β with $\nu = 0.342$ and (b) for $\beta = -0.20$ with ν ranging between 0 and 0.5.

crack tip and transitionally along the plastic zone boundary. For this to be true, two conditions must be satisfied. First, crack-tip closure must exist and the crack-tip closure length must be the relevant characteristic dimension. Using the CTOD expression for the oscillatory stress field given in Eq.(P2.32), crack-face contact is estimated, in terms of ζ , by assuming that it occurs whenever $\Delta u_v \leq 0$ or

$$\cos \zeta + 2\epsilon \sin \zeta \leq 0. \quad (2.37)$$

The second condition which must be satisfied, if Eqs.(2.19) to (2.21) are to describe the actual field existing transitionally along the plastic zone, is that any perturbations within the field must be small and be centered about the crack tip. Again, such perturbations include non-linear crack-tip zones. Using a conservative restriction, this is mathematically expressed, via a St. Venant's type argument, as

$$r_{\text{perturbation,max}} \leq \frac{3\delta}{100}, \quad (2.38)$$

where δ is the length of the closed crack-tip face. The numerical value used in Eq.(2.38) is based upon the same assumptions as Eq.(P2.28), namely we suppose that the dominant asymptotic solution is appropriate for radial distances $r < \delta/10$ and restrict perturbations within this dominant field to at most $\sim 1/3$ of the latter dimension. The characteristic plastic zone dimension r_p^c chosen for the closed crack-tip model is $3K_{II}^c{}^2/2\sigma_{ys}^2$, which roughly corresponds to the approximated maximum radial extent of the plastic zone.

The previous conditions of closure and (plastic) perturbation zone length are now restated in terms of ζ . Closed crack-tip fields exist transitionally along the plastic zone boundary if and only if

$$\cos \zeta + 2\epsilon \sin \zeta \leq 0 \quad \begin{cases} \epsilon > 0 & \zeta_0^c \leq \zeta \leq \zeta_\delta \\ \epsilon < 0 & \zeta_\delta \leq \zeta \leq \zeta_0^c \end{cases} \quad (2.39)$$

and

$$\frac{3K_{II}^c{}^2}{2\sigma_{ys}^2} \leq \frac{3\delta}{100}, \quad (2.40)$$

where

$$\zeta_0^c = \angle \mathbf{K} + \epsilon \ln\left(\frac{3K_{II}^c}{2\sigma_{ys}^2}\right) \quad (2.41)$$

and

$$\zeta_\delta = \angle \mathbf{K} + \epsilon \ln(\delta). \quad (2.42)$$

The conditions expressed in Eq.(2.39) require that continuous crack-face contact exists from the edge of the plastic zone to the end of the contact length. Eq.(2.39) assumes that the plastic zone, along the crack face, can be approximated by the closed crack-tip plastic zone dimension r_p^c . For a more consistent and convenient relationship in small scale contact (SSC), but a somewhat more conservative restriction, ζ_0 can be used in place of ζ_0^c in Eq.(2.39). (SSC will be discussed in Section 2.3) Use of ζ_0 in SSC is more conservative because the oscillatory characteristic plastic zone dimension r_p is smaller than the closed crack-tip characteristic dimension r_p^c , thus requiring that crack-face closure exist, theoretically, deeper within the plastic zone.

Comparisons

Plastic zones for precise solutions of an elastic/perfectly-plastic material idealization and for the elastic approximation correlate reasonably. The location of yielding integration points, obtained from a finite element calculation for an elastic/perfectly-plastic medium bonded to a rigid medium, and the associated approximated plastic zone are shown in *Figure 2.9* for a closed interfacial crack tip. In the figure, the yielding points near the crack-tip are not plotted. The approximation does not reproduce the exact shape, but the general size and distributions of the various features are well represented. The scale of this figure shows that the closed crack-tip characteristic plastic zone dimension of $r_p^c = 3K_{II}^c/2\sigma_{ys}^2$ is indeed appropriate. Since perfect plasticity formally represents a strain hardening exponent of $n = \infty$, *Figure 2.9* depicts a “worst case” comparison. As observed previously in the traction-free crack-tip case, an elastic approximation increasingly overestimates the plastic zone behind the crack tip and

Bi-material Crack-Tip

Plastic Zone

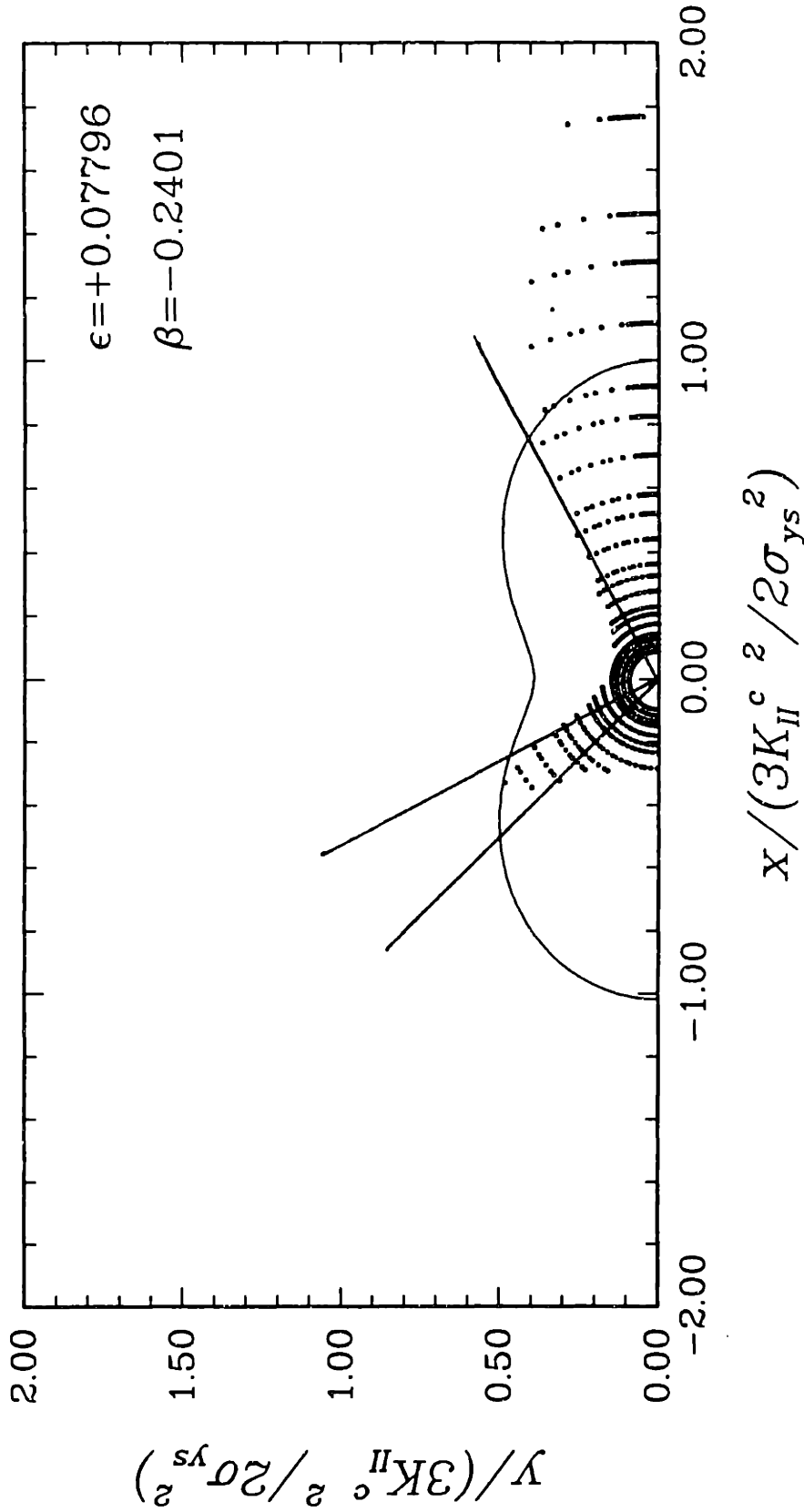


Figure 2.3 Approximate plastic zone, along with the location of actively yielding integration points, from a finite element calculation of contact SSY in an elastic/perfectly-plastic material atop a rigid substrate. Radial lines are boundaries between centered fan and constant state regions of slip-line field.

underestimates the plastic zone size ahead of the crack tip as the strain hardening exponent, n , increases [strain \propto (stress) n]. For materials with smaller values of n , the discrepancy between the elastic approximation and the exact solution should be less.

Contact Length Approximation

At this point no attention has been given to determining the exact length of the contact zone, δ . An estimation of δ can be made using the definition of ζ , Eq.(P2.31), and the critical value ζ_c , Eq.(P2.34), which represent the beginning and ending points of interpenetration. By setting $\zeta = \zeta_c$ and assuming contact occurs any time interpenetration is predicted, the contact length is estimated to be

$$\delta = \exp \left[\frac{1}{\epsilon} \left\{ \tan^{-1} \left(\frac{1}{-2\epsilon} \right) + m\pi - \angle \mathbf{K} \right\} \right], \quad (2.43)$$

where m is an integer determining the branch cut used for the \tan^{-1} function, which is obtained by considering the sign of ϵ and the length of δ . Verification of the branch cut can be made by checking if ζ_δ satisfies the contact closure conditions given in Eq.(2.37).

Conclusion

An asymptotic planar approximation for the plastic zone around an interfacial crack tip with closed frictionless crack-tip faces has been presented. This approximation captures the general plastic zone characteristics with increased accuracy as the strain-hardening exponent approaches unity. Under SSY assumptions, plastic zone growth was found to be proportional to the characteristic plastic zone dimension $3K_{II}^\epsilon / 2\sigma_y^2$, and the plastic zone shape was uniquely determined by the bi-material constant ϵ , expressed in an alternative fashion as β , and the Poisson's ratio of the yielding material. Conditions for determining the applicability of this plastic zone expression and for approximating the crack-tip closure length δ were derived from the traction-free crack-tip model.

Explicit conditions for the existence of closed crack-tip zones and their associated inelastic crack-tip behavior were assembled. However, no analytical relation between K_{II}^ϵ and the far-field loads or \mathbf{K} was made. This means that for a particular geometry,

the characteristic crack-tip field is identifiable, but the magnitude and extent of any non-linear behavior can not be quantified. Thus, the precise conditions necessary for SSY for a particular geometry were not determined. (Section 2.3 formulates explicit relationships between K_{II}^c and \mathbf{K} for a limited subset of loading conditions for which SSC exists.)

Based upon this derivation, it appears that the governing local interfacial fracture mechanics variables needed to investigate SSY behavior for closed crack-tip faces are ϵ (or β), the ILPA (ζ_0), the magnitude of K_{II}^c , and possibly ν . Because the magnitude of K_{II}^c enters only in determining the plastic zone size and appears as $K_{II}^c{}^2$, it can be replaced by J , where J is the value of the J -Integral. Using the same parametric framework assembled here to approximate the plastic zone and the conditions along the plastic zone boundary, the SSY behavior deep within the plastic zone should be addressable.

2.3 Small Scale Contact

Thus far the traction-free crack-tip model and the closed crack-tip model have been analyzed separately. There exist circumstances for which the elastic (and plastic) closed crack-tip model exists embedded within the traction-free crack-tip model. Under the appropriate loading conditions, the crack-face contact is appropriately small such that the traction-free crack-tip model describes the fields within a small proximity near the crack tip. The actual asymptotic crack-tip fields are defined by the closed crack-tip face model. Separating the two crack-tip models is a boundary layer which transmits the surrounding traction-free crack-tip stress field as “pseudo far-field” loads to the local closed crack-tip model. This section formally addresses small scale contact (SSC) and the correspondence of the various individual model parameters for such a circumstance.

2.3.1 Loading Restrictions for SSC

The requirements for SSC are that the elastic oscillatory traction-free crack-tip field exists in a region surrounding the crack tip and that the resulting contact is small compared to the distance over which that the oscillatory elastic field dominates. It was established in Section P2.3.4 Eqs.(P2.26), that the asymptotic oscillatory elastic field represents the actual crack-tip behavior for radial distances r from the crack tip [Eq.(P2.27)] such that

$$r_{\text{perturbation}_{\text{max}}} \ll r \leq l/10, \quad (2.44)$$

where l is the characteristic geometric length dimension in the problem. Eq.(2.44) is applicable if all perturbations within the crack-tip vicinity are small. Expressing this perturbation limit in terms of the contact length size δ , yields

$$\delta \leq \frac{3l}{100}. \quad (2.45)$$

The previous SSC conditions, Eqs.(2.44) and (2.45), are now restated in terms of ζ , \mathbf{K} , and the material properties. First, no (additional) contact may exist from the end of the contact zone, $r = \delta$, to the outer edge of the oscillatory field, $r = l/10$. Using the definition for the value of ζ at the outer edge of the elastic field, ζ_{max} [Eq.(P2.38)], and the definition of ζ at the end of the contact length, ζ_δ [Eq.(2.42)], SSC exists if and only if

$$\cos \zeta + 2\epsilon \sin \zeta > 0 \begin{cases} \epsilon > 0 & \zeta_{\text{max}} \leq \zeta \leq \zeta_\delta \\ \epsilon < 0 & \zeta_\delta \leq \zeta \leq \zeta_{\text{max}}, \end{cases} \quad (2.46)$$

and Eq.(2.45) is satisfied. Although multiple crack-tip contact zones do not actually occur [Shield (1982) showed that Comninou's solution for the contact length was unique.], the approximate asymptotic expression for $\Delta \mathbf{u}$, Eq.(P2.32), predicts multiple contact zones as $r \rightarrow 0$, and thus Eq.(2.46) is a necessary mathematical condition when Eq.(P2.32) is used as a closure criterion.

Within the framework of SSC, the admissibility of SSY is not excluded. The SSY requirements established for the general closed crack-tip model must be met in addition

to the SSC requirements. [i.e., The characteristic plastic zone size r_p^c must be small compared to the contact length δ , Eq.(2.40).] For SSY to exist during SSC, Eqs.(2.40), (2.45), and (2.46) must all be satisfied. Using the relationship between K_{II}^c and \mathbf{K} derived in the next section, the characteristic plastic zone sizes in SSC are related to one another by $r_p^c/r_p = (3/2) \cosh^2(\pi\epsilon)$. Also, for SSY in SSC, the maximum difference between ζ_0 , Eq.(2P.19), and ζ_0^c , Eq.(2.41), is less than 7° .

2.3.2 Correspondence of K_{II}^c to \mathbf{K}

Unfortunately, since the singular integral formulation presented by Comninou cannot be totally evaluated in closed form, no connection between the elastic \mathbf{K} and K_{II}^c has been made, under any conditions. However, for a Griffith crack under far-field tensile stress, K_{II}^c can be directly related to \mathbf{K} by using the exact solution of Gdoutos and Dundurs (1987), Eq.(2.29), and the expression for \mathbf{K} from *Table 2.1*. Solving for $\sigma_{\nu\nu}^\infty$ from the stress intensity factor \mathbf{K} and substituting it into Eq.(2.29) results in

$$K_{II}^c \cong \frac{\mathbf{K} \sqrt{1 + \left(\frac{\beta_0}{\pi}\right)^2} (2a)^{i\epsilon}}{\sqrt{\pi} (1 + i2\epsilon)} \cong \sigma_{\nu\nu}^\infty \sqrt{a} \sqrt{1 + 4\epsilon^2}, \quad (2.47)$$

for $0 \leq \beta \leq 0.5$. [The predicted contact length δ for this geometry is $\delta/2a \leq 1.2 \times 10^{-4}$ (England, 1965; Comninou, 1977a), thus SSC conditions exist for this geometry.]

Connections between the elastic \mathbf{K} and K_{II}^c can be made for other SSC cases by taking advantage of the path independent nature of the J -Integral (Rice, 1967). For the Griffith crack geometry it has been shown that, with sufficient loading to produce a small contact zone compared with crack length, the oscillatory stress field is recovered sufficiently far away from the contact zone (Comninou, 1977a; Atkinson, 1982); i.e., SSC conditions exist. Since both crack-tip models have path-independent J -Integrals and both fields dominate over some distance, a direct evaluation of K_{II}^c is obtainable from \mathbf{K} by evaluating the J -Integral in regions where each model is dominant, and equating them. Recall that for elastic materials the J -Integral is equal to the energy release rate \mathcal{G} . After some manipulation of material constants, the energy release rate given by Comninou (1977a) for the closed crack-tip face model, is

$$\mathcal{G} = \frac{K_{II}^c{}^2 \pi (C_1 + C_2)}{16 \cosh^2(\pi \epsilon)}. \quad (2.48)$$

Recalling the energy release rate given by Rice (1988) for the traction-free crack-tip model, Eq.(2.16), and assuming that such a crack-tip configuration as just described exists, we find that for SSC

$$K_{II}^c = \pm \sqrt{\frac{1}{\pi} \mathbf{K} \bar{\mathbf{K}}}, \quad (2.49)$$

where the sign of K_{II}^c must be determined by other conditions. [See discussion following Eq.(2.22).]

To verify Eq.(2.49), the Griffith crack described above was considered. The stress intensity factor K_{II}^c was evaluated by Eq.(2.29) and then used to calculate the energy release rate via Eq.(2.48). Simultaneously, \mathbf{K} was evaluated using its value for a Griffith crack from *Table 2.1*, and then the energy release rate was calculated with Eq.(2.16). The two energy release rates were identical, proving that Eq.(2.49) was indeed correct for a Griffith crack in SSC.

Using this approach, a generalization of Eq.(2.47) to include far-field shear loading of a Griffith crack in SSC is made. First, all assumptions regarding SSC must be met. Using Eq.(2.49) and the value of \mathbf{K} for a Griffith crack from *Table 2.1*, the closed crack-tip stress intensity factor for the right hand crack tip of a Griffith crack in SSC is

$$K_{II}^c \cong \pm \sqrt{(\sigma_{yy}^\infty{}^2 + \sigma_{xy}^\infty{}^2) \times (1 + 4\epsilon^2)} a. \quad (2.50)$$

The sign of K_{II}^c is determined using the conditions for compressive normal crack-face tractions on the right hand crack tip of a Griffith crack, namely $K_{II}^c < 0$ for $\epsilon > 0$ and $K_{II}^c > 0$ for $\epsilon < 0$. Observe that for $\sigma_{xy}^\infty = 0$, Eq.(2.50) reduces to Eq.(2.29). Verification that the contact zone length is small compared to crack length is done by using the approximation for δ , Eq.(2.43), and the contact conditions given by Eq.(2.39).

Unfortunately, due to the non-uniqueness in defining $\angle \mathbf{K}$, obtaining \mathbf{K} from from K_{II}^c is not as simple. If K_{II}^c and δ are known and $\delta/2a$ is “small,” \mathbf{K} can be estimated

by determining $\|\mathbf{K}\|$ from Eq.(2.49) and by determining $\angle\mathbf{K}$ by inverting Eq.(2.43). For certain geometries, \mathbf{K} can be estimated at one crack-tip, and then inferred values of \mathbf{K} for the other crack-tip can be obtained by consideration of the stress intensity factor for that geometry. However, further work on closed form definitions of (K_{II}^c, δ) will allow for more complete relationships between K_{II}^c and \mathbf{K} .

Finally, due to the unfortunate numbering of material domains describing β in the closed crack-tip face model and ϵ in the traction-free crack-tip model, various minus signs may enter into the analytical solution when converting from one model to the other. Extreme caution must be used to prevent accidental sign errors, as the author discovered.

2.3.3 Accuracy of Contact Length Estimation

This section considers the accuracy of the asymptotic prediction for crack-face contact, as expressed by Eqs.(P2.33), (2.37), and (2.43). Using the stress intensity factor \mathbf{K} for a Griffith crack (geometry and loading) from *Table 2.1*, Eq.(P2.33), and the condition represented by Eq.(P2.35), the crack-face contact length for the right hand crack tip, normalized by crack length, is given by

$$\frac{\delta}{2a} = \exp \left\{ \frac{m\pi + \psi}{\epsilon} \right\}, \quad (2.51)$$

where

$$\tan \psi = \frac{\sigma_{yy}^{\infty}}{\sigma_{xy}^{\infty}} \quad \left(-\frac{3\pi}{2} < \psi < \frac{\pi}{2} \right) \quad (2.52)$$

and m is an integer. The actual branch cut, which determines the value of m , is obtained by considering the sign and magnitude of ψ and ϵ , and the range of $\delta/2a$ of the crack tip being investigated. (The restriction on admissible values of ψ is chosen so that approximately $|\angle\mathbf{K}| < \pi$.) *Figure 2.4* shows the crack-tip contact length for $\epsilon = -0.1748$ ($\beta = 0.5$), as a function of ρ [$\rho = (2/\pi) \tan^{-1}(\sigma_{xy}^{\infty}/\sigma_{yy}^{\infty})$] for the asymptotic traction-free crack-tip approximation (with branch cut $m = 0$) and for Comninou's solution (Comninou and Schmueser, 1979). Agreement between the two solutions is

Crack-Face Contact

Right Crack Tip

$$\epsilon = -0.1748 \quad (\beta = 0.5)$$

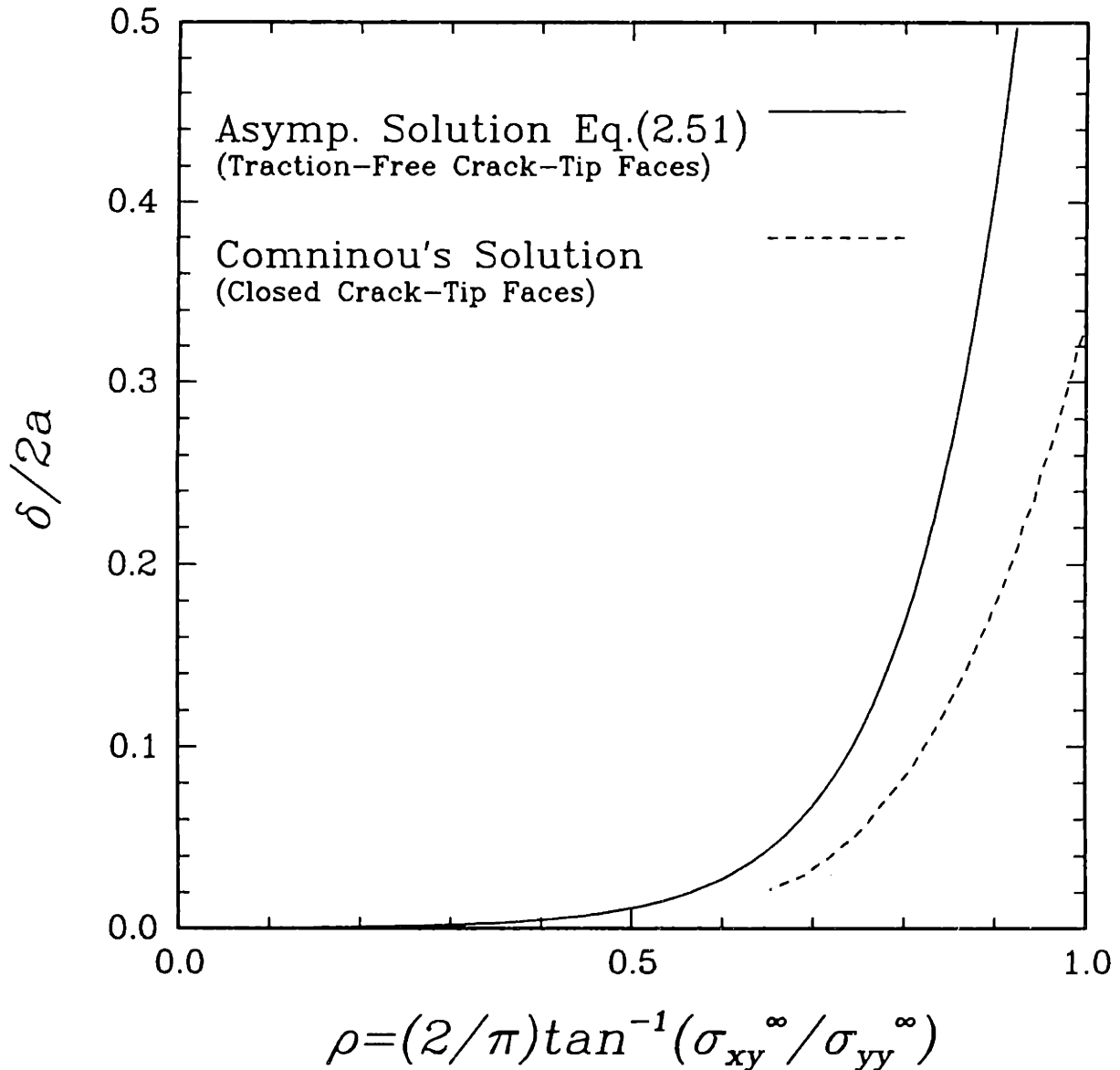


Figure 2.4 Normalized crack-face contact length $\delta/2a$ for the right hand crack-tip of a Griffith crack geometry with far-field positive shear (σ_{xy}^{∞}) and tensile normal (σ_{yy}^{∞}) loads. The solid line is the back extrapolated contact length from the traction-free crack-tip model [Eq.(2.37)] and the dashed line is the solution for frictionless closed crack-tip model from Comninou and Schmueser (1979).

clearly sufficient to justify using the approximation for $\rho < 0.85$. Since the asymptotic expression Eqs.(2.43) and (2.51) overestimate the contact length, the validity condition represented in Eq.(P2.33) is also conservative with respect to crack-face contact.

Based upon the previous comparison, the contact length approximations, Eqs.(2.43) and (2.51), yield reasonable results for $\epsilon = -0.1748$ when ψ or Φ ($\Phi = \{\tan^{-1}(1/ - 2\epsilon) + m\pi - \angle K - \epsilon \ln(l)\}$) are greater than 0.24 (13.5°). For this range, the previous comparison shows that the predicted contact length only overestimates the “actual” contact length by less than a factor of two. For values of Φ and ψ less than 0.24, closure length predictions for $\epsilon = -0.1748$ are no longer reasonable. However, for Φ and ψ less than 0.24 and $\epsilon = -0.1748$, a minimum contact length of $\delta/2a = 0.13$ exists. For $\epsilon = +0.1748$ with branch cut $m = -1$, Φ and ψ must be greater than -0.24 (-13.5°) in order for Eqs.(2.43) and (2.51) to yield reasonable overestimated contact lengths (within a factor of two). As the magnitude of the bi-material constant ϵ approaches zero, the minimum (or maximum) angles of Φ and ψ , for which reasonable overestimated contact lengths are obtained, also approaches zero. If loading conditions produce a plastic zone size which marginally violates or satisfies the restriction given by Eq.(P2.36) or Eq.(2.39), or the contact conditions in Eqs.(2.45) and (2.46), more precise solutions for δ should be consulted, *e.g.*, Comninou (1977a, 1978) and Comninou and Schmueser (1979).

2.3.4 SSC Summary

Explicit conditions which produce SSC were formally identified in terms of ζ , K , and material properties. Under SSC conditions, an explicit relationship between the closed crack-tip face stress intensity factor, K_{II}^c , and the traction-free crack-tip stress intensity factor, K , was derived for a specific geometry. Based upon equal energy release rates, a more general extension of this relationship was given. Finally, the accuracy of the predicted contact length, in terms of the oscillatory traction-free crack-tip field, was compared against that of precise full-field closed crack-tip solutions. This comparison

identified the loading range for which the contact length approximation, Eq.(2.43), was sufficiently accurate to provide useful results and define SSC.

2.4 Overview

2.4.1 Load Map

To help visualize when crack-tip conditions exist for each model, with or without plasticity, consider the load map shown in *Figure 2.5* (conceived by Prof. D. M. Parks). This map denotes the various model domains for the right hand crack tip of a Griffith crack geometry, as a function of the far-field loading combinations. The appropriate crack-tip model for monotonically and proportionally increasing far-field loads is obtained by constructing a ray from the origin the desired load point. For all load excursions which terminate in the SSY traction-free crack-tip domain, an undefined intermediate state exists when the plastic zone r_p is less than, but nearly the same size (order of magnitude) as, the contact length dimension δ . The crack-tip behavior in this intermediate state is not defined by either model. Although not clearly visible in *Figure 2.5*, all traction-free crack-tip loadings produce SSC unless plasticity is included.

In the load map, the loadings which produce acceptable SSY conditions are those contained within the $r_p/2a = 0.03$ circle. The line separating the SSY traction-free crack-tip region from the intermediate undefined region, $r_p = 3\delta$, is the locus of points producing plastic zones three times larger than the accompanying elastically predicted contact length. The corresponding boundary of the closed crack-tip SSY region is defined by the $r_p^c/2a = 0.03$ circle, where r_p^c is approximated by r_p , and the $r_p = 0.3\delta$ line. (The closed crack-tip boundary is defined by $r_p = 0.3\delta$ instead of $r_p = 0.03\delta$, as suggested by Eq.(2.40), because K_{II}^c is not explicitly known nor is the extent that the K_{II}^c -field represents the far field solution known.) Between the $r_p = 3\delta$ and $r_p = 0.3\delta$ lines is an “uncertain” region where it is unclear whether sufficient plastic deformation would occur under the dominance of either elastic crack-tip model.

The precise location and distribution of each sector in the load map is significantly

Load Map

$\epsilon = -0.1748$ ($\beta = 0.5$)

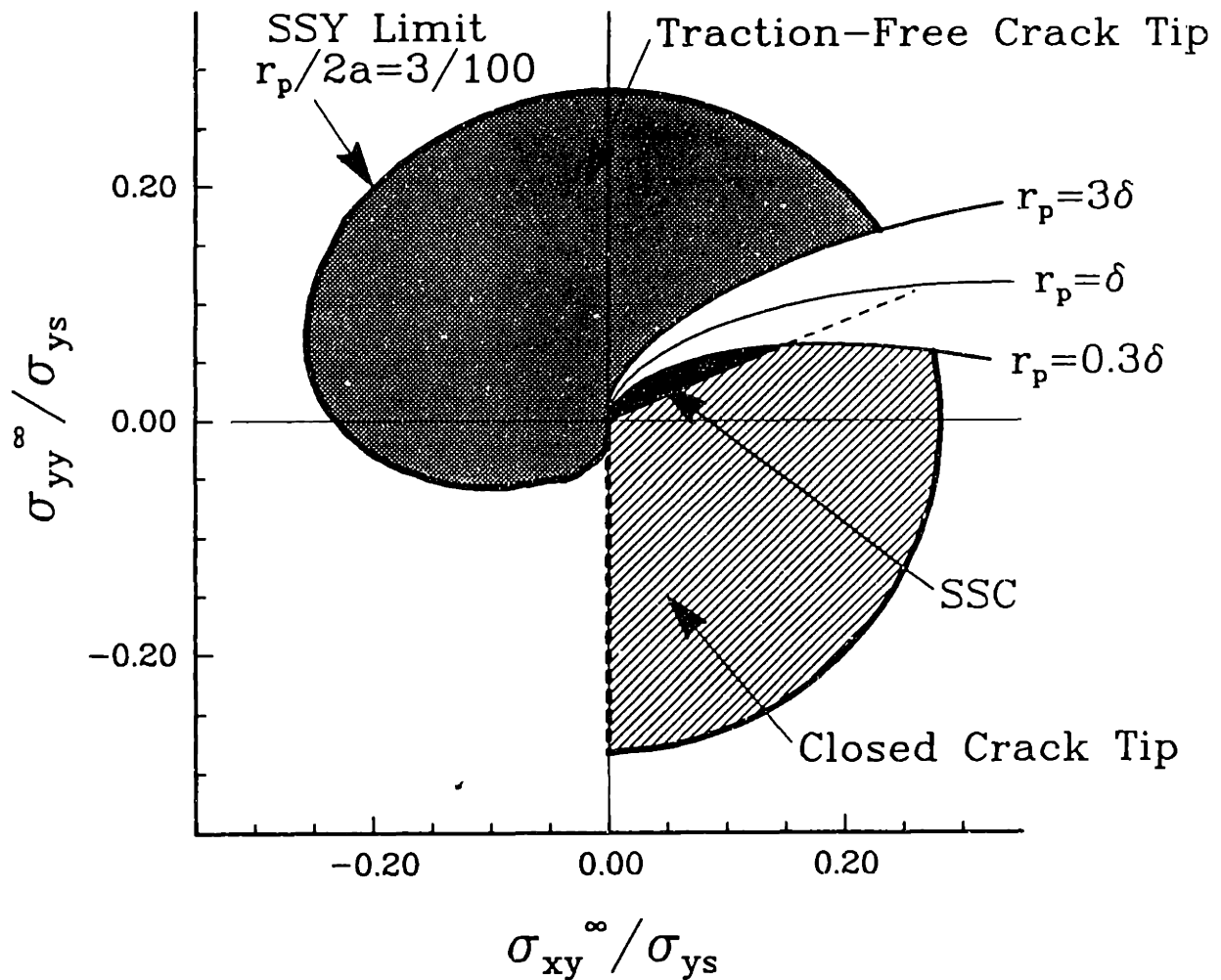


Figure 2.5 Load map for right crack-tip of a Griffith crack geometry with far-field normal (σ_{yy}^{∞}) and shear (σ_{xy}^{∞}) loads, showing approximate SSY limits for traction-free and closed frictionless crack-face conditions; $\beta = 0.5$ and $\epsilon = -0.1748$.

influenced by the value of ϵ . For smaller magnitudes of ϵ , the family of boundary-contact lines compress toward the abscissa, eventually coinciding there for $\epsilon = 0$. For positive values of ϵ , the family of boundary-contact lines appear as mirrored reflections across the ordinate axis. For all values of ϵ , the SSC region is a very small subset of the closed crack-tip domain with the SSC SSY domain being even smaller.

The load map is constructed in the following manner. The characteristic plastic zone size r_p is obtained, as a function of far-field load, by substituting the stress intensity factor for the Griffith crack, from *Table 2.1*, into the characteristic plastic zone size $r_p = K\bar{K}/\sigma_{ys}^2 \pi \cosh^2(\pi\epsilon)$. This yields

$$\frac{r_p}{2a} = \left(\left(\frac{\sigma_{yy}^\infty}{\sigma_{ys}} \right)^2 + \left(\frac{\sigma_{xy}^\infty}{\sigma_{ys}} \right)^2 \right) \frac{1 + 4\epsilon^2}{2 \cosh^2(\pi\epsilon)}. \quad (2.53)$$

To maintain SSY conditions Eq.(P2.37) requires $r_p \leq 0.032a$. The set of points which satisfy Eq.(2.53) when $r_p/2a = 0.03$ defines the SSY limit, to within the approximation that r_p can be used to define the maximum extent of the plastic zone. The boundary lines are obtained by determining the appropriate loads which produce a characteristic plastic zone size f times the contact length ($r_p/2a = f \times \delta/2a$), for a fixed ratio of $\sigma_{yy}^\infty/\sigma_{xy}^\infty$. Using the contact length approximation for a Griffith crack, Eq.(2.51), and Eq.(2.52), the equation describing the boundary lines is given by

$$\frac{2f \cosh^2(\pi\epsilon)}{1 + 4\epsilon^2} \exp \left\{ \frac{m\pi + \psi}{\epsilon} \right\} = \left(\frac{\sigma_{yy}^\infty}{\sigma_{ys}} \right)^2 + \left(\frac{\sigma_{xy}^\infty}{\sigma_{ys}} \right)^2. \quad (2.54)$$

In *Figure 2.5* the branch cut is chosen to be zero since $\epsilon < 0$.

It was noted by Rice (1988) that for a Griffith crack, the behavior at the left hand crack tip with negative applied shear stress is identical to that at the right hand crack tip when an equivalent positive shear stress and normal stress is applied. By considering the work of Comninou and Schmueser (1979) and the observation made by Rice, it is concluded that for $\epsilon < 0$ the contact length at the right hand crack tip, δ_r , decreases as negative shear stress is applied, but the left hand crack-tip contact length, δ_l , increases. This increase in δ_l reduces the actual open crack length to an effective crack size of $2a_{eff} = 2a - \delta_l$. The (modified) SSY boundary for $\sigma_{xy} < 0$ shown in *Figure 2.5*, is

constructed by determining the locus of points which satisfy $r_p/2a_{eff} = 0.03$. [When $\sigma_{xy}^\infty < 0$, the value of δ used is based upon the more precise values of Comninou and Schmueser (1979).] Additionally, when $\sigma_{xy} = 0$ and $\sigma_{yy} < 0$, the crack is completely closed and no singularities exist at either crack tip.

Finally, in constructing the load map, 10° was added to the actual value of ψ used in Eq.(2.54) to calculate $\delta/2a$. For small angles of ψ , the additional 10° produced contact lengths which were closer to those determined by Comninou and Schmueser (1979) and allowed for a better representation of the closed crack-tip and SSC boundaries. For large angles of ψ , no noticeable effects were produced in the load map because of the actual size of $\delta/2a$.

2.4.2 Conclusion

From examination of the elasticity solutions for the two crack-tip models considered and the load map, it is evident that a single crack-tip model is not completely capable of capturing the linear elastic portion of crack-tip behavior under arbitrary loading conditions. Rather, one must first identify the relevant characteristic dimensions in the problem; *i.e.* crack length, contact length and plastic zone size, and then choose a model which gives the correct physical interpretation on these size scales. As pointed out earlier, both models produce physically unrealistic predictions when extrapolated outside their applicable (linear elastic) domain. For example, under the appropriate far-field loads, the traction-free crack-tip solution produces crack-face interpenetration. Additionally, singularities exist at the crack tip in both models, clearly invalidating their linear elastic material assumptions in the very near crack-tip region; *i.e.*, isotropic linear elastic material response, small strains, and small rotations. Obviously additional crack-tip models are necessary to bridge the gap between these two elasticity models, such as closed crack-tip models with crack-face friction, as well as other models which incorporate more physically realistic material idealizations.

At this juncture, plastic zone growth for two continuum crack-tip models has been

investigated by using elastic approximations for the plastic zone. Loadings have been only loosely restricted to those which produce a plastic zone that is small compared to the next relevant characteristic dimension (*e.g.*, contact length or crack length) in the problem and to those which have crack faces continuously apart or in continuous contact from the plastic zone edge to the end of the next relevant characteristic dimension. (Henceforth, the set of admissible planar interfacial cracks is limited to those which fit the two models discussed.) Plastic zone size, shape, and growth characteristics, with respect to applied increasing loads, have been identified and parametrized into convenient dimensional and dimensionless quantities. In terms of these quantities, explicit conditions which approximately determine the applicability of each model have been given. In fact, these models remain appropriate outside their identified domains providing the underlying conditions on which the governing assumptions are based (*i.e.*, contacting or traction-free crack-tip faces), are not violated. Since the validity conditions are based upon asymptotic or approximate formulae, certain geometries may warrant more precise analyses.

The elastically-calculated yield zone and associated inelastic characteristic lengths are based on a Mises yield criterion, but the mathematical approach of determining the loci of points in an elastic field which satisfies a yield criterion is not limited to the Mises criterion. Any other yield criteria, such as the single crystal Schmid criteria, the generalized (anisotropic) Hill criterion, or pressure sensitive transformation criteria, that describes the initiation of an inelastic deformation mechanism, like transformation plasticity, micro-cracking, single crystal slip, and Coulomb friction controlled sliding (in granular materials), can be used to estimate the extent of non-linear behavior contained in an elastic field and *qualitatively* correlate far-field and local-field quantities. This approximate approach may be quite useful in investigating other phenomena like bi-crystal grain boundaries, micro-delamination or damage in fiber reinforced composite laminates, and any other system where difficulties arise in precisely determining the complete exact response.

Chapter 3

Description of Solution Technique

In this chapter, the individual components which are assembled together to solve the BV problem outlined in Chapter 1 are described. The first section discusses the numerical model in terms of imposed boundary conditions, elastic and plastic domains, and the governing global variational principle, along with modeling simplification-reduction techniques. The second section presents the elastic/perfectly-plastic constitutive relationship along with discussion concerning notation, kinematics, and the constitutive integration operator used. The final section discusses the details of the actual finite element (FE) procedures and meshes used for each of the crack-tip models.

3.1 Crack-Tip Model Formulation

The asymptotic local crack-tip behavior of all numerical models are numerically investigated using, to some extent, the FE approach proposed by Hilton and Hutchinson (1971) for cracks in homogeneous media. Consider the schematic crack-tip region shown in *Figure 3.1*. Near the crack tip, as compared to the characteristic geometric dimension, unique “K”-fields emerge, that asymptotically describe the elastic stress, strain, and displacement fields (within the limits outlined in Section 2.2). The core region is defined to lie within Γ^∞ such that the value of \mathbf{K} , along with Eqs.(P2.2) to (P2.5), or the value of \mathbf{K}_{II}^c , along with Eqs.(2.19) to (2.21), completely characterizes the linearly elastic fields in the region enclosed by Γ_∞ . The core region is then extracted by cutting

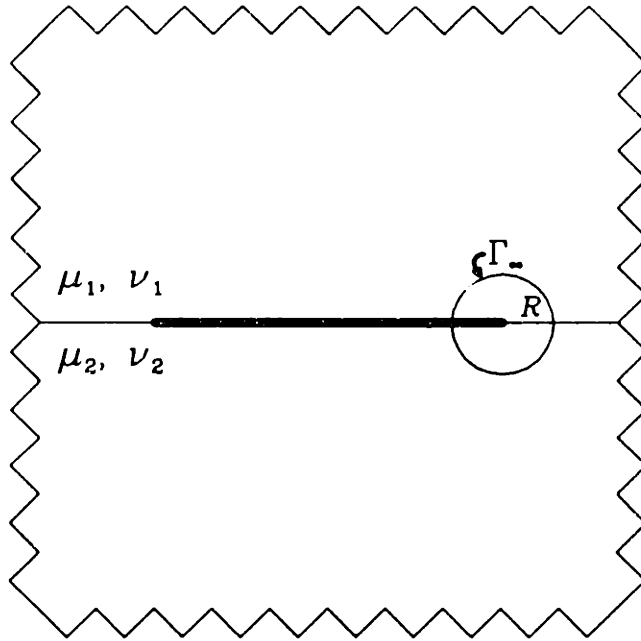


Figure 3.1 Schematic bi-material interfacial crack-tip region, showing core region and domain numbering convention.

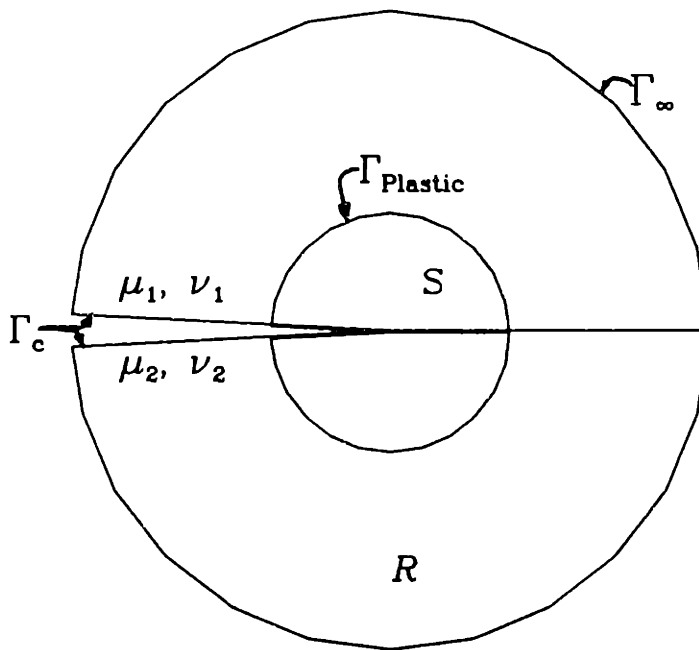


Figure 3.2 Schematic traction-free bi-material interface crack-tip core region, including the elastic (\mathcal{R}) and plastic (\mathcal{S}) domains and the crack-face (Γ_c), plastic (Γ_{plastic}), and core (Γ_∞) boundaries.

along Γ_∞ , as shown in *Figure 9.1*. By imposing tractions along Γ_∞ of the extracted core region consistent with Eqs.(P2.2) to (P2.5) or Eqs.(2.19) to (2.21) and scaled by the appropriate \mathbf{K} or K_{II}^c , the fields within the core region are totally recovered. Alternatively, displacements can be imposed on Γ_∞ to yield the same results. For the traction-free crack-tip model, the displacements are obtained using Eqs.(P2.4), (P2.5), and the following (Muskhelishvili, 1953)

$$2\mu_k (u_x + iu_y) = n_k \phi_k + (\bar{z} - z) \bar{\phi}_k' - \bar{\Omega}_k, \quad (3.1)$$

where $z = x + iy = re^{i\theta}$ is measured from the crack tip, u_x and u_y are Cartesian based displacements, and the remaining terms have the same meaning as before. For the closed crack-tip face model, the dominant asymptotic displacement field can be obtained from the power series expansion (Comninou, 1977a), and in polar coordinates is given by

$$u_r = -\frac{K_{II}^c \sqrt{2r}}{8\mu_j} \left\{ (2n_j - 1) (1 \mp \beta) \sin \frac{\theta}{2} - (3 \pm \beta) \sin \frac{3\theta}{2} \right\} \quad (3.2)$$

and

$$u_\theta = -\frac{K_{II}^c \sqrt{2r}}{8\mu_j} \left\{ (2n_j + 1) (1 \mp \beta) \cos \frac{\theta}{2} - (3 \pm \beta) \cos \frac{3\theta}{2} \right\}, \quad (3.3)$$

where the upper and lower signs are used in the lower and upper material domains, respectively.

This approach eliminates the need to model the entire structure containing the crack and allows more mesh refinement in the immediate crack-tip vicinity. Local crack-tip material non-linearities are acceptable, via a St. Venant type argument, as long as they are confined to a zone which is small ($\sim 10\%$) with respect to Γ_∞ (Larsson and Carlsson, 1973; Rice, 1974).

3.1.1 Traction-Free Crack-Tip Faces: Boundary Layer Approach

In addition to the model reduction technique proposed by Hilton and Hutchinson, a further model simplification was used for the traction-free crack-tip model. What follows is a theoretical interpretation and description of this additional method.

Theoretical Considerations

Additional model reduction and computational savings were obtained for the traction-free crack-tip model using Sham's boundary layer method (Sham, 1983). *Figure 3.2* shows a schematic crack-tip core region where Γ_∞ and $\Gamma_{Plastic}$ denote the outer edge of the model and the maximum extent of the plastic zone, respectively. The region \mathcal{R} , by definition of $\Gamma_{Plastic}$, remains elastic during the entire analysis. The boundary layer method reformulates this problem while maintaining the stress, strain, and displacement fields and taking advantage of the elastic region \mathcal{R} . For brevity, a short outline of Sham's boundary layer method follows, and the reader is referred to Sham (1983) for a more complete description.

The boundary layer method recasts the simplification proposed by Hilton and Hutchinson (1971) by altering the physical model depicted in *Figure 3.2*. Consider the boundaries Γ_∞ and $\Gamma_{Plastic}$ to be circles of radii r_∞ and $r_{Plastic}$, respectively, centered about the crack tip. For any value of r_∞ chosen such that $r_\infty \gg r_{Plastic}$, the elastic field within Γ_∞ is reproduced by enforcing Eqs.(2.4) and (2.5) via Eq.(3.1) along Γ_∞ . For convenience, the boundary Γ_∞ will be relocated to $r_\infty = \infty$. Therefore the restriction that $\Gamma_{Plastic}$ be located at a distance close to the crack tip, with respect to Γ_∞ , shall be trivially satisfied for all finite values chosen for $r_{Plastic}$.

To describe the elastic region between Γ_∞ and $\Gamma_{Plastic}$, additional series terms which account for the non-linearities altering the fields within $\Gamma_{Plastic}$ must be included in addition to Eqs.(P2.4) and (P2.5). Using the general series potential identified by Rice (1988), Eqs.(P2.A.1) to (P2.A.4), an inner or Laurent series expansion for the potentials can be constructed. This is accomplished by redefining Eqs.(P2.A.5) and (P2.A.6) to be

$$f(z) = \sum_{N=-\infty}^0 a_N z^N, \quad (3.4)$$

and

$$g(z) = \sum_{M=-\infty}^{-2} b_M z^M. \quad (3.5)$$

Note that an outer series expansion would produce unbounded stresses, strains, and displacements as $r \rightarrow \infty$, while an inner series yields terms which are bounded or tend to zero as $r \rightarrow \infty$. Also, the first term, $M = -1$, for the $g(z)$ expression is excluded since it physically represents point loads applied at the crack tip. For convenience, Eq.(3.4) additively decomposes into

$$f(z) = f^K(z) + f^T(z) = a_0 + f^T(z), \quad (3.6)$$

where

$$f^T(z) = \sum_{N=-\infty}^{-1} a_N z^N. \quad (3.7)$$

Since Eq.(3.5) contains no terms associated with the K-field, Eq.(3.5) should be interpreted as the definition of $g^T(z)$; i.e., $g^T(z) = g(z)$. All terms with the superscript K shall refer to quantities, which assume that only the **K**-field is present (terms of order $r^{(-1/2)\pm i\epsilon}$ in stress) and those with the superscript T shall be used to identify all the quantities associated with the remaining outer expansion of the inner series terms. Using the potentials represented by Eqs.(P2.A.1) to (P2.A.4), along with Eqs.(3.4) and (3.5), and the displacement relationship, given by Eq.(3.1) the complete field in S can be expressed in terms of the coefficients a_N and b_N .

The boundary layer method requires solving the field equations within Γ_∞ by minimizing the modified rate potential function, given by Sham (1983) as

$$\bar{\Pi} = \int_S \Phi(\dot{\underline{\epsilon}}) dS + \int_R \Phi(\dot{\underline{\epsilon}}^T) dS - \int_{\Gamma_{Plastic}} (\mathbf{n} \cdot \dot{\sigma}^K(t)) \cdot \dot{\mathbf{u}}^T ds. \quad (3.8)$$

Here Φ is the strain rate potential, $\dot{\underline{\epsilon}}$ is the strain tensor, \mathbf{n} is the unit outward normal vector, $\dot{\sigma}^K(t)$ is the stress rate tensor attributable to the **K**-field, and $\dot{\mathbf{u}}$ is the velocity vector.

The modified potential can be interpreted on a term by term basis. The integral $\int_R \Phi(\dot{\underline{\epsilon}}^T) dS$ corresponds to the elastic strain rate energy in the region between $\Gamma_{Plastic}$ and Γ_∞ attributable to the lower order terms. It can be given explicitly in the form $\frac{1}{2} \dot{\mathbf{q}}^{\epsilon T} \mathbf{S} \dot{\mathbf{q}}^{\epsilon T}$, where $\mathbf{q}^{\epsilon T}$ is the vector of generalized degrees of freedom [the unknown

coefficients a_N and b_M from Eqs.(2.2) and (2.3)], $\dot{\mathbf{q}}^{eT}$ is time derivative of \mathbf{q}^{eT} , and \mathbf{S} is an appropriate stiffness matrix. Since the region \mathcal{R} is elastic, the stiffness matrix \mathbf{S} is independent of time and is more conveniently evaluated from the associated relationship $\frac{1}{2}\mathbf{q}^{eT}\mathbf{S}\mathbf{q}^{eT} = \int_{\mathcal{R}} \Phi(\underline{\epsilon}^T) dS$ where Φ is now the strain energy density function. In Appendix A.1 the stiffness matrix \mathbf{S} is calculated using the known analytical expressions found in Eqs.(P2.A.1) to (P2.A.4), (3.4), and (3.5). (Note, in Appendix A the stress potential χ is used instead of Ω . The two stress potentials are related via $\chi'' = \Omega' - \phi' - z\phi''$.) An equivalent line integral along the boundary Γ_{∞} , $\Gamma_{Plastic}$, and the crack face (Γ_c), Eq.(A.7), is used to evaluate the surface integral. In evaluating the line integral, it can be shown [Eqs.(A.13) and (A.14)] that the only non-zero contribution arises along the $\Gamma_{Plastic}$ boundary. The next integral in Eq.(3.8), $\int_{\Gamma_{Plastic}} (\mathbf{n} \cdot \dot{\sigma}^K(t)) \cdot \dot{\mathbf{u}}^T ds$, can be explicitly expressed as $\dot{\mathbf{q}}^{eT} \dot{\mathbf{F}}^e(t)$, where $\mathbf{F}^e(t)$ is the vector of integrated work conjugate forces to the (T -terms) generalized degrees of freedom. The time derivative of the work conjugate force vector, $\dot{\mathbf{F}}^e(t)$, can be written in component form as

$$\dot{\mathbf{F}}_j^e(t) = \int_{\Gamma_{Plastic}} (\mathbf{n} \cdot \dot{\sigma}^K(t)) \cdot \dot{\mathbf{u}}_j^T ds, \quad (3.9)$$

where $\dot{\mathbf{u}}_j^T(r, \theta, \epsilon)$ is the j th component of the known velocity mode shape vector; (*i.e.*, the components of the velocity mode shape vector are related to the velocity vector via $\dot{\mathbf{u}}_j^T(r, \theta, \epsilon) = \dot{q}_j^T \hat{\mathbf{u}}_j^T(r, \theta, \epsilon)$, with no summation on j .) The term $\dot{\sigma}^K(t)$ is dependent only on time via the scaling variable $\dot{\mathbf{K}}(t)$ and is otherwise known. Since $\dot{\mathbf{K}}(t)$ is known, and is chosen to be of the form $\dot{\mathbf{K}}(t) = \mathbf{K}_0 \dot{L}(t)$, where $\dot{L}(t)$ is a real scalar function of time, $\dot{\mathbf{F}}^e(t)$ need only be evaluated as \mathbf{F}_0^e at $\mathbf{K}(t=0) = \mathbf{K}_0$ and then scaled by $\dot{L}(t)$ as $\dot{\mathbf{F}}^e(t) = \mathbf{F}_0^e \dot{L}(t)$. The remaining integral in Eq.(3.8) corresponds to the standard rate potential such that $\dot{\sigma} = \partial\Phi(\underline{\epsilon})/\partial\underline{\epsilon}$ within the region inside $\Gamma_{Plastic}$, and is evaluated using finite elements.

To maintain a well posed mathematical BV problem, the additional lower order terms in \mathcal{R} must be accompanied by additional mode shapes along the $\Gamma_{Plastic}$ boundary. In region \mathcal{R} , $2(N+M-1)$ additional unknowns, contained in the vector \mathbf{q}^{eT} , are added to give the complete representation. The addition of these terms compensates for any

deviations from \mathbf{K} -fields which may occur in R due to nonlinearities within S . At the same time, $2(N + M - 1)$ additional constraint equations are imposed along $\Gamma_{Plastic}$, thus making it a well posed mathematical problem. As the behavior in region S deviates from the asymptotic dominant field, Eqs.(2.4) and (2.5), lower order mode shapes are activated by making amplitude coefficients in \mathbf{q}^{eT} non-zero. However, this occurs at the expense of adding additional strain deformation in region \mathcal{R} such that equilibrium and compatibility between the two regions is achieved via Eq.(3.8).

By consideration of the previous observations, the modified potential energy function was incorporated into the FE code *ABAQUS* (Hibbitt, 1984). At the outer edge of the FE boundary, taken to be $(\Gamma_{Plastic})$, constraint equations, written in the form of a user-defined multiple point constraint (MPC) subroutine, were used to enforce nodally the admissible displacement eigenmodes in accordance with Eqs.(P2.A.1) to (P2.A.4), (3.1), (3.4), and (3.5). The amplitudes for the dominant singular (\mathbf{K} -field) modes were externally prescribed, $\mathbf{K} = \mathbf{K}_0 L(t)$, while for the other modes, the coefficients (generalized degrees of freedom – \mathbf{q}^{eT}) were considered solution dependent unknowns. Connected to the lower order coefficients, \mathbf{q}^{eT} , was a spring-element network which had equivalent stiffness \mathbf{S} . The complete boundary condition and spring network derivation is formally given in Appendix A. The actual MPC subroutine is listed in Appendix C. The integrated work conjugate forces \mathbf{F}_0^e were obtained from the reaction forces of an initial elastic FE analysis, which had all the lower order generalized degrees of freedom zeroed ($\mathbf{q}^{eT} = 0$) and an appropriate \mathbf{K}_0 value imposed. The vector of generalized reaction forces required to sustain $\mathbf{q}^{eT} = 0$ was taken as \mathbf{F}_0^e .

Boundary Layer Verification

To verify the boundary layer method implementation, two *homogeneous* test problems were first performed. These were the same two problems considered by Needleman and Sham (1980): (a) a semi-infinite crack with point loads applied normal to the crack face at $x = -a$; and (b) a semi-infinite crack with the crack tip translated such that it

was located at $x = a$. *Figures 3.3 and 3.4* show the two geometries.

An equivalent inner series expansion about the origin ($z = 0$) which exactly represents their potentials can be explicitly given for these geometries. For the point load the stress potential functions are given by

$$\phi' = \Omega' = \frac{P}{2\pi(z+a)} \sqrt{\frac{a}{z}} = \frac{P}{2\pi} \sum_{n=1}^{\infty} \frac{a^{(n-1/2)}}{z^{(n+1/2)}} (-1)^{n+1}. \quad (3.10)$$

By comparing these potentials with those used in Eqs.(A.1) to (A.4), the series coefficients are related to the components in q^{eT} via

$$q_n^{eT} = \frac{P}{2\pi} \frac{a^{n-\frac{1}{2}} (-1)^{n+1}}{2(n-\frac{3}{2})(n-\frac{1}{2})}, \quad (3.11)$$

for $n = 1$ to ∞ . For the translated crack tip the stress potential functions are

$$\phi' = \Omega' = \frac{K_I}{2\sqrt{2\pi(z-a)}} = \frac{K_I}{2\sqrt{2\pi z}} + \sum_{n=1}^{\infty} f_n \frac{a^n}{z^{(n+1/2)}}, \quad (3.12)$$

where f_n are known constants. Again, by comparing these potentials with those used in this analysis, Eqs.(A.1) to (A.4), the coefficients q_n^{eT} can be obtained in terms of f_n . Unlike Eqs.(2.4) and (2.5), neither of these expansions contain any whole powers of z .

To verify the boundary layer implementation, homogeneous elastic FE analyses were performed and comparisons between the analytically determined coefficients and the FE calculated coefficients, q^{eT} , were made. *Table 3.1* lists the analytical and FE determined coefficients for the two geometries. In both problems the outer boundary of the FE mesh had a radius of 1.0(m). Thus the ratio of $a/|z|$ in the series expansion was 0.3981 for the point load example and was 0.10 for the translated crack tip example.

The FE determined coefficients shown in *Table 3.1* are in good agreement with the analytically determined coefficients for the higher order terms, but the agreement diminishes for lower order terms. (Note that lower order terms correspond to components in q^{eT} with "larger" subscripts.) For the translated crack, this deterioration is attributed to inaccuracies in determining $F^e(t)$, mesh construction, series truncation, and numerical noise. The reaction forces F_0^e for the translated crack were obtained by sewing up the crack face such that the crack tip was artificially located at $x = 0$ and by

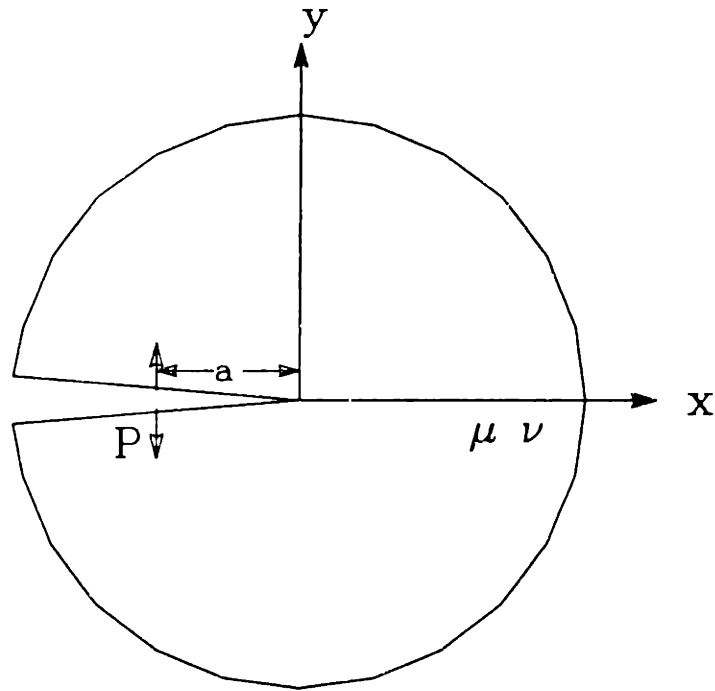


Figure 3.3 Schematic homogeneous crack-tip region with opening crack-face point loads (P) applied at a distance a from the crack-tip.

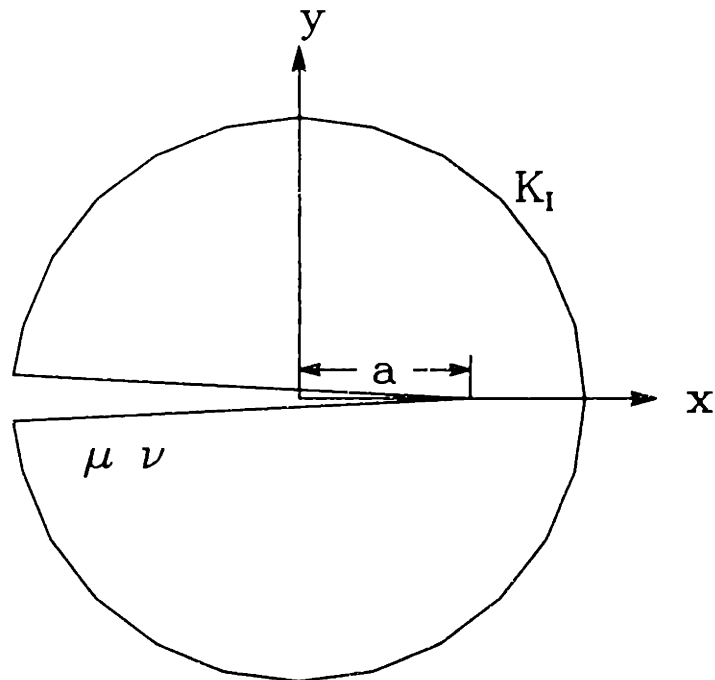


Figure 3.4 Schematic homogeneous crack-tip region and coordinates, showing translated crack tip at $x = a$.

applying \mathbf{K}_0 in an initial elastic analysis. Since, in the translated crack case, the mesh was designed to have the crack tip at $x = a$, and no refinement of the mesh existed at $x = 0$, inaccuracies in \mathbf{F}_0^e may have arisen. Similarly, the mesh used in the point load case was not refined where the point loads were applied. (This will not be an issue during the actual SSY analysis because the forces \mathbf{F}_0^e will be found for the actual unsewed and untranslated meshes.) It was assumed that since the higher order terms matched, the implementation was performed correctly and the dominant behavior was captured even though numerical noise existed.

Coefficient	Analytical [Eq.(3.11)]	FE
q_1	-.2008	-.20084
q_2	-2.6559E-2	-2.6651E-2
q_3	2.0731E-3	2.1220E-3
q_4	-3.2279E-4	-3.6204E-4
q_5	5.6005E-5	8.0071E-5
q_6	-3.3130E-6	-2.0285E-5

(a)

Coefficient	Analytical [Eq.(3.12)]	FE
q_1	-1.9394E-2	-1.9947E-2
q_2	4.6966E-4	4.9868E-4
q_3	7.2501E-6	8.3145E-6
q_4	6.5413E-8	3.1183E-7
q_5	-1.2820E-8	1.5594E-8

(b)

Table 3.1 Analytical and numerical coefficients for a plane-strain crack-tip problem with: (a) opening normal point loads applied at $x = -0.3981$; (b) the crack tip translated to $a = 0.1$.

To verify that the bi-material portion of the boundary layer formulation was correctly implemented, various independent tests were conducted. First, several (bi-material) elastic cases with various material combinations were loaded by prescribing a specific value of \mathbf{K} and setting all inner series coefficients equal to zero ($\mathbf{q}^{eT} = 0$).

Boundary node displacements, which correspond to the dominant asymptotic solution, were compared with the known analytical solution. Because the user written MPC subroutine, used in prescribing the displacements, was coded in a manner such that one index determined all the powers of the root being imposed (*i.e.*, $\lambda_j = (j + 1/2) + i\epsilon$ where j is the index of interest), it was felt that, the coding for that entire family of roots was performed correctly, as long as the limits on this index were chosen correctly and one specific index value yielded the correct results. In a similar fashion, the whole-integer (real) root set [$\Re(\lambda_j) = \lambda_j = j$] was verified by prescribing \mathbf{K} and setting all but one value of \mathbf{q}^{eT} equal to zero. The coefficient not set equal to zero was the one producing a domain-wise uniform stress parallel to the interface ($M = 0$ term). (In the actual potentials used, Eqs.(A.1) to (A.4), the constants multiplying the coefficients (\mathbf{q}^{eT}) in the displacement relationship were not *trivially* zero when $M = 0$.) Again, since the results of this one specific case were correct and the coding was written in an unbiased manner with respect to indices, it was felt that the coding for the entire set of whole-integer real roots was performed correctly.

In a similar spirit, the spring stiffness constants were verified. For the homogeneous case, several specific spring stiffnesses were analytically and numerically integrated to ensure proper coding. Once again, a single index was used to generate the stress potentials, thus guaranteeing that the entire set of spring stiffness coefficients were determined correctly. *Complex* FORTRAN coding was utilized in such a manner that if the homogeneous case was performed correctly and the bi-material potentials were correct, then the bi-material spring constants would also be determined correctly. Additionally, several spring constants were integrated via other methods to provide an additional check. All homogeneous tests were performed using the actual bi-material subroutines and programs, but with identical elastic properties in each domain.

A crack-face point load elasticity problem, similar to the one used previously, was considered to ensure that the boundary layer extension for bi-materials was implemented correctly. *Figure 9.5* shows the crack-tip geometry and the direction and loca-

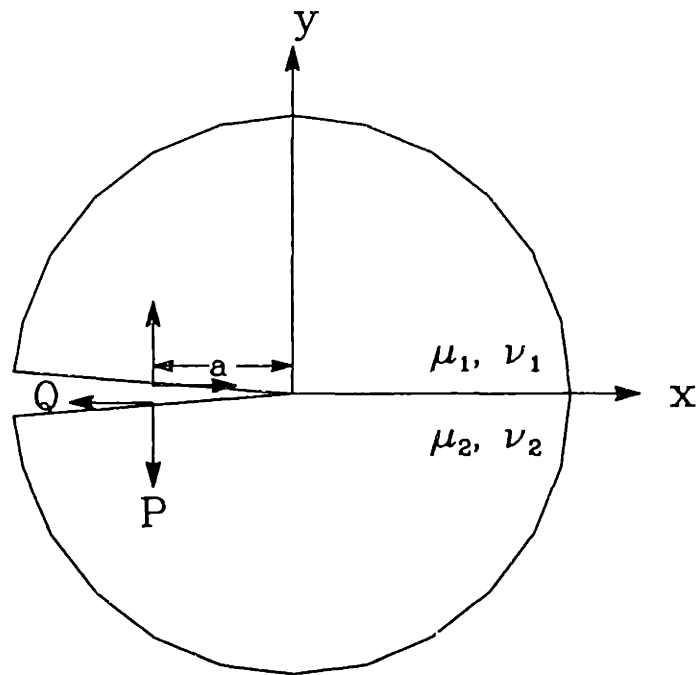


Figure 3.5 Schematic bi-material interfacial crack-tip region with crack-face opening (P) and shearing (Q) point loads applied at a distance a from the crack-tip, showing coordinates and domain numbering conventions.

tion of the crack-face point loads P and Q . From Rice and Sih (1965), the ϕ'_1 stress potential function for this configuration is given by

$$\phi'_1 = \Omega'_1 = \frac{P - iQ}{2\pi e^{\pi\epsilon}} \frac{1}{z + a} \left(\frac{a}{z}\right)^{\frac{1}{2} + i\epsilon} \quad (3.13)$$

and the equivalent inner series expansion about the origin ($z = 0$) is expressed as

$$\phi'_1 = \Omega'_1 = \frac{P - iQ}{2\pi e^{\pi\epsilon}} \frac{1}{z} \left(\frac{a}{z}\right)^{i\epsilon} \sum_{n=1}^{n=\infty} \left(\frac{a}{z}\right)^{n - \frac{1}{2}} (-1)^{n+1}. \quad (3.14)$$

By comparing this expansion of the ϕ'_1 potential with the general potential used in Eqs.(A.1) to (A.4), the series coefficients q^{eT} in the general potential, Eqs.(A.1) to (A.4), are determined to be

$$q_n^{eT} = \frac{P - iQ}{4\pi e^{\pi\epsilon}} \frac{[\cos(\epsilon \ln a) + i \sin(\epsilon \ln a)]}{\left[\left(\frac{1}{2} - n\right) - i\epsilon\right] \left[\left(-n - \frac{1}{2}\right) - i\epsilon\right]} a^{n + \frac{1}{2}} (-1)^n, \quad (3.15)$$

for $n = 0$ to ∞ .

A plane-strain FE analysis was used to evaluate the bi-material point load problem. It used the elastic properties of aluminum in the upper region and steel in the lower region, and the bi-material constant was $\epsilon = 0.03220$. (See *Table 4.3* for the elastic constants used.) The crack face was loaded with several different combinations of point loads P and Q , while maintaining $\mathbf{K} = 0$, and only positive values of P were considered. The values of the analytical and FE determined coefficients for the case where loads of magnitude $P = Q = 1$ are applied at $x = -0.3981$ are listed in *Table 3.2*. (The FE mesh had a radius of 1.0(m) which yielded a ratio of $a/|z| = 0.3981$.) The discrepancy between the coefficients can be attributed to the coarse mesh, lack of mesh refinement near the point loads, and the fact that the Laurent series expansion was truncated after only six terms. It was assumed that since each individual component and the complete implementation was verified for both homogeneous and bi-material cases, the boundary layer method was extended and implemented correctly for the bi-material problem.

Coefficient	Analytical [Eq.(3.15)]	FE
q_1	$-.17456 + i.18557$	$-0.1747 + i0.1855$
q_2	$-2.0939 \times 10^{-02} + i2.6627 \times 10^{-02}$	$-2.1073 \times 10^{-02} + i2.6346 \times 10^{-02}$
q_3	$1.7809 \times 10^{-03} - i2.0330 \times 10^{-03}$	$1.7875 \times 10^{-03} - i1.9540 \times 10^{-03}$
q_4	$-3.0828 \times 10^{-04} + i3.4306 \times 10^{-04}$	$-3.1094 \times 10^{-04} + i2.9619 \times 10^{-04}$
q_5	$6.8632 \times 10^{-05} - i7.5474 \times 10^{-05}$	$6.3699 \times 10^{-05} - i5.2252 \times 10^{-05}$
q_6	$-1.7453 \times 10^{-05} + i1.9061 \times 10^{-05}$	$-1.4279 \times 10^{-05} + i3.4650 \times 10^{-06}$

Table 3.2 Analytical and numerical coefficients for a plane-strain bi-material crack-tip problem with point load, $P = Q = 1$, applied at $x = -0.3981$.

3.1.2 Closed Crack-Tip Faces

The asymptotic local crack-tip behavior for the closed crack-tip face model was numerically investigated with the FE method proposed by Hilton and Hutchinson (1971). Since no parametric study was to be performed and no numerically difficult oscillatory stress fields exist in the closed crack-tip elasticity solution, Sham's boundary layer approach was not utilized. The displacements were obtained via Eqs.(3.2) and (3.3), rotated into a Cartesian coordinate frame, and imposed along Γ_∞ , the FE mesh boundary. For the FE analysis, the displacements, Eqs.(3.2) and (3.3), were incorporated into a user-written MPC subroutine and nodes along Γ_∞ were constrained with a free node, whose displacement was associated with the value of K_{II}^c , via the MPC. As before, the magnitude of K_{II}^c was scaled with $L(t)$. Appendix C contains a listing of the MPC subroutine used.

3.2 Elastic/Perfectly-Plastic Constitutive Relationship

This section describes the constitutive relationship used, as well as the integration operator and the associated notation. The material relationship was incorporated in the FE analysis via a user-written subroutine called UMAT. A listing of the UMAT subroutine is included in Appendix C.

3.2.1 Kinematics

It is assumed that infinitesimal strain theory (linearized kinematic theory) is used. It is therefore assumed *a priori* that all strains and physical rotations are small such that all rotation tensors can be approximated by the identity tensor and that the symmetric part of the (spatial) velocity gradient can be approximated by the strain rate.

3.2.2 Notation

Using Gurtin's notation convention (Gurtin, 1981), the evolution equation and the definition of various relevant variables are as follows. The Cauchy stress rate tensor, $\dot{\sigma}$, is given by

$$\dot{\sigma} = \mathcal{L}[\dot{\underline{\epsilon}} - \dot{\underline{\epsilon}}^P], \quad (3.16)$$

with the fourth order elasticity tensor \mathcal{L} , defined as,

$$\mathcal{L} = 2\mu I + (\kappa - \frac{2}{3}\mu)\mathbf{1} \otimes \mathbf{1}, \quad (3.17)$$

where $\dot{\underline{\epsilon}}$ is the total strain rate tensor, $\dot{\underline{\epsilon}}^P$ is the plastic strain rate tensor, I is the fourth order identity tensor, $\mathbf{1}$ is the second order identity tensor, and κ is the bulk modulus. (Note that the strain tensor is designated with $\underline{\epsilon}$ since the usual symbol associated with it is used to define the bi-material constant.) The deviatoric stress rate tensor, $\dot{\sigma}'$, is given by

$$\dot{\sigma}' = \dot{\sigma} - \frac{1}{3}\text{tr}(\dot{\sigma}) \mathbf{1}. \quad (3.18)$$

Similarly, the strain rate tensors can also be decoupled into deviatoric and hydrostatic parts. The Mises equivalent stress, $\bar{\sigma}$, is defined as

$$\bar{\sigma} = \sqrt{\frac{3}{2}\sigma' \cdot \sigma'}, \quad (3.19)$$

and \mathbf{N} , the instantaneous normal to the yield locus at the current stress state, is given by

$$\mathbf{N} = \sqrt{\frac{3}{2}} \frac{\sigma'}{\bar{\sigma}}. \quad (3.20)$$

3.2.3 Constitutive Relationship

The elastic/perfectly-plastic continuum constitutive relationship is based upon several assumptions. It assumes that elastically, as well as plastically, the material is isotropic and that all plastic deformation is volume preserving (incompressible). The yield locus, in the π -plane, is spherical (*i.e.*, not pressure sensitive) and does not translate or change size with plastic flow (*i.e.*, no isotropic or kinematic hardening). All plastic flow occurs only in the direction instantaneously normal to the yield locus, at the current point. The flow rule, Λ , is defined as

$$\Lambda = \begin{cases} 1 & \text{If } \bar{\sigma} = \sigma_{ys} \text{ and } \mathbf{N} \cdot \{\mathcal{L}[\dot{\underline{\epsilon}}]\} \geq 0 \\ 0 & \text{Otherwise.} \end{cases} \quad (3.21)$$

where σ_{ys} is the tensile yield strength of the material. The interpretation of the flow rule is that $\dot{\underline{\epsilon}}^P$ is non-zero only when $\Lambda = 1$. The portion of this constitutive relationship describing plastic straining, written in rate form, is

$$\dot{\underline{\epsilon}}^P = \Lambda \{\mathbf{N} \otimes \mathbf{N}\} [\dot{\underline{\epsilon}}]. \quad (3.22)$$

The stress rate $\dot{\sigma}$ is obtained by substituting the definition for $\dot{\underline{\epsilon}}^P$, Eq.(3.22), directly into Eq.(3.16) as

$$\dot{\sigma} = \{\mathcal{L}\} [\{I - \mathbf{N} \otimes \mathbf{N}\} [\dot{\underline{\epsilon}}]]. \quad (3.23)$$

To facilitate the incorporation of this constitutive relationship into the numerical model, an incremental form is utilized. This incremental form is exact only in the limit that

$$\lim_{\Delta \underline{\epsilon} \rightarrow 0} (\Delta \underline{\epsilon}) = \frac{\partial \underline{\epsilon}}{\partial t} \Delta t = \dot{\underline{\epsilon}} \Delta t. \quad (3.24)$$

3.2.4 Constitutive Integration Operator

The elastic/perfectly-plastic material response is numerically integrated using the Rice-Tracey Mean Normal integration operator (Rice and Tracey, 1973). The material response is integrated under the assumption that during an increment in time, Δt , between the n th and $(n + 1)$ th state, $\dot{\underline{\epsilon}}$ remains constant such that

$$\epsilon_{n+1} - \epsilon_n = \int_n^{n+1} \dot{\epsilon} dt \approx \dot{\epsilon} \Delta t = \Delta \epsilon. \quad (3.25)$$

The deviatoric stress σ'_{n+1} at the $(n + 1)$ state is given by

$$\sigma'_{n+1} = \sigma'_n + \Delta \sigma' \quad (3.26)$$

and, when $\Lambda = 0$,

$$\Delta \sigma' = 2\mu \Delta \epsilon', \quad (3.27)$$

where σ'_n is the deviatoric stress at the n th state, $\Delta \sigma'$ is the deviatoric stress increment, and $\Delta \epsilon'$ is the postulated deviatoric strain increment tensor.

An increment in stress where the initial stress state is elastic and the final state is yielding ($\Lambda = 1$) is now considered, and *Figure 3.6* schematically shows such a stress state in the π -plane. The initial elastic stress state σ'_n does not satisfy the yield condition and lies within the $R = \sigma_{y0}$ sphere. The increment in deviatoric stress, $\Delta \sigma'$, is obtained by traveling from the original stress state along the path of the elastic predictor, $2\mu \Delta \epsilon'$, until the yield surface is reached. The fraction of the total elastic predictor which must be traveled to reach the yield surface is α , and α is given by

$$\alpha(\Delta \epsilon') = \frac{-(\Delta \epsilon' \cdot \sigma'_n) \pm \sqrt{(\Delta \epsilon' \cdot \sigma'_n)^2 - (\Delta \epsilon' \cdot \Delta \epsilon') [(\sigma'_n \cdot \sigma'_n) - \sigma_{y0}^2]}}{\mu (\Delta \epsilon' \cdot \Delta \epsilon')} \quad (3.28)$$

The correct root of α is the one that lies between 0 and 1. Once the yield surface is reached, an intermediate state \mathbf{T}^* is constructed using the remaining portion of the elastic predictor $(1 - \alpha)2\mu \Delta \epsilon'$ and the stress state at the yield surface, $\sigma'_n + \alpha 2\mu \Delta \epsilon'$. The intermediate state \mathbf{T}^* is defined as

$$\mathbf{T}^*(\Delta \epsilon) = 2\sigma'_n + (1 + \alpha)2\mu \Delta \epsilon', \quad (3.29)$$

where \mathbf{N}^* , the normalized direction of \mathbf{T}^* , is defined as

$$\mathbf{N}^*(\Delta \epsilon) = \frac{\mathbf{T}^*(\Delta \epsilon)}{2\sqrt{\frac{1}{2}\mathbf{T}^*(\Delta \epsilon) \cdot \mathbf{T}^*(\Delta \epsilon)}}. \quad (3.30)$$

The deviatoric stress increment $\Delta \sigma'$ is then obtained by projecting $(1 - \alpha)2\mu \Delta \epsilon'$, the remaining fraction of the elastic predictor, onto a vector normal to \mathbf{N}^* such that

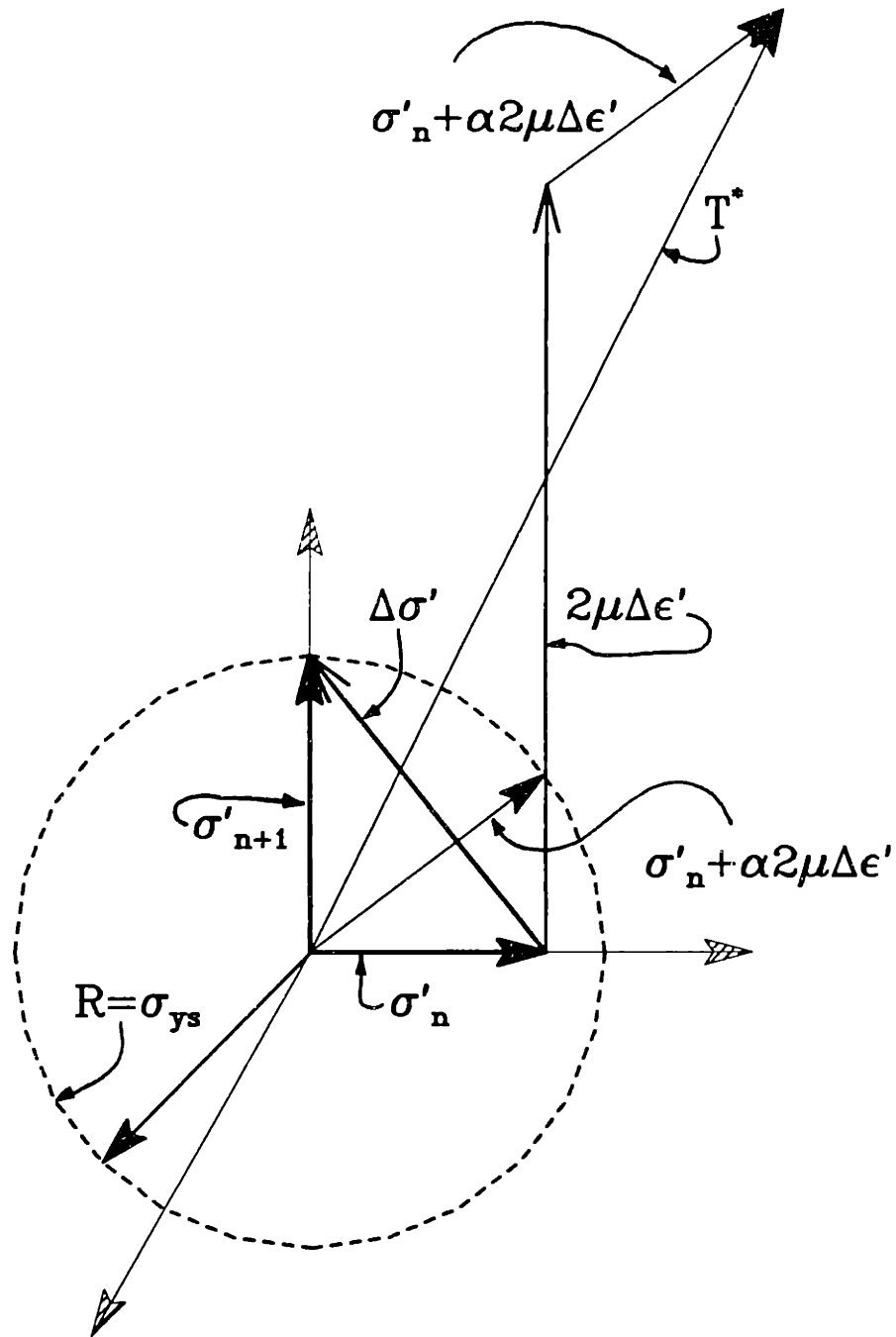


Figure 3.6 Schematic π -plane representation of a stress increment obtained by the Rice-Tracey mean normal integration operator; showing the various vectorized (tensor) stress states and the yield sphere.

$$\Delta\sigma' = 2\mu \{I - (1 - \alpha)2\mathbf{N}^* \otimes \mathbf{N}^*\} [\Delta\epsilon'] . \quad (3.31)$$

This operator always places σ'_{n+1} exactly on the yield surface for any strain increment with $\bar{\sigma} \leq \sigma_{ys}$ and elastic predictor state having $\sqrt{\frac{3}{2}(\sigma'_n + 2\mu\Delta\epsilon') \cdot (\sigma'_n + 2\mu\Delta\epsilon')} \geq \sigma_{ys}$. To obtain the updated total stress, σ_{n+1} , the hydrostatic stress must also be integrated. Since ϵ_{n+1} is postulated as being known (given), the hydrostatic stress is trivially obtained and is

$$\sigma_{n+1} - \sigma'_{n+1} = \{\kappa \mathbf{1} \otimes \mathbf{1}\} [\epsilon_{n+1}] . \quad (3.32)$$

Using Eqs.(3.26), (3.31), and (3.32), the total $(n+1)$ th stress state, when $\Lambda = 1$ during an increment, is given by

$$\sigma_{n+1} = \left\{ \begin{array}{l} 2\mu (I - (1 - \alpha(\Delta\epsilon)) 2\mathbf{N}^* (\Delta\epsilon) \otimes \mathbf{N}^* (\Delta\epsilon)) \\ + (\kappa - \frac{2\mu}{3}) (\mathbf{1} \otimes \mathbf{1}) \end{array} \right\} [\Delta\epsilon] + \sigma_n . \quad (3.33)$$

Eq.(3.31) is general and valid for all stress states except when both σ_n and σ_{n+1} lie within the yield radius. In conjunction with Eq.(3.27), Eqs.(3.28) to (3.33) describe the stress state for all possible loading increments.

In addition to calculating the final stress state, a material Jacobian, defined as

$$J = \frac{\partial\Delta\sigma}{\partial\Delta\epsilon} , \quad (3.34)$$

is also required for the global Newton-Rapson (FE) iteration procedure (Hibbit, Karlsson, and Sorensen, 1987). The Jacobian for this operator is given by,

$$\begin{aligned} J = & G_1 I + (\kappa - \frac{G_1}{3}) \mathbf{1} \otimes \mathbf{1} + G_2 \mathbf{N}^* \otimes \mathbf{N}^* + G_3 \mathbf{N}^* \otimes \gamma \\ & + G_4 \mathbf{N}^* \otimes \Delta\epsilon' + G_5 \Delta\epsilon' \otimes \gamma, \end{aligned} \quad (3.35)$$

where,

$$G_1 = 2\mu - (1 + \alpha)(1 - \alpha) \frac{4\mu^2}{\tau^*} (\mathbf{N}^* \cdot \Delta\epsilon') , \quad (3.36)$$

$$G_2 = 4\mu(\alpha - 1) - (1 + \alpha)(1 - \alpha) \frac{16\mu^2}{\tau^*} (\mathbf{N}^* \cdot \Delta\epsilon') , \quad (3.37)$$

$$G_3 = 4\mu(\mathbf{N}^* \cdot \Delta\epsilon') + (1 - \alpha) \frac{16\mu^2}{\tau^*} (\mathbf{N}^* \cdot \Delta\epsilon')^2 - (1 - \alpha) \frac{4\mu^2}{\tau^*} (\Delta\epsilon' \cdot \Delta\epsilon') , \quad (3.38)$$

$$G_4 = -(1 + \alpha)(1 - \alpha) \frac{4\mu^2}{\tau^*}, \quad (3.39)$$

$$G_5 = (1 - \alpha) \frac{4\mu^2}{\tau^*} (\mathbf{N}^* \cdot \Delta \underline{\epsilon}'), \quad (3.40)$$

$$\gamma = -\frac{[2\mu\alpha^2 \Delta \underline{\epsilon}' + \alpha \sigma'_n]}{2\mu\alpha (\Delta \underline{\epsilon}' \cdot \Delta \underline{\epsilon}') + (\sigma'_n \cdot \Delta \underline{\epsilon}')}, \quad (3.41)$$

and

$$\tau^* = \sqrt{\frac{1}{2} \mathbf{T}^* \cdot \mathbf{T}^*}. \quad (3.42)$$

Use of the mathematically exact (generally) non-symmetric Jacobian would require that the FE procedure solve the complete set of equations, as opposed to a symmetric subset. This procedure would be considerably more costly, and thus a symmetrized (approximate) Jacobian is used (Bathe, 1982). The symmetrized Jacobian, J_{sym} , is defined as

$$\begin{aligned} J_{sym} = & G_1 I + \left(\kappa - \frac{G_1}{3}\right) \mathbf{1} \otimes \mathbf{1} + G_2 \mathbf{N}^* \otimes \mathbf{N}^* + G_3 \frac{1}{2} (\mathbf{N}^* \otimes \gamma + \gamma \otimes \mathbf{N}^*) \\ & + G_4 \frac{1}{2} (\mathbf{N}^* \otimes \Delta \underline{\epsilon}' + \Delta \underline{\epsilon}' \otimes \mathbf{N}^*) + G_5 \frac{1}{2} (\gamma \otimes \Delta \underline{\epsilon}' + \Delta \underline{\epsilon}' \otimes \gamma). \end{aligned} \quad (3.43)$$

The use of this Jacobian yielded nearly quadratic global convergence, as would be expected in a Newton-Raphson method. (Aside: A radial return operator [Krieg and Krieg, 1977] was also tried, but yielded very poor convergence. It is speculated that because the Jacobian for the Mean-Normal operator is based upon an intermediate stress state halfway between σ'_{n+1} and σ'_n , it does not result in the same sort of radial softening that would be predicted using a radial return Jacobian. This (relative) radial stiffening is thought to retard small to modest changes in the direction of σ'_{n+1} during iterations.)

3.3 FE Model Considerations

This last section is divided into three parts. The first part discusses the “simplified,” but efficient, FE model used to obtain the characteristics of the traction-free crack-tip model for different loadings ($\angle \mathbf{K}$) and material combinations considered. Since this

mesh would subsequently be used many times and each run represents a substantial investment in CPU time (due to the complexity of the oscillatory elastic fields), much effort was spent on designing it. The second FE model discussed is again a traction-free crack-tip model, however, the purpose this model was to unequivocally determine whether or not oscillatory stress fields, analogous to those found in the elastic solution, exist within the elastic/perfectly-plastic deformation zone. Material properties were chosen and the mesh design was performed in such a manner to yield the maximum amount of information with only a relatively modest investment in computational time. Although many of the same details from the first model were utilized, the goal was to maintain simplicity and thereby ensure an unquestionable result. The third section concerns itself with the FE model assembled to investigate the closed crack-tip face model. Since little complexity was anticipated based upon the elastic solution, a simple, but sufficient, FE model was assembled.

3.3.1 Traction-Free Crack-Tip Face Model

Boundary Layer Implementation

Various common features were incorporated in all the traction-free crack-tip FE models that used the boundary layer method. The FE code *ABAQUS* (Hibbitt, 1984) was used with the user-added subroutines UMAT and MPC. Slight modifications when needed were made in the UMAT to obtain only an elastic response. The boundary layer formulation series were truncated after the first seven half-integer (Williams type) terms ($N = 0, -1, -2, \dots, -6$), and after five even-integer terms ($M = -2, -3, -4, \dots, -6$), where the variables N and M refer to the indices in Eqs.(3.4) to (3.7) or Eqs. (A.1) to (A.4). The term $N = 0$ corresponds to the dominant asymptotic power, and the power $M = -1$ was excluded from the formulation since it represents an applied concentrated crack-tip force and produces infinite far-field elastic strain energy in the boundary layer formulation. The vector \mathbf{q}^T was represented by 24 degrees of freedom (12 “free” nodes each with two active degrees of freedom). These free nodes, which actually behave as

Lagrange multipliers in the FE program, were the vertices in the spring network and the nodes to which all outer FE boundary nodes were constrained.

FE Mesh

Prior to elaborating on the actual meshes used, the procedure used to evaluate mesh accuracy will be outlined.

In order to judge the capability of the FE meshes to reproduce at least the elastic \mathbf{K} -fields, elastic test runs were performed on each mesh by imposing assorted values of \mathbf{K} with $\mathbf{q}^{eT} = 0$. The averaged nodal stresses were then examined in the radial and circumferential directions and compared to the dominant asymptotic stress expressions. To evaluate the radial dependence, the stress components were plotted against the natural logarithm of the radial distance r . Excluding the first and last elements, the numerical and analytical results were usually indistinguishable. For a better comparison, the stresses were normalized (multiplied by \sqrt{r}) and plotted against the natural logarithm of the radial distance. In this way, any discrepancy existing in the phase or period between the analytical and numerical solutions would be immediately obvious. One particularly beneficial result emerged from this plotting procedure. The numerically obtained stresses alternatively overestimated and then underestimated the analytical solution, from node to node, with a mean value which was coincidental with the analytical solution. The magnitude of these oscillations (local maximum to minimum) decreased as the number of elements used in the radial direction increased. The oscillation magnitude is thought to represent the actual discretization error attributable to the inability of the element to reproduce the approximate $1/\sqrt{r}$ stress distribution. This parameter was used to estimate when sufficient mesh refinement was achieved. In addition to this measure, the interfacial tractions between the domains were examined to ensure continuity. Finally, numerically obtained elastic energy release rates were compared against theoretical values.

All traction-free crack-tip models had the same geometrical mesh design. An actual

mesh is shown in *Figure 3.7* without the inner core elements. All crack-tip elements were collapsed into a triangular geometry. To maintain physical significance, interface elements were incorporated into the crack-face region, as necessary, to prevent crack face interpenetration during the transient portion of the analysis. (Prior to “steady-state.”) The mesh contained 18 and 25 elements circumferentially in the elastic and elastic/perfectly-plastic regions, respectively, with a high concentration of elements around the interface. The mesh contained five logarithmically spaced elements per each of its three concentric rings. Each ring spanned a decade, with the inner ring extending all the way to the crack tip. The outer mesh boundary was located at $R = 1.0$ m in order to circumvent computational difficulties associated with the boundary layer formulation. Plane-strain elements were used.

Two different meshes, differing only in element type, were employed. The initial mesh consisted of 8-node isoparametric elements with full 3×3 Gaussian integration in the elastic region and 8-node isoparametric fully integrated linear pressure hybrid elements in the elastic/perfectly-plastic domains. This mesh was run on ABAQUS, version 4.5.174, and was used for almost all ζ_0 and material combinations considered, since it was relatively small (645 elements) and efficient to run. (Each iteration required approximately 8 minutes per iteration on a FX-8 Alliant mini-supercomputer running on one computational element. Typical job times were around 100 CPU hours.) If sufficient global convergence or resolution of stresses was not achievable, which often happened due to oscillatory pressure noise, the following alternative model was used.

This FE model used plane-strain 9-node isoparametric elements with selective integration in both domains. Full 3×3 Gaussian integration was performed on the deviatoric stresses along with 2×2 Gaussian integration of the pressure, values of which were interpolated–extrapolated to the 3×3 Gaussian points. This model was analyzed with ABAQUS, version 4.6.160, and reduced the time per iteration to about 4 minutes on the Alliant FX-8 mini-super computer. Use of this model significantly reduced the pressure noise as compared to the hybrid 8-node elements used previously.

Representative Mesh

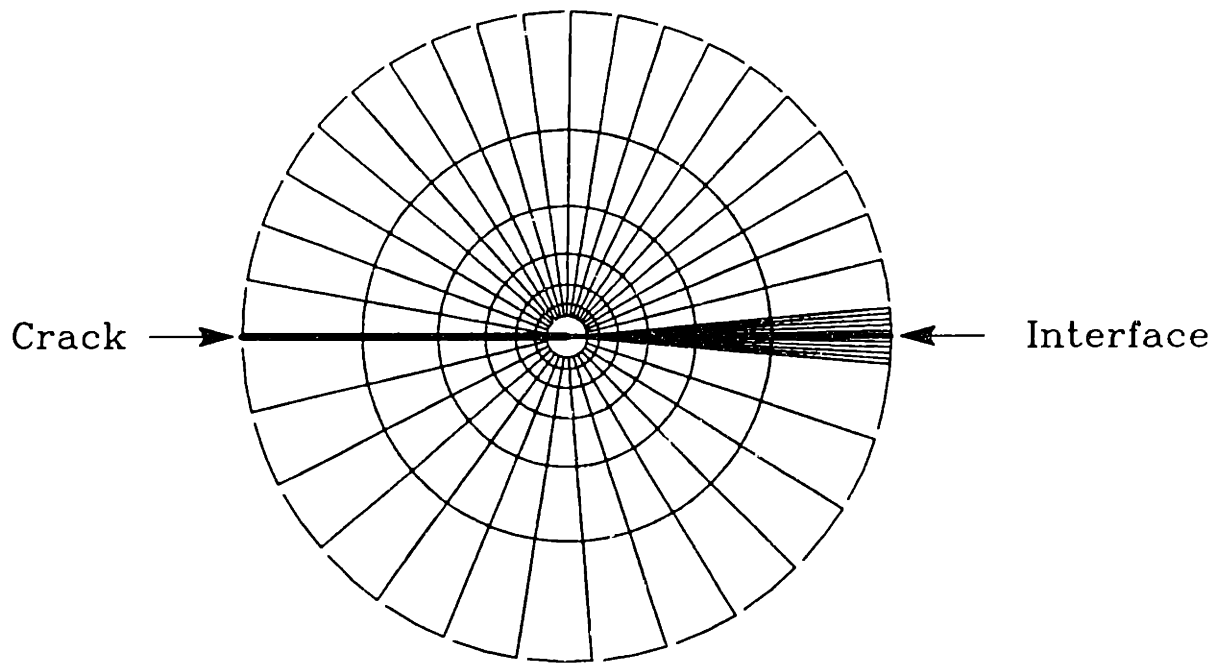


Figure 3.7 Representative finite element crack-tip mesh (excluding actual crack-tip elements), showing circumferential element distribution, crack-face and interface locations, and radial spacings of elements.

Due to the substantial time savings, this model completely replaced the initial model described above.

Procedures

The procedures used in all analyses performed with the boundary layer method were identical. An initial linear run, in terms of constitutive and kinematic theories, was done with the appropriate \mathbf{K}_0 applied to determine the reaction force vector \mathbf{F}_0^e and to check the assemblage of the model. Comparisons between the numerically obtained J -Integral by the virtual crack extension method (VCEM) and the theoretical value, Eq.(2.16), were made and typically only differed by 0.1%. The actual non-linear analysis used a "STATIC" time procedure with infinitesimal strain theory (HKS, 1987). Loading was accomplished by prescribing "displacements" to the \mathbf{K} -term free nodes, in a square root fashion with respect to internal analysis time, to achieve quasi-linear plastic zone growth. The reaction forces from the initial elastic run were imposed as concentrated loads on the T -term free nodes and were scaled using the same amplitude-time function as the \mathbf{K} -term displacements. The static parameter **CYCLE**, which is the maximum number of iterations that can be performed during a time increment before a smaller time increment is tried, was set to 9. This parameter also controls the increase in time increment size by reviewing the number of iterations in the previous two increments necessary to achieve an acceptable solution, and if the number of iterations is less than $(\lfloor \text{CYCLE}/2 \rfloor - 1)$, the time increment size is increased. An initial suggested time increment size was provided such that at no time during the first increment was the yield condition satisfied anywhere in the mesh. The error tolerance **PTOL**, which is the maximum acceptable residual nodal force after all element contributions and applied loads are summed up, is set to 1.0×10^{-5} MN. This value of **PTOL** corresponds to 0.02% of $\sigma_{ys} \cdot l \cdot t$, where l and t are the radial length and thickness of the smallest (radial) element, respectively. The solution procedure iterates until the **PTOL** condition is satisfied throughout the mesh, cutting back the time increment

size as necessary. Loading was done until the plastic zone nearly touched the FE mesh boundary.

3.3.2 Traction-Free Crack-Tips: Existence of Stress Oscillations Within The Plastic Zone

This section describes the FE model used to investigate the extent of stress oscillations occurring within the plastic zone of a traction-free crack tip. It was assumed that the lower region was rigid ($\mu_2 = \infty$), and that the upper material had the elastic properties of aluminum [$\mu = 26.1$ MPa and $\nu = .342$ (Hertzberg, 1976)] with a yield strength of 32.5 MPa. This results in a bi-material constant of $\epsilon = 0.07796$. Based upon this value of ϵ , a mesh spanning 36 decades in the radial direction would be required to achieve one complete period of elastic stress oscillation. It was felt that plastic deformation extending one-quarter of the elastic period would be sufficient to determine the extent, if any, of plastic stress oscillations. Therefore, mesh spanning 12 decades, which allowed for 3 decades of elastic material outside the plastic zone, was utilized.

Since this model considered the bottom medium to be rigid, only the upper region needed to be modeled. To simulate the rigid lower region, all nodes along the intact interface were pinned. The mesh has 25 elements spanning the circumferential direction, with the same distribution as shown in *Figure 3.7*. Because of the appreciable radial extent of this mesh, only three logarithmically spaced, 9-node selectively reduced elements spanned each of its twelve concentric rings. Crack-tip element geometry, identical to that described previously, was used at the crack-tip. To avoid numerical solver problems associated with large differences in element stiffnesses, the boundary layer method was not employed. Instead, displacements consistent with the dominant asymptotic \mathbf{K} -field were imposed along the Γ_∞ boundary. The Γ_∞ boundary itself was located at $r = 1.0 \times 10^5$ m. All nodes along this boundary were constrained via a user written MPC to prescribe the nodal displacements.

The procedural aspects of this model were basically the same as before. Again, the elastic/perfectly-plastic material behavior was incorporated with the same UMAT.

The error tolerance **PTOL** used for this analysis was set to 5.0×10^{-8} MN and was 0.7% of $\sigma_{ys} \cdot l \cdot t$. The value of **CYCLE** was varied between 7 and 9, depending upon the progress of the analysis. Loading was applied by scaling the displacement of the **K**-field node in a square root fashion with respect to internal analysis time, to achieve quasi-linear plastic zone growth. The $\angle \mathbf{K}$ prescribed was chosen to be $\angle \mathbf{K} = 35.0^\circ$. This was necessary to keep the value of ζ_0 within the valid domain during loading; *i.e.*, ζ_0 always satisfied the no crack-face contact conditions predicted by Eq.(P2.33).

3.3.3 Closed Crack-Tip Faces

The FE model used to investigate the crack-tip fields around the closed crack tip utilized many of the same features as the previous FE model. The subroutines UMAT and MPC were included in the analysis. The material in the lower region was assumed to be rigid ($\mu_2 = \infty$), thus only the upper crack-tip region was modeled. The actual mesh used 25 9-node isoparametric elements in the circumferential direction. Radially, the mesh had four concentric rings with five logarithmically spaced elements per each of its four rings. Again, the outer boundary of the mesh was set at $r = 1.0$ m. Since the lower half was rigid, the edge of the mesh corresponding to the intact interface was clamped. Along the crack face, interface elements were attached, thus allowing for possible gap formation. The nodes along the outer edge of the mesh were constrained in accordance with Eqs.(3.2) and (3.3) by a closed crack-tip user-written MPC. Loading was accomplished by prescribing the displacement to the K_{jI}^c -term node in a square root fashion with respect to internal analysis time. The FE model was loaded until the maximum extent of the plastic zone reached $r = 0.1$ m. Since the “STATIC” analysis procedure was used, the **CYCLE** parameter was set to 9, and the error tolerance parameter **PTOL** was set to 1.0×10^{-6} MN (0.02% of $\sigma_{ys} \cdot l \cdot t$).

Chapter 4

Elastic-Plastic Interfacial Crack-Tip Fields

In this chapter the results obtained from the various numerical crack-tip calculations for the BV problem stated in Chapter 1 will be described. The behavior of each crack-tip model will be outlined along with the assumed material idealizations. In order to organize the vast quantity of numerically obtained information into a more manageable format, explicit representation forms will be used which reconstruct all or portions of the actual solution in terms of only a few variables. The characteristics and notation of the representative forms will be introduced and discussed. The local crack-tip fields for all the various material combinations and loadings will be presented via these representative forms and in terms of the dimensional framework outlined in Chapter 2. "Geographical" inner bounds of inelastic crack-tip fields are established from evaluating limitations imposed by the underlying mathematical assumptions.

4.1 Asymptotic Crack-Tip Forms

The purpose of this section is to present the anticipated asymptotic crack-tip forms by reviewing in detail those forms obtained for the cases of a homogeneous stationary crack and for homogeneous quasi-static crack growth. This review is focused solely upon isotropic elastic/perfectly-plastic media whose yield criteria are described by the Mises yield condition. In general, the only restriction placed on the value of the Poisson's

ratio is that it must be positive ($0 < \nu \leq 0.5$). Anticipated differences between the homogeneous and bi-material behavior of the crack-tip forms is discussed along with the conditions necessary to properly assemble these forms into the complete crack-tip fields. Finally, because slip-line theory is used extensively to describe various deforming portions of the crack-tip regions, a brief review of slip-line notation is made.

4.1.1 Summary of Slip-Line Theory

To familiarize the reader with slip-line theory and to assign notation, a short summary follows. The reader is referred to Hill (1983) and Kachanov (1974) for a more complete description and comprehensive derivation.

For a plane-strain rigid/perfectly-plastic material state, two families of curves, referred to as α -lines and β -lines, uniquely describe the material stress state and are derived from equilibrium arguments and the yield criterion. (Slip-line theory is loosely analogous to stream functions used to describe inviscid flow in fluid dynamics.) Along an α -line

$$p + 2k\phi = C_\alpha, \quad (4.1)$$

while along a β -line

$$p - 2k\phi = C_\beta. \quad (4.2)$$

Here p is the mean pressure [$p = -(1/3)tr(\sigma)$], k the material yield strength in shear ($k = \sigma_{ys}/\sqrt{3}$), ϕ is the angle measured from the positive x-axis to the α -line in an anti-clockwise direction, and C_α and C_β are constants associated with each α -line and β -line, respectively. The stress components are obtained by considering the angle ϕ of the α -line or β -line at the material point of interest and are given by Hill (1983) as

$$\sigma_{xx} = -p - k \sin 2\phi, \quad (4.3)$$

$$\sigma_{yy} = -p + k \sin 2\phi, \quad (4.4)$$

and

$$\sigma_{xy} = k \cos 2\phi. \quad (4.5)$$

The value of p is determined from Eqs.(4.1) and (4.2) and by the slip-line constants, C_α and C_β . Once the constants C_α and C_β along an α - and a β -line are determined at some point, usually via boundary conditions, the complete stress state within the slip-line field can be evaluated. *Figure 4.1* shows a representative element with respect to a family of slip lines along with the associated stress state. Although slip-line theory does not completely describe the strain state in a body, it does describe certain features of the deformation. The α and β characteristic slip-lines are orientated parallel to the direction of maximum shear stress, and they represent directions of zero extension. (i.e., no normal strain is produced in directions parallel to slip lines.

Rigid-plastic slip-line theory is often used to describe elastic/perfectly-plastic materials capable of compressible elastic deformation ($\nu \neq 0.5$) and incompressible plastic deformation. To use rigid-plastic slip-line fields for these materials, it is assumed that the effect of elastic strains are negligible. This assumption is only valid in the asymptotic sense that

$$\dot{\underline{\epsilon}}^P = \left\{ \lim_{\dot{\underline{\epsilon}}^P \rightarrow \infty} \dot{\underline{\epsilon}}^T \right\}, \quad (4.6)$$

where $\dot{\underline{\epsilon}}^T$ is the total strain rate, and $\dot{\underline{\epsilon}}^P$ and $\dot{\underline{\epsilon}}^T$ are the total plastic strain and strain rate components, respectively. In general, the use of slip-line theory and accompanying representative forms for elastically compressible materials does not necessitate that the elastic strain components are zero.

4.1.2 Stationary and Quasi-Static Crack-Tip Forms

The admissible plane-strain asymptotic crack-tip fields have been reviewed extensively for stationary and quasi-static homogeneous cracks in isotropic elastic/perfectly-plastic media; e.g., Rice (1982), Rice, Drugan, and Sham (1980), Rice and Tracey (1973), and Nemat-Nasser and Obtata (1984). For a stationary crack with $\nu = 0.5$, Nemat-Nasser and Obtata identified that three distinct crack-tip sectors *may* exist; namely an elastic

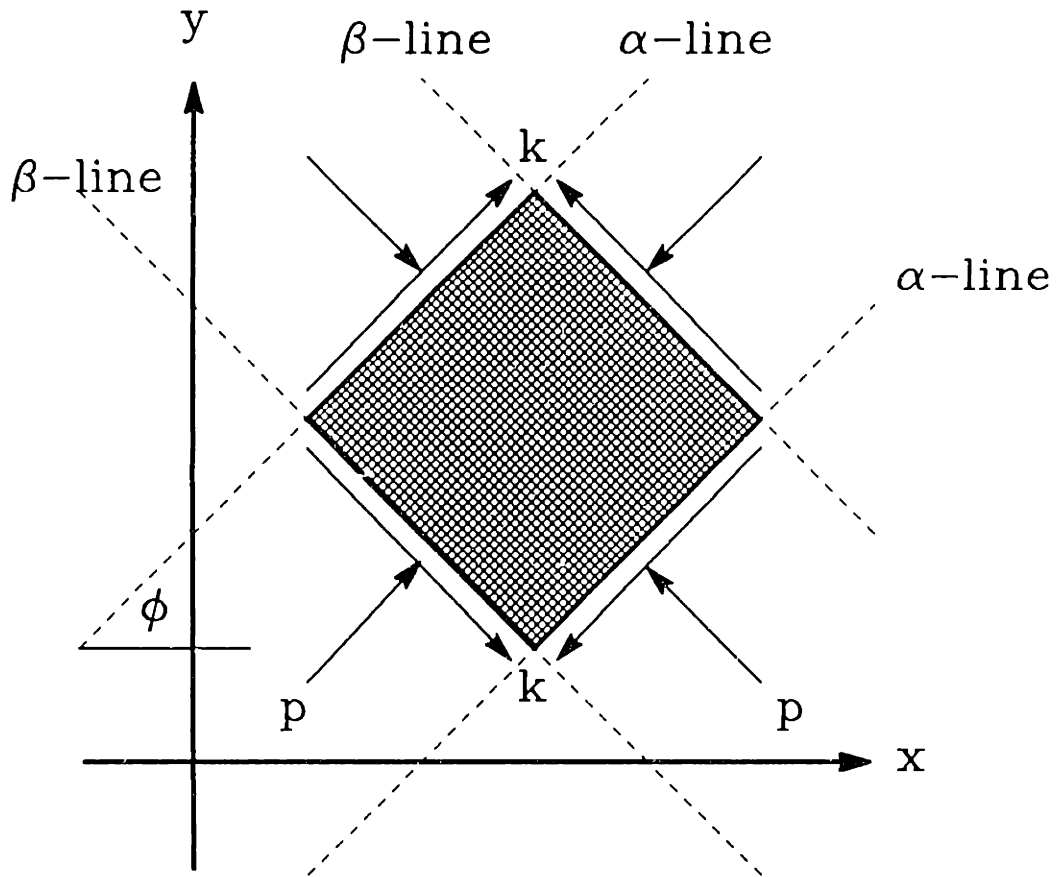


Figure 4.1 Schematic slip-line field element, showing the normal pressure (P) and shear (k) stress states, the orientation of α - and β - lines and the inclination angle ϕ with respect to the coordinates.

sector, a yielding constant state sector, and a yielding centered fan sector. (Nemat-Nasser and Obdatta showed all the admissible combinations of these sectors, but their asymptotic analysis does not determine which assemblage is appropriate for a specific problem.) An elastic sector which has not experienced any prior plastic deformation is representable by a planar elastic wedge with constant, but not necessarily identical, tractions on each of its sides. To produce finite stresses at the crack-tip and to eliminate any net crack-tip forces, the angular function associated with the singular radial stress component is taken to be zero; i.e., $\sigma_{rr}(r, \theta) = P(\theta) + Q(\theta)/r \Rightarrow Q(\theta) = 0$. Appendix B contains the Airy stress potential and stress distribution for such a wedge. The yielding sectors, formally identified by Rice and Tracey (1973), are obtained from the equilibrium equations and the yield criterion. The stress distribution in the constant state is characterized as having stress components σ_{xx} , σ_{yy} , and σ_{xy} constant everywhere in the sector such that the yield criterion is satisfied. Generally, in constant state regions $\sigma_{\theta\theta}(r, \theta) \neq \sigma_{rr}(r, \theta)$. In centered fan sectors, however, the stress distribution is $\sigma_{rr}(r, \theta) = \sigma_{\theta\theta}(r, \theta)$ and $\sigma_{r\theta} = \text{constant}$, where in the absence of the other deviatoric stress components, $\sigma_{r\theta}$ alone satisfies the yield criterion. When elastic strains are negligible compared to plastic strains or when $\nu = 0.5$, the stress distribution in a centered fan is given by $\sigma_{r\theta} = \pm k$, and $\sigma_{rr}(r, \theta) = \sigma_{\theta\theta}(r, \theta) = (A - 2\phi/\sqrt{3})\sigma_{ys}$, where A is a constant. In terms of rigid-plastic slip-line theory (Hill, 1983), a centered fan is a sector where α -lines emanate radially from the crack tip with circular and concentric β -line arcs (or vice versa), while in constant state sectors the α - and β -lines are straight and normal to each other. Thus in a fan region $\phi = \theta + b$, where b is a constant.

Rice (1982) summarizes the asymptotic distribution of velocities and strain rates for quasi-static crack growth in each of the three previously identified sectors. By setting the crack-tip velocity equal to zero, the predominant behavior of each sector is obtained for the stationary case. Excluding rigid rotations, the non-zero velocity components in a stationary centered fan are

$$V_r = \frac{\partial f(\theta, t)}{\partial \theta} \quad (4.7)$$

and

$$V_\theta = -f(\theta, t), \quad (4.8)$$

and the only non-zero strain rate component is

$$\dot{\epsilon}_{r\theta} = \frac{1}{2r} \left(\frac{\partial^2 f(\theta, t)}{\partial^2 \theta} + f(\theta, t) \right). \quad (4.9)$$

Here V_r and V_θ are the radial and hoop velocity components, respectively, t is time, and $f(\theta, t)$ is a function whose form cannot be determined from an asymptotic analysis. Integration of the strain rates over a finite period of time produces finite strain for all strain components except for the $\epsilon_{r\theta}$ component. Integration of Eq.(4.9) with respect to time yields

$$\epsilon_{r\theta}(\theta, r) = \frac{\gamma_{r\theta}(r, \theta)}{2} = \frac{1}{2} A(\theta, t) \frac{\gamma_0}{R} + C_1(\theta). \quad (4.10)$$

In this equation, $A(\theta, t)$ is defined such that $\partial A(\theta, t)/\partial t = [(\partial^2 f(\theta, t)/\partial^2 \theta) + f(\theta, t)]$ and represents the unknown angular distribution of shear strain, while γ_0 is the shear yield strain of the material, $C_1(\theta)$ is a bounded constant of integration usually taken to be equal to zero, and $R \equiv r/r_p$, where r_p is the characteristic plastic zone dimension and r is the radial distance from the crack tip. In a centered fan $\epsilon_{r\theta} \propto 1/r$ as $r \rightarrow 0$. At the plastic zone boundary, $R = 1$, the shear strain must be approximately equal to γ_0 , thus $A(\theta, t)$ is of order unity.

The non-singular yielding constant state sector behaves in a significantly different manner. It is best described in an auxiliary (m, n) coordinate system whose axes are chosen to lie parallel to the α - and β - lines and whose origin is at the crack tip. The x and y components of the (x, y) coordinate frame, shown in *Figure 4.1*, are related to the components in the $m - n$ coordinate frame by

$$x = m \cos \phi - n \sin \phi \quad (4.11)$$

and

$$y = m \sin \phi + n \cos \phi. \quad (4.12)$$

As $r \rightarrow 0$, the constant state velocity components in the m and n directions are given by

$$V_m = g(n) \quad (4.13)$$

and

$$V_n = h(m), \quad (4.14)$$

respectively. Here $g(n)$ and $h(m)$ are functions whose precise forms cannot be determined from an asymptotic analysis. In a constant state region, the only non-zero strain component as $r \rightarrow 0$ is $\dot{\epsilon}_{mn}$, and it is related to the velocity field via

$$\dot{\epsilon}_{mn} = \frac{1}{2} \left(\frac{\partial g(n)}{\partial n} + \frac{\partial h(m)}{\partial m} \right). \quad (4.15)$$

Integration of the strain rates over a discrete time interval produces finite strains for all components. Plane-strain conditions require that $\epsilon_{xx} = 0$, but for elastically compressible materials (those with $\nu \neq 0.5$) a transient period exists for which $\dot{\epsilon}_{xx}^{Plastic} \neq 0$. During this transient period finite plastic strains accumulate, and therefore in a constant state region it is generally expected that $\epsilon_{xx}^{Plastic} \neq 0$.

The strain rates in an isotropic elastic sector are obtainable from the elastic wedge potential, given in Appendix B, by interpreting the boundary tractions H , T , Q , and K as applied traction rates; *i.e.*, \dot{H} , \dot{T} , \dot{Q} , and \dot{K} . From Eqs.(B.9) to (B.11) and by use of the elasticity tensor \mathcal{L} defined in Eq.(3.17), the non-zero strain rate components for an isotropic elastic wedge are

$$\begin{aligned} \dot{\epsilon}_{rr} = & \left(\frac{1 - \nu^2}{E} \right) \left\{ \dot{K} - 2\dot{T}\gamma - 2\dot{a}_2(\cos 2\gamma + 1) - 2\dot{c}_2(\sin 2\gamma + 2\gamma) \right\} \\ & - \left(\frac{\nu(1 + \nu)}{E} \right) \left\{ \dot{K} - 2\dot{T}\gamma + 2\dot{a}_2(\cos 2\gamma - 1) + 2\dot{c}_2(\sin 2\gamma - 2\gamma) \right\}, \quad (4.16) \end{aligned}$$

$$\begin{aligned} \dot{\epsilon}_{\theta\theta} = & \left(\frac{1 - \nu^2}{E} \right) \left\{ \dot{K} - 2\dot{T}\gamma + 2\dot{a}_2(\cos 2\gamma - 1) + 2\dot{c}_2(\sin 2\gamma - 2\gamma) \right\} \\ & - \left(\frac{\nu(1 + \nu)}{E} \right) \left\{ \dot{K} - 2\dot{T}\gamma - 2\dot{a}_2(\cos 2\gamma + 1) - 2\dot{c}_2(\sin 2\gamma + 2\gamma) \right\}, \quad (4.17) \end{aligned}$$

and

$$\dot{\epsilon}_{r\theta} = \left(\frac{2(1+\nu)}{E} \right) \{2\dot{c}_2(\cos 2\gamma - 1) - 2\dot{a}_2 \sin 2\gamma\}. \quad (4.18)$$

In these expressions the coefficients \dot{a}_2 and \dot{c}_2 are given by Eqs.(B.7) and (B.8) when H , T , Q , and K are interpreted as \dot{H} , \dot{T} , \dot{Q} , and \dot{K} . Integration of the strain rates, Eqs.(4.16) to (4.18), over a finite time interval produces finite strains in elastic sectors.

Having identified the three basic admissible sectors, asymptotic crack-tip behavior is obtainable by assembling a combination of these sectors in a manner consistent with the far-field conditions. Rice (1982) states that the necessary requirements for assembling these sectors are that " $\sigma_{r\theta}$, $\sigma_{\theta\theta}$, and u_θ must be continuous along radial lines emanating from the crack tip and that any discontinuities in yielding sectors must be consistent with the flow rule." An additional constraint, given by Kachanov (1974), is that "the [energy] dissipation be positive everywhere in the slip-line field."

Before proceeding, several additional observations regarding the behavior and assemblage of the sectors should be made. In yielding regions with incompressible plasticity where the plastic strains are large compared to the elastic strains, the "apparent" Poisson's ratio is $\nu_a \approx 0.5$; i.e., $(1/3)\text{tr}(\sigma) \approx (\sigma_{rr} + \sigma_{\theta\theta})/2$. In general, fan sectors have large plastic strains as $r \rightarrow 0$ ($\epsilon_{r\theta} \propto 1/r$); therefore in a fan region the apparent Poisson's ratio is $\nu_a \approx 0.5$, and $\sigma_{r\theta} \approx \pm k$. Compressible elastic sectors in which there are no residual strains cannot be adjacent to fan sectors (when, at the border, $A(\theta, t) \neq 0$ in the fan region). If $\sigma_{r\theta}$ is equal to $\pm k$ at the elastic sector boundary, the requirement of continuous $\sigma_{\theta\theta}$ produces an Mises equivalent stress greater than the yield stress in the elastic sector. This is true even if a jump in σ_{rr} is allowed between the fan and elastic sector. In general, it is necessary to have a constant state sector between an elastic sector (with no residual strains) and a fan, and the apparent Poisson's ratio across this constant state varies from $\nu_a \neq 0.5$ on the elastic boundary, where plastic strains are negligible, to $\nu_a = 0.5$ on the fan border, where plastic strains dominate.

To verify that an elastic sector with no residual strains and $\nu \neq 0.5$ cannot exist next to a fan which has an apparent Poisson's ratio of $\nu_a \approx 0.5$, consider the following

argument. Evaluate the Mises equivalent stress in the elastic sector at the postulated elastic-fan border. At such a point $\sigma_{r,\theta}$ must be equal to $\pm k$. Substituting this value into the expression for the Mises equivalent stress, Eq.(2.31), yields

$$\bar{\sigma}^2 = (\sigma_{rr}^2 + \sigma_{\theta\theta}^2)D + (\sigma_{rr}\sigma_{\theta\theta})F + \sigma_{ys}^2, \quad (4.19)$$

where $D(\nu)$ and $F(\nu)$ are given in Eqs.(2.32) and (2.33), respectively. For $\bar{\sigma} \leq \sigma_{ys}$ (for $\sigma_{\theta\theta} \neq 0$),

$$\left(\frac{\sigma_{rr}}{\sigma_{\theta\theta}}\right)^2 + \frac{F}{D} \left(\frac{\sigma_{rr}}{\sigma_{\theta\theta}}\right) + 1 \leq 0. \quad (4.20)$$

For positive values of ν , the ratio F/D varies from -1 to -2, and the condition required by Eq.(4.20) has real solutions only when $F/D = -2$ ($\nu = 1/2$) and $\sigma_{rr} = \sigma_{\theta\theta}$.

Prior to discussing the bi-material asymptotic crack-tip fields, it is useful to examine several additional features present in the homogeneous analysis. For a stationary homogeneous plane-strain crack subjected to tensile opening loads (mode I), the crack-tip field is that of the classic Prandtl distribution (Hill, 1983). In the Prandtl field, all crack-tip material points are in either yielding constant states or centered fan regions and remain in their respective sectors during the entire loading history. Additionally, the Prandtl stress distribution is independent of the far-field load magnitude as long as SSY conditions exist, although the actual extent of the distribution is dependent on the load magnitude. In the growing quasi-static (opening) case, the crack-tip distribution remains constant with respect to the moving crack tip; however, any material point which does not lie in the plane of the advancing crack front accumulates strains in each of the four quasi-static crack-tip regions (Rice, 1982). Therefore, it is necessary to account for these accumulated residual strains when assembling the crack-tip fields from an instantaneous stress distribution. In general the instantaneous stress distribution of a plane-strain elastic sector with fixed tractions is different for regions which do or do not have out-of-plane residual strains. (In plane strain the out-of-plane stress must account for any residual out-of-plane strains.)

It is anticipated that the major difference between the homogeneous and traction-free bi-material crack-tip fields will result from the continuous shift, in plastic zone

shape and tractions along the plastic zone boundary, which arises with increasing load. The shift between solutions should occur in a continuous fashion with respect to ζ_0 , in a manner analogous to the continuous shift observed in homogeneous crack-tip fields by Shih (1974) for mixed-mode loading between pure mode I and mode II. A continuous evolution with increasing applied load has the potential to alter residual strains and thereby significantly influence stresses in elastic sectors. Also, such continuous evolution may produce oscillatory plastic bi-material crack-tip fields, as observed by Shih and Asaro (1987) for nonlinear elastic strain hardening bi-material interfacial cracks.

Thus far, discussion has been limited to asymptotic forms which are typically interpreted as occurring “at” the crack tip. This interpretation is only a first order approximation and does not address the possibility that away from the crack tip a cusp may form between different sectors. Although such cusps are not found in stationary homogeneous crack solutions, recent work by Narasimhan, Rosakis, and Hall (1987) indicates that a cusp forms ahead of a growing plane-stress homogeneous crack tip, and that the boundary of the cusp separates the regions in which the equations of stress are hyperbolic and elliptic, respectively.

4.2 Traction-Free Crack-Tip Model

The numerical results for the traction-free crack-tip model will be presented in this section, and in conjunction with the previously identified asymptotic forms, approximate local crack-tip fields will be assembled. Discussion will be initially focused on the “high resolution,” quarter wave-length model so that the transitional period of plastic flow can be quantified from the elastic-plastic boundary towards the crack-tip to the establishment of a “steady-state,” and so that the extent of oscillatory behavior, if any, can be identified. Interfacial tractions and strain distributions will be tracked as a function of ζ_0 , as well as the finite crack tip opening displacement, δ_{CTOD} . A general elastic potential which describes the lower elastic domain will be identified, although not directly from the quarter wave-length model. All results will be analyzed at an

instantaneously fixed value of ζ_0 . In general, steady state and transitional behavior shall refer to spatial and not chronological (analysis or loading time) behavior.

4.2.1 Deformable Upper Half-Plane

Asymptotic Crack-Tip Behavior

The behavior within the deforming bi-material crack-tip zone is similar to that found in homogeneous crack-tip plastic zones. *Figures 4.2 to 4.6* show the location of yielding integration points ($\bar{\sigma} \geq 0.99\sigma_{ys}$), as a function of angle θ from the interface and normalized radial distance $R \equiv r/r_p$ from the crack tip, at several values of ζ_0 between 1.34° and 30.04° for $\epsilon = 0.07796$ and $\nu = 0.342$. In these figures, the location of integration points whose stress state is that of a fan sector, namely $|\sigma_{r\theta}| \geq 0.99k$ and $|(\sigma_{\theta\theta} - \sigma_{rr})/\sigma_{ys}| < 0.02$, are identified by + marks. The fan region dominates the yielding crack-tip fields at small values of R , and *once a fan has developed, the stresses along a ray are independent of radial distance*. Radially as $R \rightarrow 0$, oscillatory stress fields do not exist after a fan sector develops. As is common in the homogeneous fields, a transitional layer exists between the plastic zone boundary and the steady-state fan region. *Figure 4.7* shows the development of stress as a function of R at $\theta = 3.1^\circ$ from the elastic region ($R > 1$) to deep within the plastic zone ($R \ll 1$) for $\zeta_0 = 30.04^\circ$. As seen from *Figures 4.2 to 4.6* and *4.7*, the establishment of a fan usually occurs only deep within the plastic zone at radial distances smaller than approximately 1% to 5% of the *actual plastic zone radius at that angular location*. The behavior of the inelastic transition region between the plastic zone boundary and the establishment of fans or “steady-state” constant state sectors is similar to that of a constant state region, however in such transition regions the associated α - and β - lines have a large but finite radius of curvature. Henceforth, regions where the curvature of α - and β -lines is very small with respect to unity shall be identified as “quasi-constant state regions.”

All features seen in the bi-material fields are not present in the homogeneous asymptotic fields. A large elastic sector exists from the crack face ($\theta = 180^\circ$) to $\theta \approx 135^\circ$ for

Bi-material Crack Tip

Plastic Zone $\epsilon=0.07796$

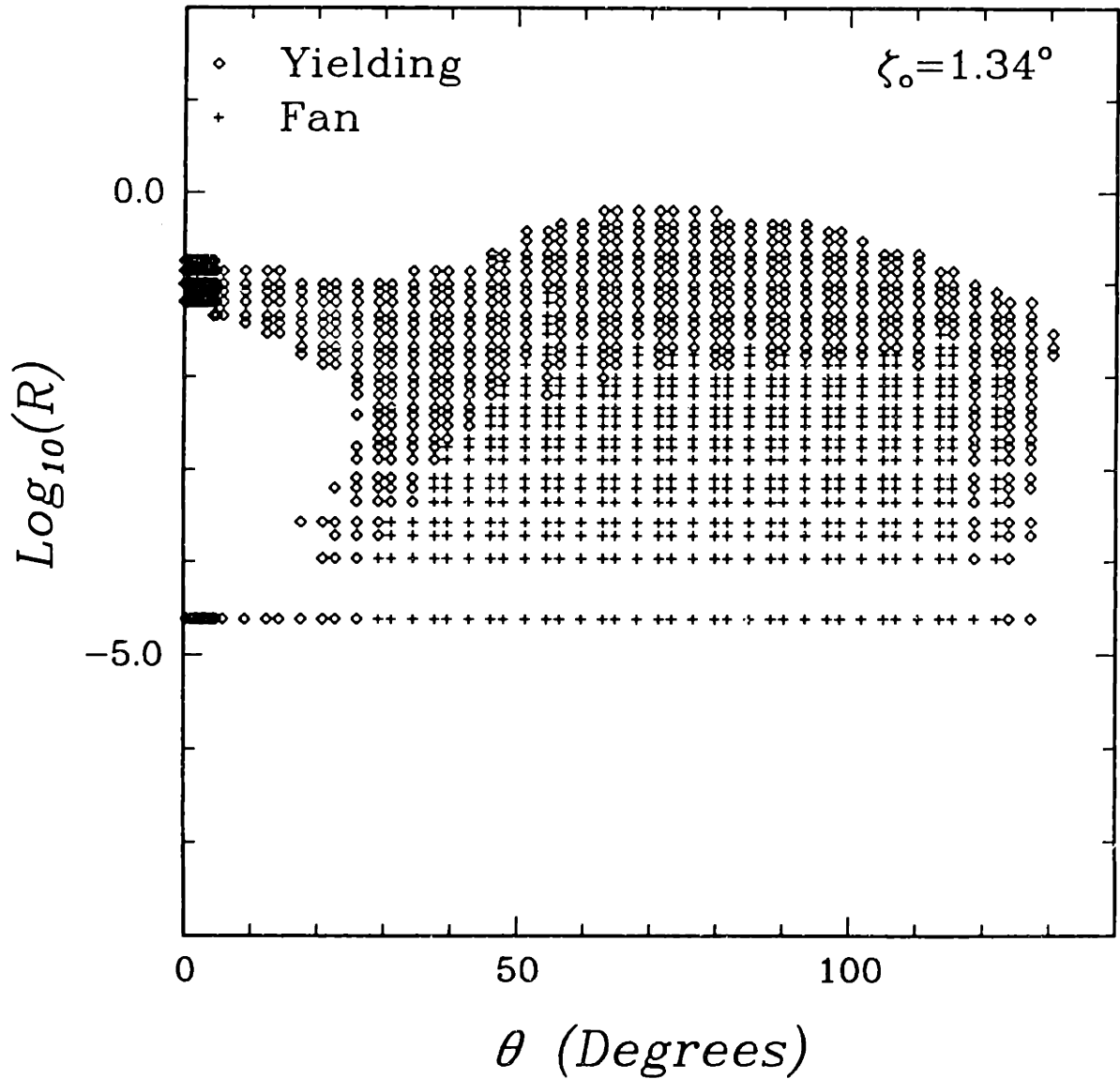


Figure 4.2 Locations of actively yielding ($\bar{\sigma} > 0.99\sigma_{ys}$) integration points around a traction-free bi-material crack-tip for $\epsilon = 0.07796$ and $\zeta_0 = 1.34^\circ$; elastic/perfectly-plastic material bonded to a rigid substrate. Locations indicative of a fan stress state ($|\sigma_{r\theta}| \geq 0.99k$ and $|(\sigma_{\theta\theta} - \sigma_{rr})/\sigma_{ys}| < 0.02$) are shown by a “+”.

Bi-material Crack Tip Plastic Zone $\epsilon=0.07796$

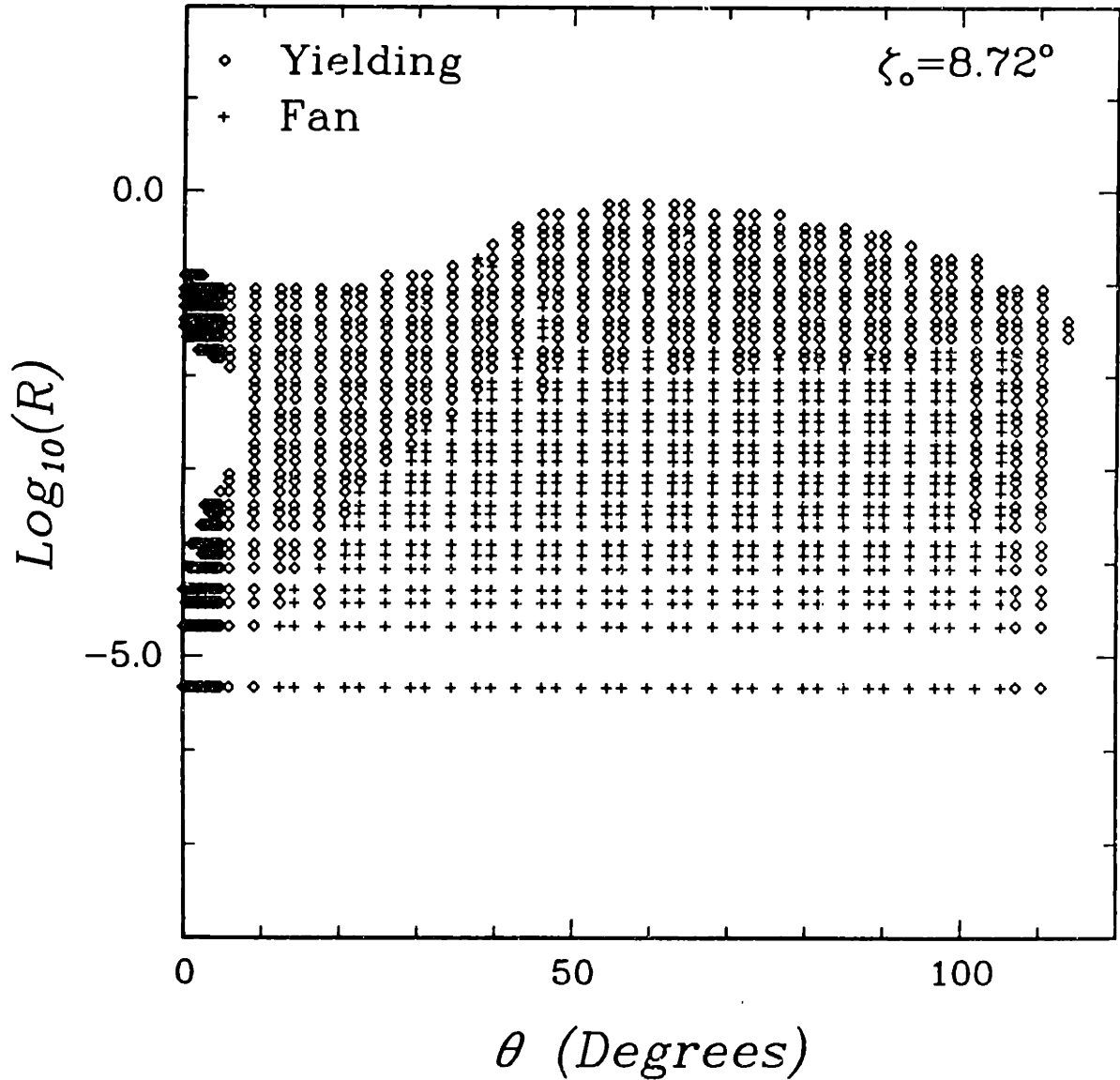


Figure 4.9 Locations of actively yielding ($\bar{\sigma} > 0.99\sigma_{ys}$) integration points around a traction-free bi-material crack-tip for $\epsilon = 0.07796$ and $\zeta_0 = 8.72^\circ$; elastic/perfectly-plastic material bonded to a rigid substrate. Locations indicative of a fan stress state ($|\sigma_{r\theta}| \geq 0.99k$ and $|(\sigma_{\theta\theta} - \sigma_{rr})/\sigma_{ys}| < 0.02$) are shown by a “+”.

Bi-material Crack Tip Plastic Zone $\epsilon=0.07796$

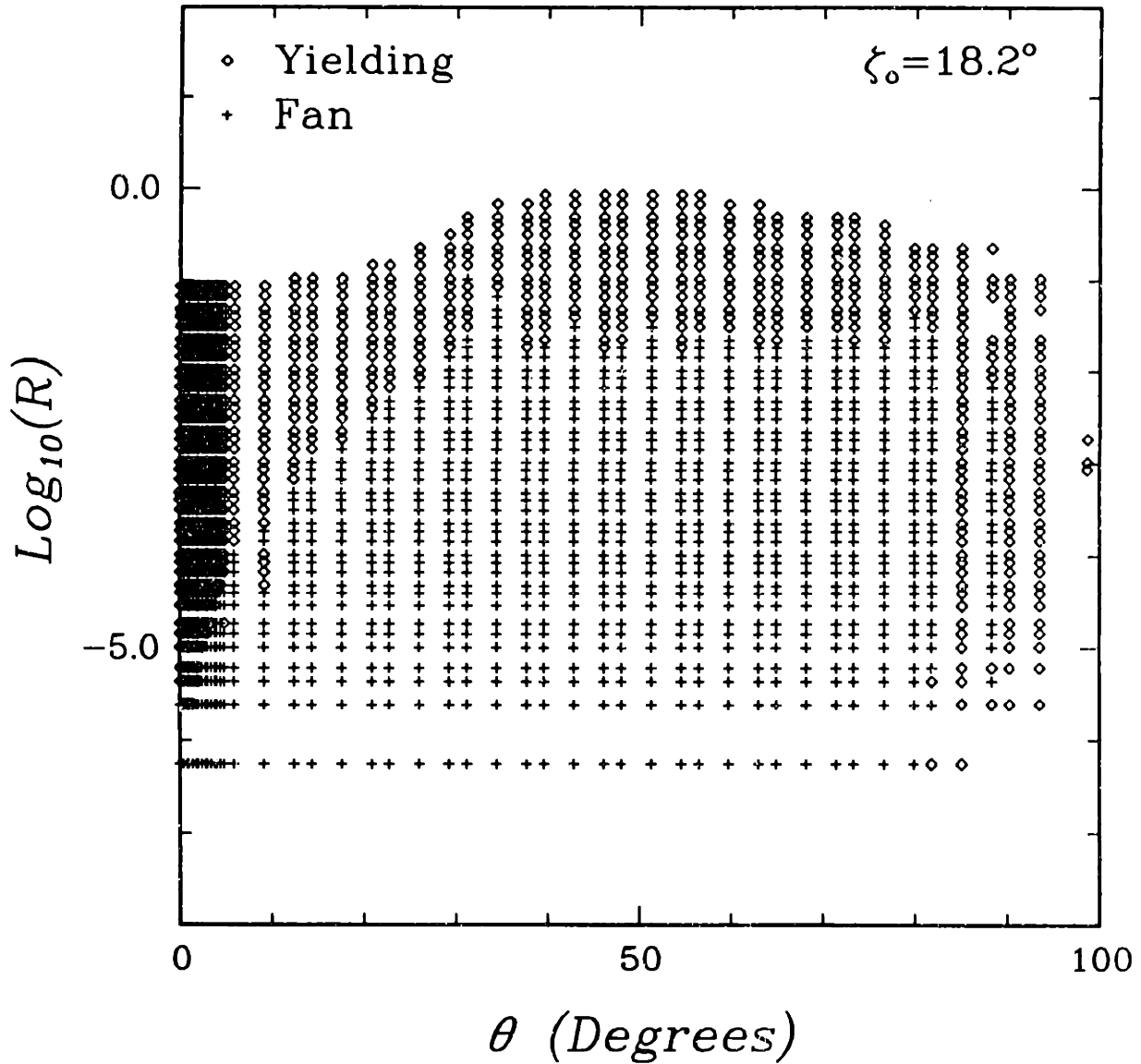


Figure 4.4 Locations of actively yielding ($\bar{\sigma} > 0.99\sigma_{ys}$) integration points around a traction-free bi-material crack-tip for $\epsilon = 0.07796$ and $\zeta_0 = 18.2^\circ$; elastic/perfectly-plastic material bonded to a rigid substrate. Locations indicative of a fan stress state ($|\sigma_{r\theta}| \geq 0.99k$ and $|(\sigma_{\theta\theta} - \sigma_{rr})/\sigma_{ys}| < 0.02$) are shown by a “+”.

Bi-material Crack Tip

Plastic Zone $\epsilon=0.07796$

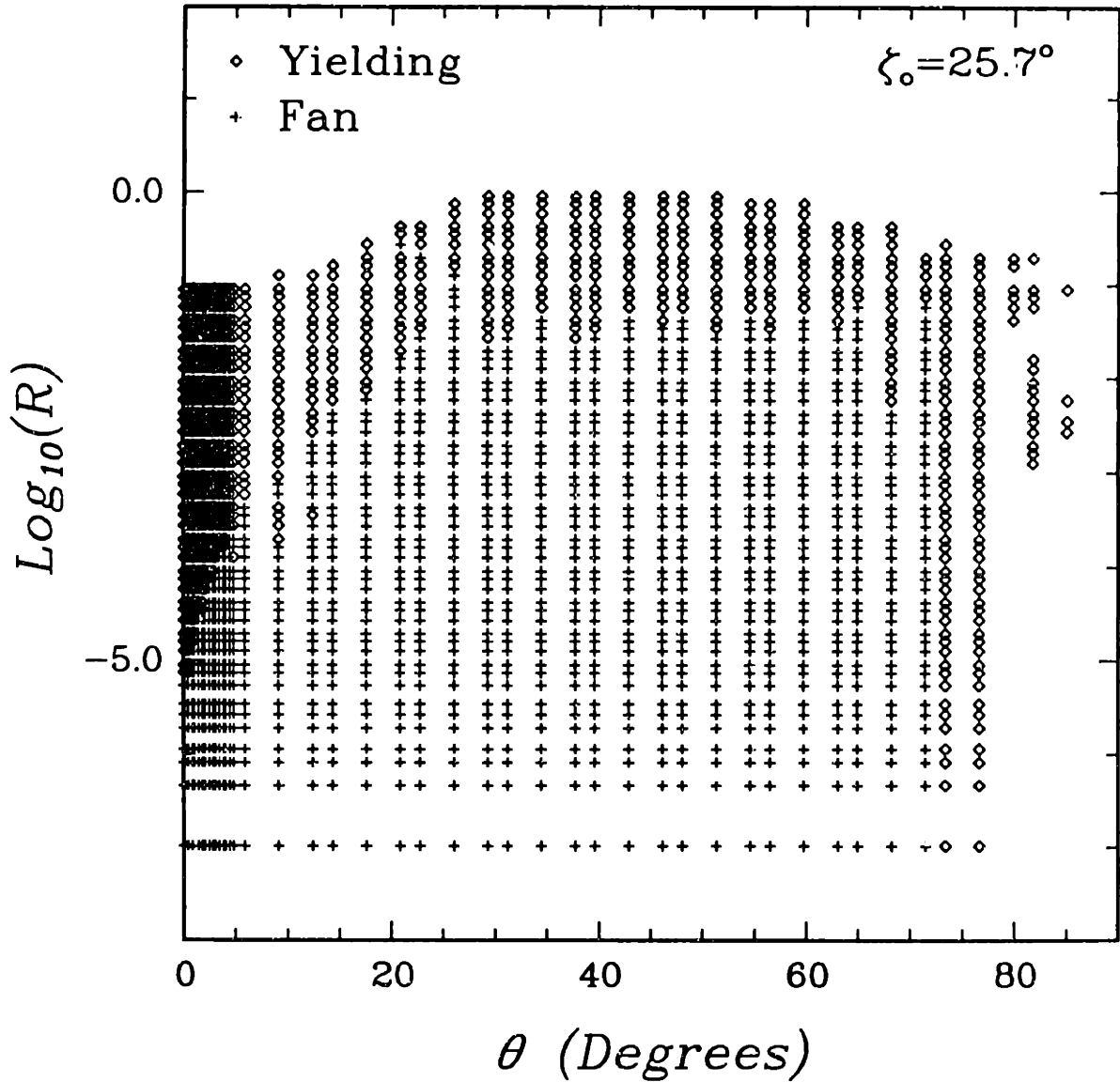


Figure 4.5 Locations of actively yielding ($\bar{\sigma} > 0.99\sigma_{ys}$) integration points around a traction-free bi-material crack-tip for $\epsilon = 0.07796$ and $\zeta_0 = 25.7^\circ$; elastic/perfectly-plastic material bonded to a rigid substrate. Locations indicative of a fan stress state ($|\sigma_{r\theta}| \geq 0.99k$ and $|(\sigma_{\theta\theta} - \sigma_{rr})/\sigma_{ys}| < 0.02$) are shown by a “+”.

Bi-material Crack Tip

Plastic Zone $\epsilon=0.07796$

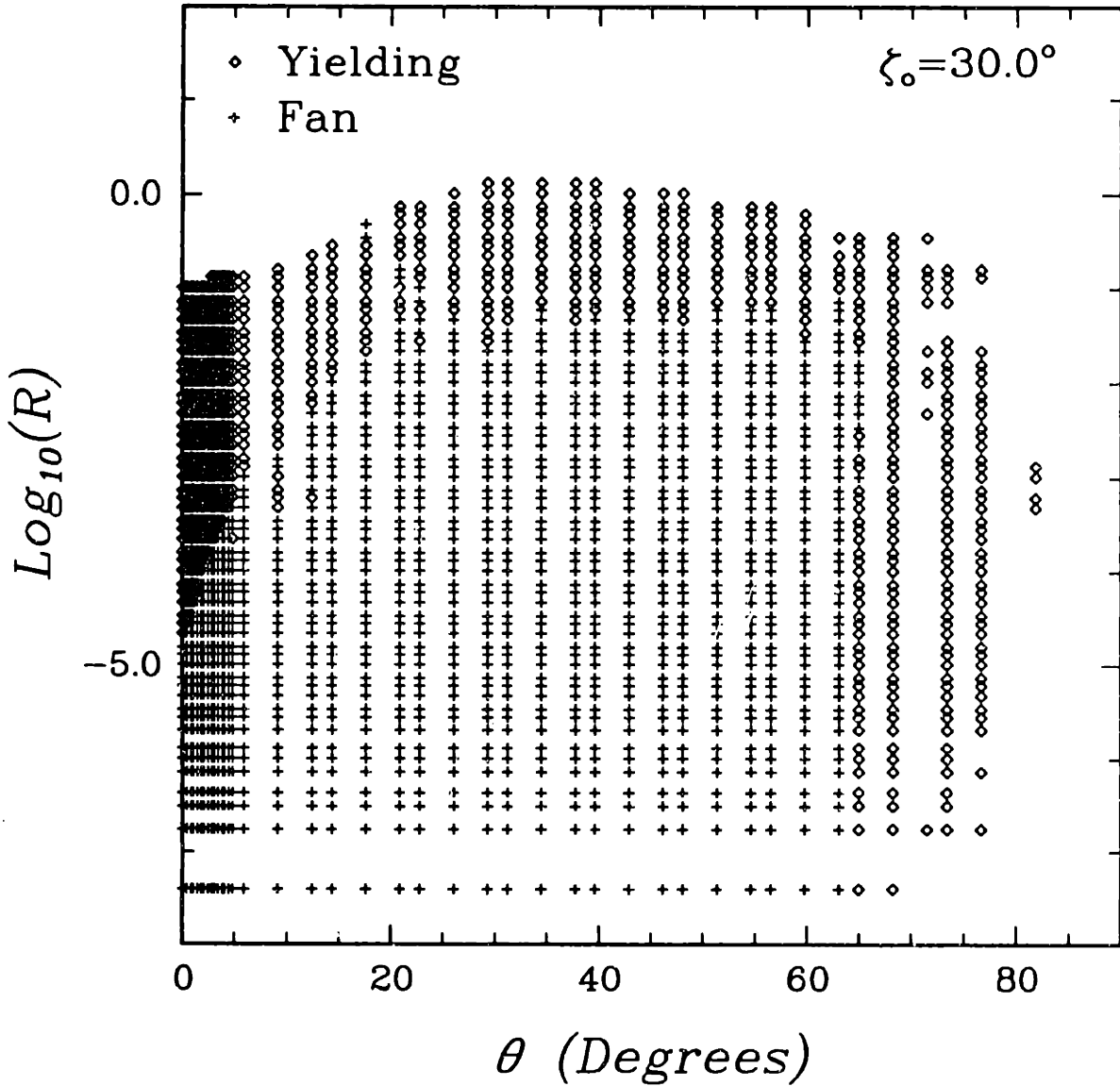


Figure 4.6 Locations of actively yielding ($\bar{\sigma} > 0.99\sigma_{ys}$) integration points around a traction-free bi-material crack-tip for $\epsilon = 0.07796$ and $\zeta_0 = 30.0^\circ$; elastic/perfectly-plastic material bonded to a rigid substrate. Locations indicative of a fan stress state ($|\sigma_{r\theta}| \geq 0.99k$ and $|(\sigma_{\theta\theta} - \sigma_{rr})/\sigma_{ys}| < 0.02$) are shown by a “+”.

Bi-material Crack-Tip Stresses

$\zeta_0 = 30.0^\circ$ $\epsilon = 0.07796$

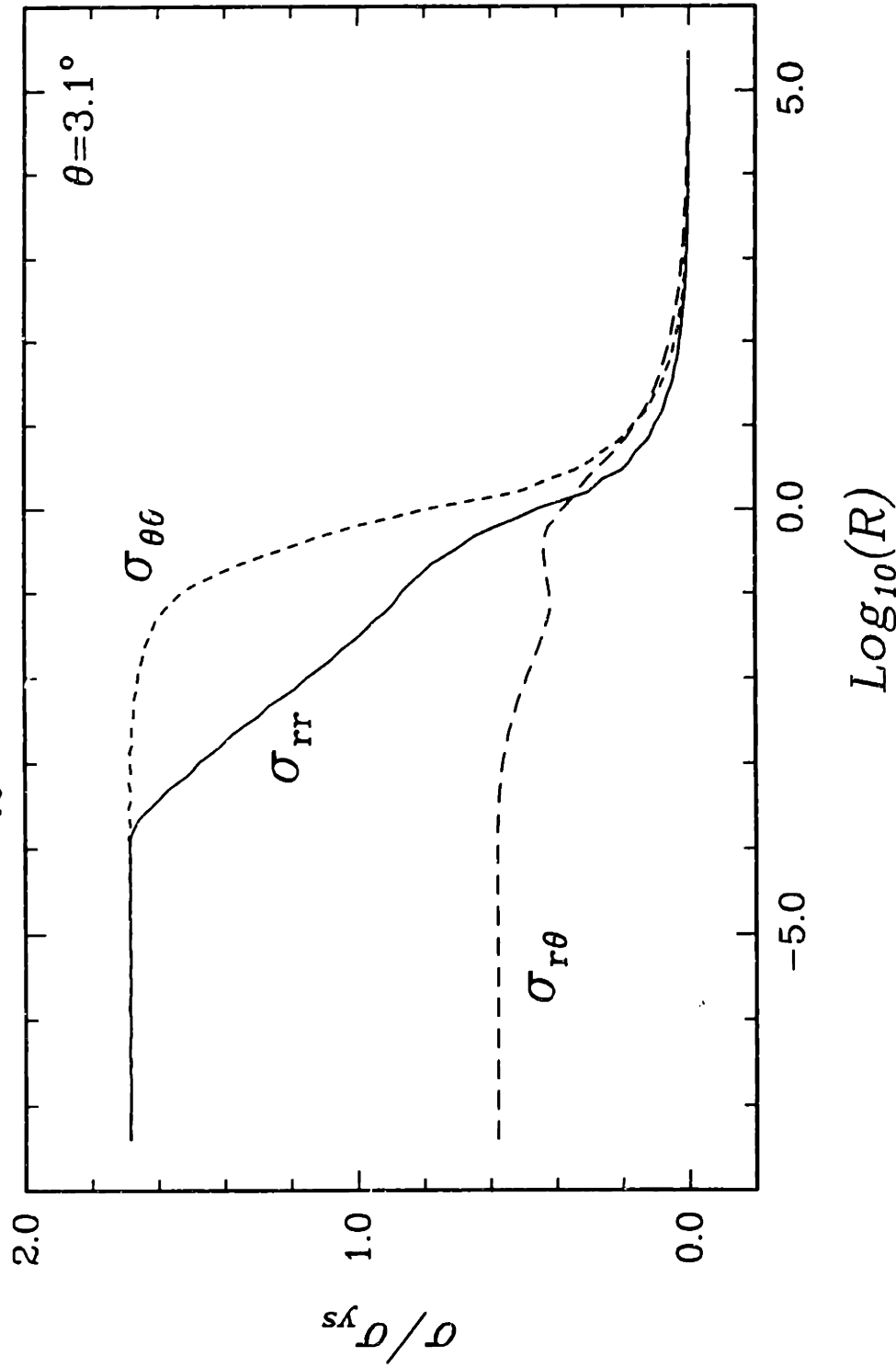


Figure 4.7 Radial variation of normalized stress components for a traction-free bi-material crack-tip (elastic/perfectly-plastic material atop a rigid substrate) under SSY conditions at $\theta = 3.1^\circ$; $\epsilon = 0.07796$ and $\zeta_0 = 30.0^\circ$.

$\zeta_0 = 1.34^\circ$ and to $\theta \approx 73^\circ$ for $\zeta_0 = 30.0^\circ$. Such elastic sectors are not observed in stationary homogeneous crack fields nor are they predicted from the elastically-calculated plastic zone boundary derived in Section 2.2.1. The location of actively yielding integration points and the corresponding elastically-calculated plastic zone shape [from Eq.(P2.6)] for $\epsilon = 0.07796$ ($\nu = 0.342$) at $\zeta_0 = 1.34^\circ$ and $\zeta_0 = 30.0^\circ$ are plotted in *Figures 4.8* and *4.9*, respectively. (Due to the presence of the crack-face elastic sector, the plastic zone shape predicted by the elastic approximation when $\zeta_0 \geq 0$ is less representative of the actual zone shape, especially near the crack-face region.) Recall that for $\epsilon > 0$, ζ_0 increases at fixed $\angle \mathbf{K}$ when $\|\mathbf{K}\|$ increases. At material points in the crack-face elastic sector which are very near the crack tip, prior plastic deformation would produce residual strains. At radial distances far from the crack tip relative to the characteristic plastic zone size, no residual plastic strains accumulate in the crack-face elastic wedge. Furthermore, an unloaded elastic sector exists along the interface spanning a maximum of about 22° for $\zeta_0 = 1.34^\circ$ and approximately 8° for $\zeta_0 = 8.72^\circ$. The interfacial elastic sector is small and barely visible in *Figure 4.8*, but is more easily seen in *Figures 4.2* and *4.9*. (Again, this feature is not predicted by the elastically-calculated plastic zone; however, for $\zeta_0 \approx 0$, the approximated plastic zone does have a local minimum or rounded “kink” in its shape near $\theta \approx 30^\circ$, and this rounded kink may be related to the development of the interfacial elastic wedge.) Active plasticity exists both radially ahead and behind this elastic sector, indicating that the material points within this elastic region once reached yield, deformed plastically, unloaded to an elastic state, and will again yield and deform plastically.

The presence of a cusp in the crack-tip field is another feature of the bi-material fields which is not observed in the stationary homogeneous asymptotic fields. At small to modest angles from the interface, the length of the transition region from the elastic-plastic boundary to the fan region increases with decreasing θ , producing a cusp in the slip-line field. The cusp itself is not a characteristic slip-line, but merely a boundary line separating two regions. The characteristic α - and β - lines appear continuous and

Bi-material Plastic Zone

$$\zeta_0 = 1.34^\circ \quad \epsilon = 0.07796$$

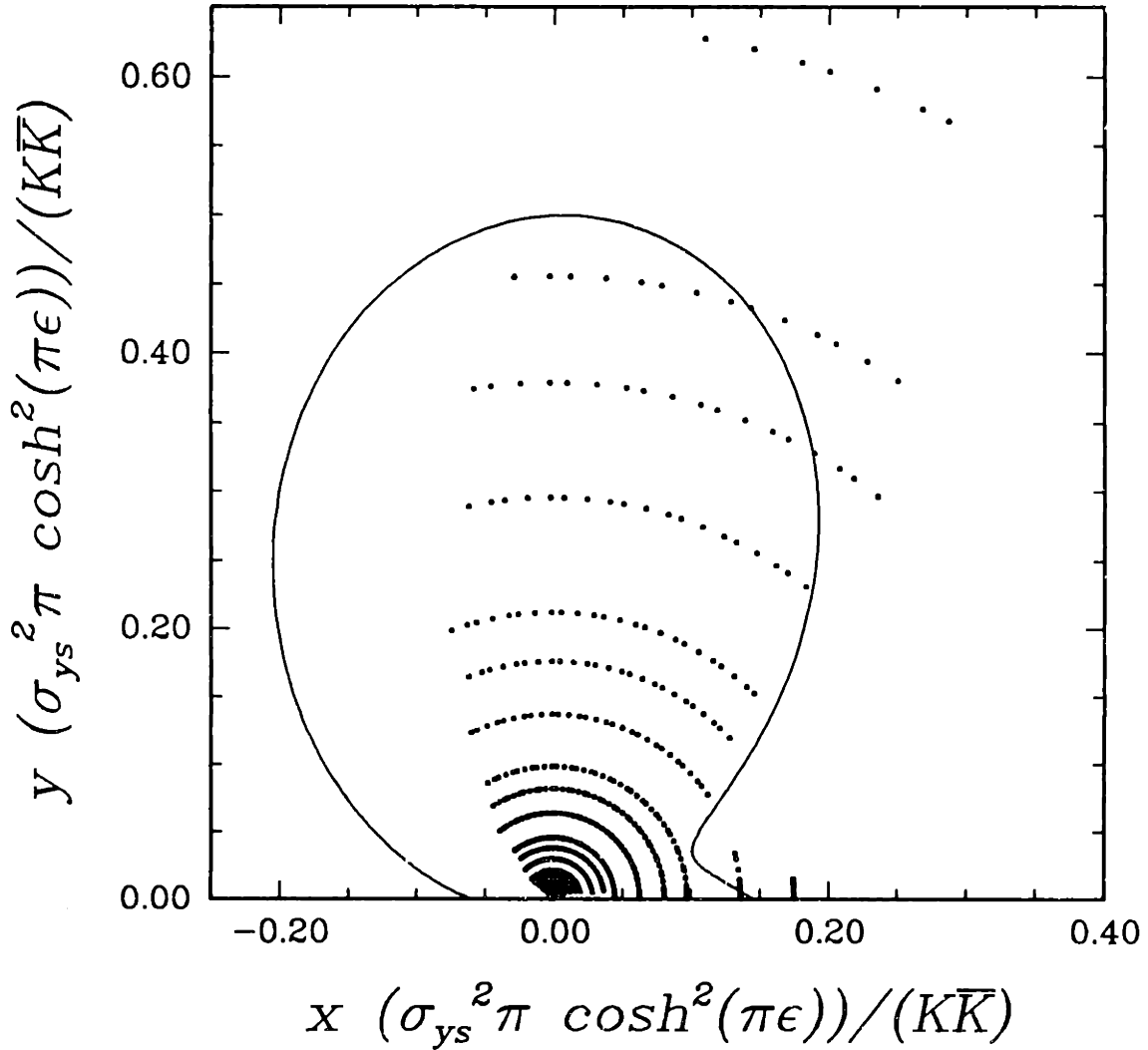


Figure 4.8 Approximate plastic zone, along with the location of actively yielding integration points, from a finite element calculation of traction-free SSY in an elastic/perfectly-plastic material atop a rigid substrate; $\epsilon = 0.07796$ and $\zeta_0 = 1.34^\circ$.

Bi-material Plastic Zone

$\zeta_0 = 30.0^\circ$ $\epsilon = 0.07796$

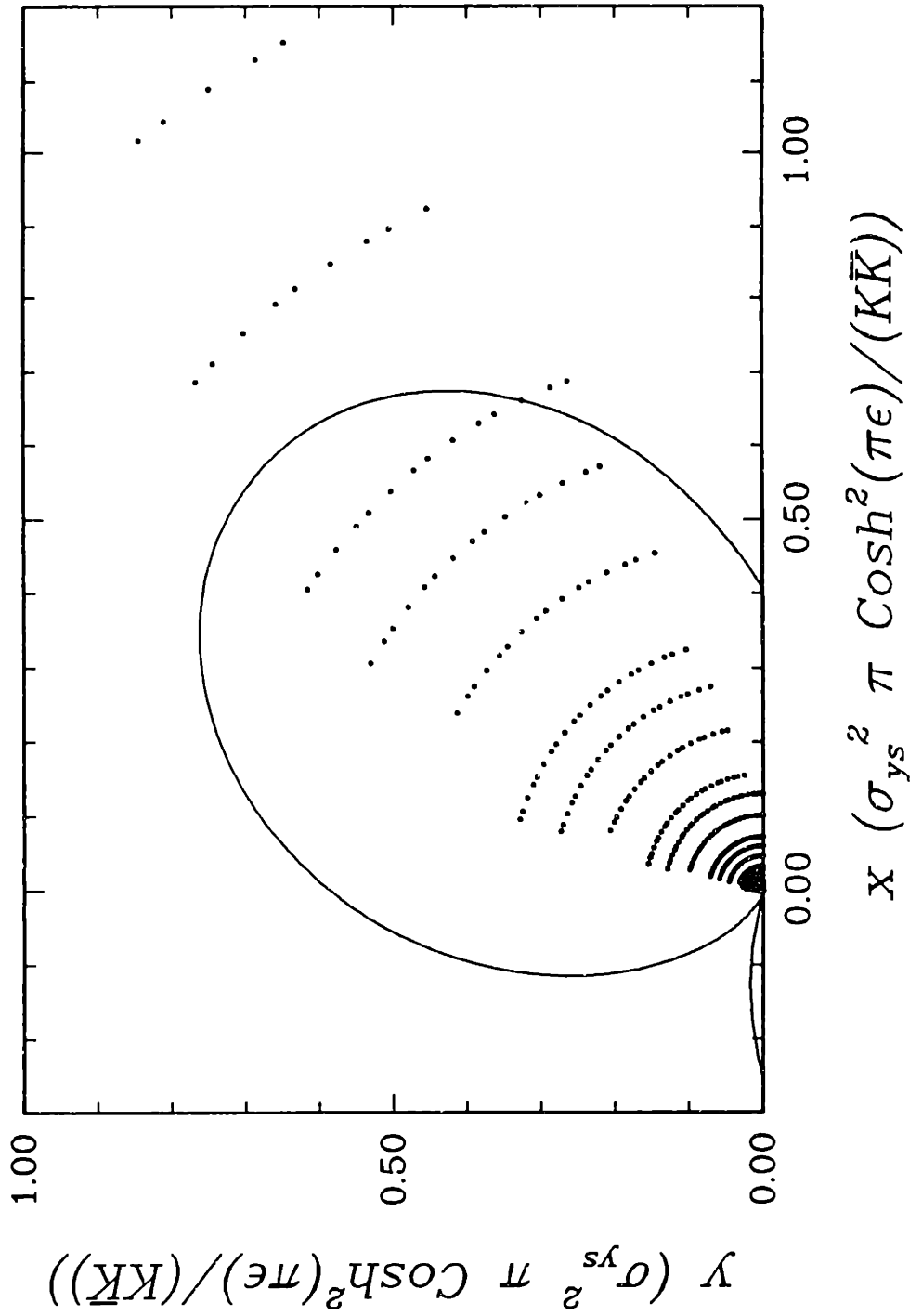


Figure 4.9 Approximate plastic zone, along with the location of actively yielding integration points, from a finite element calculation of traction-free SSY in an elastic/perfectly-plastic material atop a rigid substrate; $\epsilon = 0.07796$ and $\zeta_0 = 30.0^\circ$.

smooth across the cusp. The behavior of the material between the interface and the fan sector; *i.e.*, the material between the cusp and interface, behaves as a quasi-constant state region or, for values of ζ_0 between 1.34° and about 11° , as an unloaded elastic sector. (The value of 11° is obtained by linearly extrapolating the maximum angular extent of the elastic sector as a function of ζ_0 from data at $\zeta_0 = 1.34^\circ$ and $\zeta_0 = 8.72^\circ$.)

Even with a cusp present, the local angular stress distribution at a given value of R is reconstructed by properly assembling the three asymptotic forms identified in Section 4.1.2. *Figure 4.10* shows a schematic crack-tip field for a traction-free crack-tip. The crack-tip distribution deep within the plastic zone is determined by the values of the slip-line angles ξ , γ , η , α , and ξ_1 as a function of R . From *Figures 4.2* to *4.6*, it appears that the slip-line angles ξ and γ are independent of R for $R \ll 1$, but due to the presence of the cusp, the slip-line angles α , η , and ξ_1 are dependent upon R . In the limit as $R \rightarrow 0$, it appears that $\alpha = 0$, suggesting from a purely mathematical point of view, the asymptotic crack-tip fields should be constructed with $\alpha = 0$.

At this point, a definition of “asymptotic SSY bi-material crack-tip field” is necessary. In homogeneous fracture mechanics, the asymptotic fields are those which emerge as r tends toward zero, with the restriction that r remains large as compared to the CTOD. [This restriction on r is necessary because at radial distances smaller than several times the CTOD, the asymptotic field around the now blunted “circular” crack-tip is that of the logarithmic spiral (Rice, 1968b; Kachanov, 1974).] Furthermore, it is implicitly understood that such asymptotic fields are only valid in regions where their fundamental assumptions of linear kinematics and a mathematically sharp crack tip are not violated. It will be shown in Section 5.1 that use of linear kinematics is only valid in fan sectors for radial distances $R > \gamma_0$, where γ_0 , the initial shear yield strain, typically ranges from 10^{-4} to 10^{-2} for polycrystalline metals. For values of R smaller than γ_0 , the resulting strains are no longer small; *i.e.*, less than unity. *Henceforth, asymptotic SSY bi-material crack-tip fields shall be defined as those which emerge as $R \rightarrow \gamma_0$.*

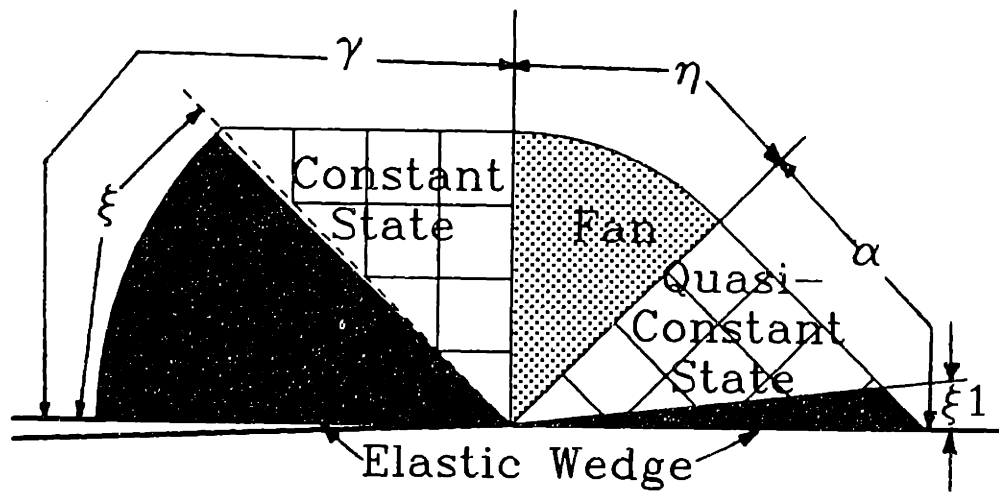


Figure 4.10 Slip-line field at a traction-free interfacial crack for an elastic/perfectly-plastic upper region bonded to a rigid (or elastic) substrate. See *Table 4.1* and *4.5* for numerical values of indicated angles.

Assemblage of Crack-Tip Fields

The asymptotic crack-tip fields are assembled from the numerical results in the following manner. The elastic wedge coefficients a_2 and c_2 along the crack face are obtained by matching the analytical elastic wedge expressions for stress and pressure with the numerical results over the range of θ where no prior inelastic deformation has occurred. With these coefficients, the elastically predicted location where $\bar{\sigma} = \sigma_{\nu\theta}$ is identified, and the corresponding angle is taken to be ξ . The stress state at ξ in the elastic and constant state sectors are assumed to be equal, and from the elastically predicted stress state at ξ , a Mohr's circle calculation is performed to estimate the rotation in the constant state region necessary to achieve a state of pure shear ($\sigma_{rr} = \sigma_{\theta\theta}$). This rotation angle is interpreted as $\gamma - \xi$. In making this estimate, it is assumed that σ_{rr} is continuous from the elastic-wedge/constant-state border through the entire constant state sector, up to the constant-state/fan border. To determine the angle η , the pressure distributions in the fan and the adjacent constant state sectors are fit to linear expressions (with respect to θ), and their extrapolated intersection defines the angle η . This approach circumvents problems associated with a lack of mesh refinement and numerical noise at boundaries between constant state and fan sectors. The angle α is then back calculated as $\alpha = \pi - \gamma - \eta$, and is compared to the angular location of the last node or integration point whose stress state is indicative of a centered fan.

In assembling the assumed asymptotic fields, the stress distribution in the unloaded elastic sector is obtained by projecting the stress distribution from the "virgin" elastic sector. Although such an extrapolation is not strictly acceptable since it does not account for the residual $\epsilon_{zz}^{Plastic}$ strain, modest agreement between the numerical and elasticity solutions does exist for the $\sigma_{r\theta}$ and $\sigma_{\theta\theta}$ components. This extrapolation is done for several reasons. For the smaller values of ζ_0 , it is not clear that the initial (numerical) transient period accumulates the same amount of strain as it would have had the analysis been initially started from a smaller value of ζ_0 . Second, if ζ_0 uniquely defines the assemblage of the asymptotic crack-tip fields independently of ν and ϵ , then

these results are directly applicable for negative values of ϵ . (For $\epsilon < 0$, ζ_0 decreases as $\|\mathbf{K}\|$ increases, and no prior plastic deformation would occur in the elastic sector.)

Interfacial Traction and Crack-Tip Fields

Due to the elastic/perfectly-plastic constitutive assumption, the interfacial tractions are bounded and are constant as $R \rightarrow 0$. The maximum magnitude of the shear traction, t_s , is $|t_s| = k$, and for a fully plastic crack tip the maximum value of the normal traction, t_n , is $t_n = 3.298\sigma_{ys}$. The development of the asymptotic interfacial tractions is identical to that of the asymptotic crack-tip fields. At normalized radial distances several times greater than $R = 1$, the elastic interfacial tractions are recovered, and the asymptotic interfacial tractions are fully established at radial distances less than 2% to 10% of the actual plastic zone radius along the interface. The interfacial tractions appear to reach their steady state values slightly faster than the crack-tip fields, except when a cusp or an interfacial elastic sector is present. The stress state shown in *Figure 4.7* is indicative of the transient period necessary to establish asymptotic interfacial tractions when a cusp is present.

The assembled asymptotic crack-tip fields for six values of ζ_0 ranging from 1.34° to 30.04° are summarized for $R = \gamma_0$ in the *Table 4.1*. Included in the table are the far-field values of the J -Integral, the numerical values of the slip-line angles α , η , γ , ξ , and ξ_1 , the elasticity potential coefficients a_2 and c_2 for the interfacial elastic sectors denoted by the angle ξ , and the normalized hoop [$H \equiv \sigma_{\theta\theta}(\theta = \pi - \xi)/\sigma_{ys}$] and shear stress [$K \equiv \sigma_{r\theta}(\theta = \pi - \xi)/\sigma_{ys}$] components at $\theta = \xi_1$. The first value of η corresponds to the value obtained by the previously described procedure, and the value of η in parentheses represents the value based solely upon the last node or integration point whose stress state is that of a centered fan. Also included in the table are the normalized interfacial traction coefficients P and S which are related to the interfacial shear, t_s , and normal, t_n , tractions by

$$t_n(R = \gamma_0) \equiv P\sigma_{ys} \quad (4.21)$$

and

$$t_s(R = \gamma_0) \equiv S\sigma_{ys}. \quad (4.22)$$

From *Table 4.1*, the schematic bi-material crack-tip configuration shown in *Figure 4.10*, and the elasticity potential given in Appendix B, the stress distribution in the deformable upper half-plane is completely described.

ζ_0	J MPa m	α	η	γ	ξ	ξ_1
1.34°	1.12×10^{-5}	40°	90° (82°)	50°	45°	23°
8.72°	5.83×10^{-5}	26°	88° (79°)	66°	61°	6°
18.2°	4.49×10^{-4}	14°	68° (74°)	98°	92°	0°
25.7°	2.63×10^{-3}	13°	58° (59°)	109°	79°	0°
30.0°	6.90×10^{-3}	6°	64° (57°)	110°	87°	0°
ζ_0	a_2	c_2	P	S	H	K
1.34°	-0.234	-0.0348	2.89	0.103	2.71	0.448
8.72°	-0.104	-0.113	2.86	0.298	2.77	0.372
18.2°	0.063	-0.136	2.41	0.462	—	—
25.7°	0.157	-0.133	1.99	0.524	—	—
30.0°	0.185	-0.115	1.74	0.546	—	—

Table 4.1 Crack-tip slip-line angles, crack-face elastic wedge and interfacial traction coefficients, and the stress state at the interfacial elastic-wedge/constant state boundary; $R = \gamma_0$, $\epsilon = 0.07796$, and $\nu = 0.342$.

Comparison

The accuracy of the slip-line angles identified in the manner discussed previously is very good when no elastic sectors are nearby, however, the accuracy is significantly reduced when elastic sectors are present. The transition from an elastic sector to a fan sector usually spans only 2 to 4 elements (each element covers approximately 8°) and seldom occurs at an element boundary. Sector boundaries which occur within an element are poorly resolved because the deviatoric and hydrostatic stress states within an element are only bi-quadratically and bi-linearly represented, respectively. Consequently, accurate data from constant state sectors needed to precisely determine the elastic/constant-state/fan boundaries is not available.

The numerical and analytically inferred stress states are compared for $\zeta_0 = 30.0^\circ$ at $R = \gamma_0$ ($\epsilon = 0.07796$) and are plotted in *Figure 4.11*. Substantially away from the fan/elastic-wedge transition, little discrepancy exists between the inferred analytical solution, represented by solid lines, and the FE calculations, whose values at integration points are plotted with symbols. Near the constant-state elastic-wedge transition, accumulated residual strains influence the stress state, especially the σ_{rr} component, and the inferred stress state is not continuous at the actual boundary. In the construction of this figure, rigid-plastic slip-line theory is used in the plastically deforming regions, and the pressure distribution is arrived at by matching a point within the fan region. The constant-state elastic-wedge transition shown in the figure is not accurate because it fails to reflect the elastically compressible material behavior in the constant state region and the effect of residual strains in the elastic sector. Also, the stress states in elastic and plastic regions are reached from different conditions, and therefore continuity of stress is not guaranteed. Furthermore the apparent “almost continuous” stress state at $\theta = \pi - \gamma$ results from the technique used to approximate γ . Overall, the asymptotic crack-tip fields reproduce the stress distribution accurately near a fan/elastic-wedge transition, with the exception of the σ_{rr} component

Asymptotic Strain Distribution and CTOD

At plastically deforming crack tips, knowledge of the stress distribution is not sufficient to completely characterize the crack-tip regions because the strain distribution is not uniquely defined from the stress distribution. Unfortunately, convenient asymptotic forms to describe the strain distribution do not exist as they do to describe the stress distribution. Due to the asymptotic nature of deformation in a centered fan sector (*i.e.*, $\dot{\gamma}_{r\theta}$ is the only non-zero strain rate component) $|\dot{\gamma}_{r\theta}|$ is generally large compared to all other strain components. In constant state regions, large strains are not anticipated since they must occur uniformly throughout the region or along crack-tip rays where $\sigma_{r\theta} = \pm k$ (Rice and Tracey, 1973), and, in general, strains in constant state regions are

Bi-material Crack-Tip Stresses

$\zeta_0 = 30.0^\circ$ $\epsilon = 0.07796$ $R = \gamma_0$

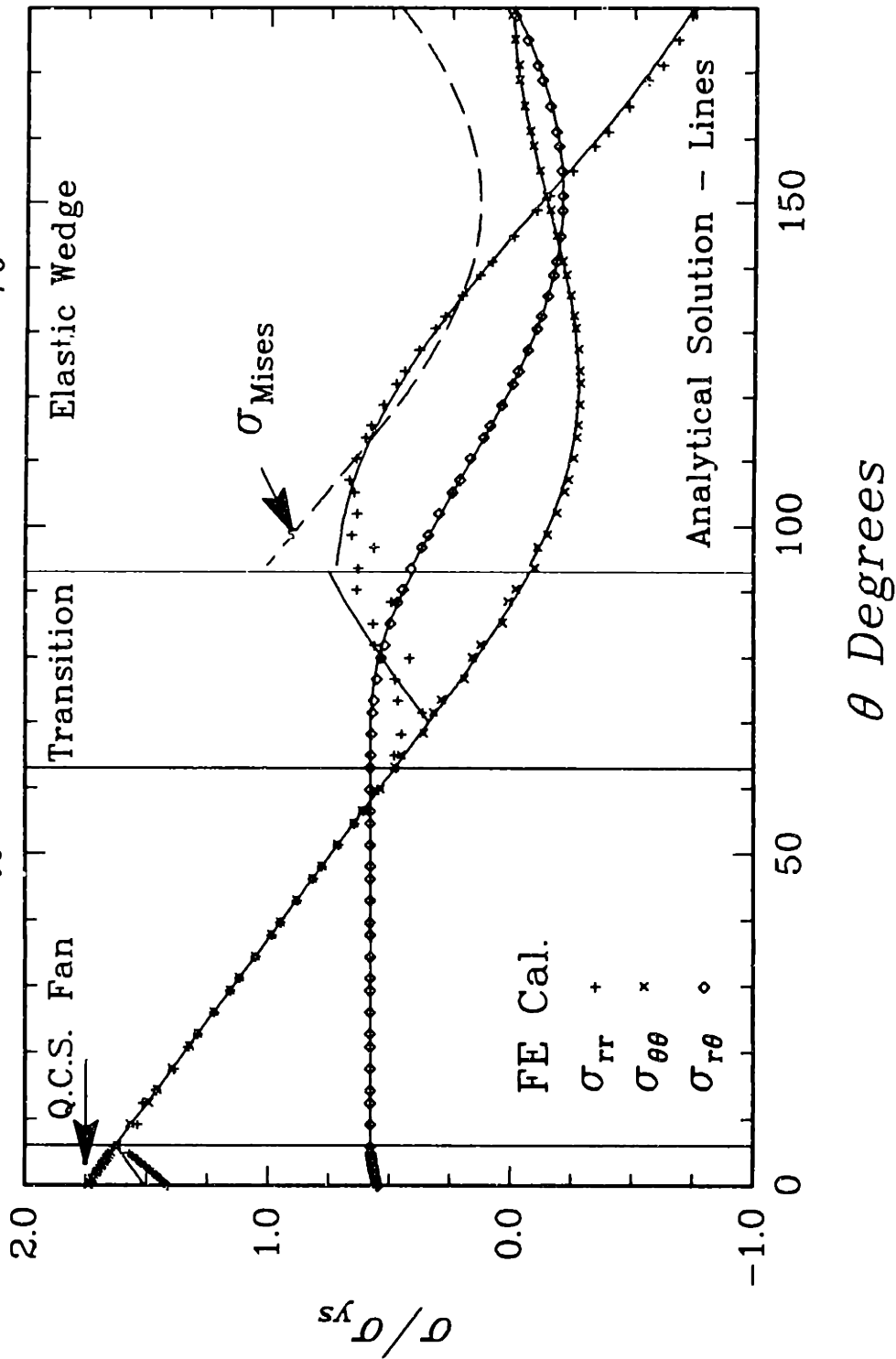


Figure 4.11 Normalized circumferential stress distribution for an elastic/perfectly-plastic upper region bonded to a rigid substrate at $R = \gamma_0$; $\epsilon = 0.07796$ and $\zeta_0 = 30.0^\circ$. Symbols represent the integration point stress states and the lines reproduce the inferred analytical solution. Included is the inferred Mises equivalent stress in the crack-face elastic wedge.

small compared to those found in centered fans. For these and other reasons, the most significant strain component in the crack-tip region is the $\gamma_{r\theta}$ component, and therefore $\gamma_{r\theta}$ is the only strain component considered.

The $\gamma_{r\theta}$ strain distribution is normalized by considering its functional form within a centered fan sector. From Eq.(4.10), the shear strain distribution is given approximately by $R\gamma_{r\theta}/\gamma_0 \approx A(\theta)$, when $R \ll 1$. *Figure 4.12* shows the normalized distribution of $\gamma_{r\theta}$ for $\epsilon = 0.07796$ at six values of ζ_0 between 1.34° and 30.0° . Comparing the radial shear strain distributions with the asymptotic crack-tip forms, the largest strains occur in fan regions approximately 15° away from the fan-elastic boundary, and from *Figure 4.12*, the maximum shear strain increases as ζ_0 increases. Although not shown, the normalized shear strain distributions deep within the plastic zone ($R < 0.01$) are independent of R . Thus the presence of a cusp strongly influences the entire asymptotic crack-tip deformation, even in regions where the cusp is not present.

An additional quantity directly related to the strain field is the CTOD. The bi-material CTOD is defined as

$$\delta_{CTOD} \equiv \mathbf{u}(R = 0, \theta = \pi) - \mathbf{u}(R = 0, \theta = -\pi), \quad (4.23)$$

where \mathbf{u} is the displacement vector. The CTOD physically represents the displacement of the crack faces relative to one another and also represents an integrated vector sum of the strain field on a path about the crack tip. To uniquely define δ_{CTOD} , both its magnitude and orientation are required. In *Figure 4.13* a schematic crack tip and the associated coordinate system used to define δ_{CTOD} are sketched. *Figure 4.14* shows the normalized magnitude of δ_{CTOD} and ω , the angle of δ_{CTOD} , for $\epsilon = 0.07796$ as a function of ζ_0 . Also plotted in the figure is the angle $\omega_{Elastic}$, which is the angle of δ_{CTOD} obtained from the elasticity solution by evaluating Eq.(P2.32) at $\zeta = \zeta_0$ and $r = r_p$. The difference between ω and $\omega_{Elastic}$ is less than 15° for the range of ζ_0 shown. The corresponding elastically-calculated magnitude of δ_{CTOD} , defined as

$$\left| \frac{\delta_{CTOD}\sigma_{ys}}{J} \right|_{Elastic} \equiv \frac{4\sqrt{2}}{\pi\sqrt{1+4\epsilon^2}}, \quad (4.24)$$

is $|\delta_{CTOD}\sigma_{ys}/J|_{Elastic} = 1.779$ for $\epsilon = 0.07796$ and is independent of ζ_0 .

Bi-material Crack-Tip Shear Strain

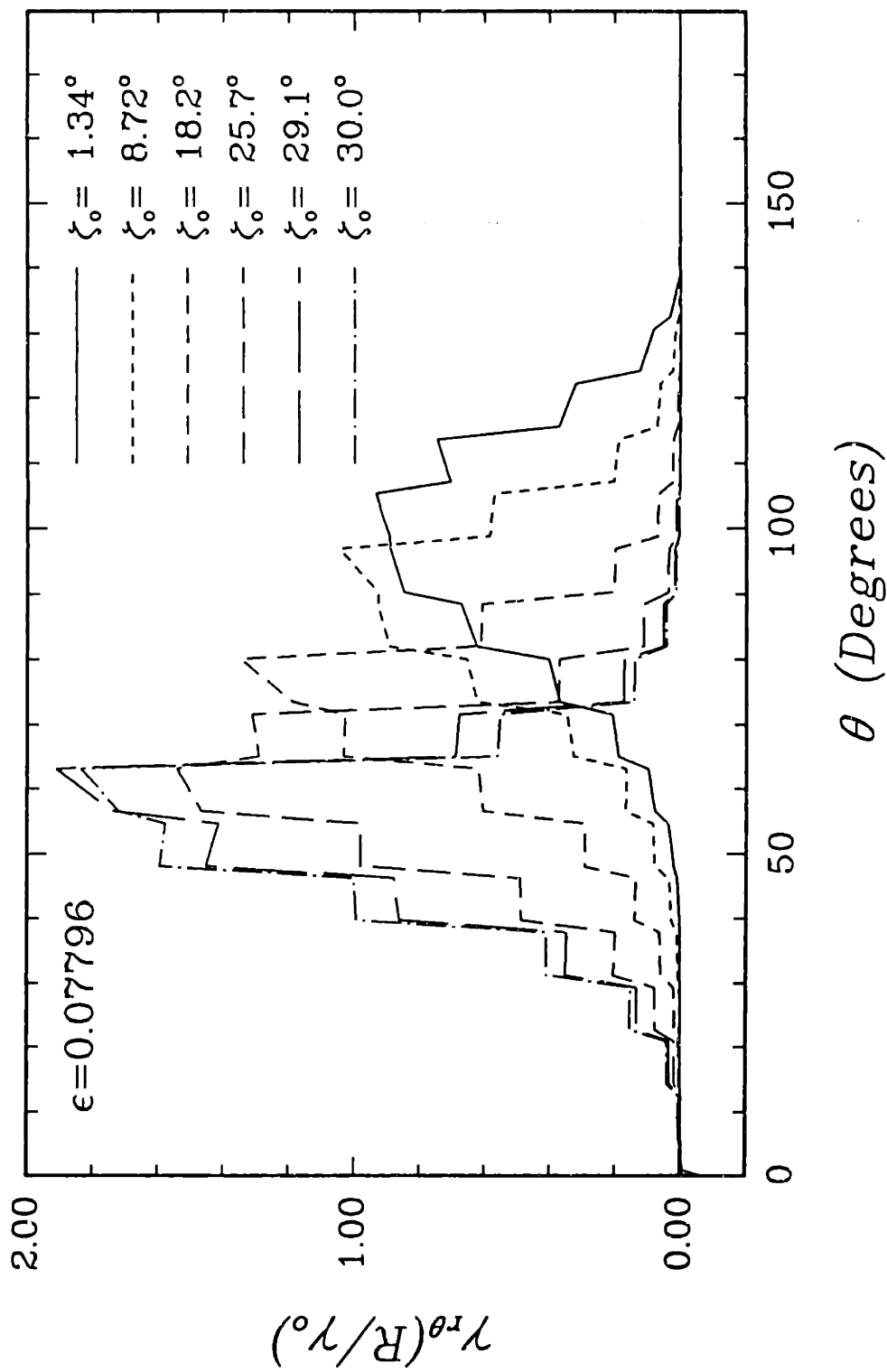


Figure 4.12 Circumferential variation of normalized $\gamma_{r\theta}$ shear strain deep in the plastic zone ($R = \gamma_0$) for an elastic/perfectly-plastic upper region bonded to a rigid substrate at various values of ζ_0 ; $\epsilon = 0.07796$.

Schematic Crack Tip

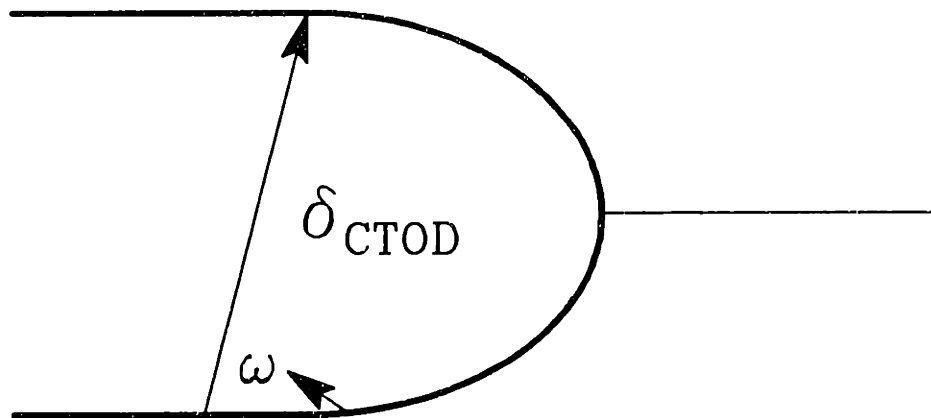
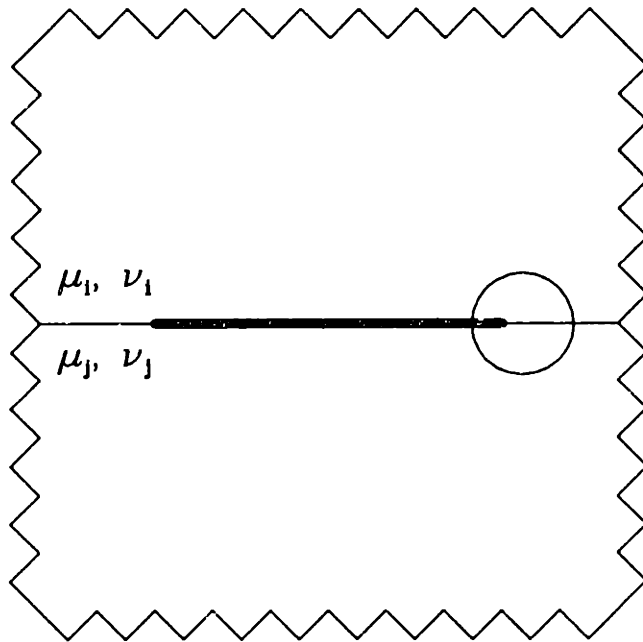


Figure 4.19 Schematic interfacial crack-tip region showing the crack-tip opening displacement (δ_{CTOD}) and its associated angle ω .

Bi-material Crack-Tip δ_{CTOD}

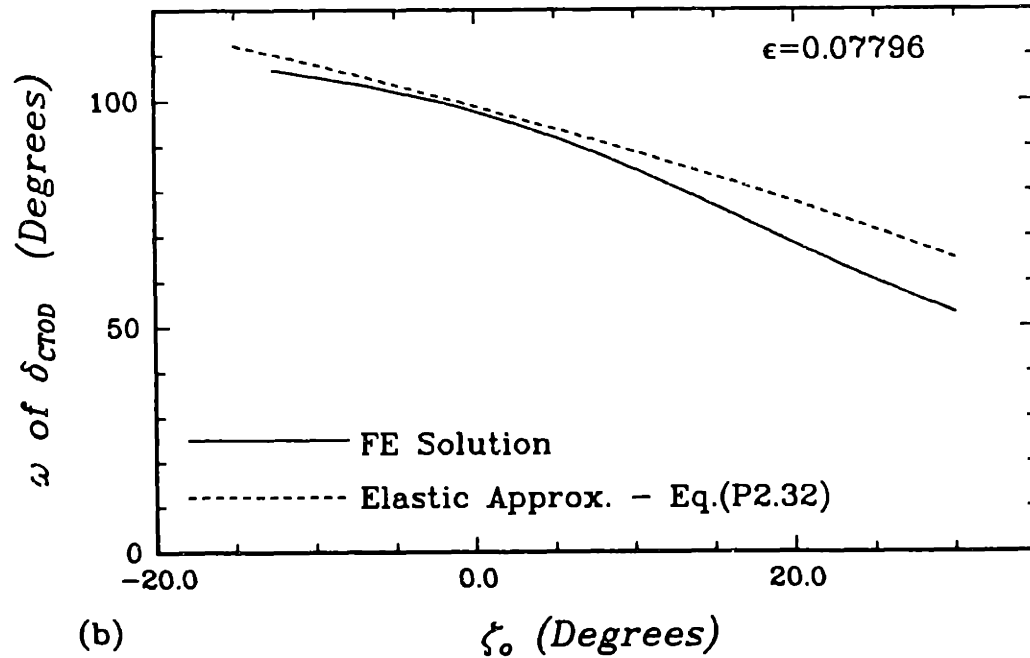
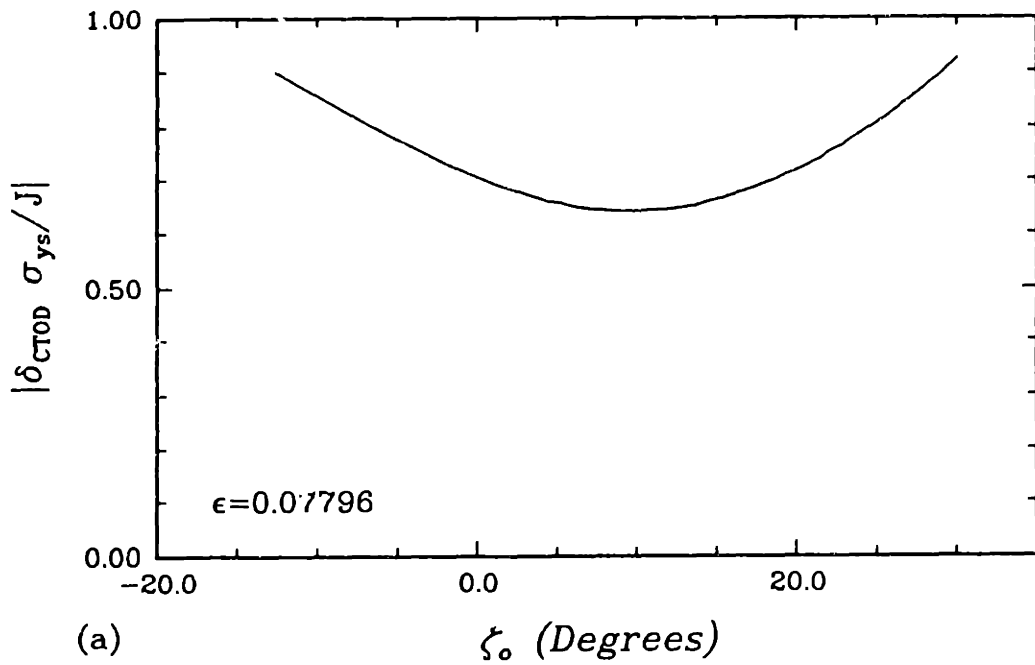


Figure 4.14 Traction-free bi-material δ_{CTOD} from a finite element calculation of an elastic/perfectly-plastic upper region atop a rigid substrate for ζ_0 between -20° and 30° ; $\epsilon = 0.07796$. (a) shows the magnitude normalized with respect to yield strength and the far-field elastic J -Integral and (b) shows the crack-tip angle ω from the finite element calculations and from Eq.(P2.32) evaluated at $r = r_p$ and $\zeta = \zeta_0$.

Path Dependence of J-Integral

The J -Integral is evaluated within the asymptotic crack-tip fields by considering the contributions to it from each of the various sectors. Rice (1968b) states that since the strains are bounded as $R \rightarrow 0$ in a constant region, constant state sectors produce no contribution to J . Extending this rationale, it is concluded that no contributions to J are made from either the rigid lower half or from any of the (non-singular) crack-tip elastic sectors. Therefore, the entire local contribution to J comes from the centered fan region(s) and is given by (Rice, 1967)

$$J = \int_{\theta_{Fan}} r \gamma_{r\theta}(r, \theta) [k \cos \theta + \sigma_{rr}(r, \theta) \sin \theta] d\theta. \quad (4.25)$$

Here the integration path is chosen to be a circular arc about the crack tip, and in terms of the schematic slip-line field shown in *Figure 4.10*, the upper and lower limits of integration are $\theta = \eta$ and $\theta = \alpha + \eta$, respectively.

Local J -Integral estimates were calculated by the virtual crack extension method (VCEM). The VCEM uses the divergence theorem to convert the contour integral of J to a surface integral and then calculates the change in energy associated with a virtual extension of the crack front. The J estimate is interpreted as $J \approx -\Delta\pi/\Delta a$, where $\Delta\pi$ is the change in energy and Δa is the virtual increment of crack advancement. *Table 4.2* summarizes the local J_{VCEM} normalized by $J_{Elastic}$, the far-field elastic J -Integral, for $\epsilon = 0.07796$ and ζ_0 between 1.34° and 30.0° . Included in the table are the average values of the second, third, and fourth contour values of J . A considerable amount of non-proportional loading occurs, especially with the presence of the cusps and growth of the crack-face elastic wedge, thus local J values which are appreciably lower than the far-field J are expected. The contour values of J typically decreased slightly from the second contour to the ninth contour. Growth of J as $R \rightarrow 0$ is not anticipated, but may be attributable to both the stress and strain distributions asymptotically approaching a steady state as $R \rightarrow 0$.

ζ_0	$J_{VCEM}/J_{Elastic}$
30.0°	0.86
25.7°	0.75
18.2°	0.61
8.72°	0.49
1.34°	0.41

Table 4.2 Local J -Integral estimates, normalized by the elastic far-field value of J , obtained by the VCEM for various values of ζ_0 with $\epsilon = 0.07796$.

4.2.2 Solution in the Lower Elastic Half-Plane

Due to the use of a rigid material adjoint to the elastic/perfectly-plastic material in the quarter wave-length calculation, no results are obtained for the lower elastic half-plane. The nature of the elastic half space is instead obtained from one of the other, less focused, analyses. Because contact between the upper and lower half-planes is made only via the interface, the behavior of the asymptotic interfacial conditions very deep within the plastic zone, described previously, are reflective of the stress behavior in the elastic half-plane.

Unlike the upper yielding region, no significantly different behavior is observed in the elastic region at r_I , the plastic zone radius along the interface [$r_I \equiv r_p(\theta = 0^\circ)$], and at distances much closer to the crack-tip, $r \approx r_I/10$, certain dominant features begin to emerge. Consider the results obtained for the material combination of yielding aluminum in region 1 and graphite in region 2, ($\epsilon = -0.07923$) loaded until $\zeta_0 = -2.70^\circ$. (*Table 4.4* contains the elastic properties of all material used.) *Figure 4.15* shows the normalized stress components in the elastic interfacial region as a function of the logarithm of the normalized radial distance R_I ($R_I \equiv r/r_I$). The normalized hoop and shear components experience a transitional period from $\log_{10}(R_I) = 0$ up to $\log_{10}(R_I) = -1.0$, at which point they level off and achieve a steady state behavior as $R_I \rightarrow 0$. The normalized radial stress experiences a similar transitional period, but it increases linearly in the region where the other components reach their steady-state values ($R_I < -1$). This indicates that the radial stress component is logarithmically

Bi-material Crack-Tip Stresses

$\epsilon = -0.07923$ $\theta = 0.0^\circ$

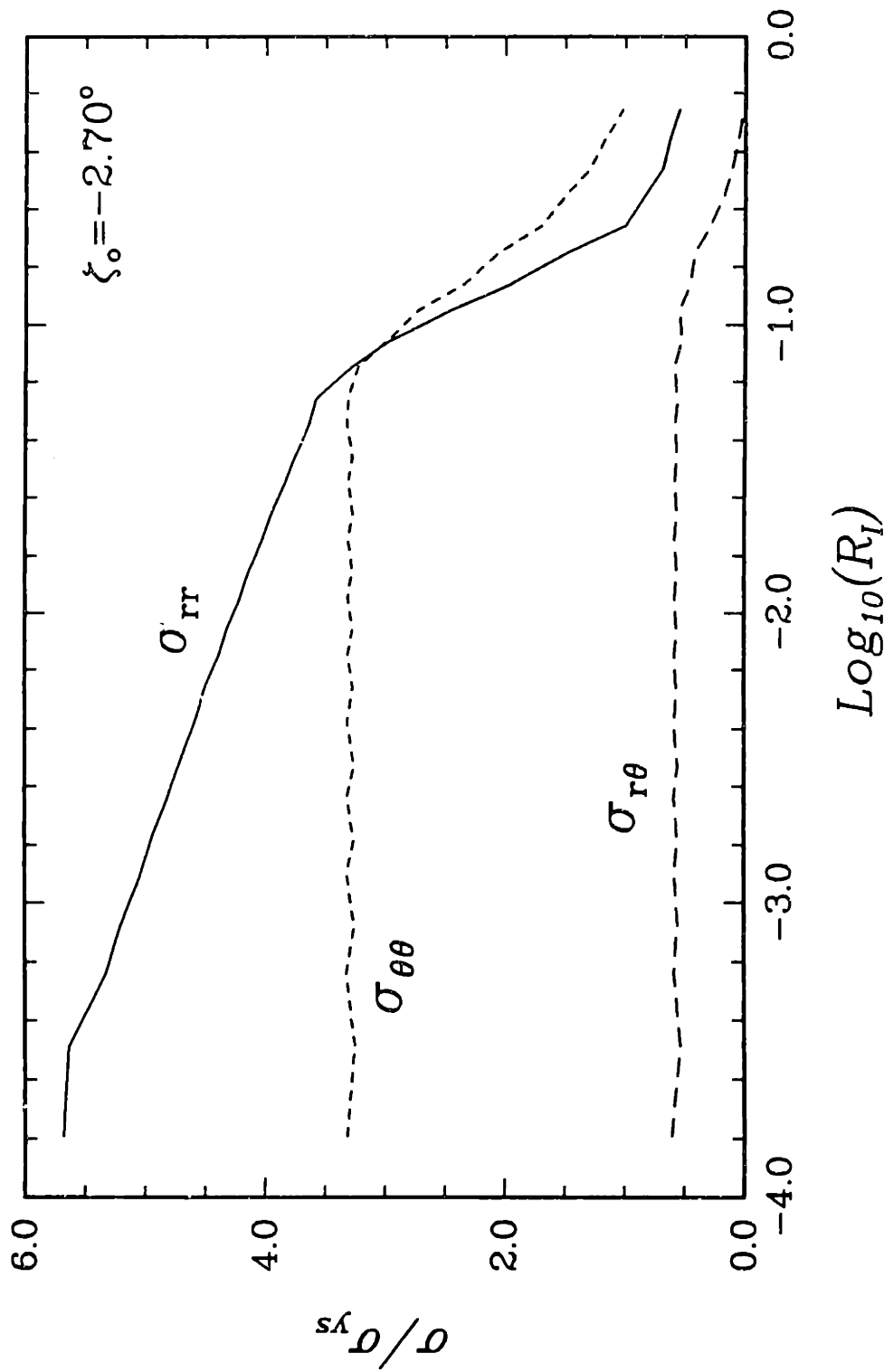


Figure 4.15 Normalized interfacial stress variation with normalized radial distance in the lower region for a traction-free bi-material crack-tip under SSY conditions; elastic/perfectly-plastic upper region bonded to a rigid substrate ($\zeta_0 = -2.70^\circ$, $\epsilon = -0.07923$, and $\theta = 0.0^\circ$).

singular. *Figure 4.16* shows the normalized elastic stress components plotted versus normalized radial distance R at $\theta = -86^\circ$. At this angle, all the stress components experience some transitional behavior at $R_I > -1$ before they reach a linear region. In *Figure 4.17* the angular distribution of the normalized stress components at $R = 0.00551$, $R = 0.0138$, and $R = 0.0551$ are plotted. It is obvious that the asymptotic stress distribution does not generally reach a steady-state as $R \rightarrow 0$ (or $R_I \rightarrow 0$), as is observed in the upper domain, nor does it reach a self similar distribution as is observed in homogeneous asymptotic elastic and plastic crack-tip fields (Rice and Rosengren, 1968; Hutchinson, 1968).

Formulation of an Elasticity Potential

To describe the stress field very near the crack tip, beneath the region where the solution in the upper domain has achieved a steady state, a closed form elasticity solution will be formulated. The planar elasticity solution will describe the asymptotic characteristic as $R \rightarrow 0$ in the lower field and will be expressed in the form of an elasticity potential.

It has been shown that any planar stress function, $\phi(x, y)$, which satisfies the differential equation

$$\frac{\partial^4 \phi}{\partial x^4} + 2 \frac{\partial^4 \phi}{\partial x^2 \partial y^2} + \frac{\partial^4 \phi}{\partial y^4} = 0, \quad (4.26)$$

also satisfies the basic equations of isotropic linear elasticity, namely the constitutive, equilibrium, and the compatibility equations (Timoshenko and Goodier, 1970). In addition to satisfying Eq.(4.26), the stress function must also satisfy all accompanying boundary conditions. The individual stress components for a body with stress function, ϕ (with negligible body forces) are:

$$\sigma_{xx}(x, y) = \frac{\partial^2 \phi(x, y)}{\partial y^2}, \quad (4.27)$$

$$\sigma_{yy}(x, y) = \frac{\partial^2 \phi(x, y)}{\partial x^2}, \quad (4.28)$$

and

Bi-material Crack-Tip Stresses

$\epsilon = -0.07932$ $\theta = -86^\circ$

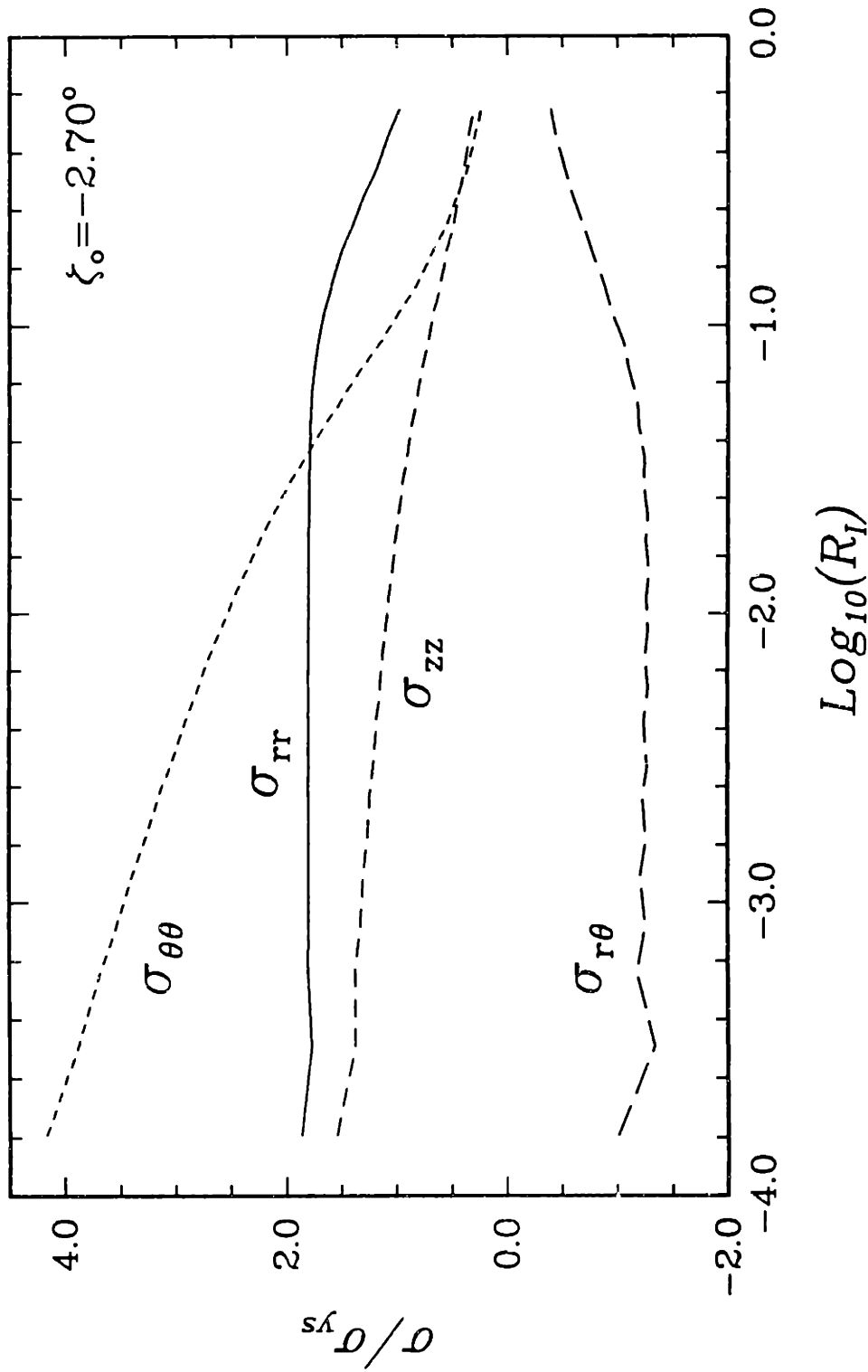


Figure 4.16 Normalized interfacial stress variation with normalized radial distance in the lower region for a traction-free bi-material crack-tip under SSY conditions; elastic/perfectly-plastic upper region bonded to a rigid substrate ($\zeta_0 = -2.70^\circ$, $\epsilon = -0.07923$, and $\theta = -89^\circ$).

Bi-material Crack-Tip Stresses

$\epsilon = -0.07932$ $\zeta_0 = -2.70^\circ$

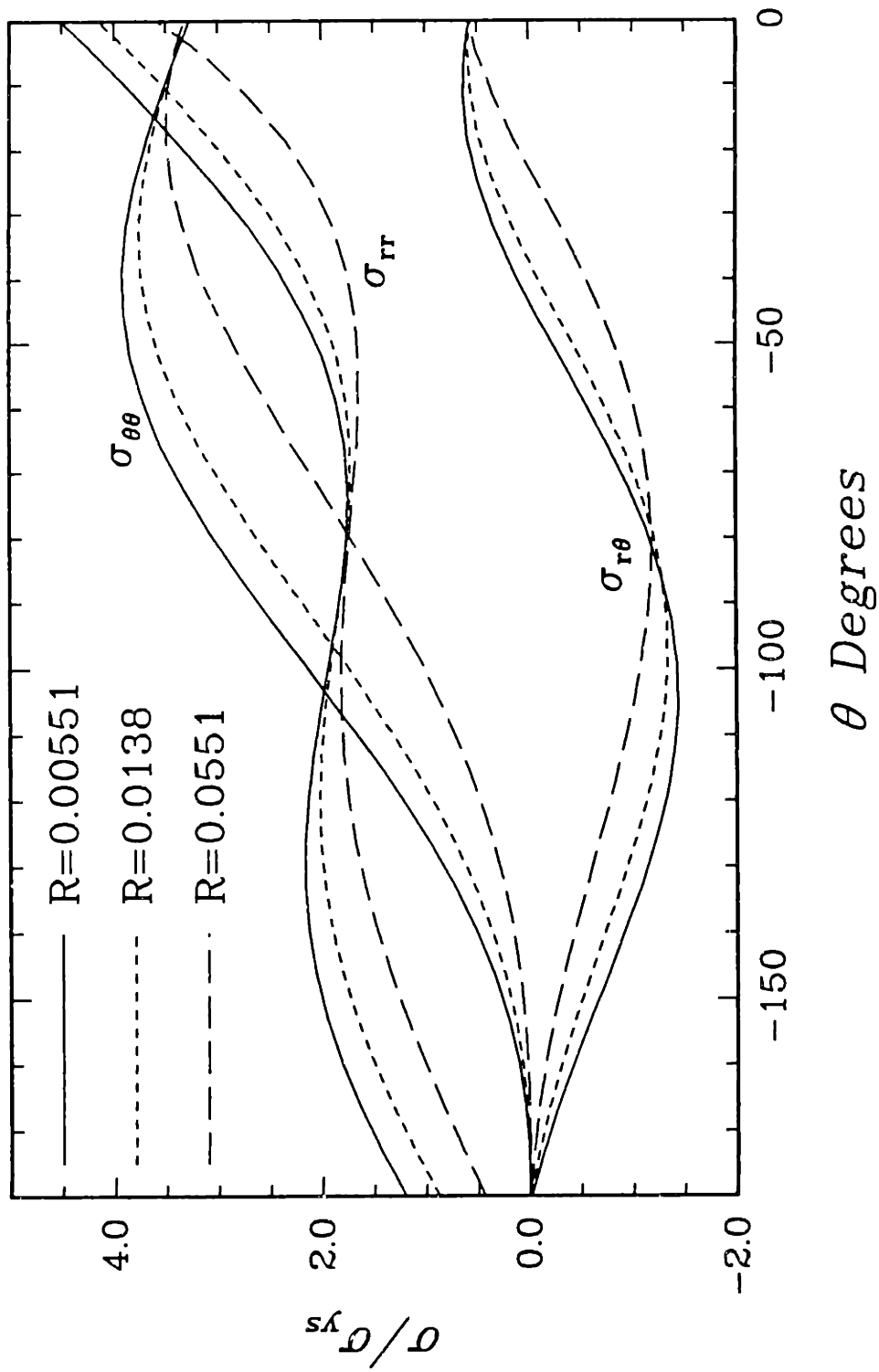


Figure 4.17 Normalized angular stress distribution in lower region for a traction-free bi-material crack-tip under SSY conditions at various radial distances; elastic/perfectly-plastic material bonded to an elastic substrate ($\zeta_0 = -2.70^\circ$ and $\epsilon = -0.07923$).

$$\sigma_{xy}(x, y) = -\frac{\partial^2 \phi(x, y)}{\partial x \partial y}. \quad (4.29)$$

The strain field is found by inverting the appropriate isotropic elasticity tensor, \mathcal{L} , defined in Eq.(3.14), and using it to operate directly on the stress field. Assumptions regarding plane-strain (or plane-stress) conditions are necessary to fully define the stress and strain fields. Integration of the strain field uniquely determines the displacement field, to within a rigid body motion. Therefore, the determination of ϕ , in conjunction with the planar assumptions and two elastic material properties, completely describes the elastic fields.

The stress function ϕ need not be expressed in Cartesian coordinates. It can be found in any coordinate frame and, via the proper coordinate transformation, transformed into any other coordinate frame. For example, it is more convenient to express the stress components around the crack tip in a polar coordinate frame. The polar stress components can be obtained from ϕ by (Timoshenko and Goodier, 1970):

$$\sigma_{\theta\theta}(r, \theta) = \frac{\partial^2 \phi(r, \theta)}{\partial r^2}, \quad (4.30)$$

$$\sigma_{r\theta}(r, \theta) = -\frac{\partial}{\partial r} \left(\frac{1}{r} \frac{\partial \phi(r, \theta)}{\partial \theta} \right), \quad (4.31)$$

and

$$\sigma_{rr}(r, \theta) = \frac{1}{r} \frac{\partial \phi(r, \theta)}{\partial r} + \frac{1}{r^2} \frac{\partial^2 \phi(r, \theta)}{\partial \theta^2}, \quad (4.32)$$

where r is the radial coordinate and θ is the angular coordinate.

In general, the stress potential ϕ is obtained by considering the assorted boundary conditions and the desired asymptotic behavior. In an attempt to find ϕ for the problem at hand, the contributions to ϕ from the local crack-face and interfacial tractions are first examined.

The major factor which governs the behavior of the elastic domain is the interfacial traction. Because of the elastic/perfectly-plastic material idealization used in the upper domain, and to within the limits discussed previously, the asymptotic crack-face and interfacial tractions, t , as $R \rightarrow \gamma_0$, assume constant values of:

$$t_n = \begin{cases} P\sigma_{ys} & \theta = 0^\circ \\ 0 & \theta = -180^\circ, \end{cases} \quad (4.33)$$

and

$$t_s = \begin{cases} S\sigma_{ys} & \theta = 0^\circ \\ 0 & \theta = -180^\circ. \end{cases} \quad (4.34)$$

Here σ_{ys} refers to the yield strength of the material in the upper domain σ_{ys1} , and the subscripts n and s designate the normal and shear components, respectively. Although these asymptotic interfacial tractions extend only over a "short" distance within the plastic zone, the actual traction distribution is approximated by considering that these tractions exist over the entire interface within the plastic zone. Outside the plastic zone region, the asymptotic elastic stresses are small with respect to σ_{ys} and decay rapidly as the radial distance r increases. To describe the asymptotic behavior in the crack-tip region it is assumed that the interfacial tractions in the elastic portion of the upper region are negligible. The interfacial tractions are idealized as being equal to zero everywhere beyond the plastic zone and within the plastic zone are equal to t_n and t_s , as given by Eqs.(4.33) and (4.34). This idealized traction distribution around the crack tip is drawn in *Figure 4.18*.

By consideration of this idealized interfacial traction distribution, an elasticity potential is assembled which asymptotically reproduces the stress and strain state in the elastic lower domain as $r \rightarrow 0$. From the known solutions for semi-infinite bodies with constant normal and shear surface tractions across half of their free surface (Timoshenko and Goodier, 1970), the stress potential, ϕ , for the lower crack-tip domain is assembled by superposition of the various known solutions and is expressed as

$$\begin{aligned} \phi = & -\frac{S\sigma_{ys}}{\pi} \left[\frac{1}{2}y^2 \ln \left(\frac{x^2 + y^2}{(x + r_I)^2 + y^2} \right) + xy \arctan \left(\frac{y}{x} \right) \right. \\ & \left. + (x - r_I) y \arctan \left(\frac{y}{x + r_I} \right) \right] \\ & + \frac{P\sigma_{ys}}{2\pi} \left[(x^2 + y^2) \arctan \left(\frac{y}{x} \right) - xy + (x + r_I) y \right. \\ & \left. - ((x + r_I)^2 + y^2) \arctan \left(\frac{y}{x + r_I} \right) \right]. \end{aligned} \quad (4.35)$$

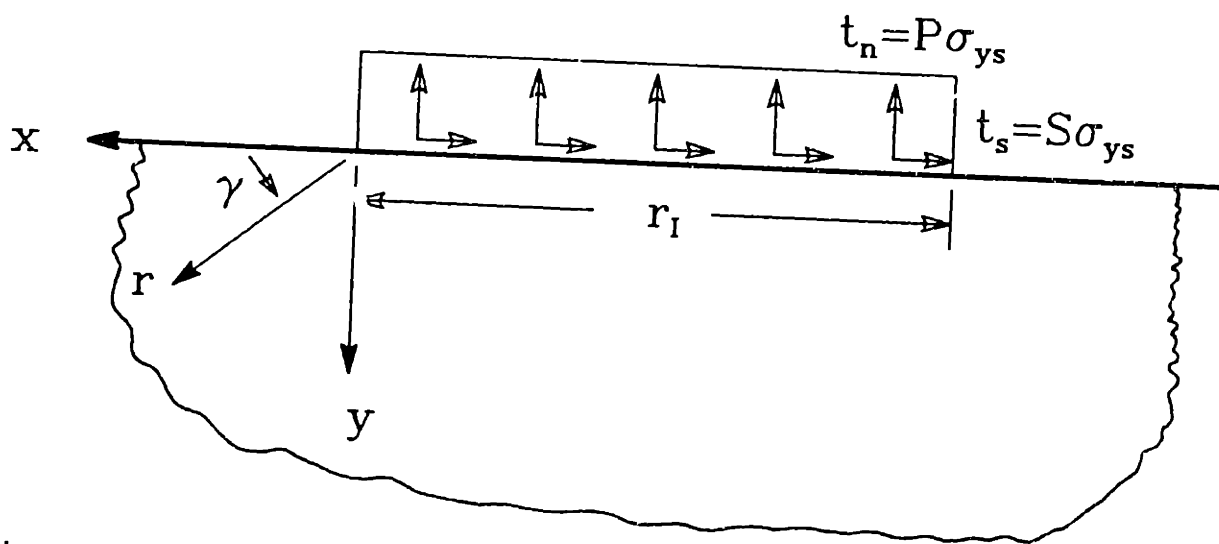


Figure 4.18 Idealized interfacial traction distribution for a traction-free crack-tip in SSY conditions, showing interfacial normal (t_n) and shear (t_s) tractions, plastic zone radius of upper material (r_I), and polar (r, γ) and Cartesian (x, y) coordinates.

Here r_I is the plastic zone radius along the interface. (The stress potential for a semi-infinite body is a special case of the general wedge solution with the enclosed wedge angle equal to 180° .) Since only the asymptotic crack-tip elastic stress field is desired and the traction distribution outside the crack-tip region is only approximate, attention is focused upon the very near crack-tip field. By dividing Eq.(4.29) by r_I^2 , defining two new relative coordinate measurements $X = x/r_I$ and $Y = y/r_I$, and by assuming $X \ll 1$ and $Y \ll 1$, the local asymptotic stress potential is obtained, as $R_I \rightarrow 0$ (where $R_I^2 = X^2 + Y^2$), and it is given by

$$\begin{aligned} \phi = & -\frac{S\sigma_{ys}}{\pi} \left[\frac{1}{2}Y^2 \ln(X^2 + Y^2) + XY \arctan\left(\frac{Y}{X}\right) - Y^2 \right] \\ & + \frac{P\sigma_{ys}}{2\pi} \left[(X^2 + Y^2) \arctan\left(\frac{Y}{X}\right) - XY \right]. \end{aligned} \quad (4.36)$$

At small distances along the interface relative to the interfacial plastic zone radius, r_I , the tractions appear to remain constant for increasing or decreasing x . Thus, by observation of the traction behavior, the stress potential for a semi-infinite body with constant normal and shear surface tractions across half of its free surface could be obtained directly. Note, Eq.(4.36) is the stress potential for such a semi-infinite body, except that the coordinates X and Y are normalized by the plastic zone radius along the interface.

Timoshenko and Goodier (1970) pointed out that prescribing only the surface tractions and determining their resultant stress potential does not always uniquely characterize the stress field. Stress fields which require no surface tractions or displacement boundary conditions on the free surface ($y = 0$) can be arbitrarily superimposed. Due to these boundary constraints, certain restrictions are imposed on the otherwise arbitrary fields. Since no free-surface shear tractions are allowed in these fields,

$$\sigma_{xy}(X, Y = 0) = 0 \quad \Rightarrow \quad -\frac{\partial^2}{\partial X \partial Y} \phi(X, Y = 0) = 0, \quad (4.37)$$

and because no normal tractions are admissible,

$$\sigma_{yy}(X, Y = 0) = 0 \quad \Rightarrow \quad \frac{\partial^2}{\partial X^2} \phi(X, Y = 0) = 0. \quad (4.38)$$

For small values of X and Y as $R_I \rightarrow 0$, the most dominant field which satisfies these conditions is that of a uniform stress field parallel to the interface, defined such that $\sigma_{xx} = T\sigma_{ys}$. The stress potential for this uniform field is given by

$$\phi = \frac{1}{2}T\sigma_{ys}[Y^2]. \quad (4.39)$$

The total asymptotic stress potential for the elastic lower domain as $R_I \rightarrow 0$ is now assembled. Summing the various stress potentials, Eqs.(4.30) and (4.33), the total stress potential, expressed in a polar coordinate frame, is

$$\begin{aligned} \phi = & -\frac{S\sigma_{ys}}{\pi} \left[R_I^2 \ln(R_I) \sin^2(\gamma) + R_I^2 \gamma \sin(\gamma) \cos(\gamma) - R_I^2 \sin(\gamma) \right] \\ & + \frac{P\sigma_{ys}}{2\pi} \left[R_I^2 \gamma - R_I^2 \sin(\gamma) \cos(\gamma) \right] + \frac{1}{2}T\sigma_{ys} \left[R_I^2 \sin^2(\gamma) \right]. \end{aligned} \quad (4.40)$$

Asymptotic Characteristic

The stress components are obtained from Eq.(4.40) using Eqs.(4.30) to (4.32), and are converted to the polar coordinate frame used shown in *Figures 1.1* and *2.1* (via $\theta = \gamma - \pi$). The normalized stress components are expressed as

$$\begin{aligned} \frac{\sigma_{\theta\theta}}{\sigma_{ys1}} = & -\frac{S}{\pi} \left[(1 + 2 \ln(R)) \sin^2(\theta) + (\pi + \theta) \sin(2\theta) \right] \\ & + \frac{P}{\pi} \left[\pi + \theta - \sin(\theta) \cos(\theta) \right] + T \left[\sin^2(\theta) \right], \end{aligned} \quad (4.41)$$

$$\begin{aligned} \frac{\sigma_{rr}}{\sigma_{ys1}} = & -\frac{S}{\pi} \left[2 \ln(R) \cos^2(\theta) - (\pi + \theta) \sin(2\theta) - \sin^2(\theta) \right] \\ & + \frac{P}{\pi} \left[\pi + \theta + \sin(\theta) \cos(\theta) \right] + T \left[\cos^2(\theta) \right], \end{aligned} \quad (4.42)$$

and

$$\begin{aligned} \frac{\sigma_{r\theta}}{\sigma_{ys1}} = & \frac{S}{\pi} \left[\frac{1}{2} (1 + 2 \ln(R)) \sin(2\theta) + (\pi + \theta) \cos(2\theta) \right] \\ & - \frac{P}{\pi} \left[\sin^2(\theta) \right] - T \left[\sin(\theta) \cos(\theta) \right]. \end{aligned} \quad (4.43)$$

It is assumed here that the plastic zone radius along the interface, r_I , can be approximated by the characteristic plastic zone dimension, r_p , such that $R_I \approx R$.

The total stress state at any point in the elastic domain can be decomposed into the three individual components which describe the entire field. From both a physical and mathematical point of view, the uniform T-stress produces no startling or unusual features. The field which results from a uniform normal interfacial traction ($P\sigma_{\nu_s}$) produces normalized stress components of order P/π which are solely a function of angular location. The third field which arises, due to the uniform interfacial shear traction, is logarithmically singular as $R \rightarrow 0$ (and mathematically as $R \rightarrow \infty^+$). The stress components behave as $\sigma \sim [(S/\pi)\sigma_{\nu_s} \ln(R)]$ as $R \rightarrow 0$, indicating that large stresses are present and that yielding in the lower material domain is expected near the crack tip. *This means that the inclusion of non-linear deformation in the upper region does not completely eliminate the stress singularity at the crack tip; rather it only changes the relative degree of singularity at the crack tip.*

The actual asymptotic stress field is completely defined by substituting in the appropriate numerical values for S , P , and T . The numerical values of S and P are solely determined by the deformation pattern of the upper domain; however, the value of T is a function of the local asymptotic deformation and the far-field loads. In the traction-free crack-tip analyses the $M = 0$ "T-term" and associated eigenmode directly correspond to the uniform in-plane T stress. (In the boundary layer formulation the coefficient of the T-term is set to zero.) The value of T arrived at here does not include far-field loading effects and only reflects the interaction of the local crack-tip elastic-plastic fields with the elastic \mathbf{K} -fields. The elastic far-field contribution in homogeneous cracks is typically small compared to the yield stress, but as pointed out by Larsson and Carlsson (1973), a non-zero T-stress does alter the local plastic fields.

The individual elastic stress fields are completely characterized when the precise numerical values of P , S , and T are determined from the numerical analyses. From the slip-line model used to describe the plastically deforming upper region, the interfacial traction coefficients P and S are extracted, and the value of T is obtained by matching the predicted behavior in the lower elastic region with the actual numerical results.

To determine the value of T , any number of matches can be made which theoretically should produce identical results; *e.g.*, matching the radial strain, ϵ_{rr} , along the interface. In the work described herein, T represents the average of matching σ_{rr} at $\theta = 0^\circ$ and $\theta = -180^\circ$, typically at $R = 0.01$. This is done in an attempt to minimize the effects of numerical noise.

Comparison

Comparisons between the asymptotic fields based upon the elasticity potential and those numerically calculated are now made. *Figure 4.19* shows the angular distribution of the normalized stress components for the case of a deformable aluminum medium atop a graphite substratum loaded with $\angle\mathbf{K} = 0$ until $\zeta_0 = -2.70^\circ$ ($\epsilon = -0.07923$). In judging this comparison, one should bear in mind that $\sigma_{\theta\theta}$ and $\sigma_{r\theta}$ are mathematically required to match by definition of the boundary conditions imposed in obtaining the stress potential. The radial strain along the interface as a function of the $\ln R$ is plotted in *Figure 4.20* for the same conditions as in *Figure 4.19*. Here development of the asymptotic “logarithmically singular” solution is evident. The fields described by the elasticity potential, Eq.(4.40), represent the actual crack-tip fields at radial distances where $R_I < 0.05$ or (in terms of the normalized radial distance R) where $R < 0.01$. The additional restriction on R , as compared to R_I , is necessary to compensate for any overestimation that the assumption $r_I \sim r_p$ causes, since *the characteristic dimension in the lower half-plane is r_I , not r_p* . Clearly, sufficient agreement exists between the numerical result and the stress potential to justify use of the stress potential for describing the lower half-plane asymptotic crack-tip fields in SSY.

4.2.3 Parametric Study

This section explores the dependence of the SSY asymptotic crack-tip field on the ILPA (ζ_0) and on material properties, namely ϵ and ν_1 . The stress intensity factor angle ($\angle\mathbf{K}$) is varied in an attempt to cover the full range of admissible ILPA for several values

Bi-material Crack-Tip Stresses

$\epsilon = -0.07923$ $\zeta_0 = -2.70^\circ$ $R = 0.00551$

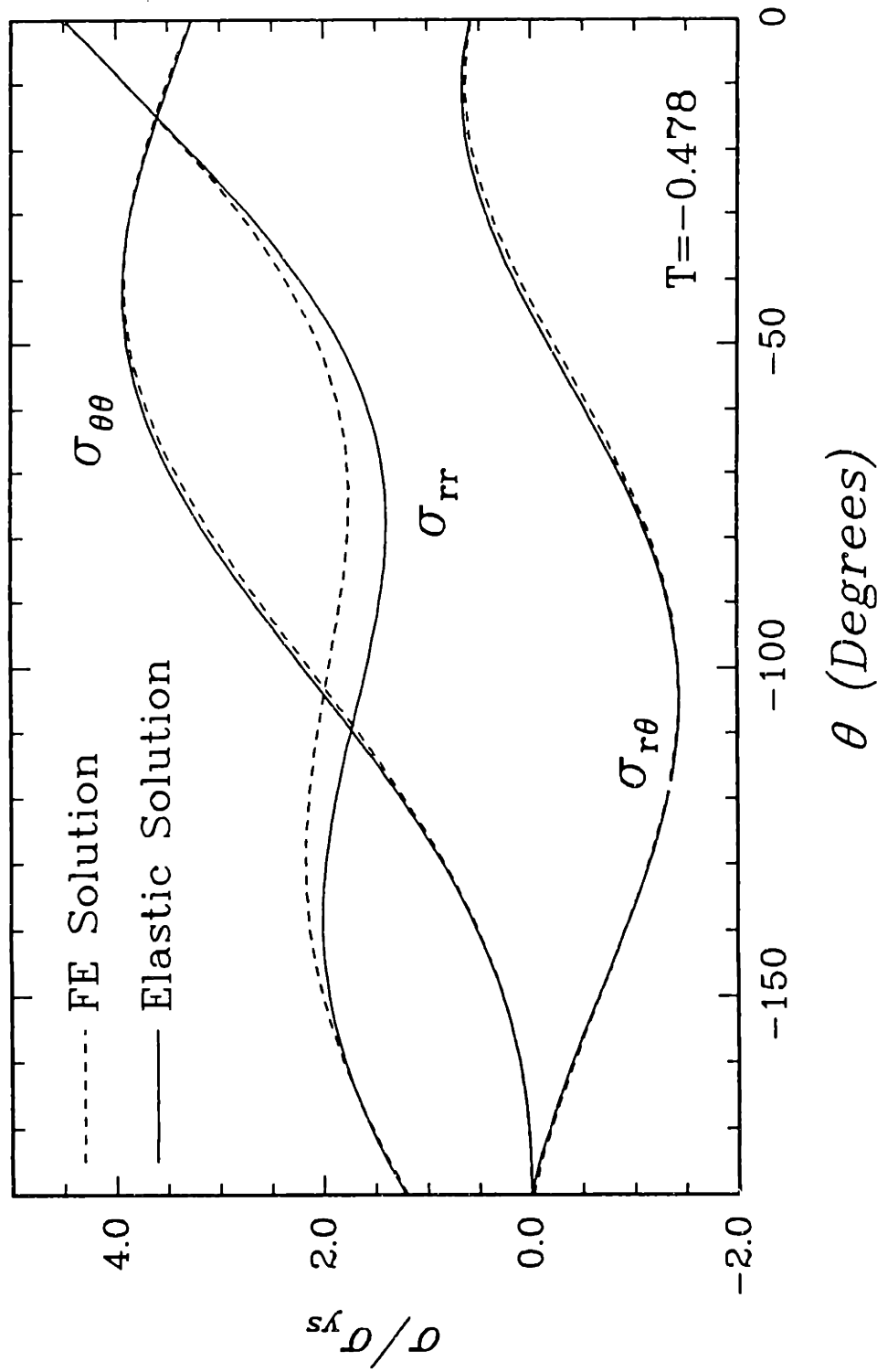


Figure 4.19 Normalized angular stress distributions in lower region of a traction-free interfacial crack-tip under SSY conditions; elastic/perfectly-plastic upper region bonded to an elastic substrate. Solid line solution obtained from finite element calculations and dashed line is inferred elasticity solution; $\epsilon = -0.07923$, $R = 0.00551$, and $\zeta_0 = -2.70^\circ$.

Bi-material Crack-Tip Strains

$\epsilon = -0.07923$ $\theta = 0.0^\circ$

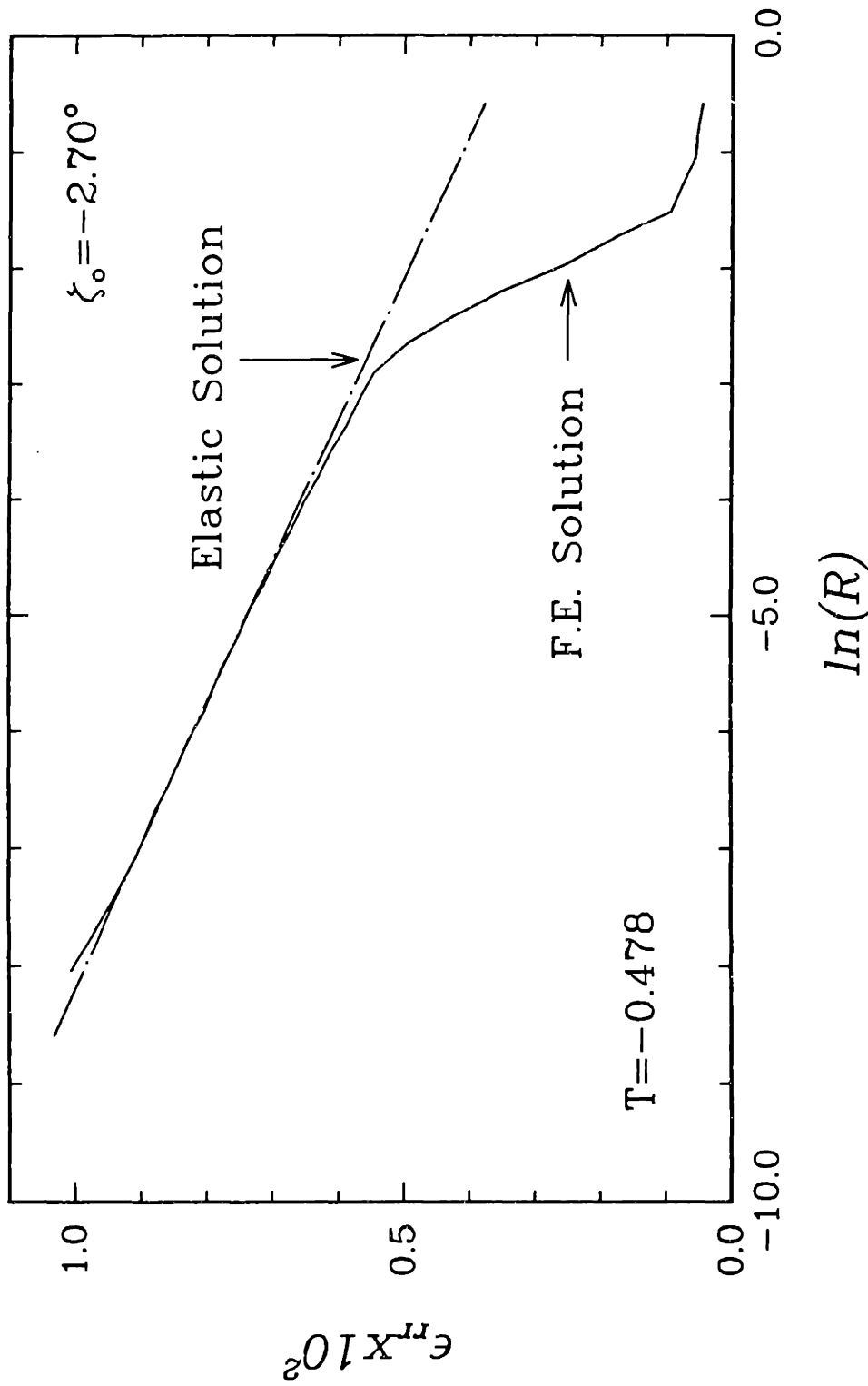


Figure 4.20 Interfacial radial strain variation with radial distance in lower region of a traction-free interfacial crack-tip under SSY conditions; elastic/perfectly-plastic material bonded to an elastic substrate. Solid line solution obtained from FE calculation and dashed line is inferred elasticity solution; $\epsilon = -0.07923$, $T = -0.478$, $\zeta_0 = -2.70^\circ$, and $\nu = 0.342$.

of ϵ . Various materials and material combinations are used to span nearly the entire plane strain range of ϵ for positive Poisson's ratio ($-0.170 < \epsilon < 0.170$). By use of six materials, whose isotropic elastic properties are listed in *Table 4.3*, the various values of ϵ obtained by pairing the materials are shown in *Table 4.4*. It is not possible to isolate the dependence upon the Poisson's ratio ν_1 , since varying ν_1 simultaneously alters ϵ , except in the degenerate case $\epsilon = 0$.

	μ (GPa)	E (GPa)	κ (GPa)	ν	Reference
"Soft"	1.00	2.04	0.708	0.02	
Graphite	5.48	13.7	9.13	0.25	Chamis, 1984 †
Aluminum	26.1	70.1	73.9	0.342	Hertzberg, 1976
Steel	80.7	210.0	175.0	0.293	Hertzberg, 1976
"Stiff"	249.2	722.7	2409.0	0.45	
"Rigid"	∞	∞	∞	0.0	

† Approximate isotropic (transverse) properties from a Pitch-55 fiber.

Table 4.3 Idealized elastic material properties.

ϵ	β	Region 1 Upper Domain	Region 2 Lower Domain
-0.1700	0.4885	"Stiff"	"Soft"
-0.07923	0.2439	Aluminum	Graphite
0	0	Aluminum	Aluminum
0.03320	-0.1039	Aluminum	Steel
0.07796	-0.2400	Aluminum	"Rigid"
0.07923	-0.2439	Graphite	Aluminum
0.1700	-0.4885	"Soft"	"Stiff"

Table 4.4 Material combinations used in analyses to obtain the various ϵ .

For all the cases considered, the evolution of steady-state solutions, interfacial tractions, and strains are fundamentally the same as discussed previously. In the upper domain, the plastic zone boundary separates the elastic and yielding regions. The shape, size, and growth characteristics of this boundary, along with its dependence upon ϵ , $\angle K$, and ν_1 are essentially represented by the plastic zone approximation, Eq.(P2.6), and thus the ILPA, ζ_0 . The plastic zone grows in a periodic fashion with respect to ζ_0 , which,

along with ϵ , completely determines the plastic zone shape. *Figures P2.4 to P2.7* show the actual numerically calculated plastic zones for the various values of ζ_0 and ϵ along with the elastically approximated plastic zone shapes. The actual plastic zone features are always elongated ahead of the crack tip, as compared to the elastic approximation, while the features in the region along the crack face are “stunted” as compared to the elastic solution. In combinations of ζ_0 and ϵ in which the elastic approximation predicts small crack-face plastic zone lobes (usually $\zeta_0 > 0$), the elastic/perfectly-plastic material idealization totally suppresses the formation of any crack-face lobes. The suppression of these crack-face plastic zone lobes has a pronounced effect on the asymptotic SSY crack-tip fields, as elaborated upon earlier. Subsequent discussion is, therefore, limited to describing the asymptotic fields via representative forms and discussing unique or unusual features that arose in specific cases.

Plastic Crack-Tip Fields and Interfacial Traction

The tensile yield strength used for all analyses is 32.5 MPa, however, the numerical value used for σ_{ys} is irrelevant in slip-line representation, because all stress components are linearly dependent upon σ_{ys} . In the interpretation of these results, it is the initial shear strain to yield, γ_0 , which is important, since γ_0 is used to judge where the elastic strains are small relative to total strains, thereby defining the domain where the asymptotic slip-line solution accurately represents the stress field. In this parametric study the initial tensile yield strain ranges between 1.6% for the elastically “soft” material, and 0.0045% for the elastically “stiff” material.

The asymptotic crack-tip field can now be assembled for each individual case. From *Figure 4.10*, the schematic slip-line field, and *Table 4.5*, which lists the slip-line field angles, all the asymptotic stress fields considered are defined. As alluded to earlier, an elastic wedge with uniform surface tractions along its sides is necessary to complete some of the slip-line fields. Included in *Table 4.5* is the elastic far-field value of J . The stress potential and stress components for the elastic wedge are given in Appendix

B. Table 4.6 contains the values of the elastic wedge coefficients a_2 and c_2 required to match the numerical stress states. Although the general stress potential for such a wedge, Eq.(B.4), allows for singular radial stresses ($\sigma_{rr} \approx 1/r$), no such behavior is found in the numerical calculation. Because of this, the coefficients a_1 and c_1 in the potential, Eq.(B.4), are zero.

ϵ	ζ_0	$\angle K$	J MPa m	α	η	γ	ξ
-0.07923	29.1°	26.6°	7.713×10^{-2}	0°	83° (76°)	97°	84°
-0.07923	4.62°	0°	4.853×10^{-2}	0°	135°	45°	0°
-0.07923	-25.0°	-26.6°	9.552×10^{-3}	0°	135°	45°	0°
-0.07923	-41.4°	-45.0°	6.094×10^{-2}	61°	74°	45°	0°
-0.07923	-57.2°	-63.4°	3.428×10^{-2}	80°	55°	45°	0°
-0.07923	-81.8°	-90.0°	2.191×10^{-2}	90°	45°	45°	0°
0	0°	0°	5.066×10^{-2}	0°	129° (115°)	51°	49°
0.03320	0.127°	0°	2.986×10^{-2}	0°	123° (117°)	57°	56°
0.03320	-46.2°	-45.0°	1.453×10^{-2}	88°	47°	45°	0°
0.07923	-0.980°	0°	0.1159	47°†	83° (77°)	50°	44°
0.1700	-1.08°	0°	0.7291	74°	61°	45°	0°

ϵ	ζ_0	P	S	T
-0.07923	2.91°	1.83	$1/\sqrt{3}$	0.42
-0.07923	4.62°	3.30	$1/\sqrt{3}$	-0.48
-0.07923	-25.0°	3.30	$1/\sqrt{3}$	-2.3
-0.07923	-41.4°	1.99	-0.31	-0.9
-0.07923	-57.2°	1.88	-0.54	-1.2
-0.07923	-81.8°	1.48	$-1/\sqrt{3}$	-0.95
0	0°	3.21	$1/\sqrt{3}$	-1.10
0.03320	0.127°	3.14	$1/\sqrt{3}$	-1.56
0.03320	-46.2°	1.69	-0.57	-0.68
0.07923	-0.980°	2.68†	0†	-0.96
0.1700	-1.08°	2.11	-0.49	-0.55

Table 4.5 Traction-free crack-tip slip-line angles and traction coefficients for various values of ϵ and applied K . The slip-line angle $\xi_1 = 0$ except as noted; † - $\xi_1 = 20^\circ$.

Hydrostatic noise present in the deforming constant state sectors limited the analyses resolution for certain cases. Crack-tip fields which contained interfacial elastic wedges or interfacial constant state sectors (with $\alpha < 90^\circ$), probably contained cusps.

The stress state weakly depended upon R along the interfacial constant-state/fan border ($\theta = \alpha$), however conclusive verification of a cusp presence was not possible due to the limited extent of the mesh. For some cases hydrostatic noise in interfacial constant state regions perturbed interfacial normal tractions and stresses in the lower elastic region appreciably, and this limited the resolution of the T -stress. It should be noted that in inelastic sectors hydrostatic noise alone did not severely restrict identification of asymptotic crack-tip fields because deviatoric stresses and the shear strain, which were unaffected by hydrostatic pressure, were used.

The asymptotic traction-free crack-tip fields and interfacial tractions for an elastic/perfectly-plastic media adjoint to an elastic substratum are qualitatively identifiable for the full range of admissible ζ_0 , and are outlined for the material combination where the upper region is aluminum ($\nu = 0.342$). The following discussion is only schematic, and based upon the data, the actual asymptotic slip-line fields are (only) mildly dependent upon ν and ϵ . *Figure 4.21* qualitatively depicts the anticipated slip-line angles as a function of ζ_0 and (selective) known data points are represented by a “+”. The associated assemblage of asymptotic crack-tip sectors, sketched schematically in *Figure 4.22*, shows the evolving generic crack-tip behavior with respect to the ILPA and simulates the crack-tip evolution for monotonically increasing proportional loading. For positive values of ϵ and fixed $\angle K$, the crack-tip fields evolve with increasing load in the direction of increasing ζ_0 . The arrows on the sector boundaries indicate the direction that each boundary moves as ζ_0 increases.

ϵ	ζ_0	a_2	c_2
-0.07923	29.1°	0.153	-0.113
0	0	-0.221	-0.053
0.03320	0.127°	-0.185	-0.080
0.07923	-0.980°	-0.228	-0.040

Table 4.6 Interfacial elastic wedge coefficients.

A natural separation in the asymptotic crack-tip fields occurs at $\zeta \approx 0^\circ$. For negative ILPA ($\zeta_0 < 0$) the crack-tip fields are fully plastic and consist of only fan and constant

Bi-material Crack-Tip Fields

Schematic Evolution of Asymptotic Slip-Line Field

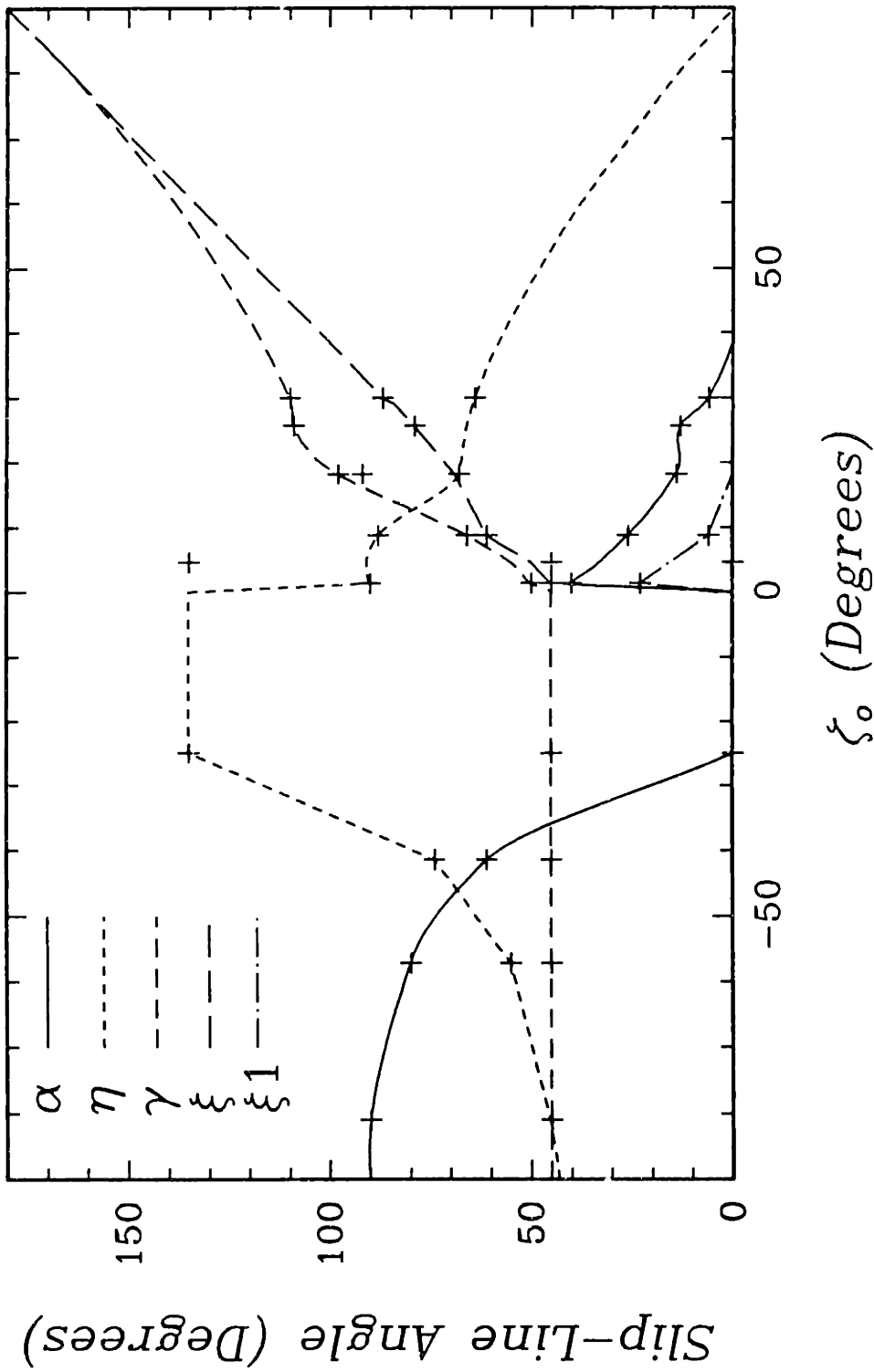


Figure 4.21 Schematic asymptotic slip-line angle evolution with the ILPA for an elastic/ perfectly-plastic material ($\nu \approx 0.342$) atop an elastic substrate, for $\xi_0 \leq 0$ ($\epsilon = -0.07923$), or atop a rigid ($\epsilon = 0.07796$) substrate, for $\xi_0 > 0$. Known data points are shown by “+” marks.

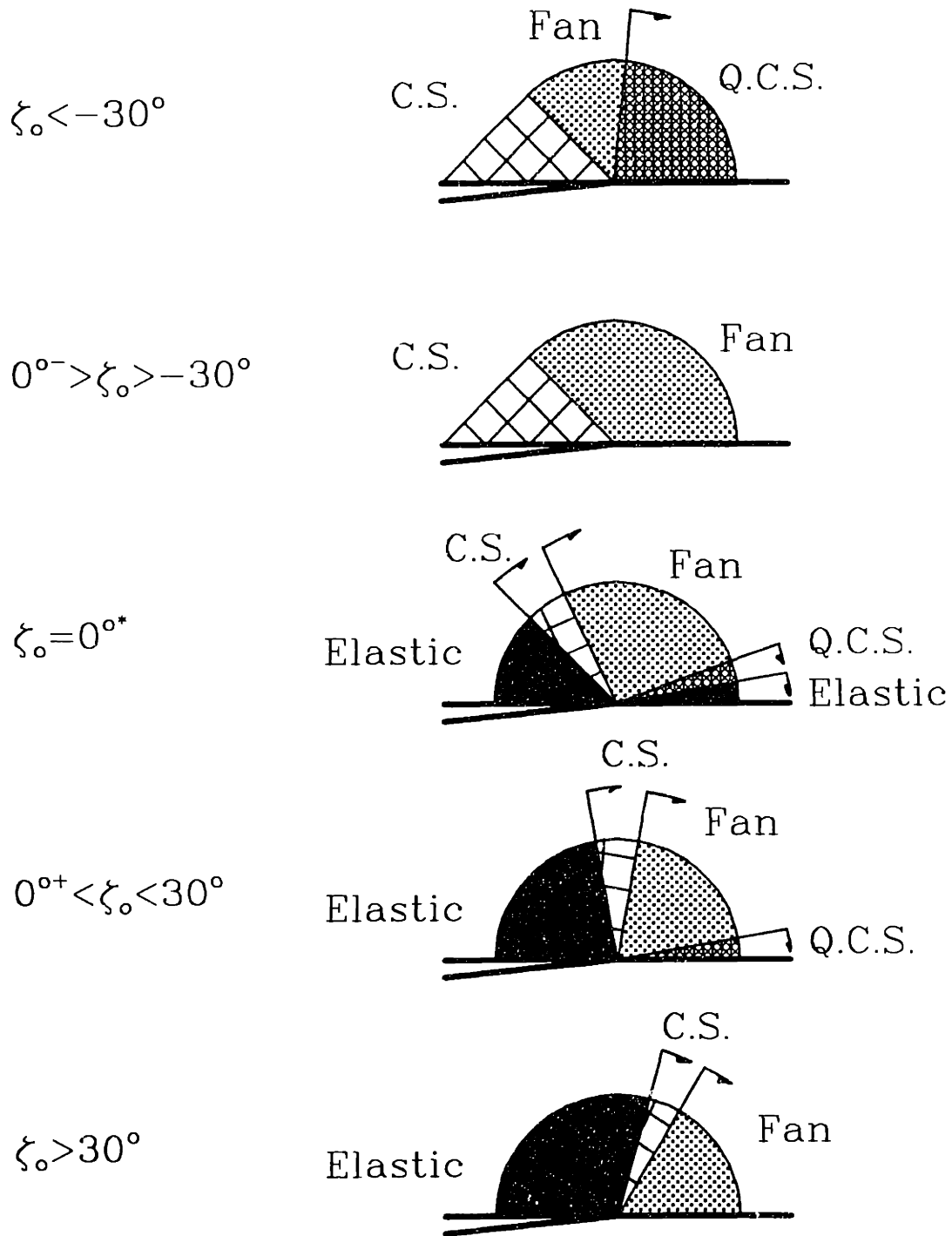


Figure 4.22 Schematic evolution of asymptotic slip-line, fields as a function of ζ_0 , for an elastic/perfectly-plastic material bonded atop an elastic or rigid substrate. Figure based upon data for $\epsilon = -0.07923$ when $\zeta \leq 0$ and $c = 0.07796$ when $\zeta_0 > 0$ with $\nu = 0.342$.

state sectors. To meet the traction-free crack-face boundary condition, a constant state sector always exists along the crack face which extends 45° ($\gamma = 45^\circ$). For ζ_0 between -90° and -30° , an interfacial quasi-constant state region is present whose angular extent (α) varies from 90° when $\zeta_0 = -90^\circ$ to 0° when $\zeta_0 \approx -30^\circ$. The interfacial tractions vary from their minimum ($t_s = -k$ and $t_n = 1.48\sigma_{ys}$) at $\zeta_0 = 90^\circ$ to their maximum ($t_s = k$ and $t_n = 3.30\sigma_{ys}$) when ζ_0 equals -30° . The interfacial tractions and assemblage of crack-tip sectors remain unchanged as the ILPA increases from $\zeta_0 \approx -30^\circ$ to some critical value near zero.

When the ILPA is positive, the crack-tip fields consist of both elastic and plastic sectors. It is speculated that as ζ_0 increases and approaches zero, the stress state everywhere in the crack-face constant state region falls simultaneously below the yield stress, and this produces a crack-face elastic wedge which extends a minimum of 45° . Along the interface an elastic sector, with a quasi-constant state sector adjacent to it, emerges and whose appearance is speculated to be linked with formation of a local plastic-zone boundary kink. [From Eq.(F2.6) it appears that both ζ_0 and the angular location at which this kink forms are dependent upon ν and ϵ .] Adjacent to both elastic wedges are constant-state regions which in turn border opposite sides of a centered fan. Near the interface, a cusp boundary separates the fan and the constant state region. The angular extent of the interfacial constant-state region approaches zero ($\alpha \rightarrow 0$) as $R \rightarrow 0$ and as ζ_0 increases to approximately 35° . The crack-face elastic wedge size increases with the ILPA from $\xi = 45^\circ$ at $\zeta_0 \approx 1^\circ$ to $\xi = 87^\circ$ at $\zeta_0 = 30^\circ$, and it is speculated that the size of the crack-face elastic wedge increases toward $\xi = 180^\circ$ as ζ_0 approaches 90° . Because various interfacial zones emerge, the interfacial tractions fluctuate appreciably over the range of positive ILPAs. The smallest interfacial shear traction, $t_s = 0.10\sigma_{ys}$, appears near $\zeta_0 = 1^\circ$, and then increases to its maximum value, $t_s = k$, for values of the ILPA equal to or greater than 35° . The normal interfacial traction decreases from its maximum value at $\zeta_0 = 0^\circ$ as the ILPAs increase.

Strain Distribution and CTOD

The strain fields are again represented by the $\gamma_{r\theta}$ distribution. The normalized strain distributions at six values of ζ_0 between -81.8° and 21.9° are plotted in *Figure 4.23* at $R = \gamma_0$ for $\epsilon = -0.07923$. To accommodate plotting, the minimum value on the ordinate axis is set to -15, which truncates two strain distributions. At $\theta = 0^\circ$ the values of $\gamma_{r\theta}(R/\gamma_0)$ are -899 and -49.8 when the ILPA (ζ_0) equals -57.2° and -81.8° , respectively. Drawn in *Figure 4.24* are the normalized strain distributions for four values of ϵ at $R = \gamma_0$ and $\zeta_0 \approx 0^\circ$. *Figure 4.24* (b) shows the strain distribution for $\epsilon = 0.03220$ when the ILPA equals -46.2° . In this figure, the truncated value of $\gamma_{r\theta}(R/\gamma_0)$ at $\theta = 0^\circ$ is -41.5.

To further summarize the strain fields, *Table 4.7* contains the numerically calculated magnitude of δ_{CTOD} , normalized by σ_{ys}/J , and its associated angle ω . (J is the far-field elastic J -Integral value.) For comparison, the elastically calculated CTOD angle, obtained by evaluating Eq.(P2.32) at $r = r_p$, is also given. The difference between ω and $\omega_{Elastic}$ is typically less than 30° , and ω is always less than $\omega_{Elastic}$.

ϵ	ζ_0	$\angle K$	J MPa m	$ \sigma_{ys}\delta_{CTOD}/J $	ω	$\omega_{Elastic}$
-0.07923	29.1°	26.6°	7.713×10^{-2}	1.008	21.4°	56.7°
-0.07923	4.62°	0°	4.853×10^{-2}	0.489	42.5°	76.7°
-0.07923	-25.0°	-26.6°	9.552×10^{-3}	0.621	83.1°	108.4°
-0.07923	-41.4°	-45.0°	6.094×10^{-2}	0.815	98.9°	130.1°
-0.07923	-57.2°	-63.4°	3.428×10^{-2}	1.086	107.2°	151.6°
-0.07923	-81.0°	-90.0°	1.867×10^{-2}	1.246	165.3°	179.9°
0	0°	0°	5.066×10^{-2}	0.598	81.2°	90°
0.03320	0.127°	0°	2.986×10^{-2}	0.668	88.8°	93.7°
0.03320	-46.7°	-45.0°	1.152×10^{-2}	1.364	130.7°	136.5°
0.07923	-0.980°	0°	0.1159	0.759	98.3°	99.9°
0.1700	-0.568°	0°	0.8387	0.876	107.3°	109.2°

Table 4.7 Traction-free crack-tip CTOD and CTOD angle (ω) for various values of ϵ and applied K .

From the information in the quarter wave-length analysis and this parametric study, the strain distribution in an aluminum upper region ($\nu = 0.342$) is qualitatively de-

Bi-material Crack-Tip Shear Strain

$\epsilon = -0.07932$

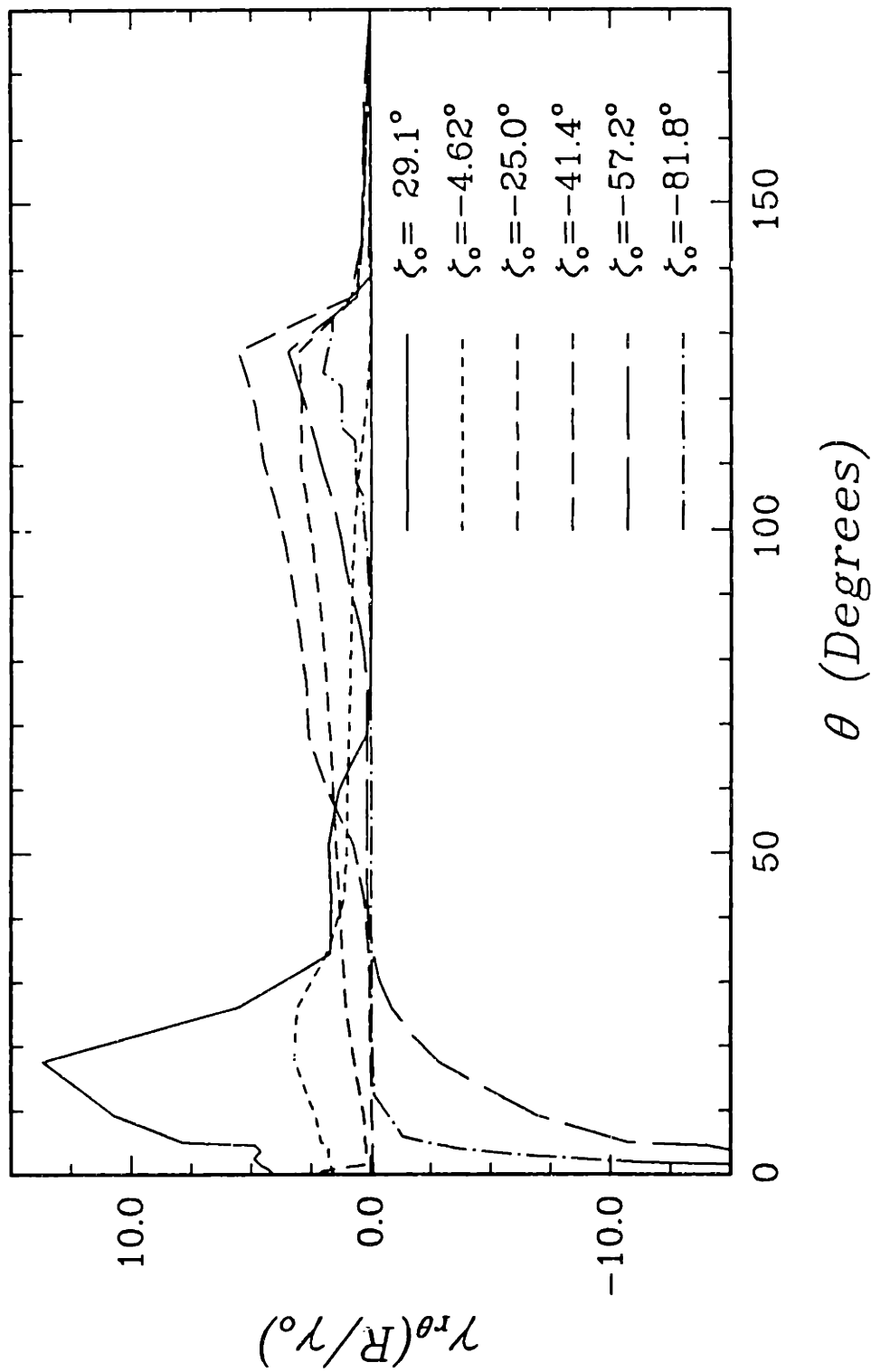


Figure 4.29 Angular variation of normalized $\gamma_{r\theta}$ shear strain deep in the plastic zone ($R \approx \gamma_0$) for a SSY traction-free interfacial crack-tip at various values of ζ_0 ; elastic/perfectly-plastic material atop a rigid substrate ($\epsilon = -0.07923$).

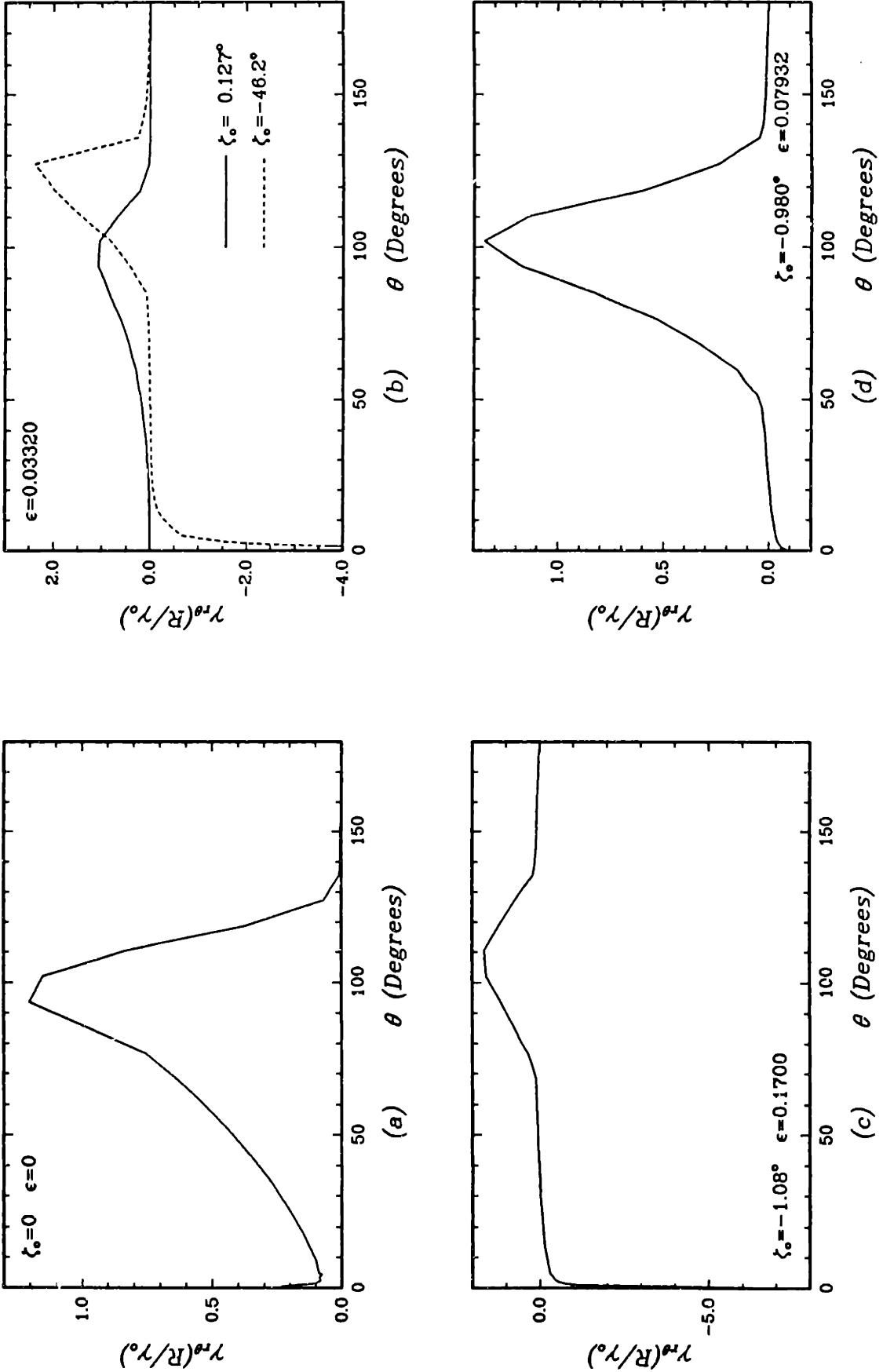


Figure 4.24 Angular distribution of normalized $\gamma_{r\theta}$ shear strain deep within the plastic zone ($R \approx \gamma_0$) for SSY traction-free interfacial crack-tips; elastic/perfectly-plastic material atop a rigid substrate. (a) through (d) show distributions at various values of ζ_0 and ϵ .

scribed for the full admissible range of the ILPA. When the ILPA is between -90° and -50° , the largest strains (in magnitude) occur at the interface [$\gamma_{r\theta}(R/\gamma_0) < -40$], while modest positive strains [$\gamma_{r\theta}(R/\gamma_0) \approx 4$] are produced in the fan region near the crack-face constant-state sector ($\theta \approx 130^\circ$). As ζ_0 approaches zero, negligible interfacial strains are present and the location of maximum strains [$\gamma_\theta(R/\gamma_0) \approx 3$] migrates from $\theta = 130^\circ$ to approximately $\theta = 90^\circ$. For positive ζ_0 , the location of maximum strains is in the centered fan, about 15° to 20° away from the crack-face elastic wedge, and moves toward the interface as the fan region shrinks. Finally, the maximum strains for ζ_0 between 0° and 30° are relatively small [$\gamma_{r\theta}(R/\gamma_0) \approx 2$].

When $\epsilon > 0$, large residual plastic shear strains would appear to accumulate and reside in portions of the non-singular sectors due to the continuously changing angular extent of the fan region. In centered fans the angular locations of the largest radial shear strains generally exist 10° to 15° away from the crack-face elastic-fan transition border, and for small to modest values of ϵ the asymptotic fields and ILPA change slowly with increasing magnitude of \mathbf{K} ($\Delta\zeta_0/\Delta\|\mathbf{K}\| = 2\epsilon/\|\mathbf{K}\|$) as compared to the plastic zone size ($\Delta r_p/\Delta\|\mathbf{K}\| = 2r_p/\|\mathbf{K}\|$). Thus, by the time an elastic sector is positioned in a region previously occupied by a centered fan (where large strains existed), the plastic zone size and blunted crack-tip opening size would have grown by at least one order of magnitude or more. As the plastic zone size and CTOD grow, the inner limit of the radial extent of the “asymptotic crack-tip fields” ($r = r_p\gamma_0$), also grows. Therefore only a small portion of the elastic sector which is very near the crack tip could potentially contain large (previously singular) residual shear strains ($\gamma_{r\theta} \propto 1/r$), and, mathematically, these residual singular strains would be those that accumulated at $r \gg \gamma_0 r_p$.

Path Dependence of J -Integral

In the parametric study, local crack-tip J -Integrals were only estimated by the VCEM. Nine contours centered about the crack tip were evaluated, and the average of the second to fourth contours are tabulated in *Table 4.8* for various ζ_0 and ϵ . The nine J

estimates typically vary by less than 5%, and except for the case where $\zeta_0 = -57.2^\circ$, no discernible trends are evident; i.e., J does not consistently increase or decrease as $R \rightarrow 0$. In the case where $\epsilon = -0.07923$ and $\zeta_0 = -57.2^\circ$, the J estimate increases by 89% from the ninth to the first contour (as $R \rightarrow 0$). However it is thought that this increase reflects the limited radial extent of the steady-state solution, and therefore it is insignificant. In general, the degree of crack-tip shielding or intensification is strongly dependent upon ζ_0 .

ϵ	ζ_0	$J_{VCEM}/J_{Elastic}$
-0.07923	29.1°	0.43
-0.07923	4.62°	0.77
-0.07923	-25.0°	0.94
-0.07923	-41.4°	1.06
-0.07923	-57.21°	1.11
-0.07923	-81.8°	0.25
0	0	0.90
0.03320	0.127°	0.92
0.03320	-46.2°	0.68
0.07923	-0.980°	0.97
0.1700	-1.08°	0.92

Table 4.8 Local J -Integral values, normalized by the elastic far-field value of J , estimated by the VCEM for various values of ζ_0 and ϵ .

Conclusion

The bi-material traction-free crack-tip fields for an elastic/perfectly-plastic material atop an elastic (or rigid) medium are represented by perfectly-plastic slip-line theory in the upper region and by an elasticity potential in the lower region. This representation is accurate at radial distances less than 1% to 5% of the characteristic plastic zone dimension r_p . The local stress and strain fields are strongly dependent upon the ILPA (ζ_0) and modestly dependent upon the bi-material constant (ϵ) and the Poisson's ratio of the plastically deforming media. No oscillations exist in elastic/perfectly-plastic bi-material crack-tip fields, however, cusps are found in some crack-tip fields which couple portions of the stress state to the radial distance from the crack-tip.

In the upper region, plastic deformation completely surrounds the crack tip for most values of ϵ when the ILPA is negative, thus the interfacial tractions are bounded between $|t_s| \leq k$ and $1.48 < t_n/\sigma_{ys} < 3.30$. In loadings where the ILPA is less than -50° , extremely large shear strains accumulate near the interface. The crack-tip behavior is significantly different for positive ILPA in the sense that elastic sectors are present. Interfacial elastic wedges are found embedded within the plastic zone, and a crack-face elastic sector grows (for $\epsilon > 0$) in angular extent as $|\mathbf{K}|$ increases. Interfacial tractions vary between $0 \leq t_s \leq k$ and $1.7 < t_n/\sigma_{ys} < 2.9$, however, the interfacial strains are typically very small.

The asymptotic fields in the lower elastic region are represented by the superposition of three individual stress fields. The three stress fields are represented by a semi-infinite body with uniform:

1. Shear tractions ($t_s = S\sigma_{ys}$) across half of its free surface.
2. Normal tractions ($t_n = P\sigma_{ys}$) across (the same) half of its free surface.
3. Uniform stress (of magnitude $T\sigma_{ys}$) in the direction parallel to the free surface.

The free surface tractions simulate the conditions existing along the postulated intact interface in the immediate crack-tip proximity. Due to the jump in interfacial shear tractions, the elastic fields in the lower region are logarithmically singular and crack-tip yielding is expected. The radial strain along the interface is not zero, even though the interface is a line of zero extension (according to rigid-plastic slip-line theory).

The elastically-calculated and numerically obtained CTOD, the J -Integral, and the plastic zone shapes can differ appreciably. The CTOD angle ω was smaller than its elastic estimate, and no crack-face contact occurred over the range of ζ_0 explored. However, prior to establishing steady-state asymptotic crack-tip fields, oscillations present during initial plastic deformation may induce crack-face contact within the plastic zone for values of ζ_0 less than the elastically predicted critical values ζ_c , [Eq.(P2.35)]. Although plastic deformation reduces the range of admissible “traction-free crack-tip”

loadings, for many load states it also helps shield the crack-tip. The local J values are lower than the far-field elastic J -Integral by as much as 58%, but the significance of this is unclear.

4.3 Closed Crack-Tip Model

The local behavior around a closed bi-material crack tip varies much less than the local behavior around a traction-free crack tip. The approximated plastic zone shape in *Figure 2.2* is relatively independent of the precise values chosen for β and ν . Because a large lobe extends along the crack face, it is anticipated that the actual plastic zone in the upper medium will always completely surround the crack tip. Even if the same degree of plastic zone suppression occurs along the crack face, as seen in the traction-free model, the plastic zone should still completely engulf the crack tip. *Figure 2.3* shows the approximated plastic zone along with the location of actively yielding integration points from the numerical calculations, represented as black dots. To accommodate plotting, not all of the actively yielding integration points near the crack tip were drawn.

4.3.1 Plastic Fields

The transition from the remote K_{II}^c -field to the asymptotic plastic field is similar to that observed in the traction-free crack-tip model. A steady-state solution is achieved at radial distances less than 1% to 5% of the characteristic plastic zone dimension r_p^c . During this same transition period, the interfacial tractions and the now non-zero crack-face tractions also establish themselves. Similarity profiles of the normalized crack-face and interfacial tractions are shown as functions of the normalized radius, $R \equiv r/r_p^c$, in *Figure 4.25*. (The sign convention for positive normal traction is tensile stress, and shear traction has the same sign as $\sigma_{r\theta}$.) No gaps open along the crack face, and the minimum crack-face traction occurs prior to reaching its steady state value near the plastic zone boundary.

Closed Crack-Tip Traction

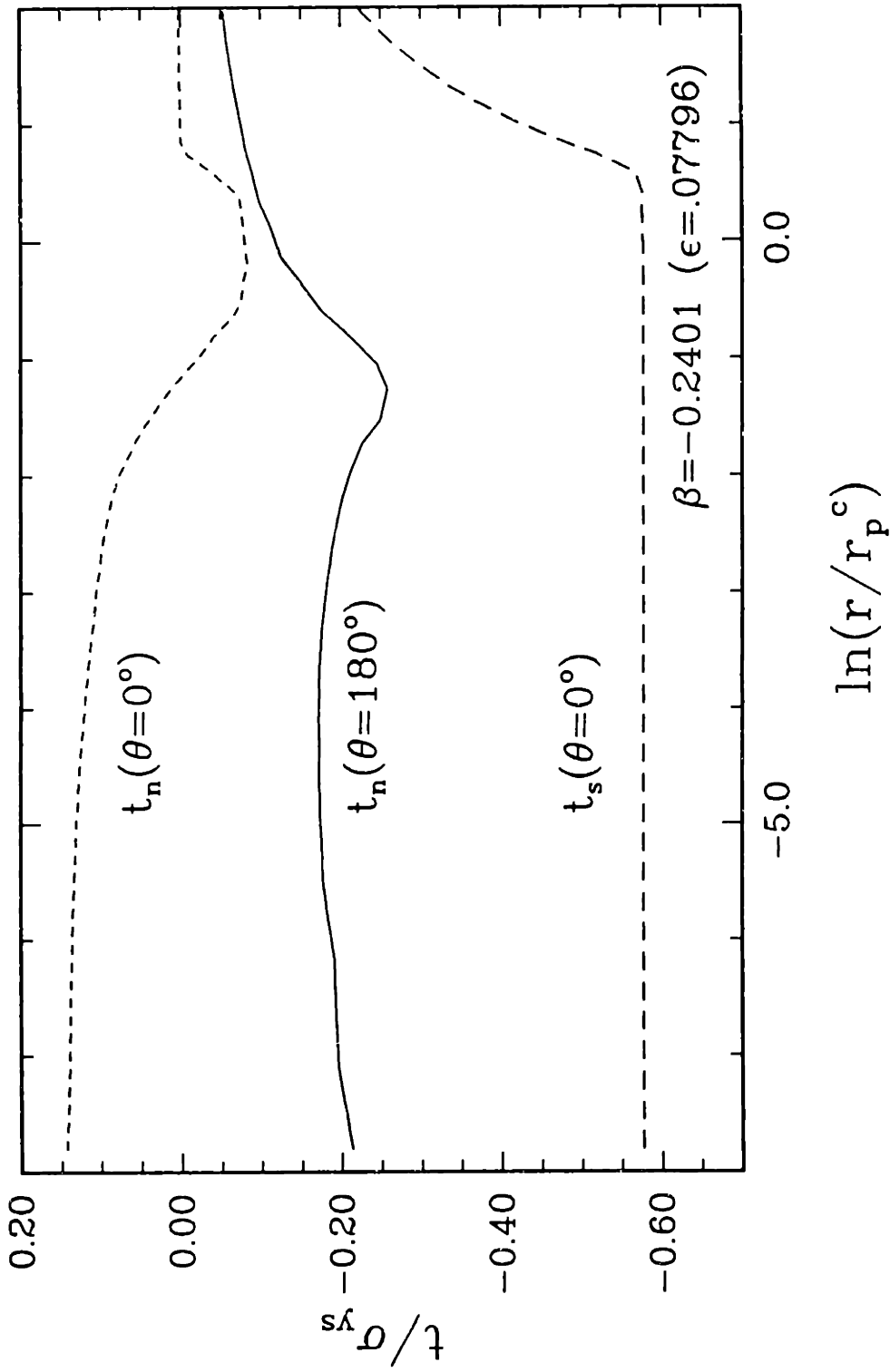


Figure 4.25 The interfacial [$t(\theta = 0^\circ)$] and crack-face [$t(\theta = 180^\circ)$] tractions for a closed bi-material crack tip under SSY conditions; elastic/perfectly-plastic upper region bonded to a rigid substrate.

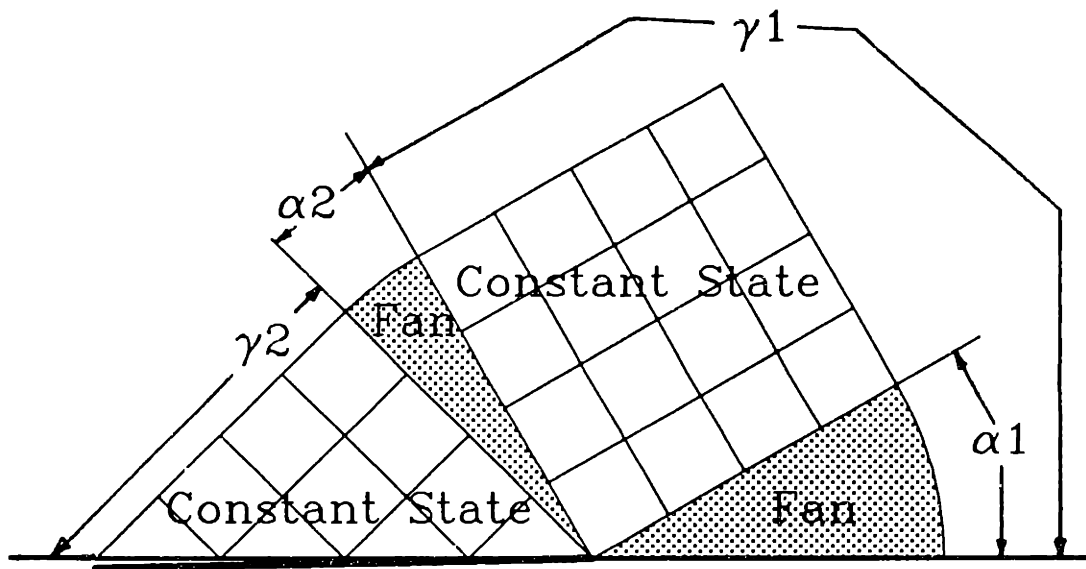


Figure 4.26 Slip-line field at a closed SSY interfacial crack for an elastic/perfectly-plastic upper region bonded to a rigid substrate. See *Table 4.9* for numerical values of indicated angles.

As $r \rightarrow 0$, the asymptotic interfacial and crack-face tractions t take on constant values of

$$t_n = \begin{cases} P\sigma_{ys} & \theta = 0^\circ \\ -Q\sigma_{ys} & \theta = -180^\circ, \end{cases} \quad (4.44)$$

and

$$t_s = \begin{cases} S\sigma_{ys} & \theta = 0^\circ \\ 0 & \theta = -180^\circ. \end{cases} \quad (4.45)$$

The asymptotic crack-tip stress state is completely constructed from fan and constant state regions. A schematic closed crack-tip slip-line field is sketched in *Figure 4.26*, while *Table 4.9* lists the schematic slip-line angles and the crack face and interfacial tractions obtained from the numerical calculations. (The slip-line angles for the closed crack-tip case were extracted from the numerical calculations in the same way as the traction-free crack-tip slip-line angles were.) Due to the crack-face contact, it is necessary to know the precise value of the normal traction on either the crack face or interface in order to construct the stress field in the upper domain. In this closed crack-face case, the crack-tip displacement represents sliding parallel to the interface, $\omega = 180^\circ$, and has a normalized magnitude of $|\delta_{CTOD}\sigma_{ys}/J| = 1.914$.

β	ϵ	$\alpha 1$	$\gamma 1$	$\alpha 2$	$\gamma 2$	P	S	T	Q
-0.2401	0.07796	29°	119°	16°	45°	0.131	$-1/\sqrt{3}$	-	0.183

Table 4.9 Asymptotic SSY slip-line angles and traction coefficients for closed crack-tip model; elastic/perfectly-plastic material atop a rigid substrate.

Computationally, the shear strain at the fan near the crack face extends slightly beyond its purported angular extent. This is likely an artifact of the mesh discretization in this region, since the crack-face constant-state zone has no shear traction and there is no indication of an elastic wedge (see *Figure 2.9*). Thus the transition from constant state to centered fan must occur at $\theta = 135^\circ$. Indeed, the circumferential extent of the elements is nearly equal to the amount by which the shear zone in *Figure 4.27* extends beyond the fan/constant-state boundary. The numerical and assumed asymptotic stress

Closed Crack-Tip Strain Distribution

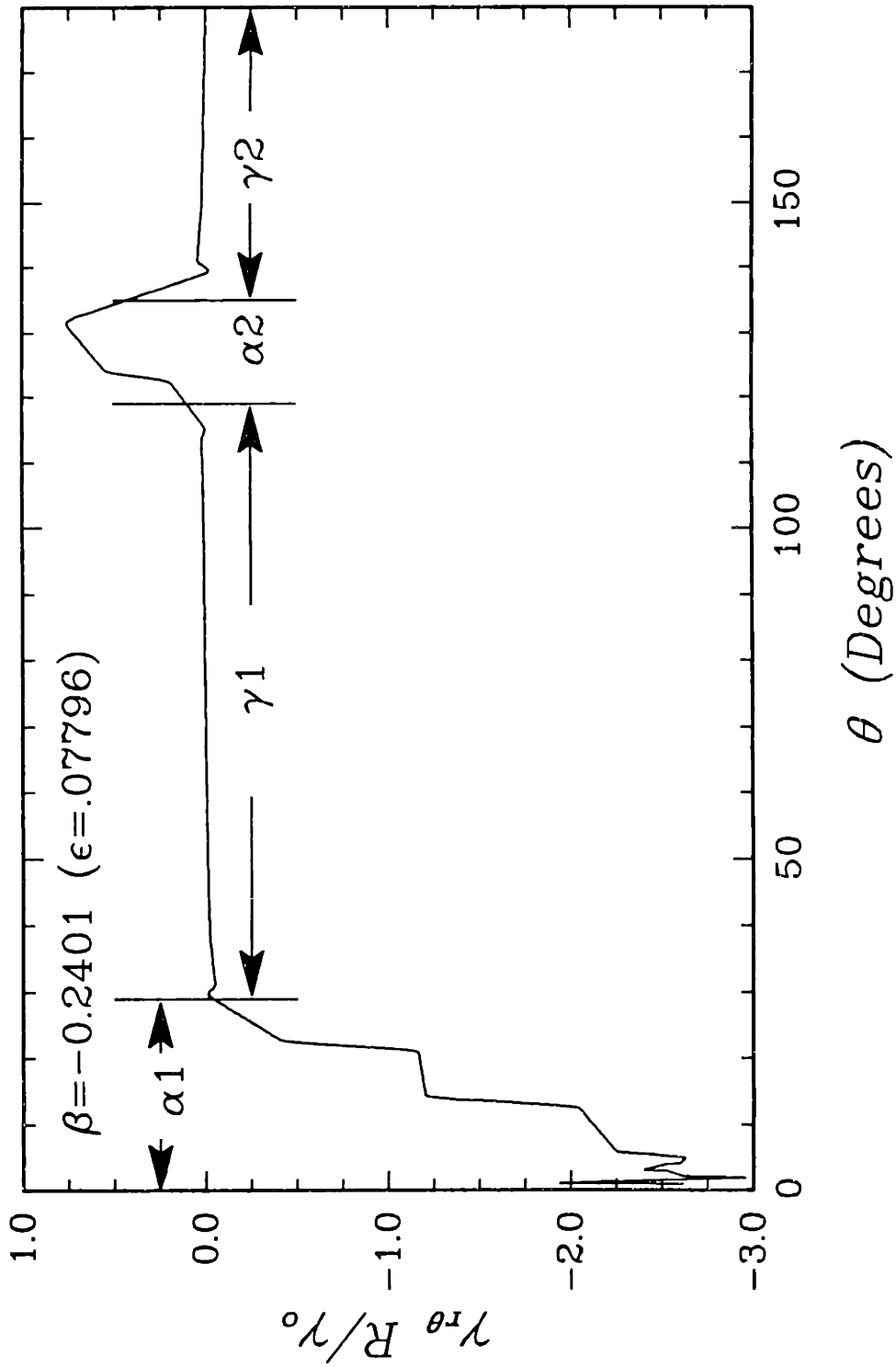


Figure 4.27 Circumferential variation of normalized $\gamma_{r\theta}$ shear strain deep in the plastic zone ($R = r/r_p^c = 3.12 \times 10^{-3}$), for an elastic/perfectly-plastic upper region bonded to a rigid substrate. Angular extents of centered fan and constant state regions of slip-line fields are also indicated.

distributions plotted in *Figure 4.28* differ only near the fan/constant-state borders, again over angular distances which correspond to the angular span of several elements. Excluding mesh discretization error, the assembled and numerically calculated crack-tip fields are in excellent agreement.

It is enlightening to compare the slip-line field, plastic zone shape, and the shear strain distribution. In *Figure 2.3*, the radial lines emanating from the crack-tip represent the slip-line field boundaries, and *Figure 4.27* is a plot of the asymptotic shear strain distribution. The shear strains are largest (in magnitude) at $\theta = 0^\circ$ (negative) and 130° (positive), which correspond to local maximum plastic zone radii. Near the center of the constant state regions the plastic zone radius exhibits a local minimum and the shear strain are nearly zero. It is evident that the radial shear strain distribution significantly influences the plastic zone shape and, to some extent, the local asymptotic stress field, and vice versa.

4.3.2 Elastic Field

Although the lower region was idealized in this work as being rigid, certain features of adjacent elastic fields can be ascertained in the same fashion as they were for the traction-free crack-tip model. Consider the conditions that exist along the common boundary of the elastic and plastic regions. The traction distribution beneath the plastic zone can be idealized such that they are described by Eqs.(4.22) to (4.23) and zero elsewhere. *Figure 4.29* is a schematic representation of the assumed traction distribution. The elastic stress potential for the closed crack-tip model is obtainable by superimposing an additional stress field, attributable to contact traction [$t_n(\theta = \pi) = -Q\sigma_{ys}$], to that previously obtained for the traction-free model Eq.(4.40). The total stress potential from the three individual traction contributions and the general uniform parallel stress field is

$$\phi = -\frac{S\sigma_{ys}}{\pi} \left[\frac{1}{2}y^2 \ln \left(\frac{x^2 + y^2}{(x + r_I)^2 + y^2} \right) + xy \arctan \left(\frac{y}{x} \right) + (x - r_I) y \arctan \left(\frac{y}{x + r_I} \right) \right]$$

Closed Bi-material Crack-Tip Stresses

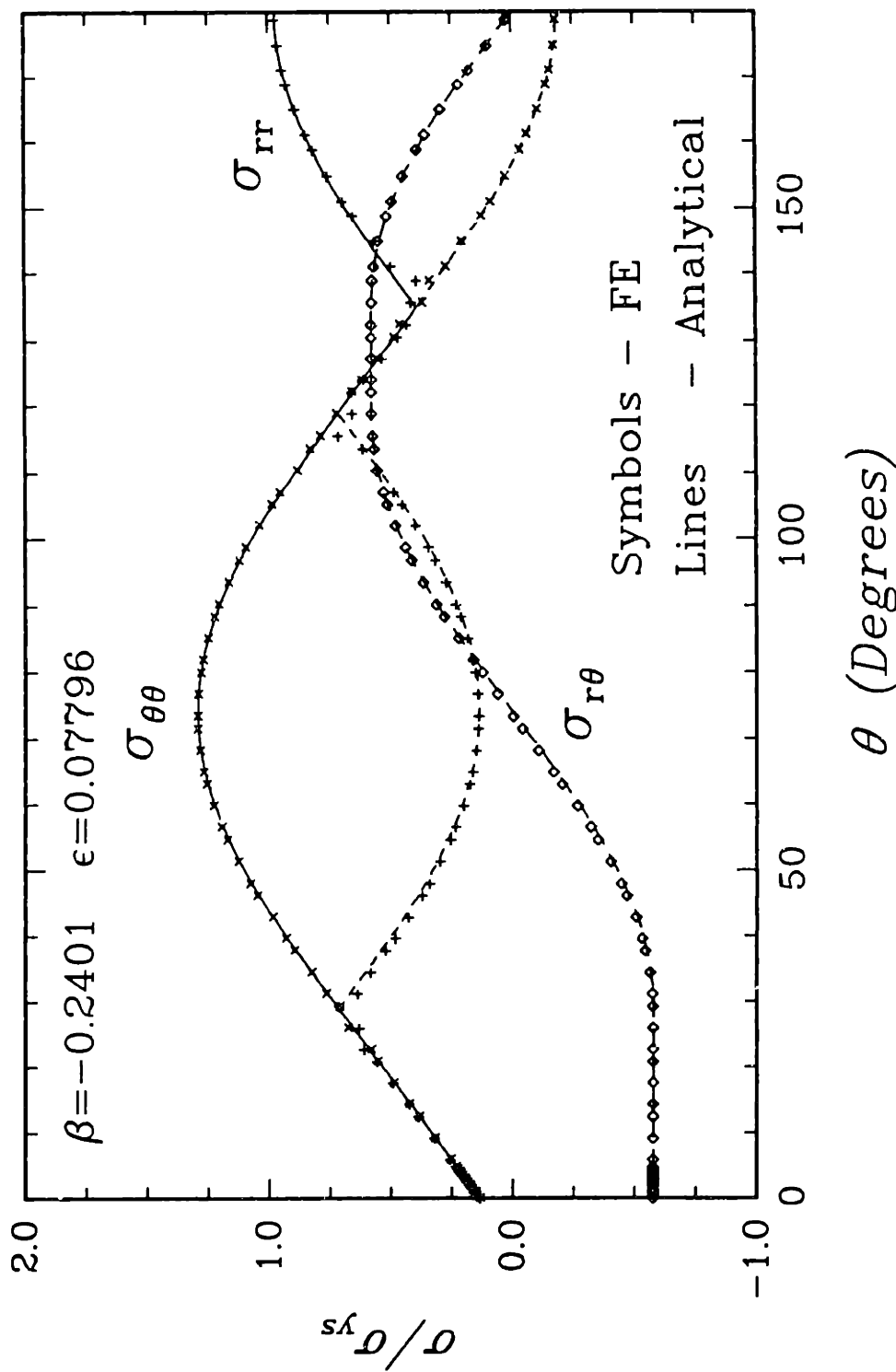


Figure 4.28 Normalized angular stress distribution, from a finite element calculation (plotted with symbols) of contact SSY in an elastic/perfectly-plastic upper region bonded to a rigid substrate and from the inferred slip-line field; $R = 3.12 \times 10^{-3}$, $\beta = -0.2401$ and $\epsilon = 0.07796$.

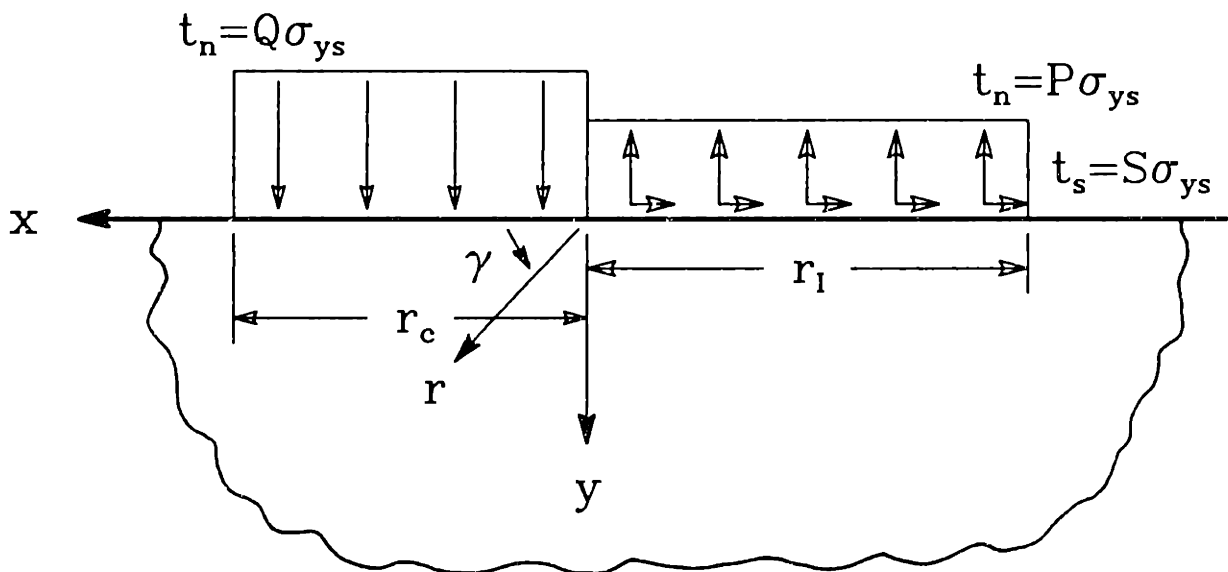


Figure 4.29 Idealized crack-face and interfacial traction distributions for a closed frictionless crack-tip in SSY, showing plastic zone radius along interface (r_I) and crack-face (r_c) and polar (r, γ) and Cartesian (x, y) coordinates.

$$\begin{aligned}
& + \frac{P\sigma_{vs}}{2\pi} \left[(x^2 + y^2) \arctan\left(\frac{y}{x}\right) - xy + (x + r_I) y \right. \\
& \left. - ((x + r_I)^2 + y^2) \arctan\left(\frac{y}{x + r_I}\right) \right] \\
& - \frac{Q\sigma_{vs}}{2\pi} \left[(x^2 + y^2) \arctan\left(\frac{y}{x}\right) + xy - (x - r_c) y \right. \\
& \left. - ((x - r_c)^2 + y^2) \arctan\left(\frac{y}{r_c - x}\right) \right] + \frac{1}{2} T\sigma_{vs} [y^2]. \tag{4.46}
\end{aligned}$$

Here r_c is the size of the plastic zone along the crack face ($\theta = 180^\circ$) and r_I is the size of the plastic zone along the interface ($\theta = 0^\circ$).

The asymptotic crack-tip behavior, as $r \rightarrow 0$, is found by defining $X = x/r_I$ and $Y = y/r_I$, assuming $r_c \approx r_I$, and assuming $X \ll 1$ and $Y \ll 1$. The asymptotic stress potential, as $R_I \rightarrow 0$, is given by

$$\begin{aligned}
\phi = & -\frac{S\sigma_{vs}}{\pi} \left[\frac{1}{2} Y^2 \ln(X^2 + Y^2) + XY \arctan\left(\frac{Y}{X}\right) - Y^2 \right] \\
& + \frac{P\sigma_{vs}}{2\pi} \left[(X^2 + Y^2) \arctan\left(\frac{Y}{X}\right) - XY \right] \\
& - \frac{Q\sigma_{vs}}{2\pi} \left[(X^2 + Y^2) \arctan\left(\frac{Y}{-X}\right) + XY \right] + \frac{1}{2} T\sigma_{vs} [Y^2], \tag{4.47}
\end{aligned}$$

or when expressed in a polar coordinate frame is given by

$$\begin{aligned}
\phi = & -\frac{S\sigma_{vs}}{\pi} \left[R_I^2 \ln(R_I) \sin^2(\gamma) + R_I^2 \gamma \sin(\gamma) \cos(\gamma) - R_I^2 \sin(\gamma) \right] \\
& + \frac{P\sigma_{vs}}{2\pi} \left[R_I^2 \gamma - R_I^2 \sin(\gamma) \cos(\gamma) \right] \\
& - \frac{Q\sigma_{vs}}{2\pi} \left[R_I^2 (\pi - \gamma) + R_I^2 \sin(\gamma) \cos(\gamma) \right] + \frac{1}{2} T\sigma_{vs} \left[R_I^2 \sin^2(\gamma) \right]. \tag{4.48}
\end{aligned}$$

The individual stress components can be obtained directly from the potentials via the relationships in Eqs.(4.2) to (4.4) or Eqs.(4.5) to (4.7).

In general, the elastic stress and strain field for the closed crack-tip model differs fundamentally only slightly from that derived for the traction-free crack-tip model. The addition of the crack-face tractions only contributes to the individual stress component terms of order $Q\sigma_{vs}/\pi$. For non-zero values of S , the stress field is logarithmically singular.

Comparison between the stresses based upon the elastic potential and the numerical calculations are not possible because the lower domain was idealized as being rigid. For

the same reason, explicit values for T were not expressed. As for agreement between the two solutions, one can only speculate that it would be comparable to that achieved in the traction-free crack-tip model (*i.e.*, very good) and would be accurate at radial distances less than 1% of R .

4.3.3 Conclusion

The asymptotic stress field around a closed bi-material crack tip are completely represented by deforming slip-line fields in the upper domain and by an elastic potential in the lower domain. The asymptotic solution has interfacial shear tractions equal to the shear yield strength of the material (k) and small tensile normal tractions ($\sim 0.13\sigma_{ys}$). On the frictionless crack face, the asymptotic compressive normal tractions is also small ($\sim 0.18\sigma_{ys}$). The resulting plastic zone shape reflects certain features of the shear strain distribution and stress distribution.

Although no parametric study was performed, it is anticipated that asymptotic closed-face slip-line fields for an elastic/perfectly-plastic medium adjoint to a dissimilar elastic material are only weakly dependent on β . As discussed previously, the elastically-calculated plastic zone is rather insensitive to the precise values of β and ν used. In the degenerate case $\beta = 0$, the far-field elastic homogeneous mode II solution is recovered, it is therefore expected that as $\beta \rightarrow 0$, $t_n(\theta = \pm\pi) \rightarrow 0$. Finally, the homogeneous mode II slip-line field, whose slip-line angles are $\alpha_1 = 36.8^\circ$, $\gamma_1 = 126.8^\circ$, $\alpha_2 = 8.2^\circ$, and $\gamma_2 = 45^\circ$ for $\theta > 0$ (Hutchinson, 1968), does not differ substantially from the asymptotic field obtained for $\beta = -0.2401$.

4.4 Limitations

In this work the term “asymptotic crack-tip fields” has been extensively used to describe local crack-tip phenomena, but what are asymptotic fields? Webster (1979) defines an asymptote as “a line which continually approaches nearer to some curve, but, though infinitely extended, would never meet it.” Fracture mechanics commonly

uses expressions to reproduce the dominant features and near-tip behavior which it terms as asymptotic. However these relationships are not truly asymptotic by definition in that they are only representative over a *discrete* interval because their underlying assumptions simplify and exclude a portion of the physics and mechanics. This section defines the limits for which the asymptotic characteristics are appropriate by identifying length scales for which the simplifications or omissions made in the mechanics are admissible.

In Chapter 2 it is established that the asymptotic elastic field equations [Eqs.(2.4) to (2.7)] represent SSY traction-free crack-tips for radial distances between $3r_p$ and $l/10$, where r_p is the characteristic plastic zone dimension and l is the characteristic geometric length. The outer limit defines the point where the local solution reproduces only 90% (in magnitude) of the full elasticity stress solution. (This happens because the asymptotic solution excludes the homogeneous far-field contribution.) The inner limit represents the point where the solution is significantly influenced by the exclusion of inelastic deformation. Deep within the plastic zone “steady-state inelastic” behavior appears at $r \approx 0.01r_p$, where deformation in plastic sectors is dominated by incompressible plasticity and the affects of compressible elasticity are generally negligible. Therefore inelastic (SSY) asymptotic crack-tip fields composed of some perfectly-plastic sectors describe the actual fields at radial distances less than $0.01r_p$. (Recall, it is necessary to account for compressible elasticity in constant state sectors when an elastic-wedge/fan transition exists.) Thus by examination of the mechanics or physics excluded, both bounds of the asymptotic elasticity solution and the outer bound of the inelastic asymptotic crack-tip solution have been quantified for SSY conditions. The minimum radial distance at which inelastic asymptotic crack-tip fields depict the actual crack-tip behavior is dependent upon various material attributes, mathematical assumptions, and micro or macro phenomena.

The discussion of limiting length scales, used to define the inner bound of the inelastic crack-tip fields, is divided into two parts. The first part identifies physical ma-

terial attributes in view of the necessary continuum assumptions to model them, and it qualitatively elaborates upon their associated mathematical length-scale restrictions. Quantitative results are not formally stated because the actual size varies considerably between different material systems. The second part quantitatively determines limitations imposed by modeling assumptions made and by the evolution of crack-tip features. The largest feature or mechanism is assumed to be the minimum distance for which inelastic asymptotic crack-tip fields are appropriate.

4.4.1 Physical Attributes

The physical material structure limits the representative element size necessary for continuum constitutive relationships to homogenize and accurately describe material behavior. For example, in crystalline materials deformation is produced by discrete movement of dislocations which each translate the crystal lattice by the interatomic distance. When many slip systems are active many discrete slip events must be averaged over a representative volume which is several hundred or thousand Burger's vectors per side, to achieve a continuum. Isotropy, as used in these analyses, poses additional restrictions because no macro preferential slip directions are allowed. Although many slip systems exist in metals [*i.e.*, aluminum (FCC) has 12 possible independent slip directions], the representative volume must usually span many grain diameters to yield an isotropic response. Second phase and intermetallic particles restrict the minimum continuum volume size, when they exceed the primary grain size or if they preferentially impede directions of deformation. In non-metallic systems the minimum volume size is a function of some characteristic material dimension. For example, in particle reinforced composites the particle diameter or mean particle spacing is the characteristic material dimension, while in ceramics and polymers the characteristic dimensions are the grain size and length of the molecular chains, respectively.

In addition to the constraints associated with the bulk materials are those constraints which arise from the interfacial thickness and properties. Use of an ideal-

perfect interface assumes *a priori* that interfacial mechanical properties are equivalent or stronger and stiffer than the surrounding bulk media and that perturbations introduced by the actual interface, such as local crack-tip separation, are confined to a small region. As discussed in Chapter 1 the interfacial make-up and size scale varies widely and the interfacial resolution limits imposed must be assessed individually for each material system.

4.4.2 Mathematical and Evolutionary Limitations

When not restricted by physical attributes, it is anticipated that the inner range of the asymptotic solution is limited by:

1. The formation of a blunted crack-tip and the emergence of the CTOD as the characteristic length in the inelastic (SSY) asymptotic field.
2. The use of linearized kinematics.
3. The idealization that the lower domain behaves elastically.

To ascertain the limitations that these impose, an estimate for the critical length scale of each is made.

For planar homogeneous cracks, the CTOD (δ_{CTOD}) is typically estimated to be (Hellan, 1984)

$$\delta_{CTOD} = 0.6 \frac{J}{\sigma_{ys}}, \quad (4.49)$$

and an estimate of δ_{CTOD} for interfacial cracks is made by evaluating Eq.(P2.32) at $\zeta = \zeta_0$ and $r = r_p$ which yields

$$|\delta_{CTOD}| = \frac{4\sqrt{2}}{\pi\sqrt{1+4\epsilon^2}} \frac{J}{\sigma_{ys}}. \quad (4.50)$$

Equation (4.50) overestimates the homogeneous δ_{CTOD} by a factor of three, and, based upon the other data in Chapter 4 for an elastic/perfectly-plastic material atop an elastic medium, typically overestimates the actual $|\delta_{CTOD}|$ by a factor of 2 to 3. For

comparison purposes, it is convenient to compare δ_{CTOD} to r_p . Division of Eq.(4.50) by r_p and by a factor of 2 (to account for the overestimation) gives

$$\left| \frac{\delta_{CTOD}}{r_p} \right| = \frac{\sigma_{ys}}{2} \sqrt{\frac{2}{1+4\epsilon^2}} \left(\frac{1-\nu_1}{\mu_1} + \frac{1-\nu_2}{\mu_2} \right) \quad (4.51)$$

or

$$\left| \frac{\delta_{CTOD}}{r_p} \right| = \frac{\sqrt{6}}{2\sqrt{1+4\epsilon^2}} \gamma_0 \left[1 - \nu_1 + \frac{\mu_1}{\mu_2} (1 - \nu_2) \right]. \quad (4.52)$$

Here γ_0 is the initial yield strain of the material in the upper region and the subscripts 1 and 2 refer to the upper and lower domains, respectively. For many material combinations the normalized magnitude of the CTOD is of order $|\delta_{CTOD}/r_p| \approx \mathcal{O}(\gamma_0)$.

Use of linearized kinematics fails when strains and rotations are no longer "small." To estimate the size of the strains and thereby infer the relative size of the rotations, the behavior of the largest strain component in a fan region, $\gamma_{r\theta}$, is considered. From Eq.(4.10) the asymptotic shear strain behavior in a fan region is approximately

$$\gamma_{r\theta} \approx A(\theta, t) \frac{\gamma_0}{R}, \quad (4.53)$$

where R is the normalized radial distance from the crack-tip and $A(\theta, t)$ is the angular distribution of shear strain. As stated previously, $A(\theta, t)$ is of order unity because at the edge of the plastic zone ($r = r_p$ or $R = 1$) the shear strain must just equal the yield shear strain ($\gamma_{r\theta} = \gamma_0$). With the assumption that $A(\theta, t) \approx 1$ and by use of the rather loose definition that strains of order unity are no longer small, the assumption of linearized kinematics is valid for radial distances such that

$$r > \gamma_0 r_p \quad \text{or} \quad R > \gamma_0. \quad (4.54)$$

For reference, a typical value of γ_0 for aluminum is 7.2×10^{-4} (Hertzberg, 1976).

In the lower domain use of an elastic material idealization is acceptable as long as the stress state is not sufficient to cause inelastic deformation. At the crack-tip the shear traction jumps by $|\mathcal{S}\sigma_{ys}|$ from the crack-face to the interface, and this step-function jump in t_s produces logarithmically singular stresses in the elastic domain

whenever $S \neq 0$. Plastic deformation is anticipated in the elastic half-plane for all non-zero values of S .

A “rough” interfacial plastic zone size is estimated by evaluating the elastic stress components at $\theta = 0^\circ$ and by determining the radial distance where the Mises equivalent stress equals $\sigma_{\nu s_2}$, the yield stress of the “elastic” lower material. Substituting the stress components, Eqs.(4.41) to (4.23), into the Mises stress expression, Eq.(2.31) (retaining only the logarithmically singular portion of σ_{rr}), and solving for the radial distance r_{p_2} at which $\bar{\sigma}_2 = \sigma_{\nu s_2}$ yields (for $S \neq 0$)

$$\frac{r_{p_2}}{r_p} \approx \exp \left\{ \frac{F P \pm \sqrt{(F P)^2 - 4D (3S^2 + D P^2 - (\sigma_{\nu s_2}/\sigma_{\nu s})^2)}}{2DS/\pi} \right\}. \quad (4.55)$$

Here F and D are defined in Eqs.(P2.A.14) and (P2.A.15), respectively. For Eq.(4.55) to have physical significance, it is required that

$$\left(\frac{\sigma_{\nu s_2}}{\sigma_{\nu s}} \right)^2 > 3S^2 + P^2 \left(D - \frac{F^2}{4D} \right). \quad (4.56)$$

When P and S take on their maximum observed values of $P = 3.27$ and $S = 1/\sqrt{3}$ the actual elastically inferred [not estimated by Eq.(4.55)] size of plastic deformation along the interface for $\nu = 0.3$ is $r_{p_2}/r_p \approx 1.08 \times 10^{-2}$ for $\sigma_{\nu s_2}/\sigma_{\nu s} = 3.0$ and $r_{p_2}/r_p \approx 3.38 \times 10^{-5}$ for $\sigma_{\nu s_2}/\sigma_{\nu s} = 4.0$. A more intuitive understanding is obtained from examination of *Figure 4.30*. By use of the stress expression, Eqs.(4.41) to (4.23) the elastically-calculated plastic zone in the lower half-plane is plotted for $P = 3.27$, $S = 1/\sqrt{3}$, and $T = -0.5$ for several ratios of $\sigma_{\nu s_2}$ to $\sigma_{\nu s}$; *i.e.*, $\sigma_{\nu s_2}/\sigma_{\nu s} = 2.5, 3.0, 3.5, 4.0$, and 4.5 . The characteristic plastic zone size of the upper domain (r_p) is used to normalize the scale of this figure. Because the stress fields are logarithmically singular, the size of the plastic zone decays rapidly as $\sigma_{\nu s_2}/\sigma_{\nu s}$ increases. The elastically-calculated plastic zones for $\sigma_{\nu s_2}/\sigma_{\nu s} \geq 3.5$ are not resolvable on this size scale. For material combinations where $\sigma_{\nu s_2}/\sigma_{\nu s}$ is greater than 3, the maximum plastic zone radius extends less than 0.1% of r_p for the extreme interfacial conditions and, for many metallic polycrystallines, $r_{p_2}/r_p < \gamma_0$.

Lower-Elastic Plastic Zone

$$\nu=0.342 \quad P=3.27 \quad S=k \quad T=-0.5$$

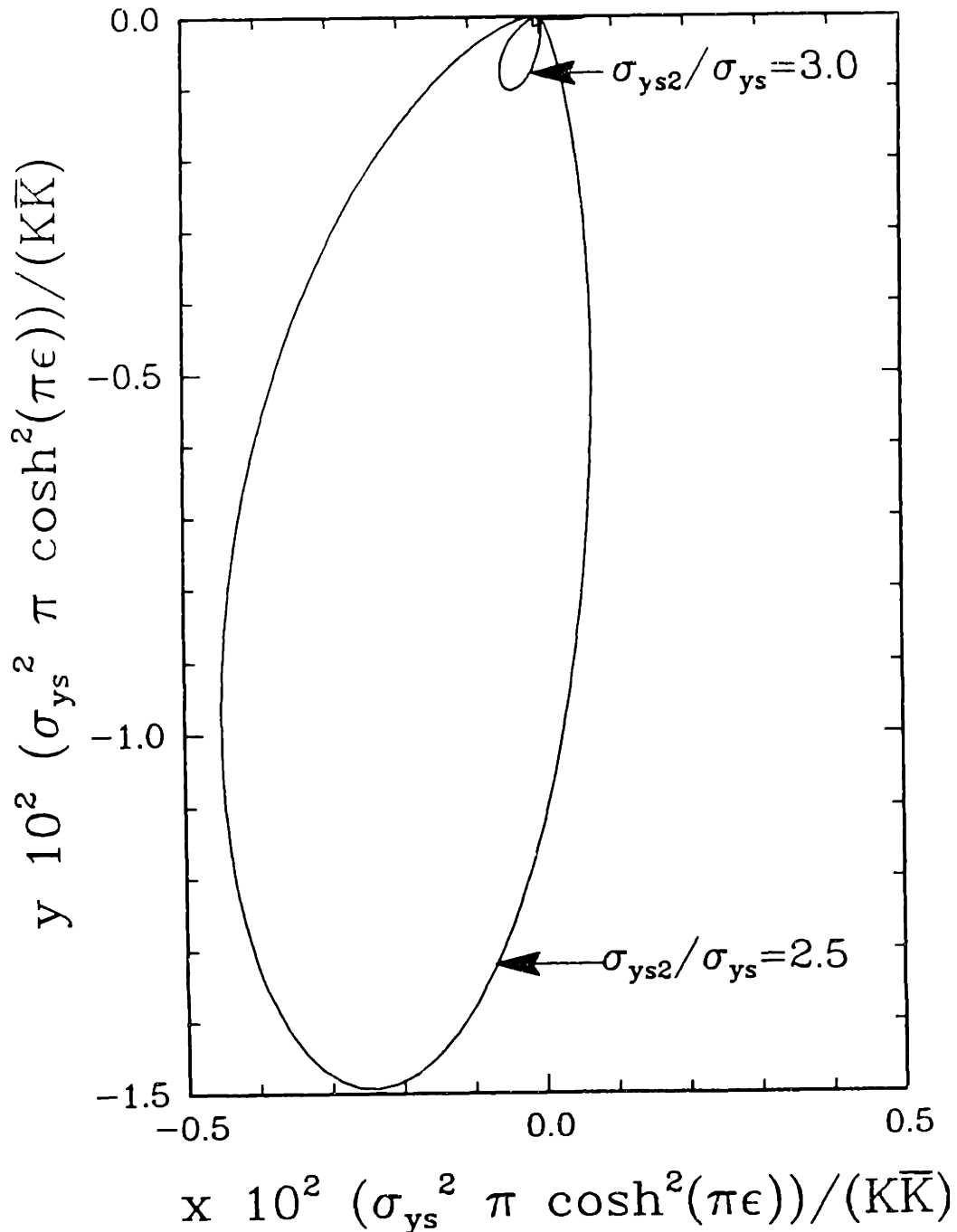


Figure 4.90 Elastically calculated yield zone for lower elastic half-space with constant normalized shear ($t_s = 0.57$) and normal ($t_n = 3.27$) tractions applied on $y = 0$ for $x \geq 0$. Scales are normalized with respect to the characteristic traction-free plastic zone radius.

When the specific material structure is excluded, it is evident that the SSY asymptotic crack-tip fields presented in sections 4.2 and 4.3 are usually applicable over the normalized radial range of $\gamma_0 < R < 0.05$. At radial distances smaller than this the assumptions of linearized kinematics and a mathematically sharp crack tip are violated, and the use of an elastic lower half-space may be inappropriate. When material structure is considered, the restrictions arise from the minimum representative element size necessary to model the material behavior as a continuum, and the actual limiting factor are only established after particular materials and their properties are identified.

Chapter 5

Summary and Discussion

In this final chapter, a brief summary qualitatively highlighting the major features of the two interfacial crack-tip models will be presented. It will touch on the major aspects of both the elasticity and plasticity solutions. Observations regarding some solution aspects and associated implications will also be discussed. This includes observations regarding crack-face conditions and the ILPA, and the anticipated effect that altering material combinations would have on interfacial separation. Finally, some suggestions regarding the direction of further work will be made.

5.1 Summary

Before reviewing specific details of the interfacial fracture mechanics, an overview of the various analyses and components which interconnect, forming a complete interfacial crack framework, is presented. Reviewing of the two commonly accepted interfacial crack-tip elasticity solutions identifies the parameters which quantify the asymptotic elastic fields, their admissible ranges, and the dominant features present in each. When appropriate, corresponding relationships between various elastic variables present in each idealization provide a link between the two models. Using the elasticity solutions, approximate descriptions of contained inelastic deformation embedded in a dominant asymptotic elastic crack-tip field (SSY) are given, along with the parameters needed to describe the plastic zone boundary. Presumably, the same variables which uniquely

relate the plastic zone shape to the asymptotic elastic solution also uniquely relate the asymptotic (inelastic) crack-tip behavior to the asymptotic elastic solution. Far-field loads producing physically admissible elastic crack-tip conditions are determined by excluding the crack-face behavior in regions where inelastic deformation is anticipated. Corresponding limits on the inelastic crack-tip parameters are then formulated, thereby reducing the spectrum of admissible inelastic crack-tip loadings. Finally, for a specific constitutive idealization, the complete range of asymptotic inelastic crack-tip fields is quantified as a function of the inelastic parameters. The discussion which follows details this schematic overview.

The asymptotic elastic behavior of interfacial cracks which occur between dissimilar isotropic media is reviewed. Traction-free crack-face boundary conditions result in oscillatory elastic fields as well as crack-face contact and mathematical interpenetration. Use of the complex traction-free bi-material stress intensity factor \mathbf{K} requires defining both a magnitude and phase angle. (Two parameters are necessary to describe the elastic singularity of a traction-free interfacial crack.) Some ambiguity exists in expressing \mathbf{K} because the phase angle of \mathbf{K} changes when different length units are used. Physically inadmissible crack-face interpenetration is eliminated by considering a closed (frictionless) crack-tip model. This model contains no oscillatory fields, and its asymptotic nature is similar to that of the homogeneous mode II solution. The sign of the (scalar) closed bi-material stress intensity factor, K_{II}^c , is restricted to ensure compressive normal crack-face tractions. When defining the elastic singularity of a closed frictionless interfacial crack, only one parameter is required. Finally, both elastic crack-tip models predict unbounded stresses as the crack tip is approached.

For both crack-tip models, approximate SSY elastically-calculated plastic zones are obtained as the locus of points where the elastically-calculated Mises stress equals the tensile yield stress. This is the first time such an approach has been used to “semi-formally” extract the inelastic behavior around interfacial crack tips. From this approach, it is found that traction-free crack-tip plastic zones grow in a periodic manner,

with respect to the ILPA, $\zeta_0 = \angle \mathbf{K} + \epsilon \ln \frac{\mathbf{K}\bar{\mathbf{K}}}{\sigma_{\nu}^2 \pi \cosh^2(\pi\epsilon)}$, and scale approximately with the characteristic plastic zone dimension, $r_p = \mathbf{K}\bar{\mathbf{K}}/(\sigma_{\nu}^2 \pi \cosh^2(\pi\epsilon))$; however, the plastic zone shapes change continuously as $\|\mathbf{K}\|$ increases since ζ_0 also changes with increasing $\|\mathbf{K}\|$. The elastically-calculated plastic zone expression modestly represents the overall size and features of the plastic zone for strain hardening and elastic/perfectly-plastic materials atop rigid or elastic substrates.

For positive ζ_0 , the elastically-calculated plastic zone expression predicts crack-face plasticity; however, for elastic/perfectly-plastic materials bonded to an elastic or rigid substrate, no crack-face plastic deformation is observed. (This is an unexpected feature since in homogeneous plane-strain stationary and quasi-static growing crack tips, active plastic deformation occurs on the crack flanks.) The closed crack-tip plastic zone approximation weakly depends upon the bi-material constant and scales with the characteristic closed plastic zone dimension, $r_p^c = 3K_{II}^c/2\sigma_{\nu}^2$. No changes in the closed plastic zone shape occur with increased load, and the homogeneous mode II characteristics are completely recovered when the bi-material constant is equal to zero. It is learned from the elastically-calculated plastic zone expressions, that it is necessary to have both a phase angle and a load magnitude to describe the inelastic traction-free crack-tip fields, while only a load magnitude and the assurance that a sufficiently large contact length exists are required to quantify the closed crack-tip fields.

The crack-tip loads which provide traction-free or closed crack-tips are approximately identified by determining when crack-face contact occurs outside the elastically-calculated SSY plastic zone. Previously, discussions concerning the admissibility of the two elastic crack-tip models usually eliminated one crack-face idealization based upon so called “physical” reasons; *e.g.*, “the crack must be traction-free because the contact length is extremely small and on the order of the interatomic spacing distance,” or “the crack tip is closed since interpenetration is predicted and is physically inadmissible.” This unified approach shows that both interfacial idealizations are admissible for SSY, and provides explicit mathematical expressions to define the loads producing traction-

free or closed crack tips. For the right hand crack tip of a Griffith crack geometry, the far-field loads which produce open or closed elastic crack-face conditions are mapped. A region, termed SSC, exists where, simultaneously, the contact length is small compared to the crack length and the plastic zone size is small with respect to the contact length. Explicit relationships between K and K_{II}^c are established for SSC based upon equivalent energy release rates. In general, determination of the appropriate elastic crack-tip model can be made for most geometries, however, the precise contact length and closed form stress intensity factors are only known for a few geometries.

The numerical procedure used in identifying the SSY asymptotic interfacial crack fields between an elastic/perfectly-plastic material and an elastic or rigid material required implementation of an effective inelastic constitutive integration operator and extension of the boundary layer formulation to bi-materials. These numerical reduction techniques were necessary, especially when one considers that each parametric analysis represents an investment of one hundred to three hundred computational hours, and the quarter wave-length analysis consumed more than seven hundred computational hours on one computational element of an Alliant FX-8 mini super-computer. To demonstrate that the boundary layer formulation had indeed been extended correctly for bi-materials, an example point load elasticity problem was performed.

The asymptotic (inelastic) traction-free crack-tip fields contained some very unusual features. The cusp and elastic sectors found in the SSY traction-free crack-tip solutions have not been observed before in homogeneous plane-strain (stationary or quasi-static) crack fields. These cusps couple the stress state in the quasi-constant state sector to the radial distance from the crack tip and propagate as ζ_0 changes or, for proportional monotonic loading, as $\|K\|$ increases. The elastic crack-face and interfacial sectors evolve with ζ_0 and may or may not contain residual plastic strain depending upon ζ_0 and the sign of ϵ .

Qualitatively, the traction-free SSY asymptotic fields for the complete range of admissible ζ_0 are assembled, and from this the crack-tip behavior for proportional

monotonically increasing loads is described. At fixed radial locations deep within the plastic zone, the SSY asymptotic fields are assembled from centered fans, constant state, quasi-constant state, and elastic sectors. Excluding the cusp effects, the crack-tip stress and strain fields are not oscillatory for an elastic/perfectly-plastic material bonded to an elastic or rigid material, unlike those obtained by Shih and Asaro (1987) for deformation theory based strain hardening materials. The asymptotic crack-tip fields continuously evolve with ζ_0 , and, in general, only contain elastic sector(s) for positive ζ_0 . Crack-tip shielding lowers the local J -Integral, as compared to the far-field elastic J , by as much as 75%, but the degree of shielding varies considerably with ζ_0 . Moreover, for some values of ζ_0 the local J is actually larger than the far-field elastic J . As is anticipated, finite crack-tip opening displacements occur for all cases analyzed. However, the CTOD angle is always less than the elastic estimate, indicating that crack-face contact may occur within the plastic zone when no crack-face contact exists outside the plastic zone. Near the crack tip, deep within the plastically deforming interfacial region, the triaxiality, defined as $\sigma_{kk}/3\bar{\sigma}$, may exceed that of the Prandtl stress distribution and reach 3.30. Because of this, the interfacial tractions are bounded; *i.e.*, $0 \leq t_n/\sigma_{ys} \leq 3.30$ and $|t_s| \leq k$, but depend strongly on ζ_0 .

No unusual features appear in the closed crack-tip model for a rigid medium beneath an elastic/perfectly-plastic medium. The asymptotic crack-tip fields are composed of two constant state and two centered fan sectors whose angular extent and arrangement are similar to homogeneous mode II fields. Compressive crack-face tractions extend from the elastic asymptotic fields, through the plastic fields, all the way to the crack-tip. Appreciable interfacial shear strains develop in the deforming medium.

For both crack-tip idealizations, asymptotic crack-tip fields in the lower elastic medium are completely described by the elastic potential for the closed crack-tip case. This potential is constructed by idealizing the interfacial tractions as constant beneath the plastic zone and zero elsewhere. It is also assumed that uniform compressive tractions exist along the crack-face within the plastic zone (the magnitudes of which are

zero in the traction-free crack-tip model). A uniform tensile field, oriented parallel to the interface, is superimposed to complete the potential. Due to the jump in shear traction at the crack-tip, the resulting field is logarithmically singular, and local crack-tip yielding is anticipated. However, for “elastic” materials with a yield strength three or more times greater than the yield strength of the perfectly-plastic material, “elastic” yielding does not restrict the application of these results.

The method used to identify the crack-tip idealization, in conjunction with the parameters necessary to define elastic and SSY inelastic crack-tip deformation, represents a rigorous framework usable in systematically quantifying interfacial crack-tip behavior. Via this framework one can determine the asymptotic stress, strain, and interfacial behavior, based upon the far-field loads and constitutive assumptions, and (by inference) provide the requisite interfacial properties necessary for sustaining the integrity of interfacial cracks. Evaluating the interfacial crack-tip conditions for a particular geometry (whose components’ constitutive behavior can be idealized as elastic and elastic/perfectly-plastic, respectively) is made as follows. First the elastic crack-tip singularity and contact length must be quantified by either determining K or K_{II}^c (and/or \mathcal{G}) and δ via numerical solutions, tables containing known solutions, *etc.* Some parameters may not be directly obtainable, however their values might be inferred by using the approximations and relationships identified in Chapter 2; *e.g.*, approximating δ from K by Eq.(2.43). Based upon this information, the bi-material constant, and the yield strength of the material, the characteristic plastic zone dimension can be compared to the contact length, thereby establishing if and when either of the two models are appropriate. Alternatively, for certain geometries and loading conditions a load map might be consulted to determine the appropriate crack-tip idealization. If the crack tip is closed (and frictionless), the asymptotic crack-tip fields are those associated with the particular values of β (and ν). On the other hand if a traction-free crack tip exists, ζ_0 must be evaluated, and then, based upon the values of ζ_0 , ϵ , and ν , the asymptotic crack-tip fields can be “looked up.” Section P2.B contains a numerical

example showing how SSY traction-free crack-tip conditions are established and how ζ_0 is evaluated for a particular geometry.

5.2 Discussion

As discussed in Chapter 1, the purpose of doing this work is to quantitatively describe the material state surrounding an interfacial crack tip. It is believed that since the largest stresses and strains evolve in this area, interfacial separation or crack deflection is completely governed by the behavior within the immediate crack-tip proximity. By analyzing and identifying the deformation patterns accompanying the maximum stresses, strains, and interfacial tractions, insight might be gained into the mechanisms and conditions which initiate separation. Unfortunately, this work only provides the conditions which must be sustained prior to unstable crack propagation and is limited to only one constitutive idealization. However, in conjunction with this study and experimental observations and measurements, the feasibility and admissibility of specific failure mechanisms postulated to be active in certain materials can be systematically evaluated.

Independent of the many observations and classifications made in regard to interfacial cracks, the present work is far from conclusive, even for elastic/perfectly-plastic materials bonded to elastic or rigid substrates. Some final comments will be made regarding interpretational aspects of the analyses, modifications to various quantities and definitions, and areas which warrant further investigation.

5.2.1 Crack-Face Contact

Various issues pertaining to the elastic and plastic crack-tip fields have been identified, with considerable attention to excluding the physically inadmissible phenomenon of crack-face interpenetration. *In SSY the complete asymptotic elasticity solution is recovered sufficiently far away from regions of inelastic crack-tip deformation, independent of whether the crack-faces are open or closed in the plastic zone.* Therefore,

crack-face contact within the plastic zone has no consequence upon the elastic crack-face conditions since it is the elastic solution which drives the inelastic deformation in SSY, and not vice versa. For proportional monotonically increasing far-field loads, conclusions based solely upon the asymptotic elasticity solutions are valid at distances larger than several times the characteristic plastic zone size, but still small compared to the next relevant characteristic geometric dimension. Within the limitations discussed in Section 2.3.3, the actual elastic crack face *is open* whenever crack-face contact or interpenetration is not predicted, independent of the crack-face conditions within the plastic zone.

In this study only frictionless closed bi-material crack-tips were considered. In actuality, frictionless crack-tips rarely occur in nature, and friction significantly alters crack-tip behavior. In the bi-material case Comninou (1977b) found that friction reduced the order of the elastic stress singularity for “closed” interfacial cracks. Obviously, the assumption of frictionless closed crack-tip faces represents a simplification which is inappropriate for many situations, and further studies which include crack-face friction are warranted.

5.2.2 Unifying ILPA

The ILPA (ζ_0) is a naturally-arising parameter which is convenient for studying and classifying plastically deformable traction-free crack tips, but it is not comprehensive in that it does not automatically compensate for different values of ϵ and ν . For example, in the elastic approximation for crack-face closure, the critical value of ζ_0 is different for different ϵ . Similarly, the asymptotic inelastic crack-tip fields, for given values of ζ_0 and ν , differ with ϵ . Deformation near open interfacial cracks is only periodic with respect to ζ_0 ; *i.e.*, it is not harmonic. (This is apparent when the additive decomposition of ζ , Eq.(P2.21), is substituted back into the plastic zone approximation, Eq.(P2.6), and the trigonometric functions are expanded. Although ζ_0 appears only as the argument of trigonometric functions, the coefficients which multiply the functions of ζ_0 change

(periodically) as ζ_0 changes.) Thus a relative shift in ζ_0 is not expected to relate the crack-tip fields' evolution (with ζ_0) for different values of ϵ . The ILPAs of the results in Chapter 4 were modified in an attempt to compensate for the dependence of crack-face closure on ϵ , however, this procedure failed to unify the asymptotic crack-tip fields (probably for the reason just discussed).

5.2.3 Anticipated Experimental Observations

To aid in experimental identification of bi-material crack-tip behavior, a qualitative overview describing the anticipated visible crack-tip features follows. Upon application of load, the extent of crack-face contact should become evident. The contact length will depend upon the direction of the applied far-field load, the characteristic geometric dimension and material properties, and it should be independent of the applied load magnitude. Experimental techniques capable of resolving elastic stress or displacement states should allow for detection and identification of the elastic asymptotic crack-tip fields and crack-face displacements. Because the period of oscillation in the traction-free crack-tip model is so large and experimental resolution and specimen size are limited, the experimentally obtained near crack-tip fields will appear as having the conventional square-root dependence on radial distance, whether or not crack-face contact occurs. In materials capable of inelastic deformation, as the load magnitude is increased the next resolvable feature should be the plastic zone. Again, due to the large oscillation period and limited realistic specimen size, the plastic zone shape will appear independent of the applied load magnitude, however, varying the direction of the load on different specimen sizes should produce different plastic zone shapes. For materials whose constitutive behavior is similar to that idealized within this study, plastic zone shapes extending only partially around the crack-tip (in the deforming medium) could be expected for certain loadings.

Resolving the asymptotic inelastic fields is not a realistic expectation at this time. Some materials may localize, *i.e.*, Fe-Si, polycarbonate, leaving traces indicative of the

asymptotic inelastic field. In addition, experimental observations of surface deformation are likely to reflect plane-stress conditions, rather than the plane-strain conditions primarily studied.

In designing experiments, it is important to keep in mind both the types of loads being applied (usually to simulate some real physical situation) and the particular materials, because altering either of these can drastically change the crack-tip conditions. For example, consider the ramifications of evaluating interfacial separation by an interfacial Griffith crack geometry loaded by far-field tension. Sketched in *Figure P2.11* is such a geometry. (To facilitate discussion, allow the magnitude of the far-field tensile load, σ_{yy}^∞ , and material properties to be unspecified.) Following the example shown in Section P2.B, both \mathbf{K} and ζ_0 can be evaluated for a specific set of material combinations and load level. Note that because no far-field shear tractions are applied, \mathbf{K} and ζ_0 are the same at both crack tips. For convention, the material with the lower yield strength is always located in the upper region, and its yield strength is used in evaluating ζ_0 . The evolution of ζ_0 with monotonically increasing SSY loading is shown in *Figure 5.1* for several different values of ϵ . For material combinations whose constitutive behavior can be idealized as an elastic/perfectly-plastic material atop an elastic medium, the crack-tip fields are those which correspond to the particular values of ζ_0 , (ν) and ϵ . Note the large range of ζ_0 produced from this one “simple” test configuration, and that the actual value of ζ_0 is strongly dependent upon the actual value of ϵ for a specific load level of $\sigma_{yy}^\infty/\sigma_{ys}$.

In light of the above example, experimentalists who simulate interfaces by using alternative material models, must insure that not only chemical similitude exists between the actual and model systems, but that mechanical properties (namely the elastic constants) are also scaled appropriately. Using only one model material which is elastically softer than its counterpart in the actual system can change ϵ , possibly even changing its sign, and produce asymptotic crack-tip fields in the model which differ drastically from those produced in the actual system. *Figure 5.1* clearly indicates how sensitive

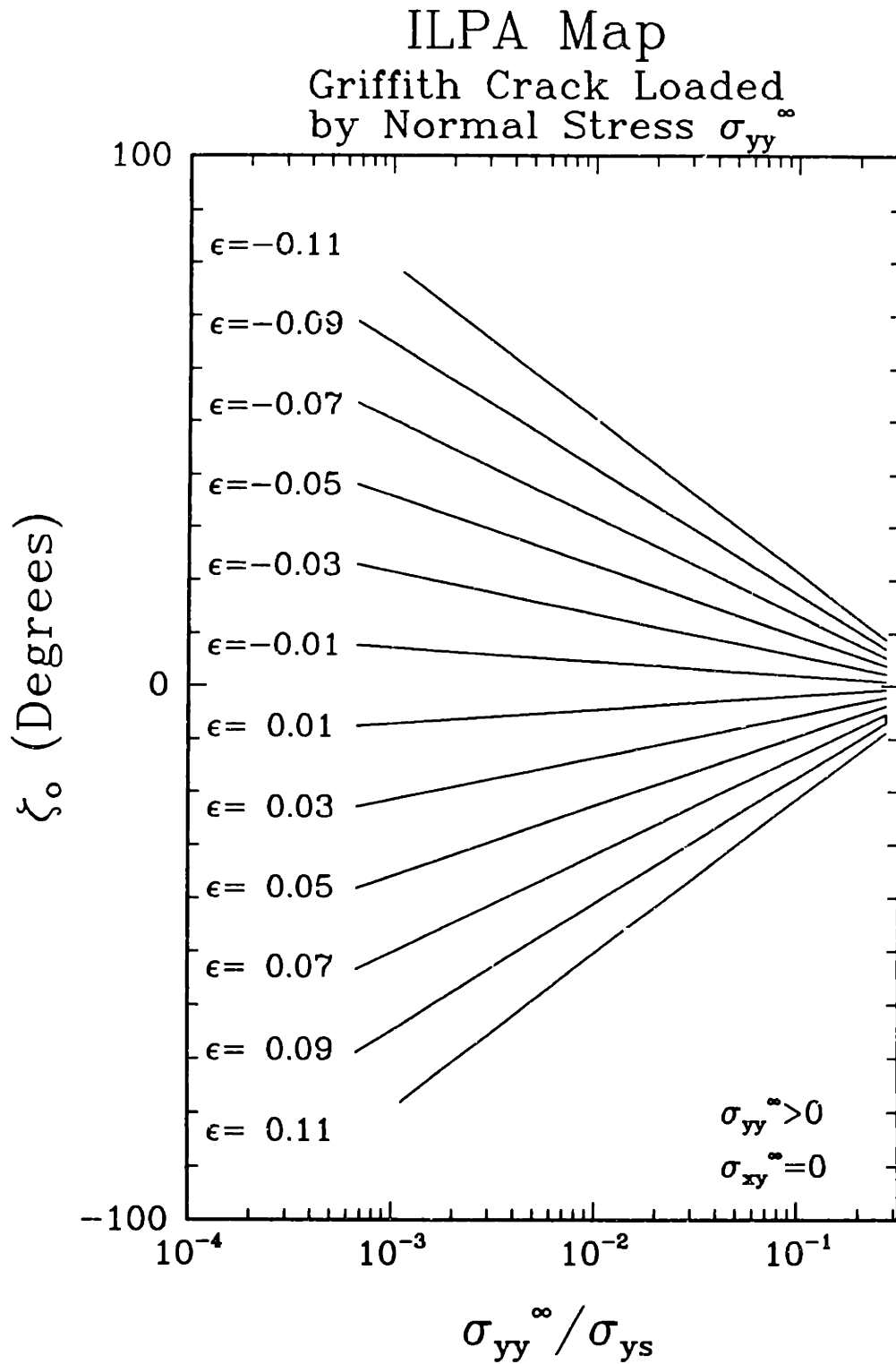


Figure 5.1 ILPA map for a Griffith crack geometry loaded with far-field tensile normal load σ_{yy} , for various values of ϵ .

the crack-tip parameter ζ_0 is to load levels and material combinations.

5.2.4 Influence of Material Properties on Separation

On the basis of the limited parametric study considered, it appears that particular material combinations do not alter the nature of the asymptotic fields produced, rather, they shift the fields in the same way that a change in ζ_0 would, and they distort the strain distribution. For an elastic/perfectly-plastic material bonded to an elastic substrate, the phase angle of the applied load, measured by ζ_0 , appears to affect the asymptotic crack-tip fields more than the choice of elastic material properties. However, for a specific set of traction-free loading conditions, altering the elastic material properties and changing the sign of ϵ can significantly alter both the asymptotic crack-tip stress and strain states, as demonstrated previously. This is extremely important when interfacial separation criteria are evaluated, because, for certain load states, it might be more advantageous to bond to a stiffer substrate or to orientate an anisotropic substrate in a different direction.

Generally, the material combination with the lowest perfectly-plastic flow strength produces the lowest tractions, since the asymptotic stress state scales with the flow strength. For a specific flow strength, minimum normal tractions occur when the material combination is subjected to the largest (positive) ζ_0 or when the crack-tip is closed. When the normal tractions are at their minimum level, substantial inelastic radial shear strains, which scale as $\gamma_{r\theta} \propto 1/R$, localize in a small band parallel to or slightly inclined from the interface. It is somewhat ironic that the minimum interfacial shear strains are present when normal interfacial tractions are at their maximum values and vice versa. Interfacial separation criteria for deformable media, which are only traction or (interfacial) strain based, may seem inappropriate in light of this trend.

In this crack-tip idealization, the resulting interfacial tractions are bounded. This implies that separation criterion for materials with strong interfaces, *i.e.*, those capable of sustaining tractions greater than the maximum asymptotic crack-tip interfacial

tractions, must be strain controlled. (If the controlling mechanism is only a maximum traction criterion, and the tractions are less than the critical traction value, separation would never occur in SSY.) However, it is impossible to predict separation without a specific criterion in mind because most separation criteria require the traction and/or strain level to reach or exceed some threshold value over a critical distance before separation is said to commence.

Micro fracture mechanisms occurring in the interfacial proximity may be indistinguishable from interfacial decohesion. One can easily visualize small particles, whose size might be 10^{-8} to 10^{-6} m, embedded in continuum crack-tip fields and whose presence does not alter the continuum idealization. The high triaxiality near the interface which accompanies the maximum tractions will promote (ductile) micro-void formation and growth in the near crack-tip field. For traction-free crack-tip loadings the maximum triaxiality always occurs at or within $(+)40^\circ$ of the interface, while in the closed crack-tip case, the region where the triaxiality is the highest extends from $\theta \approx 30^\circ$ to $\theta \approx 120^\circ$. Cleavage of brittle particles, which can initiate macro-voids, and micro-cracking are typically thought to be governed by the maximum principal stress and its associated direction. The maximum principal stress occurs along the interface [when $\sigma_{r\theta}(\theta = 0^\circ) = k$] and its direction is orientated approximately 45° from the interface. Therefore, in the plastically deforming interfacial region one might expect to find microcracks and the direction of cleaved particles inclined $(+)135^\circ$ from the interface. In the lower elastic region failure associated with a maximum principal stress criterion may deflect the crack into the lower elastic medium. At radial distances very close to the crack tip such a failure criterion predicts crack deflection at an angle inclined approximately -90° from the interface, while at larger radial distances the deflection angle would be larger ($\approx -45^\circ$).

5.2.5 Suggested Additional Work

Several avenues need to be explored to establish concisely the complete bi-material crack-tip behavior even for the case of an elastic/perfectly-plastic material adjoint to an elastic or rigid material. An analytical expression defining the cusp in terms of the far-field load parameters is essential to fully ascertain the evolution of the interfacial tractions. Incorporation of finite deformation would allow identification of the crack-tip fields all the way to the blunted crack tip and extend the mathematical range for which asymptotic inelastic fields are appropriate. Of course, the material restrictions acknowledged earlier would still limit the applicability of the results from such analyses, but additional insight may suggest a mathematical bound for the singular interfacial and the crack-tip strains.

Finite element solutions such as these “roughly” estimate the actual slip-line angles, and are severely limited by mesh fineness. Analyses which use discretized representations must carefully refine and focus these representative elements to ensure that important details are not systematically excluded from the solution. For example, in this study, no jumps in σ_{rr} were resolved. It is unclear, however, whether jumps existed or were just unresolved. To this extent a more precise asymptotic numerical solution would resolve the issue of stress jumps.

In this study, incremental plasticity is utilized as opposed to deformation theory, as used by Shih and Asaro (1987). For the constitutive idealization of an elastic/perfectly-plastic medium atop a rigid or elastic substrate, unloading usually occurred in asymptotic crack-tip fields whenever $\epsilon > 0$ and $\zeta_0 > 0$. In light of this, utilization of deformation theory in investigating interfacial cracks which have large strain hardening exponents must insure that all “plastically deforming” material points do not unload; *i.e.*, $\bar{\epsilon}(t + \Delta t) \geq \bar{\epsilon}(t)$; $\bar{\epsilon} = \sqrt{\frac{2}{3}\epsilon' \cdot \epsilon'}$.

As is usually the case, parametric studies are only of limited value, and there always exist additional material combinations and loadings for which information is sought. The major issues unresolved in this study which still need be addressed are how

and when does the crack-face constant-state sector become an elastic wedge; how and why does the interfacial elastic wedge and accompanying constant state region evolve; and what are the elastic and inelastic asymptotic crack-tip fields when the elastically-predicted crack-face contact zone is approximately the same size as the plastic zone. In addition to analyzing more material combinations, extending the assumed material idealization to include anisotropic material behavior (both elastic and inelastic), and strain-hardening would also be useful.

Although much attention has been focused upon determining the characteristics of fields very deep within the plastic zone (specifically, for the traction-free crack-tip model — nine orders of magnitude smaller than the plastic zone), such information is of little more than academic use unless it reveals the complete asymptotic structure. From a purely physical point of view, structures larger than geophysical plates must be considered before the characteristics of fields which are nine orders of magnitude smaller than the plastic zone would have meaning. [Picture the structure that would require the twelve orders of magnitude of resolution considered by Shih and Asaro (1987)!] Additionally, the limitations identified previously, (Section 4.4) would require very *unique* material properties in order to achieve a valid solution at that size scale. For most common engineering applications, resolution and identification of continuum fields three or four orders of magnitude smaller than the plastic zone should provide sufficient and (hopefully) meaningful information at that size scale.

References

- Atkinson, 1982** Atkinson, C., *Int. J. Fracture*, **18**, March 1982, pp. 161-177.
- Bathe, 1982** Bathe, K. J., Finite Element Procedures in Engineering Analysis, Prentice-Hall, Inc., Englewood Cliffs, 1982.
- Barenblatt, 1962** Barenblatt, G. I., Advances in Applied Mechanics, Eds. Dryden, H. L., and von Karman, T., Academic Press, New York, **7**, 1962, pp. 56-131.
- Bilby, Cottrell, and Swinden, 1963** Bilby, B. A., Cottrell, D. H., and Swinden, K. H., *Proc. Roy. Soc., A* **272**, 1963, pp.304-310.
- Buchholz and Herrman, 1983** Buchholz, F.G., and Herrman, K. P., Mechanical Behavior of Materials - IV, August 1983, pp. 3005-3013.
- Chamis, 1984** Chamis, C, *S.A.M.P.E. Quarterly*, **15**, No. 3, April 1984, p. 14.
- Comninou, 1979** Comninou, M., and Schmueser, D., *J.A.M.*, **46**, June 1979, pp. 345-348.
- Comninou, 1978** Comninou, M., *J.A.M.*, **45**, June 1978, pp. 287-290.
- Comninou, 1977a** Comninou, M., *J.A.M.*, **44**, Dec. 1977, pp. 631-636.
- Comninou, 1977b** Comninou, M., *J.A.M.*, **44**, Dec. 1977, pp. 780-782.
- Cooper and Kelly, 1969** Cooper, G.A., and Kelly, A., Interfaces in Composite Materials, ASTM STP 452, ASTM, Philadelphia, 1969, pp. 90-106.
- Dugdale, 1960** Dugdale, D. S., *J. Mech. Phys. Solids*, **8**, 1960, pp. 100-104.
- England, 1965** England, A. H., *J.A.M.*, **32**, June 1965, pp. 400-402.
- Erdogan, 1965** Erdogan, F., *J.A.M.*, **32**, June 1965, pp. 403-410.

- Everet, et al., 1986** Everet, R., Henshaw, W., Simons, D. G., and Land, D. J., Composite Interfaces, Eds. Ishida, H., and Koenig, J. L., Elsevier Science Publishing Co., Cleveland, OH, 1986, pp. 231-240.
- Fried and Yang, 1972** Fried, I., and Yang, S. K., *AIAA J.*, **10**, 1972, pp. 1244-1246.
- Fung, 1977** Fung, Y. C., A First Course in Continuum Mechanics, Prentice-Hall, Inc., Englewood Cliffs, 1977, pp.2-4.
- Gautesen and Dundurs, 1987** Gautesen, A. K., and Dundurs, J., *J.A.M.*, **54**, March 1987, pp. 93-98.
- Gurtin, 1981** Gurtin, M. E., An Introduction to Continuum Mechanics, Mathematics Science and Engineering, **158**, Academic Press, 1981.
- Hellan, 1984** Hellan, K., Introduction to Fracture Mechanics, McGraw-Hill Book Co., New York, 1984, p. 93.
- Hertzberg, 1976** Hertzberg, R. W., Deformation and Fracture Mechanics of Engineering Materials, J. Wiley, New York, 1976, p. 20.
- Hibbit, Karlsson, and Sorensen, 1987** Hibbitt, Karlsson, and Sorensen, Inc. (HKS), "ABAQUS User's Manual", Providence, RI, 1987.
- Hibbit, 1984** Hibbitt, H. D., *ABAQUS/EPGEN, Nuclear Eng. and Design*, **77**, 1984, pp. 271-297.
- Hill, 1983** Hill, R., The Mathematical Theory of Plasticity, Clarendon Press, Oxford, 1983, pp. 132-163.
- Hilton and Hutchinson, 1971** Hilton, P. D. and Hutchinson, J. W., *Eng. Frac. Mech.*, **3**, 1971, pp. 435-451.
- Hobbs, Means, and Williams, 1976** Hobbs, B. E., Means, W. D., and Williams, P. F., Outline of Structural Geology, J. Wiley, New York, 1976.

- Hult and McClintock, 1956** Hult, J., and McClintock, F. A., Proceedings of the 9th International Conference of Applied Mechanics, Brussels, 1956, pp. 51-58.
- Hutchinson, 1968** Hutchinson, J. W., *J. Mech. Phys. Solids*, **16**, 1968, pp. 13-31.
- Ioakimidis and Theocaris, 1979** Ioakimidis, N.I., and Theocaris, P. S., *Int. J. Fracture*, **15**, 1979, pp. 299-309.
- Johnson, 1985** Johnson, K. L., Contact Mechanics, Cambridge Univ. Press, New York, 1985.
- Kancharov, 1974** Kachanov, L. M., Fundamentals of the Theory of Plasticity, Trans. Konyaeva, M., Mir Publishers, Moscow, 1974.
- Kanninen and Popelar, 1985** Kanninen, M. F., and Popelar, C. H., Advanced Fracture Mechanics, Oxford University Press, New York, 1985.
- Krieg and Krieg, 1977** Krieg, R. D., and Krieg, D. B., *J. Pressure Vessel Tech.*, **99**, November 1977, pp. 510-515.
- Larsson and Carlsson, 1973** Larsson, S. G., and Carlsson, A. J., *J. Mech. Phys. Solids*, **22**, 1973, pp. 263-277.
- McMeeking, 1977** McMeeking, R. M., *J. Mech. Phys. Solids*, **25**, 1977, pp. 357-381.
- Mushelishvili, 1953** Mushelishvili, N. I., Some Basic Problems in the Mathematical Theory of Elasticity, Trans. Radok, J. R. M., Noordhoff, Gronngen, Holland, 1953.
- Narasimhan, Rosakis, and Hall, 1987** Narasimhan, R., Rosakis, A., J., and Hall, J. F., *J.A.M.*, **54**, Dec. 1987, pp. 838-845.
- Needleman and Sham, 1980** Needleman, A., Sham, T. L., "Final Report- General Electric Company, Subcontract to Brown University," Brown University, Providence, 1980.

- Nemat-Nasser and Obata, 1984** Nemat-Nasser, S., and Obata, M., *Mechanics of Materials*, **3**, 1984, pp. 235-243.
- Nutt and Needleman, 1987** Nutt, S. R., and Needleman, A., *Scripta METALLURGIA*, **21**, 1987, pp. 705-710.
- Ochiai and Murakami, 1981** Ochiai, S., and Murakami, Y., *Met. Trans.*, July 1981, pp. 1155.
- Ou and Bassani, 1988** Ou, J., and Bassani, J. L., "Cracks on Bimaterial and Bicrystal Interfaces," Univ. of Pennsylvania, Philadelphia, March 1988.
- Rice, 1988** Rice, J. R., *J.A.M.*, **55**, March 1988, pp. 98-103.
- Rice, 1982** Rice, J. R., Mechanics of Solids, Eds. Hopkins, H. G., and Sewell, M. J., Pergamon Press, Oxford, New York, 1982, pp.539-562.
- Rice, 1974** Rice, J. R., *J. Mech. Phys. Solids*, **22**, 1974, pp. 17-26.
- Rice, 1968a** Rice, J. R., *J. A. M.* , **35**, June 1968, pp. 379-386.
- Rice, 1968b** Rice, J. R., Fracture: An Advanced Treatise, Ed. Liebowitz, H., Academic Press, New York, **2**, 1968, pp. 191-311.
- Rice and Rosengren, 1968** Rice, J. R., and Rosengren, G. F., *J. Mech. Phys. Solids*, **16**, 1968, pp. 1-12.
- Rice, Drugan and Sham, 1980** Rice, J. R., Drugan, W. J., and Sham, T. L., Fracture Mechanics, ASTM-STP 700, ASTM, Philadelphia, 1980, pp. 189-219.
- Rice and Sih, 1965** Rice, J. R., and Sih, G. C., *J.A.M.*, **32**, June 1965, pp. 418-423.
- Rice and Tracey, 1973** Rice, J. R., and Tracey, D. M., Numerical and Computer Methods in Structural Mechanics, Academic Press, New York, 1973, pp. 585-623.

- Sham, 1983** Sham, T. L., Elastic-Plastic Fracture: Second Symposium Vol. 1 - Inelastic Crack Analysis, ASTM STP 803, ASTM, Philadelphia, 1983, pp. 52-79.
- Shields, 1982** Shields, R. T., *J.A.M.*, **49**, 1982, pp. 516-518.
- Shih and Asaro, 1987** Shih, C. F., and Asaro, R. J., "Elastic-Plastic Analysis of Cracks on Bimaterial Interfaces Part I: Small Scaling Yielding," Brown Univ., Div. of Eng., March 1987, Providence.
- Shih, 1974** Shih, C. F., Fracture Analysis, ASTM STP 560, ASTM, Philadelphia, 1974, pp. 187-210.
- Sih and Rice, 1964** Sih, G. C., and Rice, J. R., *J.A.M.*, **31**, 1964, pp. 477-482.
- Timoshenko and Goodier, 1970** Timoshenko, S. P., and Goodier, J. N., Theory of Elasticity, McGraw Hill, New York, 1970, pp. 90-145.
- Webster, 1979** Webster, N., Webster's Deluxe Unabridged Dictionary, Simon and Schuster, New York, 1979, p. 117.
- Williams, 1979** Williams, M.L., *Bul. Seis. Soc. Am.*, **49**, April 1959, pp. 199-204.
- Willis, 1971** Willis, J. R., *J. Mech. Phys. Solids*, **19**, 1971, pp. 353-368.

Appendix A

Boundary Layer Formulation

In order to impose Sham's boundary layer formulation (Sham, 1983), it is necessary to calculate consistent energy conjugate stiffnesses and boundary displacements. The first section derives the far-field stored energy, due to the lower order terms, and formulates an energy equivalent spring network to represent it. Appendix C contains the actual FORTRAN program used to determine the spring stiffness for a given material combination. The second section derives the imposed displacements in terms of the admissible eigenfunctions and coefficients (generalized degrees of freedom). These displacement constraints are then enforced on the FE boundary nodes via a user-written MPC subroutine. Again, Appendix C contains the actual FORTRAN coding used for the MPC subroutine.

In this appendix, the two stress potential functions used are ϕ and χ instead of the stress potentials ϕ and Ω , as used in the body of the text. Since χ is related to ϕ and Ω by

$$\chi'' = \Omega' - \phi' - z\phi'',$$

they produce equivalent results. However, the unknown coefficients a_n and b_n of Eqs.(3.4) and (3.5) are not the same. All Appendices, subroutines, and FORTRAN coding use $B_{(N)}$ and $D_{(N)}$ as the unknown coefficients, with the $B_{(0)}$ term being adjusted so that it is interpreted as $B_{(0)} = \bar{K}$.

A.1 Energy Considerations

A.1.1 Formulation of Equivalent Stiffness Matrix

Implementation of Sham's boundary layer formulation requires the evaluation and inclusion of the far-field energy, which is attributable to the T -field terms. This section evaluates the second term in Eq.(3.8) from its associated strain energy potential relationship.

The general series potential functions given by Sih and Rice, (1964) and Rice (1988), which satisfy the bi-material crack, are

$$\phi_1(z) = 2z^{-\frac{1}{2}-i\epsilon} \sum_N [(N + \frac{1}{2}) - i\epsilon] \bar{B}_{(N)} z^N + \frac{2C_2}{C_1 + C_2} \sum_M \frac{\bar{D}_{(M)}}{M+1} z^{M+1}, \quad (\text{A.1})$$

$$\phi_2(z) = 2e^{2\pi\epsilon} z^{-\frac{1}{2}-i\epsilon} \sum_N [(N + \frac{1}{2}) - i\epsilon] \bar{B}_{(N)} z^N + \frac{2C_1}{C_1 + C_2} \sum_M \frac{\bar{D}_{(M)}}{M+1} z^{M+1}, \quad (\text{A.2})$$

$$\begin{aligned} \chi_1(z) = & 2e^{2\pi\epsilon} z^{\frac{1}{2}+i\epsilon} \sum_N B_{(N)} z^N - 2z^{\frac{1}{2}-i\epsilon} \sum_N [(N - \frac{1}{2}) - i\epsilon] \bar{B}_{(N)} z^N \\ & - \frac{C_2}{C_1 + C_2} \sum_M D_{(M)} \bar{z}^M z^2 - \frac{2C_2}{C_1 + C_2} \sum_M \frac{\bar{D}_{(M)}}{M+2} z^{M+2}, \end{aligned} \quad (\text{A.3})$$

and

$$\begin{aligned} \chi_2(z) = & 2z^{\frac{1}{2}+i\epsilon} \sum_N B_{(N)} z^N - 2e^{2\pi\epsilon} z^{\frac{1}{2}-i\epsilon} \sum_N [(N - \frac{1}{2}) - i\epsilon] \bar{B}_{(N)} z^N \\ & - \frac{C_1}{C_1 + C_2} \sum_M D_{(M)} \bar{z}^M z^2 - \frac{2C_1}{C_1 + C_2} \sum_M \frac{\bar{D}_{(M)}}{M+2} z^{M+2}, \end{aligned} \quad (\text{A.4})$$

with

$$C_k = \frac{\eta_k + 1}{\mu_k} \quad (k = 1, 2). \quad (\text{A.5})$$

In these expressions the subscripts (1,2) indicate material domains, ϵ is the bi-material constant, $\eta_j = 3 - 4\nu_j$ for plane strain or $\eta_j = (3 - \nu_j)/(1 + \nu_j)$ for plane stress, μ_j and ν_j are the appropriate shear modulus and Poisson's ratio, respectively, and z is the complex variable measured from the crack tip. The desired lower order Laurent series displacements, u^T , and the associated stresses, σ^T , are obtained by letting $N = -1, -2, -3, \dots$ and $M = -2, -3, -4, \dots$. The $M = -1$ term is excluded from the

formulation since it represents an applied concentrated crack-tip force and produces infinite far-field elastic energy in the boundary layer formulation. For the ϕ and χ stress potentials, this represents the same modifications to the ϕ and Ω potentials as were made in Eqs.(3.4) and (3.5). From these potentials, the far-field elastic strain energy due to the lower modes, $\Phi(\underline{\epsilon}^T)$, can be evaluated and incorporated directly.

Since \mathbf{u}^T is an equilibrium solution in the far-field (Region \mathcal{R} of *Figure 8.2*),

$$2\bar{\Pi}(\mathbf{u}^T) = 2 \int_{\mathcal{R}} \Phi(\underline{\epsilon}^T) dS = \int_{\Gamma} \mathbf{t}^T \cdot \mathbf{u}^T ds. \quad (\text{A.6})$$

Here $\bar{\Pi}$ is the total strain energy in \mathcal{R} , Φ is the strain energy density, Γ represents the entire boundary around \mathcal{R} (Γ_{∞} , $\Gamma_{Plastic}$, and Γ_c), and \mathbf{t}^T is the resultant traction due to the lower order modes. Dividing the boundary into regions yields

$$2\bar{\Pi}(\mathbf{u}^T) = \int_{\Gamma_{Plastic}} \mathbf{t}^T \cdot \mathbf{u}^T ds + \int_{\Gamma_{\infty}} \mathbf{t}^T \cdot \mathbf{u}^T ds + \int_{\Gamma_c} \mathbf{t}^T \cdot \mathbf{u}^T ds. \quad (\text{A.7})$$

Recall the Kolosov-Muskhelishvili stress formulas (Sih and Rice, 1964),

$$\sigma_{rr} + \sigma_{\theta\theta} = 4\Re[\phi'] = 2[\phi' + \bar{\phi}'], \quad (\text{A.8})$$

and

$$\sigma_{\theta\theta} - \sigma_{rr} + i2\sigma_{r\theta} = 2e^{i2\theta}[\bar{z}\phi'' + \chi''], \quad (\text{A.9})$$

where a bar indicates the complex conjugate, and \Re signifies the real portion of the argument. Subtracting Eq.(A.8) from Eq.(A.9) gives

$$-2\sigma_{rr} + i2\sigma_{r\theta} = 2e^{i2\theta}[\bar{z}\phi'' + \chi''] - 2[\phi' + \bar{\phi}']. \quad (\text{A.10})$$

The displacements obtained via Kolosov-Muskhelishvili transformation are

$$\mathbf{u} + i\mathbf{v} = \frac{1}{2\mu}[\eta\phi - z\bar{\phi}' - \bar{\chi}'], \quad (\text{A.11})$$

where the shear modulus, μ , Poisson's ratio, ν , and η are those associated with the individual material domains. Transforming to a polar coordinate frame, Eq.(A.11) becomes

$$\mathbf{u}_r + i\mathbf{u}_\theta = \frac{e^{-i\theta}}{2\mu} [\eta\phi - z\bar{\phi}' - \bar{\chi}']. \quad (\text{A.12})$$

Examination of the potential functions shows that the stresses, σ_{rr}^T and $\sigma_{r\theta}^T$, behave as $z^{p-\frac{3}{2}-i\epsilon} + z^{-2-p}$ and the displacements, \mathbf{u}_r^T and \mathbf{u}_θ^T , behave as $z^{q-\frac{1}{2}-i\epsilon} + z^{-1-q}$, where $p = 0, -1, -2, \dots$ and $q = 0, -1, -2, \dots$. In general, the term $\mathbf{t}^T \cdot \mathbf{u}^T$ behaves like $z^{p+q-2-2i\epsilon} + z^{-3-p-q}$, while for large z the dominant component, $p = q = 0$, acts like $z^{-(2+i2\epsilon)}$. This means that as $r \rightarrow \infty$ on Γ_∞ ,

$$\int_{\Gamma_\infty} \mathbf{t}^T \cdot \mathbf{u}^T ds = 0. \quad (\text{A.13})$$

By the problem definition, “traction-free crack-tip faces,” $\mathbf{t}^T = 0$ on Γ_c , so that Eq.(A.7) can now be written as

$$2\bar{\Pi}(\mathbf{u}^T) = \int_{\Gamma_{Plastic}} \mathbf{t}^T \cdot \mathbf{u}^T ds. \quad (\text{A.14})$$

The traction, \mathbf{t}^T , is by definition

$$\mathbf{t}^T = \boldsymbol{\sigma}^T \cdot \mathbf{n}, \quad (\text{A.15})$$

where \mathbf{n} is the unit outward normal. Choosing $\Gamma_{Plastic}$ to be a circle of radius r , ds becomes $r d\theta$, and the cylindrical components of \mathbf{n} are $(-1, 0, 0)$. Eq.(A.14) then becomes

$$2\bar{\Pi}(\mathbf{u}^T) = \int_{\Gamma_{Plastic}} [-\sigma_{rr}^T \mathbf{u}_r^T - \sigma_{r\theta}^T \mathbf{u}_\theta^T] r d\theta. \quad (\text{A.16})$$

For convenience, C in Eq.(A.12) is defined as

$$C = \frac{e^{-i\theta}}{2\mu} [\eta\phi - z\bar{\phi}' - \bar{\chi}'] = \mathbf{u}_r + i\mathbf{u}_\theta, \quad (\text{A.17})$$

and D is defined by dividing the complex conjugate of Eq.(A.10) by two, which results in the following:

$$D = e^{-i2\theta} [z\bar{\phi}'' + \bar{\chi}''] - [\phi' + \bar{\phi}'] = -\sigma_{rr} - i\sigma_{r\theta}. \quad (\text{A.18})$$

Eq.(A.16) can then be rewritten as

$$2\bar{\Pi}(\mathbf{u}^T) = \int_{\Gamma_{Plastic}} [\Re(C)\Re(D) + \Im(C)\Im(D)] r d\theta, \quad (\text{A.19})$$

or

$$2\bar{\Pi}(\mathbf{u}^T) = \int_{\Gamma_{Plastic}} \Re(rC\bar{D})d\theta = \int_{\Gamma_{Plastic}} \Re(r\bar{C}D)d\theta, \quad (\text{A.20})$$

where \Re and \Im designate real and imaginary parts, respectively. It is convenient to factor out the coefficients \mathbf{B} and \mathbf{D} (these are the vectors which contain $B_{(N)}$ and $D_{(M)}$ as their components, respectively), and to express the potential functions, Eq.(A.1) to Eq.(A.4), in terms of their individual components as

$$\phi = \sum_{i=1}^{N+M} \bar{P}_i \phi_i \quad (\text{A.21})$$

and

$$\chi = \sum_{i=1}^{N+M} P_i \aleph_i - \sum_{i=1}^{N+M} \bar{P}_i \mathcal{U}_i, \quad (\text{A.22})$$

where

$$\{\mathbf{P}\}_{N+M-1} = \left\{ \begin{array}{c} B_{(1)} \\ \vdots \\ B_{(N)} \\ D_{(2)} \\ \vdots \\ D_{(M)} \end{array} \right\}, \quad (\text{A.23})$$

and the terms ϕ_i , \aleph_i , and \mathcal{U}_i correspond to the functional parts of Eq.(A.1) to Eq.(A.4). More specifically, this means that the functions (ϕ_1, \dots, ϕ_N) , $(\aleph_1, \dots, \aleph_N)$, and $(\mathcal{U}_1, \dots, \mathcal{U}_N)$ all correspond to the functions associated with the \mathbf{B} coefficients and the functions $(\phi_{N+1}, \dots, \phi_{N+M-1})$, $(\aleph_{N+1}, \dots, \aleph_{N+M-1})$, and $(\mathcal{U}_1, \dots, \mathcal{U}_{N+M-1})$ correspond to the functions associated with the \mathbf{D} coefficients. (The subscripts indicating the material domains are implied by the value of z chosen.) Further, four matrices, $\mathcal{B}\mathcal{B}$, $\mathcal{B}\bar{\mathcal{B}}$, $\bar{\mathcal{B}}\mathcal{B}$, and $\bar{\mathcal{B}}\bar{\mathcal{B}}$, are defined whose components are given by

$$\mathcal{B}\mathcal{B}_{ij} = \bar{z}[-z\bar{\phi}'_i e^{i2\theta} \aleph''_j + z\bar{\phi}'_i \bar{\phi}'_j + \bar{\mathcal{U}}'_i e^{i2\theta} \aleph''_j - \bar{\mathcal{U}}'_i \bar{\phi}'_j], \quad (\text{A.24})$$

$$\begin{aligned} \mathcal{B}\bar{\mathcal{B}}_{ij} &= \bar{z}[-z\bar{\phi}'_i e^{i2\theta} \bar{z}\phi''_j + z\bar{\phi}'_i e^{i2\theta} \mathcal{U}''_j + z\bar{\phi}'_i \phi'_j + \bar{\mathcal{U}}'_i e^{i2\theta} \bar{z}\phi''_j \\ &\quad - \bar{\mathcal{U}}'_i e^{i2\theta} \mathcal{U}''_j - \bar{\mathcal{U}}'_i \phi'_j], \end{aligned} \quad (\text{A.25})$$

$$\bar{\mathcal{B}}\mathcal{B}_{ij} = \bar{z}[\eta\phi_i e^{i2\theta} \aleph''_j - \eta\phi_i \bar{\phi}'_j - \eta\bar{\aleph}'_i e^{i2\theta} \aleph''_j + \bar{\aleph}'_i \bar{\phi}'_j], \quad (\text{A.26})$$

and

$$\begin{aligned} \tilde{B}\tilde{B}_{i,j} = & \bar{z}[\eta\phi_i e^{i2\theta} \bar{z}\phi_j'' - \eta\phi_i e^{i2\theta} U_j'' - \eta\phi_i \phi_j' - \bar{N}_i' e^{i2\theta} \bar{z}\phi_j'' \\ & + \bar{N}_i' e^{i2\theta} U_j'' + \bar{N}_i' \phi_j']. \end{aligned} \quad (\text{A.27})$$

By using Eq.(A.17), Eq.(A.18), and Eqs.(A.20) to (A.27), Eq.(A.16) reduces to

$$2\bar{\Pi}(\mathbf{u}^T) = \int_{R_{Plastic}} \frac{1}{2\mu} \Re[\mathbf{P}\mathcal{B}\mathcal{B}\mathbf{P} + \mathbf{P}\mathcal{B}\tilde{\mathcal{B}}\bar{\mathbf{P}} + \bar{\mathbf{P}}\tilde{\mathcal{B}}\mathcal{B}\mathbf{P} + \bar{\mathbf{P}}\tilde{\mathcal{B}}\tilde{\mathcal{B}}\bar{\mathbf{P}}]d\theta. \quad (\text{A.28})$$

At this point, the integral $\int_R \Phi(\underline{\epsilon}^T)dS$ has been recast in terms of the complex vector \mathbf{P} , which represents the unknown coefficients, and four matrices containing functions of the original stress potentials. The remaining formulation consists of various algebraic manipulations used to recast Eq.(A.28) into an expression which, when integrated, contains *real* numbers only. First, the *real* vector \mathbf{q}^{ϵ^T} is defined as

$$\{\mathbf{q}^{\epsilon^T}\} = \left\{ \begin{array}{c} \Re\mathbf{P} \\ \Im\mathbf{P} \end{array} \right\} = \left\{ \begin{array}{c} \Re B_{(1)} \\ \vdots \\ \Re B_{(N)} \\ \Re D_{(2)} \\ \vdots \\ \Re D_{(M)} \\ \Im B_{(1)} \\ \vdots \\ \Im B_{(N)} \\ \Im D_{(2)} \\ \vdots \\ \Im D_{(M)} \end{array} \right\}. \quad (\text{A.29})$$

Next, the stiffness matrix \mathbf{S} is introduced and is defined such that

$$\bar{\Pi}(\mathbf{u}^T) = \frac{1}{2}\mathbf{q}^{\epsilon^T}\mathbf{S}\mathbf{q}^{\epsilon^T}. \quad (\text{A.30})$$

Using the convention that $\bar{P}_j = e_j + if_j$, factoring out the real components, and equating Eq.(A.28) to Eq.(A.30), we can express \mathbf{S} as

$$\mathbf{S} = \int_{R_{Plastic}} \frac{1}{2\mu} \left[\begin{array}{c|c} \Re(\mathcal{B}\mathcal{B} + \mathcal{B}\tilde{\mathcal{B}} + \tilde{\mathcal{B}}\mathcal{B} + \tilde{\mathcal{B}}\tilde{\mathcal{B}}) & \Im(\mathcal{B}\mathcal{B} - \mathcal{B}\tilde{\mathcal{B}} + \tilde{\mathcal{B}}\mathcal{B} - \tilde{\mathcal{B}}\tilde{\mathcal{B}}) \\ \hline \Im(\mathcal{B}\mathcal{B} + \mathcal{B}\tilde{\mathcal{B}} - \tilde{\mathcal{B}}\mathcal{B} - \tilde{\mathcal{B}}\tilde{\mathcal{B}}) & \Re(-\mathcal{B}\mathcal{B} + \mathcal{B}\tilde{\mathcal{B}} + \tilde{\mathcal{B}}\mathcal{B} - \tilde{\mathcal{B}}\tilde{\mathcal{B}}) \end{array} \right] d\theta. \quad (\text{A.31})$$

After integration of Eq.(A.31), the integral $\int_R \Phi(\underline{\epsilon}^T)dS$ can be replaced by $\frac{1}{2}\mathbf{q}^{\epsilon^T}\mathbf{S}\mathbf{q}^{\epsilon^T}$.

A.1.2 Evaluation of Spring Constants

To incorporate this energy into the finite element code, a spring network, with appropriate stiffness, was constructed. The spring network vertices corresponded to “free” nodes and the displacements of these free nodes were governed by the value of the generalized coefficient vector \mathbf{q}^{eT} . It was observed that, since \mathbf{q}^{eT} both pre- and post-multiplied the stiffness matrix \mathbf{S} [in Eq.(A.30)], a new upper triangular stiffness matrix \mathbf{C} can be used to reduce the number of individual stiffnesses. When constructed correctly, \mathbf{C} replaces \mathbf{S} in Eq.(A.30) to produce identical results. The new stiffness matrix \mathbf{C} is related to \mathbf{S} (after evaluation of \mathbf{S}) via

$$C_{ij} = \begin{cases} S_{ij} & i = j & i = 1, 2, 3, \dots, 2(N + M - 1) \\ S_{ij} + S_{ji} & i < j & j = i, i + 1, i + 2, \dots, 2(N + M - 1) \\ 0 & \text{otherwise.} \end{cases} \quad (\text{A.32})$$

The energy associated with a spring is calculated in the finite element code as $\frac{1}{2}C_{ij}(q_i - q_j)^2$ as opposed to $\frac{1}{2}C_{ij}q_iq_j$, as assumed in Eq.(A.30). To rectify this situation, a further modified spring stiffness matrix \mathbf{C}' is defined whose components are

$$C'_{ij} = \begin{cases} -\frac{1}{2}C_{ij} & i \neq j \\ & i = 1, 2, 3, \dots, 2(N + M) \\ \frac{1}{2}\sum_{k=1}^i C'_{kj} + \frac{1}{2}\sum_{l=j}^{2(N+M-1)} C'_{il} & i = j \\ & j = i, i + 1, i + 2, \dots, 2(N + M - 1). \end{cases} \quad (\text{A.33})$$

Finally, the far-field elastic strain energy can now be expressed in terms of spring constants, C'_{ij} , as

$$\Phi(\mathbf{u}^T) = \frac{1}{2}(q_i - q_j)C'_{ij}(q_i - q_j), \quad (\text{A.34})$$

with the clarification that the term $(q_i - q_j)$ is interpreted as q_i , when $i = j$.

The actual spring stiffnesses for a particular choice of material properties were obtained by numerically integrating Eq.(A.31) using Simpson’s 1/3 Rule with $\Delta\theta = \pi/100$. The $\Gamma_{Plastic}$ boundary was chosen to be a circle, with radius $r_{Plastic} = 1.0$ m, centered about the crack tip. This prevented numerical noise associated with evaluating $r_{Plastic}$ raised to large power. To reduce other numerical noise, the integration path was divided and integrated from $\theta = \pm\pi$ to $\theta = 0$ simultaneously. The *complex* FORTRAN coding used to evaluate \mathbf{C}' is included in Appendix C.

A.2 Boundary Considerations

The boundary conditions required for Sham's boundary layer formulation are those of the general bi-material crack problem. Using the general series potential functions, Eqs.(A.1) to (A.4), and the Kolosov-Muskhelishvili relation Eq.(A.11), the displacements can be expressed in terms of the complex coefficients $\mathbf{B}_{(N)}$ and $\mathbf{D}_{(M)}$, and the location $z = re^{i\theta}$. To maintain the \mathbf{K} -field dominance at the boundary, again only the series terms corresponding to $N = 0, -1, -2, \dots$ and $M = -2, -3, -4, \dots$, are used to determine the displacements. After some algebra, the displacements for the upper half can be written as:

$$u = \sum_N \frac{r^Q}{\mu} (Fe1_N e_N + Fe2_N f_N) + \sum_M \frac{C_r^{M+1}}{2\mu} (Ge1_M c_M + Ge2_M d_M) \quad (\text{A.35})$$

and

$$v = \sum_N \frac{r^Q}{\mu} (Fe3_N e_N + Fe4_N f_N) + \sum_M \frac{C_r^{M+1}}{2\mu} (Ge3_M c_M + Ge4_M d_M), \quad (\text{A.36})$$

where (subscripts dropped for brevity),

$$P = N + 3/2, \quad (\text{A.37})$$

$$Q = N + 1/2, \quad (\text{A.38})$$

$$\mathcal{R} = PQ - \epsilon^2, \quad (\text{A.39})$$

$$S = \epsilon(P + Q), \quad (\text{A.40})$$

$$T1 = \cos[\epsilon \ln(r)] \cos(Q\theta) + \sin[\epsilon \ln(r)] \sin(Q\theta), \quad (\text{A.41})$$

$$T2 = \cos[\epsilon \ln(r)] \sin(Q\theta) - \sin[\epsilon \ln(r)] \cos(Q\theta), \quad (\text{A.42})$$

$$T3 = \cos[\epsilon \ln(r)] \cos(2Q\theta) - \sin[\epsilon \ln(r)] \sin(2Q\theta), \quad (\text{A.43})$$

$$T4 = \cos[\epsilon \ln(r)] \sin(2Q\theta) + \sin[\epsilon \ln(r)] \cos(2Q\theta), \quad (\text{A.44})$$

$$T5 = \cos[\epsilon \ln(r)] \cos(Q\theta) - \sin[\epsilon \ln(r)] \sin(Q\theta), \quad (\text{A.45})$$

$$T6 = \cos[\epsilon \ln(r)] \sin(Q\theta) + \sin[\epsilon \ln(r)] \cos(Q\theta), \quad (\text{A.46})$$

$$Fe1 = \eta e^{\epsilon\theta} [P \times T1 + \epsilon \times T2] - e^{\epsilon\theta} [\mathcal{R} \times T3 - S \times T4]$$

$$-e^{2\pi\epsilon}e^{-\epsilon\theta}[P \times T5 + \epsilon \times T6] + e^{\epsilon\theta}[\mathcal{R} \times T1 + S \times T2], \quad (\text{A.47})$$

$$\begin{aligned} Fe2 &= \eta e^{\epsilon\theta}[\epsilon \times T1 - P \times T2] - e^{\epsilon\theta}[S \times T3 + \mathcal{R} \times T4] \\ &\quad - e^{2\pi\epsilon}e^{-\epsilon\theta}[P \times T6 + \epsilon \times T5] - e^{\epsilon\theta}[\mathcal{R} \times T2 - S \times T1], \end{aligned} \quad (\text{A.48})$$

$$\begin{aligned} Fe3 &= \eta e^{\epsilon\theta}[P \times T2 - \epsilon \times T1] - e^{\epsilon\theta}[S \times T3 + \mathcal{R} \times T4] \\ &\quad + e^{2\pi\epsilon}e^{-\epsilon\theta}[P \times T6 + \epsilon \times T5] - e^{\epsilon\theta}[\mathcal{R} \times T2 - S \times T1], \end{aligned} \quad (\text{A.49})$$

and

$$\begin{aligned} Fe4 &= \eta e^{\epsilon\theta}[P \times T1 + \epsilon \times T2] + e^{\epsilon\theta}[\mathcal{R} \times T3 - S \times T4] \\ &\quad - e^{2\pi\epsilon}e^{-\epsilon\theta}[P \times T5 - \epsilon \times T6] - e^{\epsilon\theta}[\mathcal{R} \times T1 + S \times T2]. \end{aligned} \quad (\text{A.50})$$

The coefficients of the integer powers are defined as

$$\bar{D}_{(j)} = c_{(j)} + id_{(j)}, \quad (\text{A.51})$$

and the accompanying terms associated with the integer powers are

$$Ge1 = \frac{\eta + M + 1}{M + 1} \cos[(M + 1)\theta], \quad (\text{A.52})$$

$$Ge2 = -\frac{\eta + M + 1}{M + 1} \sin[(M + 1)\theta], \quad (\text{A.53})$$

$$Ge3 = \frac{\eta - M - 1}{M + 1} \sin[(M + 1)\theta] + 2 \sin[(M - 1)\theta], \quad (\text{A.54})$$

$$(\text{A.55})$$

and

$$Ge4 = \frac{\eta - M - 1}{M + 1} \cos[(M + 1)\theta] + 2 \cos[(M - 1)\theta]. \quad (\text{A.56})$$

By using the definition proposed by Rice and Sih for the stress intensity factors and the convention $\bar{B}_{(0)} = e_{(0)} + if_{(0)}$, $B_{(0)}$ can be expressed in terms of \mathbf{K} as

$$e_{(0)} = \frac{\Re\mathbf{K}(.75 - \epsilon^2) + \Im\mathbf{K}2\epsilon}{4e^{\epsilon\pi}\sqrt{2\pi} [.75 + 3\epsilon^2] \cosh(\pi\epsilon)} \quad (\text{A.57})$$

and

$$f_{(0)} = \frac{\Re\mathbf{K}2\epsilon - \Im\mathbf{K}(.75 - \epsilon^2)}{4e^{\epsilon\pi}\sqrt{2\pi} [.75 + 3\epsilon^2] \cosh(\pi\epsilon)}. \quad (\text{A.58})$$

It should be noted that the original Rice and Sih (1965) work does not give the appropriate energy release rate unless the definition relating k_I and k_{II} to \mathbf{K} , given by Hutchinson *et al.* (1987) [Eq.(2.15)], is used.

The displacement relations (A.34) and (A.35) were “coded up” as constraint equations and used along the $\Gamma_{Plastic}$ -model boundary of the finite element mesh. Appendix C contains the user MPC which was used to enforce the nodal displacement boundary conditions in terms of imposed the $\mathbf{K}(t)$ and the unknown vector \mathbf{q}^{eT} .

Appendix B

Elastic-Wedge Stress Potential

The elastic stress potentials for a semi-infinite wedge loaded by constant tractions on each of its faces is given. The individual stress components are obtained from ϕ , the stress potential, by using the definitions (Timoshenko and Goodier, 1970)

$$\sigma_{\gamma\gamma} = \frac{\partial^2 \phi}{\partial r^2}, \quad (\text{B.1})$$

$$\sigma_{r\gamma} = -\frac{\partial}{\partial r} \left(\frac{1}{r} \frac{\partial \phi}{\partial \gamma} \right), \quad (\text{B.2})$$

and

$$\sigma_{rr} = \frac{1}{r} \frac{\partial \phi}{\partial r} + \frac{1}{r^2} \frac{\partial^2 \phi}{\partial \gamma^2}. \quad (\text{B.3})$$

The stress potential for a wedge loaded along its faces by constant tractions is found from the general solution given by Timoshenko and Goodier (1970):

$$\phi = b_0 r^2 + d_0 r^2 \gamma + \frac{a_1}{2} r \gamma \sin \gamma - \frac{c_1}{2} r \gamma \cos \gamma + a_2 r^2 \cos 2\gamma + c_2 r^2 \sin 2\gamma. \quad (\text{B.4})$$

For the specific problem shown in *Figure B.1*, the stress potential constants are

$$b_0 = \frac{W}{2} - a_2, \quad (\text{B.5})$$

$$d_0 = -2c_2 - T, \quad (\text{B.6})$$

$$c_2 = \frac{(H + 2T\psi - W) \sin 2\psi - (K - T)(\cos 2\psi - 1)}{2(\cos 2\psi - 1)^2 + 2(\sin 2\psi) \times (\sin 2\psi - 2\psi)}, \quad (\text{B.7})$$

and

$$a_2 = \frac{(H + 2T\psi - W)(\cos 2\psi - 1) + (K - T)(\sin 2\psi - 2\psi)}{2(\cos 2\psi - 1)^2 + 2(\sin 2\psi) \times (\sin 2\psi - 2\psi)}. \quad (\text{B.8})$$

Using Eqs. (B.1) to (B.3) and Eq. (B.5), the stress components are

$$\sigma_{\gamma\gamma} = 2a_2(\cos 2\gamma - 1) + 2c_2(\sin 2\gamma - 2\gamma) + W - 2T\gamma, \quad (\text{B.9})$$

$$\sigma_{r\gamma} = 2a_2 \sin 2\gamma - 2c_2(\cos 2\gamma - 1) + T, \quad (\text{B.10})$$

and

$$\begin{aligned} \sigma_{rr} = & -2a_2(\cos 2\gamma + 1) - 2c_2(\sin 2\gamma + 2\gamma) + W - 2T\gamma \\ & + \frac{1}{r}(a_1 \cos \gamma + c_1 \sin \gamma). \end{aligned} \quad (\text{B.11})$$

The σ_{rr} component is singular with respect to r , and that two constants a_1 and c_1 remain unspecified from the boundary conditions prescribed. The values of these two constants are determined by matching the σ_{rr} stress, and for non-zero values of a_1 and c_1 concentrated forces must exist at $r = 0$.

A note of caution, when the coordinate frame is rotated to coincide with the crack-tip coordinate frame (via $\gamma = \pi - \theta$), the sign of the $\sigma_{r\theta}$ component must also be changed.

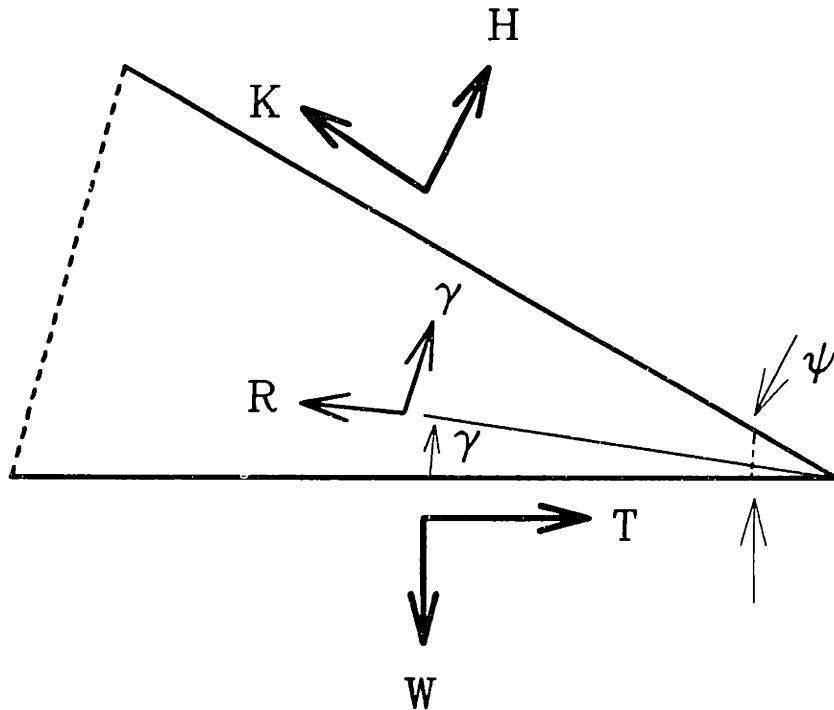


Figure B.1 Elastic wedge showing constant normal [$W = t_n(\gamma = 0)$] and shear [$T = t_s(\gamma = 0)$] tractions on its lower surface, constant normal [$H = t_n(\gamma = \psi)$] and shear [$K = t_s(\gamma = \psi)$] on its upper surface, and polar (r, γ) coordinates.

Appendix C

User-Written Software

This appendix contains the the FORTRAN coding for the user-written elastic/perfectly-plastic constitutive relationship subroutine UMAT as well as the program used to calculate the spring coefficients for the traction-free crack-tip model derived in Appendix A. The user-written MPC subroutines which impose the boundary displacements are included for both the traction-free and (frictionless) closed crack-tip models.

C.1 Elastic/Perfectly-Plastic UMAT

This routines original framework was written by Allen Lush. The author modified the original subroutine from its radial return operator to the Rice-Tracey mean normal integration operator.

```
C*****>
C                                     >
C           ABAQUS USER MATERIAL FOR  >
C           RATE INDEPENDENT PERFECT PLASTICITY >
C                                     >
C*****>
C                                     >
C Properties common to all material models: >
C   PROPS(1) = yield stress TAU   Tensile >
C   PROPS(2) = MU >
C   PROPS(3) = KAPPA >
C                                     >
C*****>
C Notes: >
```

```

C                                     >
C      1.  Compile with FORTRAN 77 only.                                     >
C      2.  Do not use this version for plane stress.                       >
C      3.  Use with the *STATIC procedure.                                 >
C                                     >
C*****>
      SUBROUTINE UMAT(STRESS,STATEV,DDSDDE,SSE,SPD,SCD,STRAN,DSTRAN,
1  TIME,DTIME,TEMP,DTEMP,PREDEF,DPRED,MATERL,NDI,NSHR,NTENS,
2  NSTATV,PROPS,NPROPS,COORDS)
      IMPLICIT REAL*8(A-H,O-Z)
      REAL*8 MU,KAPPA
      DIMENSION STRESS(NTENS),STATEV(NSTATV),DDSDDE(NTENS,NTENS),
1  STRAN(NTENS),DSTRAN(NTENS),Stressf(6),Sn(6),Gamma(6),
2  COORDS(3),PREDEF(1),DPRED(1),PROPS(NPROPS)
C
      DATA ZERO,ONE,Onep,TWO,THREE/0.0D0,1.000000D0,1.020000D0
*          ,2.000000D0,3.000000D0/
C
      NDIPL1=NDI+1
C
      TAU=32.5D0  !PROPS(1)
      MU=5.48D3  !PROPS(2)
      KAPPA=9.1333333333D3  !PROPS(3)
C*****
C Calculate the beginning state SIG1 and P1.
C Note that UMINV converts STRESS to its deviatoric part.
C*****
      CALL UMINV (STRESS,P1,SIG1,NDI,NTENS)
C*****
C Calculate the trace of the strain increment.
C*****
      TRACE=ZERO
      DO 10 I=1,NDI
10 TRACE=TRACE+DSTRAN(I)
C*****
C Convert to deviatoric tensor strain components.
C*****
      DO 15 I=1,NDI
15 DSTRAN(I)=DSTRAN(I)-TRACE/THREE
      DO 20 I=NDIPL1,NTENS
20 DSTRAN(I)=DSTRAN(I)/TWO
C*****
C Calculate the new trial stress.
C*****
      DO 30 I=1,NTENS

```



```

30 SN(I)=TWO*MU*DSTRAN(I)+STRESS(I)
C*****
C Calculate SIGTRL.
C*****
CALL UMINV (SN,PDUMMY,SIGTRL,NDI,NTENS)
C*****
C Calculate the pressure at the end of the increment.
C*****
P2=P1-KAPPA*TRACE
C*****
C Determine the state of the initial and final conditions.
C*****
Iflag=0
Close=(.99999999D0* Tau)
If(Sigtrl.Lt.Close) Then
C The final state is elastic.
ETA=ONE
C1=TWO*MU
C2=KAPPA-C1/THREE
C3=ZERO
C Check if the initial state is non-yielding, but the final state is.
Else IF (SIGTRL.Gt.Close.and.SIG1.Lt.Close) then
Iflag=1
Else
C Both initial and final states are plastic. (Use Rice-Tracey)
Iflag=2
End if
C*****
C Decide what method should be used to calculate the stresses and the
C Jacobian. The following section is used if the final state is
C elastic.
C*****
If(Iflag.Eq.0) Then
C*****
C Calculate the deviatoric stress at the end of the increment.
C*****
DO 100 I=1,NTENS
100 STRESS(I)=ETA*Sn(I)
C*****
C Calculate the Jacobian.
C*****
DO 200 I=1,NTENS
DO 200 J=1,NTENS
200 DDSDDE(I,J)=-C3*STRESS(I)*STRESS(J)
DO 210 I=1,NDI

```

```

        DDSDE(I,I)=DDSDE(I,I)+C1
        DO 210 J=1,NDI
210    DDSDE(I,J)=DDSDE(I,J)+C2
        DO 220 I=NDIPL1,NTENS
220    DDSDE(I,I)=DDSDE(I,I)+C1/TWO
C*****
C Convert deviatoric stress to complete stress.
C*****
        DO 225 I=1,NDI
225    STRESS(I)=Stress(I)-P2
C*****
        Else If (Iflag.Eq.2) Then
C*****
C This section is used to implement the Rice-Tracey Mean Normal Operator
C*****
C*****
C Calculate the trail stress and the needed direction.
C*****
        Do 230 I=1,Ntens
230    Sn(i)=Two*Stress(i)+Two*Mu*Dstran(i)
C*****
C Normalize the trail stress and the needed direction.
C*****
        Call Euminv(Sn,Taustar,Ndi,Ntens)
C*****
C Calculate the dot product between the strain increment and stress
C direction.
C*****
        RNdotE=Zero
        Do 240 I=1,Ndi
240    kRNdotE=RNdotE + Sn(i)*Dstran(i)
        Do 250 I=(Ndi+1),Ntens
250    RNdotE=RNdotE + Sn(i)*Dstran(i)*Two
C*****
C Calculate the final stress state
C*****
        Do 260 I=1,Ntens
260    Stressf(i)=Stress(I) + Two*Mu*Dstran(i)
        *    - Two*Two*Mu*RNdotE*Sn(i)
C*****
C Calculate the Jacobian - It is symmetric.
C*****
        Alpha=Two*Mu*(One-Two*Mu*RNdotE/Taustar)
        Do 290 I=1,Ntens
        Do 290 J=1,Ntens

```

```

      Ddsdde(i,j)= -Two*Alpha*Sn(i)*Sn(j)
*      -(Mu/Taustar)*Sn(i)*(Stressf(j)-Stress(j))
*      -(Mu/Taustar)*Sn(j)*(Stressf(i)-Stress(i))
      If(I.Le.Ndi.and.J.Le.Ndi)
*      Ddsdde(i,j)= Ddsdde(i,j) + Kappa - Alpha/Three
      If(I.Eq.J.and.I.Le.Ndi)
*      Ddsdde(i,j)= Ddsdde(i,j) + Alpha
      If(I.Eq.J.and.I.Gt.Ndi)
*      Ddsdde(i,j)= Ddsdde(i,j) + Alpha/Two
290      Continue
C*****
C To prevent numerical drift, the stress will be normalized and the
C equivalent stress scaled to be exactly the yield stress, Tau.
C*****
      CALL UMINV (Stressf,Pug,Scale,Ndi,Ntens)
      Factor=Tau/Scale
C If the new stress is not close to the yield surface, signal it!
      If (Factor.lt.(.99).or.Factor.Gt.(1.01)) then
          Print *,'Scaling factor is ',Factor,
*          'and Initial Equiv. stress is ',Sig1
          End if
          Do 295 I=1,Ntens
295      Stress(i)=Stressf(i)*Factor
C*****
C Convert deviatoric stress to complete stress.
C*****
      DO 300 I=1,NDI
300 STRESS(I)=Stress(I)-P2
C*****
      Else
C*****
C This section is used to implement the Rice-Tracey Mean Normal Operator
C when the initial solution is elastic and the final is plastic.
C*****
C*****
C Calculate the dot product between the strain increment and itself.
C*****
      DEdotDE=Zero
      Do 305 I=1,Ndi
305      DEdotDE=DEdotDE + Dstran(i)**Two
      Do 310 I=(Ndi+1),Ntens
310      DEdotDE=DEdotDE + Dstran(i)*Dstran(i)*Two
C*****
C Calculate the dot product between the strain increment and initial
C stress.

```

```

C*****c*****
      DEdotS=Zero
      Do 315 I=1,Ndi
315      DEdotS=DEdotS + Stress(i)*Dstran(i)
      Do 320 I=(Ndi+1),Ntens
320      DEdotS=DEdotS + Stress(i)*Dstran(i)*Two
C*****
C Calculate the dot product between the initial stress and initial
C stress.
C*****
      SIdotSI=Sig1*Dsqrt(Two/Three)
C*****
C Find beta, the fraction of the elastic strain needed to cause yield
C In the text beta is called alpha.
C*****
      Quad2=Dsqrt((DEdotS**Two)
*          -DEdotDE*(SIdotSI-Two*Close*Close/Three))
      Quad3=Two*Mu*DEdotDE
      Ibeta1=0
      Ibeta2=0
      Beta1=(-DEdotS - Quad2)/Quad3
      Beta2=(-DEdotS + Quad2)/Quad3
c          Logic to find maximum exceptable root.
      If(Beta1.Lt.Zero.or.Beta1.Gt.One) Ibeta1=1 !Unexceptable value
      If(Beta2.Lt.Zero.or.Beta2.Gt.One) Ibeta2=1 !Unexceptable value
      If(Ibeta1.Eq.1.and.Ibeta2.Eq.1) Then
          Beta=One
          Print *,'Beta roots exceed the allowable range. Beta1 ',Beta1
*          ', Beta2 ',Beta2
      Else If(Ibeta1.Eq.1.and.Ibeta2.Eq.0) Then
          Beta=Beta2
      Else If(Ibeta1.Eq.0.and.Ibeta2.Eq.1) Then
          Beta=Beta1
      Else
          Beta=Beta1
          If(Beta2.Gt.Beta1) Beta=Beta2
      End if
C*****
C Calculate the star stress state.
C*****
      Do 325 i=1,Ntens
325      Sn(i)=Two*Stress(i) + (One+Beta)*Two*Mu*Dstran(i)
C*****
C Find the N star-bar direction and it's magnitude. Normalization is
C done in the subroutine.

```

```

C*****
      Call Euminv(Sn,Taustar,Ndi,Ntens)
C*****
C Calculate the dot product between the strain increment and N star-bar
C*****
      SNdotDE=Zero
      Do 330 I=1,Ndi
330      SNdotDE=SNdotDE+ Sn(i)*Dstran(i)
      Do 335 I=(Ndi+1),Ntens
335      SNdotDE=SNdotDE+ Sn(i)*Dstran(i)*Two
C*****
C Calculate the final stress state.
C*****
      Do 340 I=1,Ntens
340      Stressf(i)=Stress(i) + Two*Mu*Dstran(i)
      *      - (One-Beta)*Two*Two*Mu*Sn(i)*SNdotDE
C*****
C Calculate the Gamma tensor.  Determines the change in beta wrt. Dstran
C*****
      Gammacon=(Two*Beta*Mu*DEdotDE+DEdotS)*(-One)
      Do 345 I=1,Ntens
345      Gamma(i)=((Two*Mu*(Beta)**Two)*Dstran(i)
      *      +Beta*Stress(i))/Gammacon
C*****
C Calculate the Jacobian - It is symmetric.
C*****
C*****
C Useful constants for the Jacobian
C*****
      C1=SNdotDE
      D1=(One-Beta)*Two*Mu
      E1=D1*Two*Mu/Taustar
      F1=DEdotDE
      G1=Two*Mu-E1*C1*(One+Beta)
      G2=Two*Two*(Mu*(Beta-One)+E1*C1*(One+Beta))
      G3=Two*Two*Mu*C1+Two*Two*C1*C1*E1-E1*F1
      G4=(-E1)*(One+Beta)
      G5=(-C1*E1)
      Do 390 I=1,Ntens
      Do 390 J=1,Ntens
      Ddsdde(i,j)=
      *      G2*Sn(i)*Sn(j)
      *      +G3*Sn(i)*Gamma(j)/Two
      *      +G4*Sn(i)*Dstran(j)/Two
      *      +G5*Dstran(i)*Gamma(j)/Two

```

```

* +G3*Sn(j)*Gamma(i)/Two
* +G4*Sn(j)*Dstran(i)/Two
* +G5*Dstran(j)*Gamma(i)/Two
  If(I.Le.Ndi.and.J.Le.Ndi)
*   Ddsdde(i,j)= Ddsdde(i,j) + Kappa - G1/Three
  If(I.Eq.J.and.I.Le.Ndi)
*   Ddsdde(i,j)= Ddsdde(i,j) + G1
  If(I.Eq.J.and.I.Gt.Ndi)
*   Ddsdde(i,j)= Ddsdde(i,j) + G1/Two
390   Continue
C*****
C To prevent numerical drift, the stress will be normalized and the
C equivalent stress scaled to be exactly the yield stress, Tau.
C*****
  CALL UMINV (Stressf,Pug,Scale,Ndi,Ntens)
  Factor=Tau/Scale
C If the new stress is not close to the yield surface, signal it!
  If (Factor.lt.(.99).or.Factor.Gt.(1.01)) Then
    Print *,'In mod R-T: Scaling factor is ',Factor,
    *      'and Initial Equiv. stress is ',Sig1
  End if
  Do 395 I=1,Ntens
395  Stress(i)=Stressf(i)*Factor
C*****
C Convert deviatoric stress to complete stress.
C*****
  DO 400 I=1,NDI
  400 STRESS(I)=Stress(I)-P2
C*****
  End if
C*****
  RETURN
  END
C*****

C*****
  SUBROUTINE UMINV (X,XINV1,XINV2,NDI,NTENS)
  IMPLICIT REAL*8 (A-H,O-Z)
  DIMENSION X(NTENS)
C*****>
C This subroutine calculates: >
C   XINV1=- (1/3)*trace(X), >
C converts X to its deviatoric part X', and calculates >
C   XINV2=DSQRT(1.5*X'*X') >
C*****>

```

```

      NDIPL1=NDI+1
      XINV1=0.ODO
      XINV2=0.ODO
C
      DO 10 I=1,NDI
10    XINV1=XINV1-X(I)
      XINV1=XINV1/3.ODO
      DO 20 I=1,NDI
20    X(I)=X(I)+XINV1
      DO 30 I=1,NDI
30    XINV2=XINV2+0.5DO*X(I)*X(I)
      DO 40 I=NDIPL1,NTENS
40    XINV2=XINV2+X(I)*X(I)
      XINV2=3.ODO*XINV2
      XINV2=DSQRT(XINV2)
      RETURN
      END
C*****
C*****
      SUBROUTINE Euminv (X,Xinv2,NDI,NTENS)
      IMPLICIT REAL*8 (A-H,O-Z)
      DIMENSION X(NTENS)
C*****>
C  This subroutine calculates: >
C     $X_{ij} = X_{ij} / (2.0 * (.5 * X_{ij} \text{ Dot } X_{ij})^{.5})$  >
C*****>
      NDIPL1=NDI+1
      XINV2=0.ODO
C
      DO 10 I=1,NDI
10    XINV2=XINV2+0.5DO*X(I)*X(I)
      DO 20 I=NDIPL1,NTENS
20    XINV2=XINV2+X(I)*X(I)
      XINV2=DSQRT(XINV2)
      Xinv=2.0000000D0*Xinv2
      DO 30 I=1,NTENS
30    X(I)=X(I)/Xinv
      RETURN
      END
C*****

```

C.2 Traction-Free Crack-Tip Model

C.2.1 Spring Coefficients

Program Mod_Stiffness

C This program calculates the stiffnesses in terms of the eigenmodes.
C It uses the assumption that twice
C the integral of the traction times the displacement is equal to
C the potential energy of the body. The potential energy is then
C just the product of the stiffness matrix and the coefficient vectors.
C This version used the square-root
C oscillatory terms and the integer homogeneous terms.
C This program has been modified to give the spring format in a
C a manner consistent with ABAQUS 4.6 version.

Complex*16 Phi(20),PhiI(20),PhiII(20),X1(20),X1I(20),X1II(20)
Complex*16 BB(20,20),BcB(20,20),cBcB(20,20),cBB(20,20),Cpss
Complex*16 X2(20),X2I(20),X2II(20),Z1
Complex*16 Con1,Con2,Con3,Con4,Con5,Con6,Z,Zb,Dthe,Ans
IMPLICIT REAL*8 (A-H,O-Z)
DIMENSION A1Aj(20,20),A1Bj(20,20),BiAj(20,20),BiBj(20,20)
DIMENSION C(40,40),D(40,40),E(40,40)

C The material identification is such that material-1 is on the
C upper half and material-2 is on the lower half.
Open(Unit=30,File="Springs")
C Set up the material properties
Em2=2.04D3
Em1=7.2267D5
P2=.02000000000000000000D00
P1=.45000000000000000000D0
Mterms=11 !This is the number of terms desired.
Nterms=5 !This is the number of integer terms desired.
Isec=20 !Number of the node corresponding to the KII term.
Zero=0.000000000000000000D0
Two=2.000000000000000000D0
Three=3.000000000000000000D0
Zepo=1.0E-12 !Minimum stiffness for stiffness to be printed.
C Determine the bi-material Constants and Moduli
G1=Em1/((1.00000000D0+P1)*Two) !Shear Modulus
G2=Em2/((1.00000000D0+P2)*Two) !Shear Modulus
F1=(3.00000000D0-(Two*Two*P1))/G1
F2=(1.00000000D0/G2)
F3=(3.00000000D0-(Two*Two*P2))/G2
F4=(1.00000000D0/G1)
Epsil=(1.00000000D0/(Two*3.14159265358979D0))


```

*          *Dlog((F1+F2)/(F3+F4))
Ps1=3.00000000D0-(Two*Two*P1) !Plain strain Poisson's ratio
Ps2=3.00000000D0-(Two*Two*P2) !Plain strain Poisson's ratio
C1=(Ps1+1.00000000D0)/G1 !Constants needed for the integer terms.
C2=(Ps2+1.00000000D0)/G2
Cc1=Two*C2/(C1+C2)
Cc2=Two*C1/(C1+C2)
Epitheta=Dexp(6.28318530717958D0*Epsil)
R=.1000000D1
C This sets up the integration rules for Simpson's 1/3 Rule.
Ninv=50          !Number of intervals per half/should be even
Nsteps=(Ninv*2)+1          !Number of steps
Tinc=3.14159265358979D0/Dble(Ninv*2)          !Integration step size.
C The integration step is one-half the interval size.
Do 50 i=1,Mterms !Zero out the matrix
Do 50 j=1,Mterms
  AiAj(i,j)=Dcplx(Zero,Zero)
  AiBj(i,j)=AiAj(i,j)
  BiAj(i,j)=AiAj(i,j)
  BiBj(i,j)=AiAj(i,j)
50 Continue
Do 300 KKK=1,Nsteps !Begin the major do loop of the intergration
Do 300 M1=1,2
c This loop is set to integrate the lower half from -pi to zero
c while at the same time integrate the upper half from pi to zero.
c The 'logic' of this is that terms of similar magnitude will be
c accumulated at the same time so that in the case of an anti-
c symmetric term it should contain less error. I hope!
If (M1.Eq.1) then !Lower half first.
  Theta =(-3.14159265358979D0)+((Dble(KKK-1))*Tinc)
  G=G2
  Cposs=Dcplx(Ps2,Zero)
  Cc=Cc2
Else          !Upper half second.
  Theta =(3.14159265358979D0)-((Dble(KKK-1))*Tinc)
  G=G1
  Cposs=Dcplx(Ps1,Zero)
  Cc=Cc1
End if
Dthe=Dcplx((Dcos(Two*Theta)),
*      (Dsin(Two*Theta)))
Z=Dcplx((R*Dcos(Theta)),(R*Dsin(Theta)))
Zb=Dconjg(Z)
Do 100 i=1,Mterms
  P=.50000000D0^(i-1)

```

```

Q=(1-i)-.5000000000D0
Con1=Dcplx(P,(-1.0000000D0+Epsil))      !P-ie
Con2=Dcplx(P,(Epsil))                  !P+ie
Con3=Dcplx(Q,(-1.0000000D0+Epsil))     !Q-ie
Con4=Dcplx(Q,Epsil)                    !Q+ie
Con5=Con3-Dcplx(1.0000000D0,Zero)      !Q-1-ie
Call Power(R,Theta,Con3,Ans)
Phi(i)=Dcplx(Two,Zero)*Con1*Ans
  If (M1.Eq.1) Phi(i)=Phi(i)*Dcplx(Epitheta,Zero)
C   !This adjusts for the lower half potential function.
PhiI(i)=Phi(i)*Con3/Z
PhiII(i)=PhiI(i)*Con5/Z
Call Power(R,Theta,Con2,Ans)
X1(i)=Dcplx(Two,Zero)*
*   Dcplx(Epitheta,Zero)*Ans
Call Power(R,Theta,Con1,Ans)
X2(i)=Dcplx(Two,Zero)*Con3*Ans
  If (M1.Eq.1) then
    X1(i)=X1(i)/Dcplx(Epitheta,Zero) !This adjusts the potential
    X2(i)=X2(i)*Dcplx(Epitheta,Zero) !functions for being on the
    End If                               !lower half.
X1I(i)=X1(i)*Con2/Z
X2I(i)=X2(i)*Con1/Z
X1II(i)=X1I(i)*Con4/Z
X2II(i)=X2I(i)*Con3/Z
  If(i.GT.(Mterms-Nterms)) Then
c   This section calculates out the terms associated with the integer
c   powers of the series expansion starting out at n=-2.
  jj=Nterms-1-1
  Call Power (R,Theta,(Dble(jj+1)),Ans)
  X1I(i)=Dcplx(-Cc,Zero)*Conjg(Ans/Z)*Z
  X1II(i)=X1I(i)/Z
  X2I(i)=Dcplx(Cc,Zero)*Ans
  X2II(i)=Dcplx((Dble(jj+1)),Zero)*X2I(i)/Z
  PhiI(i)=Dcplx(Cc,Zero)*Ans/Z
  PhiII(i)=Dcplx((Dble(jj)),Zero)*PhiI(i)/Z
  Phi(i)=PhiI(i)*Z/Dcplx((Dble(jj+1)),Zero)
  End if
100 Continue
Do 200 i=1,Mterms !The following are the individual terms
c   associated with the complex variable bb and is conjugates.
Do 200 j=1,Mterms
  BB(i,j)=Zb*(
*   (Z*Dconjg(PhiI(i)*PhiI(j)))
*   -(Z*Dconjg(PhiI(i))*Dthe*X1II(j))

```

```

*      -(Dconjg(X2I(i)*PhiI(j)))
*      +(Dconjg(X2I(i))*Dthe*X1II(j)))
BcB(i,j)=Zb*(
*      (Z*Dconjg(PhiI(i))*Dthe*X2II(j))
*      -(Z*Dconjg(PhiI(i))*Dthe*Zb*PhiII(j))
*      +(Z*Dconjg(PhiI(i))*PhiI(j))
*      +(Dthe*Zb*Dconjg(X2I(i))*PhiII(j))
*      -(Dthe*Dconjg(X2I(i))*X2II(j))
*      -(Dconjg(X2I(i))*PhiI(j)))
cBB(i,j)=Zb*(
*      (Phi(i)*Dthe*X1II(j)*Cposs)
*      -(Phi(i)*Dconjg(PhiI(j))*Cposs)
*      -(Dconjg(X1I(i))*Dthe*X1II(j))
*      +(Dconjg(X1I(i))*PhiI(j)))
cBcB(i,j)=Zb*(
*      (Phi(i)*Dthe*Zb*PhiII(j)*Cposs)
*      -(Phi(i)*Dthe*X2II(j)*Cposs)
*      -(Phi(i)*PhiI(j)*Cposs)
*      -((Dconjg(X1I(i))*Dthe*Zb*PhiII(j)) !The Problem Term.
*      +(Dconjg(X1I(i))*Dthe*X2II(j))
*      +(Dconjg(X1I(i))*PhiI(j)))
200  Continue
C    This section adjusts the weighting factor applied to each point.
C    This is in accordance with Simpson's 1/3 rule.
If (KKK.Eq.1.or.KKK.Eq.Nsteps) Then
  Rinc=Tinc/Three
Else
  K1=KKK/2
  K2=K1*2
  If (K2.Eq.KKK) Then !KKK is an even number
    Rinc=Two*Two*Tinc/Three
  Else
    Rinc=Two*Tinc/Three
  End If
End If
Do 300 i=1,Mterms
Do 300 j=1,Mterms
A1Aj(i,j)=Dreal(BB(i,j)+cBB(i,j)+BcB(i,j)+cBcB(i,j))*Rinc/(G*Two)
*      + A1Aj(i,j)
B1Bj(i,j)=Dreal(BcB(i,j)-BB(i,j)+cBB(i,j)-cBcB(i,j))*Rinc/(G*Two)
*      + B1Bj(i,j)
B1Aj(i,j)=Dimag(BB(i,j)+BcB(i,j)-cBB(i,j)-cBcB(i,j))*Rinc/(G*Two)
*      + B1Aj(i,j)
A1Bj(i,j)=Dimag(BB(i,j)-BcB(i,j)+cBB(i,j)-cBcB(i,j))*Rinc/(G*Two)
*      + A1Bj(i,j)

```

```

300 Continue      !End of the integration.
Do 400 i=1,Mterms !Form the global stiffness matrix.
Do 400 j=1,Mterms
  C(i,j)=AiAj(i,j)
  C(i,(j+Mterms))=AiBj(i,j)
  C((i+Mterms),j)=BiAj(i,j)
  C((i+Mterms),(j+Mterms))=BiBj(i,j)
400 Continue
Do 500 i=1,(2*Mterms) !Upper triangularize the global stiffness
Do 500 j=i,(2*Mterms) !matrix. Use only one spring per node set.
  D(i,j)=C(j,i)+C(i,j) !The other half is being filled in for
  If(i.Ne.j) D(j,i)=D(i,j) !convenience only.
  If(i.Eq.j) D(j,i)=D(j,i)/Two
500 Continue

C      This section adjusts for the springs working on the difference
C      between the two degrees of freedom, instead of the degree's
C      of freedom's product. It becomes very important to determine
C      at this time how many terms are actually going to be used.
Do 550 i=1,(2*Mterms)
Do 550 j=i,(2*Mterms)
  If(i.Ne.j) then
    E(i,j)=(-.500000000000)*D(i,j)
  Else
    E(i,j)=D(i,j)+(.500000000000)
    Do 525 K=1,(Mterms*2)
      E(i,j)=E(i,j)+(.500000000000)*D(i,k)
525   Continue
      End If
550 Continue
      Ncount=8999 !Set up elset numbering counter.
Do 600 i=1,Mterms
Do 600 j=i,Mterms
  Ncount=Ncount+1
  II=i+1
  JJ=j+1
  If (Dabs(E(i,j)).Gt.Zepo) then
    If(i.Ne.j) then
      Write (30,1012) Ncount,Ncount,II,JJ
      Write (30,1016) Ncount,E(i,j)
    Else
      Write (30,1011) Ncount,Ncount,II
      Write (30,1015) Ncount,E(i,j)
    End If
  End If
End If

```

```

600  Continue
      Do 700 i=1,Mterms
      Do 700 j=(Mterms+1),(2*Mterms)
          Ncount=Ncount+1
          II=i+1
          JJ=j-Mterms+1+Isec
          If (Dabs(E(i,j)).Gt.Zepo) then
              Write (30,1012) Ncount,Ncount,II,JJ
              Write (30,1016) Ncount,E(i,j)
          End If
700  Continue

      Do 800 i=(Mterms+1),(2*Mterms)
      Do 800 j=i,(2*Mterms)
          Ncount=Ncount+1
          II = i+1-Mterms + Isec
          JJ = j+1-Mterms + Isec
          If (Dabs(E(i,j)).Gt.Zepo) then
              If(i.Ne.j) then
                  Write (30,1012) Ncount,Ncount,II,JJ
                  Write (30,1016) Ncount,E(i,j)
              Else
                  Write (30,1011) Ncount,Ncount,II
                  Write (30,1015) Ncount,E(i,j)
              End If
          End If
800  Continue
1011 Format(' *ELEMENT,TYPE=SPRING1,ELSET=SP',I4,/,3I5 )
1012 Format(' *ELEMENT,TYPE=SPRING2,ELSET=SP',I4,/,3I5 )
1016 Format(' *SPRING,ELSET=SP',I4 ,/, '1',/,E17.11,',' )
1016 Format(' *SPRING,ELSET=SP',I4 ,/, '1,1',/,E17.11,',' )
      End

```

Subroutine Power(R,Theta,Con,Ans)

```

C      This subroutine calculates a complex number Z,( R,Theta),
C      raised to a another complex number Con.
      Complex*16 Z,Con,Ans
      IMPLICIT REAL*8 (A-H,O-Z)
      Ans=Dcmplx( ( R**Dreal(Con) ) ,0.000000000000000)
*      *Dcmplx( (Dexp(-1.000000000*Theta*Dimag(Con))),0.000000000000000)
*      *Dcmplx((Dcos(Dimag(Con)*Dlog(R)),(Dsin(Dimag(Con)*Dlog(R))))
*      *Dcmplx((Dcos(Dreal(Con)*Theta),(Dsin(Dreal(Con)*Theta)) )
      Return
      End

```

C.2.2 MPC Subroutine

```
Subroutine MPC (Ue,A,Jdof,N,Jtype,X,U,Nmpce)
  IMPLICIT REAL*8 (A-H,O-Z)
  DIMENSION A(n),JDOF(n),X(6,n),U(6,n)
C   This program imposes the asymptotic bi-material crack tip
C   displacements as an MPC. The order of the MPC as it should
C   appear in the deck is MPC#,Node#,Knode,Knode. Here MPC#
C   should be 1 for dof 1 and 2 for dof 2 in the upper half.
C   While 11 should be used for dof 1 and 12 for dof 2 in the
C   lower half. Note, this means that for every node to be tied
C   it has to be entered in twice; once for each dof. Node# is
C   the number of the constrained node while Knode is the number
C   of the extra node. The desired  $K_i$  strength should be given
C   as Knode's dof 1 displacement while the  $K_{ii}$  should be given
C   as Knode's dof 2 displacement. The subscript 1 and 2 refer to
C   the upper (1) and lower (2) materials respectively. The
C   Knode numbering are arranged with the first Iinteg minus one
C   terms corresponding to the square-root order terms while the
C   following terms correspond to the integer terms. (Starting from
C   the  $n=-2$  term.)
  Iinteg=7 !# of square-root terms including the K terms.
  Rone =(-1.000000000000000D0) ! Useful constants
  Zone =1.000000000000000D0
  Two  =2.000000000000000D0
  Three=3.000000000000000D0
  Pie  =3.14159265358979D0
C   Determine the R and theta coordinates.
  Theta=Datan2( X(2,1),X(1,1) )
  If(X(1,1).Lt.(0.0D0).and.Dabs(X(2,1)).Lt.(0.0001D0)) Theta=Pie
  Theta =Dabs(Theta) ! This always gives a positive theta.
  If(Jtype.Eq.11.or.Jtype.Eq.12) Theta=Theta*Rone
  R=Dsqrt(X(1,1)*X(1,1)+X(2,1)*X(2,1))
C   Set up the material properties
  Em2=70.1D03
  Em1=13.7D03
  P2=.342D0
  P1=.25D0
C   Determine the bi-material displacements
  G1=Em1/((Zone+P1)*Two) !Shear Modulus
  G2=Em2/((Zone+P2)*Two) !Shear Modulus
  F1=(Three-(Two*Two*P1))/G1
  F2=(Zone/G2)
  F3=(Three-(Two*Two*P2))/G2
  F4=(Zone/G1)
```

```

Epsil=(Zone/(Two*Pie))*Dlog((F1+F2)/(F3+F4))
C1=F1+F4          !These are constants used in the integer
C2=F3+F2          !function expansion.
Cc1=Two*C2/(C1+C2)
Cc2=Two*C1/(C1+C2)
If (Jtype.EQ.11.OR.Jtype.EQ.12) then
  G=G2  !This adjust for the material being on the down side.
  Rnj=Three-(Two*Two*P2)
  Cc=Cc2
Else
  G=G1 ! Assume that the node is on the upper half
  Rnj=Three-(Two*Two*P1) !Plain strain Poisson's ratio
  Cc=Cc1
End If
Uit=0.ODO          !Initialize the displacements before the do loop.
Vit=Uit
A(1)=Zone
MM=(N-1)/2        !Adjustment for the due loop
Coshpe=((Dexp(Epsil*Pie))+Dexp(Epsil*(Rone*Pie)))/
& Two) !Correction of Rice's original solution.
Etheta=Dexp(Epsil*Theta)
Epitheta=Dexp(Two*Pie*Epsil)
Re=Epsil*(Dlog(R))
Con3=(Three/(Two*Two)) - Epsil*Epsil
Con4= Two * Epsil
Con7=10.026513D0 * Dexp(Pie*Epsil) *
* ( Con4 * Con4 + Con3 * Con3)
Do 200 I=1,MM ! The number of terms involved is the second limit
  If (I.LE.Iinteg) then !These terms are used for the square-
    !root expansion.
    II=2-I
    P=Dble(II)+(Zone/Two)
    Q=Dble(II)-(Zone/Two)
    CRe=DCos(Re)
    SRe=DSin(Re)
    CQt=DCos(Q*Theta)
    SQt=DSin(Q*Theta)
    CQ2t=DCos((Two-Q)*Theta)
    SQ2t=DSin((Two-Q)*Theta)
    Term1=CRe*CQt+SRe*SQt
    Term2=CRe*SQt-SRe*CQt
    Term3=CRe*CQ2t-SRe*SQ2t
    Term4=CRe*SQ2t+SRe*CQ2t
    Term5=CRe*CQt-SRe*SQt
    Term6=CRe*SQt+SRe*CQt

```

```

Con1=(P*Q)-(Epsil*Epsil)
Con2=(P+Q)*Epsil
End If
C The terms Fe1 and Fe3 are associated with the e_n term in my expan.
C The terms Fe2 and Fe4 are associated with the f_n term in my expan.
If((Jtype.EQ.11.or.Jtype.EQ.12).and.I.LE.Iinteg) then
c   These are done for the lower half.
Fe1=(P*Term1 + Epsil*Term2)*(Etheta)*Rnj*Epitheta -
*   (Con1*Term3 - Con2*Term4)*(Etheta)*Epitheta -
*   (P*Term5 - Epsil*Term6)/Etheta +
*   (Con1*Term1 + Con2*Term2)*Etheta*Epitheta
Fe2=(Epsil*Term1 - P*Term2)* Etheta*Rnj*Epitheta -
*   (Con2*Term3 + Con1*Term4)* Etheta*Epitheta -
*   (P*Term6 + Epsil*Term5)/Etheta -
*   (Con1*Term2 - Con2*Term1)*Etheta*Epitheta
Fe3=(P*Term2 - Epsil*Term1)*(Etheta)*Rnj*Epitheta -
*   (Con2*Term3 + Con1*Term4)*(Etheta)*Epitheta +
*   (P*Term6 + Epsil*Term5)/Etheta -
*   (Con1*Term2 - Con2*Term1)* Etheta*Epitheta
Fe4=(Epsil*Term2 + P*Term1)*(Etheta)*Rnj*Epitheta +
*   (Con1*Term3 - Con2*Term4)*(Etheta)*Epitheta -
*   (P*Term5 - Epsil*Term6)/Etheta -
*   (Con1*Term1 + Con2*Term2)*(Etheta)*Epitheta
Rcon=(Zone/(G*Coshpe))*(R**Q)
Else If ((Jtype.EQ.1.or.Jtype.EQ.2).and.I.LE.Iinteg) then
! These are done for the upper half.
Fe1=(P*Term1 + Epsil*Term2)*(Etheta)*Rnj -
*   (Con1*Term3 - Con2*Term4)*(Etheta) -
*   (P*Term5 - Epsil*Term6)*Epitheta/Etheta +
*   (Con1*Term1 + Con2*Term2)*Etheta
Fe2=(Epsil*Term1 - P*Term2)* Etheta * Rnj -
*   (Con2*Term3 + Con1*Term4)* Etheta -
*   (P*Term6 + Epsil*Term5)*Epitheta/Etheta -
*   (Con1*Term2 - Con2*Term1)*Etheta
Fe3=(P*Term2 - Epsil*Term1)*(Etheta)*Rnj -
*   (Con2*Term3 + Con1*Term4)*(Etheta) +
*   (P*Term6 + Epsil*Term5)*Epitheta/Etheta -
*   (Con1*Term2 - Con2*Term1)* Etheta
Fe4=(Epsil*Term2 + P*Term1)*(Etheta)*Rnj +
*   (Con1*Term3 - Con2*Term4)*(Etheta) -
*   (P*Term5 - Epsil*Term6)*Epitheta/Etheta -
*   (Con1*Term1 + Con2*Term2)*(Etheta)
Rcon=(Zone/(G*Coshpe))*(R**Q)
Else If (I.GT.Iinteg) Then !This begins the integer
! section of the expansion.

```



```

Mno=Iinteg-I-1
Rmno1=Dble(Mno-1)
Rmno3=Dble(Mno+1)
Rcon=Cc*(R**Rmno3)/(Two*G)
Argp=Theta*Rmno3
Argn=Theta*Rmno1
Fe1=((Rnj+Rmno3)/Rmno3)*Dcos(Argp)
Fe2=(-(Rnj+Rmno3)/Rmno3)*Dsin(Argp)
Fe3=((Rnj-Rmno3)/Rmno3)*Dsin(Argp) + Two*Dsin(Argn)
Fe4=((Rnj-Rmno3)/Rmno3)*Dcos(Argp) + Two*Dcos(Argn)
Else
Print *, 'Your are in deep.....'
End if

```

```

C The U(*,*) are the stress intensity factors. Therefore an adjustment
C must be made to convert them into the proper form. What follows are
C the derivatives of the displacements with respect to the Stress
C Intensity factors. Or the unknown degrees of freedom.
C The conversion to the Stress Intensity Factors only occurs for
C the square root term. The remaining terms are left as the unknowns
C a+ib. This is done because the evaluation of the far-field is much
C easier using aj+ibj instead of K1j+iK2j. Another separation is
C given to the integer terms and the square-root order terms.

```

```

If(I.Eq.1) then
UK1= Rcon*(Fe1*Con3 + Fe2*Con4)/Con7
UK2= Rcon*(Fe2*Con3 - Fe1*Con4)/Con7
VK1= Rcon*(Fe3*Con3 + Fe4*Con4)/Con7
VK2= Rcon*(Fe4*Con3 - Fe3*Con4)/Con7
Else If(I.Gt.Iinteg) then
UK1=Rcon*Fe1
UK2=Rcon*Fe2
VK1=Rcon*Fe3
VK2=Rcon*Fe4

```

```

Else
UK1= Rcon*Fe1*Coshpe
UK2= Rcon*Fe2*Coshpe
VK1= Rcon*Fe3*Coshpe
VK2= Rcon*Fe4*Coshpe

```

```

End If
Jdof(2*I+1)=1 ! node in the expansion.
Jdof(2*I)=1 !Give the correct degree of freedom for each free
IF (Jtype.Eq.1) then
JDof(1)=1
A(2*I)=Rone*UK1
A(2*I+1)=Rone*UK2
Else IF (Jtype.Eq.11) then

```

```

      JDOF(1)=1
      A(2*I)=Rone*UK1
      A(2*I+1)=Rone*UK2
ELSE IF (Jtype.Eq.2) then
      JDOF(1)=2
      A(2*I)=Rone*VK1
      A(2*I+1)=Rone*VK2
ELSE      !      (Jtype.Eq.12)
      JDOF(1)=2
      A(2*I)=Rone*VK1
      A(2*I+1)=Rone*VK2
END IF
      Uit=Uit+(U(1,(2*I))*A(2*I) + U(2,(2*I+1))*A(2*I+1))
      Vit=Vit+(U(1,(2*I))*A(2*I) + U(2,(2*I+1))*A(2*I+1))
200      Continue
C      Figure out which dof is being sought and is it in the upper or
C      lower half. Also, give the total displacement.
      IF (JTYPE.EQ.1.OR.JTYPE.EQ.11) THEN
          JDOF(1)=1
          UE=Uit
      ELSE      !IF (Jtype.Eq.2.or.Jtype.Eq.12) THEN
          JDOF(1)=2
          UE=Vit
      END IF
      Return
      End

```

C.3 Closed Crack-Tip : MPC Subroutine

```

Subroutine MPC (Ue,A,Jdof,N,Jtype,X,U,Nmpce,Kstep,Kinc,Time)
IMPLICIT REAL*8 (A-H,O-Z)
DIMENSION A(n),JDOF(n),X(6,n),U(6,n)
C      For      ABAQUS - VERSION 4.6
C      This program imposes the asymptotic bi-material crack-tip
C      displacements as an MPC. This is the routine used to enforce
C      the CLOSED crack-tip model. The order of the MPC as it should
C      appear in the deck is MPC#,Node#,Knode, Here MPC#
C      should be 1 for dof 1 and 2 for dof 2 in the upper half.
C      While 11 should be used for dof 1 and 12 for dof 2 in the
C      lower half. Note, this means that for every node to be tied
C      it has to be entered in twice; once for each dof. Node# is
C      the number of the constrained node while Knode is the number
C      of the extra node. The desired Kii strength should be given
C      as Knode's dof 1 displacement. The subscript 1 and 2 refer to

```

```

C   the upper (1) and lower (2) materials respectively.
Rone =(-1.00000000000000D0) ! Useful constants
Zone =1.00000000000000D0
Two  =2.00000000000000D0
Three=3.00000000000000D0
Pie  =3.14159265358979D0

C   Determine the R and theta coordinates.
Theta=Datan2( X(2,1),X(1,1) )
If(X(1,1).Lt.(0.0D0).and.Dabs(X(2,1)).Lt.(0.0001D0)) Theta=Pie
Theta =Dabs(Theta) ! This always gives a positive theta.
If(Jtype.Eq.11.or.Jtype.Eq.12) Theta=Theta*Rone
R=Dsqrt(X(1,1)*X(1,1)+X(2,1)*X(2,1))

C   Determine the bi-material constant. Caution: use Comninou's
C   ordering. Give Beta with 1 in the lower region!
Beta=-0.24012000D0

C   Set up the material properties
Em1=70.1D03
Em2=211.4D16
P1=.342D0
P2=.300D0

C   Solve for the shear modulus
G1=Em1/((Zone+P1)*Two) !Shear Modulus upper domain
G2=Em2/((Zone+P2)*Two) !Shear Modulus lower domain
If (Jtype.EQ.11.OR.Jtype.EQ.12) then
    G=G2 !This adjust for the material being on the down side.
    Rnj=Three-(Two*Two*P2)
Else
    G=G1 ! Assume that the node is on the upper half
    Rnj=Three-(Two*Two*P1) !Plain strain Poisson's ratio
    Beta=Beta*Rone !Adjust for Beta in the upper domain.
End If
A(1)=Zone
F1=Rone*((Dsqrt(Two*R))/(Two*Two*Two*G))
F2=(Two*Rnj-Zone)*(Zone-Beta)*Dsin(Theta/Two)
F3=(Three+Beta)*Dsin(Three*Theta/Two)
Ur=F1*(F2-F3)
F4=(Two*Rnj+Zone)*(Zone-Beta)*Dcos(Theta/Two)
F5=(Three+Beta)*Dcos(Three*Theta/Two)
Uo=F1*(F4-F5)

C   Rotate the displacements into the Cartesian Coordinate frame.
Ux=(Ur*Dcos(Theta))-(Uo*Dsin(Theta))
Uy=(Uo*Dcos(Theta))+(Ur*Dsin(Theta))
    Jdof(2)=1 !Imposing DOF of K_II node.
IF ((Jtype.Eq.1).or.(Jtype.Eq.11)) then
    JDOF(1)=1

```

```

    A(2)=Rone*Ux
ELSE IF ((Jtype.Eq.2).or.(Jtype.Eq.12)) then
    JDOF(1)=2
    A(2)=Rone*Uy
ELSE
    Print *, 'You goofed up!'
END IF
    Uit= U(1,2)*A(2) !Get the actual displacement
    Vit= U(1,2)*A(2)
C Figure out which dof is being sought and is it in the upper or
C lower half. Also, give the total displacement.
IF (JTYPE.EQ.1.OR.JTYPE.EQ.11) THEN
    JDOF(1)=1
    UE=Uit
ELSE          ! IF (Jtype.Eq.2.or.Jtype.Eq.12) THEN
    JDOF(1)=2
    UE=Vit
END IF
Return
End

```